UC Santa Barbara

UC Santa Barbara Electronic Theses and Dissertations

Title

Functionalizing ortho-carboranes for redox-switchable metal capture and release of critical minerals essential for clean energy.

Permalink

https://escholarship.org/uc/item/5m4259h7

Author

Heinrich, Shannon

Publication Date

2023

Peer reviewed|Thesis/dissertation

eScholarship.org Powered by the California Digital Library
University of California

UNIVERSITY OF CALIFORNIA

Santa Barbara

Functionalizing *ortho*-carboranes for redox-switchable metal capture and release of critical minerals essential for clean energy.

A dissertation submitted in partial satisfaction of the

requirements for the degree Doctor of Philosophy

in chemistry

by

Shannon Erica Heinrich

Committee in charge:

Professor Gabriel Ménard, Chair

Professor Trevor Hayton

Professor Peter Ford

Professor Lior Sepunaru

September 2023

The dissertation of Shannon Erica Heinrich is approved.

_____
Trevor Hayton

_____
Peter Ford

_____
Lior Sepunaru

_____
Gabriel Ménard, Committee Chair

August 2023

Functionalizing *ortho*-carboranes for redox-switchable metal capture and release of critical minerals essential for clean energy.

Copyright © 2023

by

Shannon Erica Heinrich

ACKNOWLEDGEMENTS

I would like to acknowledge my advisor, Gabriel Ménard, for his support throughout the years both professionally and personally. Thank you Gab for the freedom to explore my own research interests and passions. I appreciate your mentorship, positive attitude, and your continued advisement after switching universities, albeit from afar. Most importantly, I will never forget your stellar contributions when acquiring Taylor Swift concert tickets during group meeting. Thank you for verifying that Ticket Master indeed crashed in Canada too. I would like to thank the Gab lab as a collective for being one of the most supportive environments. I had fun in the lab nearly every day, in our close office quarters and working shoulder-to-shoulder in gloveboxes. Specifically, thank you to my older graduate student mentors, Tim Carroll and Sam Jacob. You both taught me how to become a better scientist and how to treat a glovebox with unrequited love. I would like to thank my peers Maxwell Mattejat, Arunavo Chakraborty, and Hila Benhaim. Each of you brightened my graduate school experience and I could not ask for more helpful or kinder labmates and friends. I will miss our boardgame nights, potlucks/cooking sessions and reality TV binging.

I would like to thank all my graduate school friends, and particularly Vani Singhania, Greta Koumarianou, Ann Williams, and Christina Makris for the tremendous support they have provided throughout the years. Shoutout to bagel hour for becoming a place where our cohort bonded over graduate school struggles. I will miss our holiday parties but hope that we can continue them throughout the coast of California. Thank you to my Cal Poly friends, Danica Hagen, Jonathon Babila, and Sarah Wong for your continued support through college and graduate school. Phone calls and weekend visits were much needed breaks to recharge

and recuperate. Cal Poly, and specifically the community within AXΣ and copper, was a place where I could truly discover myself and meet other people passionate about chemistry. Special thanks to David Zigler, my undergraduate research advisor, for his mentorship and for introducing me to inorganic chemistry and electrochemistry. Thank you to all Cal Poly faculty within the department of chemistry and biochemistry.

I would like to thank my siblings, Justin Heinrich and Ben and Brittany Coté. Justin, thank you for always hyping me up and being a great older brother. Ben, thank you for your support and insight into graduate school, particularly at UCSB. Now our family has 2 doctors, but not the kind useful for a medical emergency! Brittany, thank you for being a fantastic older sister. I appreciate all the love you have showered me with throughout the years.

Thank you again to everyone who has been a part of my life. None of this would have been possible without the love and support of so many people and I am incredibly fortunate for your relentless, positive impacts in my life.

Shannon Heinrich

(858) 344-1911 | shannon.heinrich@gmail.com | www.linkedin.com/in/shannonheinrich

EDUCATION

University of California, Santa Barbara — Santa Barbara, CA
Ph.D. in Chemistry — August 2023

California Polytechnic State University, San Luis Obispo — San Luis Obispo, CA
B.S. in Chemistry, Magna Cum Laude with Honors — June 2018

TECHNICAL SKILLS

- *Characterization:* SEM-EDS, CV, DPV, XRD, CLSM, ICP-OES, MALDI, GCMS, ESI-MS
- *Synthesis:* Organic and Inorganic techniques, Solid-Phase, Schlenk line, Glove Box
- *Purification:* Recrystallization, Column Chromatography, Trituration, Sublimation
- *Spectroscopies:* FTIR, UV–Visible, ^{1}H–, ^{11}B–, ^{31}P–, ^{7}Li–, ^{13}C–, ^{19}F–NMR, 2D COSY, EPR

RESEARCH PUBLICATIONS

1. **Heinrich, S.;** Benhaim, H.; Mattejat, M.; Pan, D.; Dimarco, S.; Wu, G.; Ménard, G. Tuning Phosphine Oxide-Substituted *ortho*-Carboranes for Improved Biphasic Electrochemical UO_2^{2+} Capture and Release. *Inorganic Chemistry. Accepted.* https://doi.org/10.1021/acs.inorgchem.3c01960
2. **Heinrich, S.;** Wang, Z.; Yeow, A.; Sepunaru, L.; Ménard, G. Selective lithium capture and release with redox switchable ortho-carborane based crown ether. *In Preparation*
3. Newman, A.; Madriaga, J.; Sieffert, M.; Henry, A.; **Heinrich, S**.; Jarboe, J.; Swift, V.; Cheong, A.; Haynes, T.; Zigler, D. Substituent effects on the UV-visible spectrum and excited electronic states of dithiocarboxylates. *Photochem Photobiol Sci* **2022**, *21*, 303-318
4. Peterson, M.; Hunt, C.; Wang, Z.; **Heinrich, S.E**.; Wu, G.; Ménard, G. Synthesis, characterization, and electrochemical properties of a first-row metal phthalocyanine series. *Dalton Trans*. **2020**, *49*, 16268-16277
5. Owens-Baird, B.; **Heinrich, S**.; Kovnir, K. Thermoelectric Materials. *Encyclopedia of Inorganic and Bioinorganic Chemistry.* **2017**, 1–35

PATENTS

1. Ménard, G.; Sepunaru, L.; Wang, Z.; **Heinrich, S.** 2022. Selective Electrochemical Capture and Release of Lithium from Seawater. Provisional Application No. 63333278, filed April 21, 2022. *Patent pending*

RESEARCH PRESENTATIONS

1. **Heinrich, S.***;* Ménard, G. *"Polypyridyl carboranes for redox-switchable cobalt capture and release."* ACS Fall 2022, Chicago. August 2022. Oral
2. **Heinrich, S.***;* Ménard, G. *"Probing the effects of electronics in phosphine oxide carboranes for electrochemical uranyl capture."* SoCal Organometallics, Santa Barbara. June 2022. Oral
3. **Heinrich, S.***;* Ménard, G. *"Functionalizing carboranes for redox-switchable uranyl capture and release."* Pacifichem 2021, Virtual. December 2021. Poster
4. **Heinrich, S.**; Ménard, G. *"Functionalizing Carboranes for Uranyl Capture and Release."* UC Chemical Symposium 2021, Virtual. March 2021. Poster
5. **Heinrich, S.**; Mattison, M.; Zigler, D. *"Stabilization of electronic transitions in cobalt(III) trisdithiocarboxylate complexes."* CSM Student Research Conference 2018, Cal Poly SLO. May 2018. Oral

6. Mattison, M.; **Heinrich, S**.; Ford, P.; Zigler, D. *"A Spectrochemical Series of tris-(dithiocarboxylate)cobalt(III) Complexes."* Inter-American Photochemical Society Winter Conference 2018, Sarasota, FL. January 2018. Poster
7. **Heinrich, S**.; Mattison, M.; Zigler, D. *"A spectrochemical series of Co (III) complexes with varying substituent groups."* Frost Symposium 2017, Cal Poly SLO. Aug 2017. Oral
8. **Heinrich, S**.; Owens-Baird, B.; Dolyniuk, J.; Kovnir, K. *"Optimization of the CsCl reduction-oxidation flux synthesis of Cs-Zn-Sb clathrates."* American Chemical Society Spring Meeting, San Francisco, CA. April 2017. Poster
9. **Heinrich, S**.; Owens-Baird, B.; Dolyniuk, J.; Kovnir, K. *"Synthesis of $Cs_8Zn_{18}Sb_{28}$ Clathrate for Thermoelectric Applications."* UC Davis ChemEnergy REU Symposium, University of California at Davis, Aug 2016. Poster

AWARDS & FELLOWSHIPS

University of California, Santa Barbara Santa Barbara, CA

- Decolvenaere Graduate Research Accelerator Award 2022
- Outstanding Service to the Department 2022
- UC Chemical Symposium 2021 Best Inorganic Poster
- NSF GRFP Honorable Mention, 2020

California Polytechnic State University San Luis Obispo, CA

- ACS Division of Inorganic Chemistry Undergraduate Award, 2018
- Outstanding Graduate in Chemistry, 2018
- Academic Excellence in Chemistry, 2017– 2018
- Frost Research Fellow in the Frost Summer 2017 Undergraduate Research Program
- Outstanding 1st year student in Chemistry, 2015

University of California, Davis Davis, CA

- NSF ChemEnergy REU Fellow, 2016

LEADERSHIP EXPERIENCE

- Chemistry Professional Development (ChemPD) Alumni Officer, 2021–2022
- Research Mentor, 2018 – 2022
- Lead Teaching Assistant, 2020 – 2021
- Teaching Assistant, 2018 – 2020
- Women in Science and Engineering (WiSE) Mentor, 2019 – 2020
- Family Ultimate Science Exploration (FUSE), 2019 – 2020
- Alpha Chi Sigma, Gamma Zeta Community Service Representative, 2017 – 2018
- Alpha Chi Sigma, Gamma Zeta Alumni Secretary, 2016 – 2017

Abstract

Functionalizing *ortho*-carboranes for redox-switchable metal capture and release of critical minerals essential for clean energy.

by

Shannon Erica Heinrich

The transition from fossil fuels towards renewable energy and energy storage is vital for reducing greenhouse gas emissions. Uranium, lithium, and cobalt are critical for nuclear power and battery storage. The demand for these minerals is increasing rapidly because of the shift towards clean energy. However, they are typically sourced from terrestrial mining, an environmentally taxing process. The mining industry accounts for 8% of global greenhouse gas emissions. Accordingly, it is crucial that we develop new strategies for sourcing critical minerals used in clean energy technology. Advancements in selective electrochemical metal capture chemistry could expand critical mineral extraction technologies to unconventional sources – spent nuclear fuel, seawater, end-of-life batteries.

In this thesis, we present new derivatized *o*-carborane ($C_2B_{10}H_{12}$) clusters functionalized with donor (phosphine oxide, crown-ether, bipyridyl) appendages to target selective, electrochemical metal capture and release. Derivatized *o*-carboranes are redox switchable between the neutral (*closo*) and dianionic (*nido*) states. Herein, we observe metal binding in *nido* form and metal release in *closo* form. In Chapter 2, we discuss how tuning

phosphine oxide carborane basicity may alter the donicity by installing electron withdrawing or electron donating groups on the carborane cage or aryl substituents. We further investigate these effects on uranyl (UO_2^{2+}) ligation and biphasic capture/release chemistry and discover that hydrophobicity may be more important than tuning electronics. In Chapter 3, we extend carborane chemistry to crown-ether substituted derivatives for size-selective capture. We report interesting experimental and simulated voltammetry of the redox switch with alkali metals (Li^+, Na^+, K^+) and utilize the observed phenomena to derive binding constants. In Chapter 4, we target sterically encumbered carboranes with bipyridyl appendages for transition metal (Mn^{2+}, Fe^{2+}, Co^{2+}, Ni^{2+}) binding. We observe interesting electrochemistry which suggests that increasingly Lewis acidic metals may bind more strongly. We begin to probe the metal coordination environments and reveal that square pyramidal geometries may be preferred. In Chapter 5, we explore additional donor groups (carboxylic acids, amides, sulfides, sulfoxides) adhered to *o*-carborane and discover that the ligating groups have a profound impact on carborane formal reduction potentials.

Table of Contents

ACKNOWLEDGEMENTS....iv

Abstract.... viii

Table of Contents....x

List of Figures....xiv

List of Schemes.... xviii

List of Tables....xix

List of Symbols and Abbreviations....xx

Chapter 1 Introduction....1

1.1. Overview....2

1.2. Molecular Switches....3

1.2.1. Redox Switches....5

1.3. Carboranes....7

1.3.1. *Ortho*-carborane....8

1.3.2. 1,2-bis(diphenylphosphine oxide)-*o*-carborane....9

1.4. Scope of Thesis....10

1.5. References....12

Chapter 2 Diaryl Phosphine Oxide-Substituted *o*-Carboranes....20

2.1. Introduction....21

2.1.1. Nuclear Energy....21

2.1.2. Biphasic UO_2^{2+} Extraction with Phosphine Oxide Carboranes....23

2.2. Results and Discussion....25

2.2.1. Synthesis and Characterization....25

2.2.2. Electrochemistry 29
2.2.3. NMR Basicity Studies 33
2.2.4. NMR Competition Experiments 36
2.2.5. Biphasic UO_2^{2+} Capture and Release 41
2.2.6. $UO_2(NO_3)_2{}^{PO}Cb$ displacement by H_2O 47
2.2.7. Carborane Stability with EWGs and EDGs. 49
2.3. Summary 51
2.4. Experimental 51
2.4.1. Materials and Physical Measurements 51
2.4.2. Synthesis of Compounds 54
2.4.3. Procedure for NMR Basicity Studies 62
2.4.4. Procedure for NMR Competition Experiments 62
2.4.5. Biphasic Electrochemical UO_2^{2+} Capture and Release 64
2.5. References 66
Chapter 3 Crown Ether *o*-Carboranes for High Li^+ Selectivity 73
3.1. Introduction 74
3.1.1. Lithium Extraction 74
3.1.2. Materials for Li^+ Seawater Extraction 75
3.2. Results and Discussion 77
3.2.1. Synthesis and Characterization 77
3.2.2. NMR Binding Studies 85
3.2.3. Electrochemistry 91
3.2.4. Electrochemical Simulations 100

3.2.5. Limitations to Method 108
3.2.6. 18-crown-6-*o*-carborane 109
3.3. Summary.....111
3.4. Experimental.....112
3.4.1. Materials and Physical Measurements.....112
3.4.2. Synthesis of Compounds 114
3.4.3. *Closo* NMR binding procedure.....116
3.4.4. Galvanostatic Bulk Electrolysis Procedure 117
3.4.5. *Nido* NMR Binding Procedure 118
3.4.6. Electrochemical Procedures.....119
3.4.7. Simulated Voltammetry Procedures.....120
3.5. References.....122
Chapter 4 Bipyridyl *o*-Carborane for Transition Metal Capture 131
4.1. Introduction.....132
4.1.1. The Rise of Electric Vehicles 132
4.1.2. Batteries & Critical Minerals.....132
4.1.3. Battery Recycling 133
4.1.4. Pyridyl Carboranes for Metal Selectivity 134
4.2. Results and Discussion 135
4.2.1. Ligand Synthesis and Characterization 135
4.2.2. Electrochemistry.....139
4.2.3. Metal Complex Synthesis and Characterization.....146
4.2.4. DFT Calculations.....153

4.2.5. Alternative Pyridine Syntheses 155
4.3. Summary 157
4.4. Experimental 158
4.4.1. General Methods and Considerations 158
4.4.2. Synthesis of Compounds 160
4.5. References 165
Chapter 5 Other *O*-Carborane Derivatives 172
5.1. Introduction 173
5.2. Results and Discussion 173
5.2.1. Carboxylic Acid Derivatives 173
5.2.2. Amido Derivatives 177
5.2.3. Sulfido and Sulfoxyl Derivatives 183
5.3. Summary 187
5.4. Experimental 187
5.4.1. General Methods and Considerations 187
5.4.2. Synthesis of Compounds 188
5.5. References 189

List of Figures

Figure 1.1. Confirmational Switches: Molecular Tweezers. 4

Figure 1.2. Reported Redox Switches. 6

Figure 1.3. Derivatized *ortho*-carborane redox switching to *nido*-carborane. 9

Figure 2.1. PUREX Process.....23

Figure 2.2. Selective Biphasic UO_2^{2+} Extraction.....24

Figure 2.3. Phosphine Oxide Carborane Structure-Function Relationship. 25

Figure 2.4. Library of 1,2-bis(diarylphosphine oxide)-*ortho*-carboranes.....26

Figure 2.5. Solid-state molecular structures of Phosphine Oxide Carboranes 28

Figure 2.6. Stacked CVs of Phosphine Oxide Carboranes 29

Figure 2.7. CV of $[UO_2Cl_2(THF)_2]_2$ and $UO_2Cl_2(TPPO)_2$.....31

Figure 2.8. CVs of ^{PO}Cb with $[UO_2Cl_2(THF)_2]_2$ and TPPO.....32

Figure 2.9. ^{19}F NMR spectra of PFBA-carborane adducts.....35

Figure 2.10. Solid-state molecular structure of 2 deboronated carboranes bound to UO_2^{2+} 37

Figure 2.11. Established binding between *closo* carborane ^{PO}Cb and UO_2^{2+}.....38

Figure 2.12. Example competition experiment of $^{PO}CbEt_2$, TPPO, and $UO_2(NO_3)_2$. .39

Figure 2.13. Graph of pK_{eq} vs. pK_{BH^+} for each carborane species.....41

Figure 2.14. Biphasic Extraction Diagram. 42

Figure 2.15. GBE H-cell design. 43

Figure 2.16. GBE Reduction (a) and Oxidation (b) Curves. 44

Figure 2.17. $^{31}P\{^1H\}$ NMR spectra of GBE cycling of $^{PO}CbEt_2$.....45

Figure 2.18. ICP-OES of UO_2^{2+} extraction and back-extraction.....46

Figure 2.19. $^{31}P\{^1H\}$ NMR spectra of $UO_2(NO_3)_2{}^{PO}$Cb / H_2O competition.....48

Figure 2.20. Solid-state molecular structure of H-^{PO}CbMe$_8^-$ byproduct.....50

Figure 3.1. Solid-state molecular structures of a) ^{14C4}Cb b) K$_2$^{14C4}Cb 80

Figure 3.2. ^{11}B{^{1}H} NMR of kinetic Li$_2$^{14C4}Cb product acquired immediately in CD$_3$CN. 82

Figure 3.3. ^{1}H, ^{11}B{^{1}H} and ^{7}Li NMR spectra of Li$_2$^{14C4}Cb taken in CD$_3$CN. 83

Figure 3.4. 2D NMR spectra of Li$_2$^{14C4}Cb.....84

Figure 3.5. NMR binding studies ^{14C4}Cb and LiPF$_6$ in d$_8$-THF.....87

Figure 3.6. Unlocked ^{11}B{^{1}H} NMR spectrum of electrochemically-generated [Bu$_4$N]$_2$[^{14C4}Cb] 88

Figure 3.7. UV-Vis calibration curve of FcPF$_6$. 89

Figure 3.8. Unlocked ^{7}Li NMR spectra of LiTFAB with increasing equivalents of ^{14C4}Cb^{2-} 90

Figure 3.9. Example ^{11}B{^{1}H} NMR spectrum of ^{14C4}Cb^{2-} with 2 equiv. of Li$^+$. 91

Figure 3.10. CVs of 2.9 mM ^{14C4}Cb in 0.1 M [Bu$_4$N][PF$_6$] DME.....92

Figure 3.11. Varied cut off cathodic sweeps of ^{14C4}Cb without (a) and with (b) 0.87 mM LiTFAB (0.3 equiv.). 94

Figure 3.12. CV of 2.9 mM ^{14C4}Cb with alkali metal titrations.....97

Figure 3.13. Linear Regressions for determination of Log K.....98

Figure 3.14. CVs of 2.9 mM ^{14C4}Cb with competing commercial crown-ethers and alkali metals.....99

Figure 3.15. Simulated CVs of metal-free ^{14C4}Cb. 101

Figure 3.16. Proposed ECCCEC mechanism for simulations with metal binding. ...102

Figure 3.17. Simulated voltammetry of ^{14C4}Cb with Li$^+$ 103

Figure 3.18. Simulated voltammetry of ^{14C4}Cb with Na$^+$. 104

Figure 3.19. Simulated voltammetry of ^{14C4}Cb with K^+. 105

Figure 3.20. Simulated (dashed) CV of ^{14C4}Cb with 0.725 mM of Li^+ with a hypothetical increased Li^+ diffusion coefficient of 1.5 x 10^{-4} cm^2/s (10-fold increase). 106

Figure 3.21. Simulated CVs of ^{14C4}Cb with 0.87 mM Li^+ at fast scan rates. 108

Figure 3.22. CV of 2.9 mM ^{18C6}Cb with 2 equiv. of alkali metals. 111

Figure 3.23. Randles-Ševčík of ^{14C4}Cb. 119

Figure 4.1. Proposed transition metal capture and release with bipyridyl *o*-carboranes.135

Figure 4.2. Solid-state molecular structures of $^{(Cl)Py}$Cb and $^{(Br)Py}$Cb 137

Figure 4.3. Solid-state molecular structures of *closo* and *nido* 1,2-bis(2,2'-bipyridyl)*o*-carborane.....139

Figure 4.4. CVs of ^{bipy}Cb with Li^+ and Ca^{2+}.....140

Figure 4.5. CVs of 2 mM ^{bipy}Cb with 2 mM 1st row transition metals.....142

Figure 4.6. CVs of 2 mM transition metal PF_6 salts.....145

Figure 4.7. Solid-state molecular structures of metal-^{bipy}Cb complexes 149

Figure 4.8. UV-Visible Spectroscopy of ^{bipy}Cb, $K_2{}^{bipy}$Cb, and $Co_2{}^{bipy}Cb_2$.....150

Figure 4.9. CV of 1 mM $Co_2(^{bipy}Cb)_2$ in.....151

Figure 4.10. Solid-state molecular structures of deboronated Co-^{bipy}Cb complexes.152

Figure 4.11. DFT Molecular Orbitals of Fe^{bipy}Cb. 154

Figure 5.1. Solid-state molecular structure of $Li_2{}^{COO}$Cb 175

Figure 5.2. CVs of carboxylic acid-derivatized *o*-carboranes 177

Figure 5.3. Solid-state molecular structures of amido-functionalized *o*-carboranes .180

Figure 5.4. CVs of amido-substituted *o*-carboranes 181

Figure 5.5. Solid-state molecular structure of ^{SO}Cb 185

Figure 5.6. CVs of ^{S}Cb and ^{SO}Cb 186

List of Schemes

Scheme 1.1. Redox-switching UO_2^{2+} capture and release. 10

Scheme 2.1. Synthesis of 1,2-bis(diarylphosphine oxide)-*o*-carboranes 27

Scheme 2.2. Formation of HBA-HBD adduct between carboranes and PFBA. 34

Scheme 3.1. Size-selective *closo/nido* Li^+ capture and release. 77

Scheme 3.2. Synthesis of a) Precursor *p*-tosyl linker b) *closo*- and *nido*- 1,2-((6,6,7,7-Me_4)14-crown-4)-*o*-carborane. 79

Scheme 3.3. Salt swap of $K_2{}^{14C4}Cb$ with LiTFAB. 81

Scheme 3.4. Stepwise metal binding for 2 metals binding to $^{14C4}Cb^{2-}$. 96

Scheme 3.5. Synthesis of 18-crown-6-*o*-carborane. 109

Scheme 4.1. Synthesis of 1,2-bis(2,2'-bipyridyl)*o*-carborane 136

Scheme 4.2. Synthesis of potassium 1,2-bis(2,2'-bipyridyl)*o*-carborane 138

Scheme 4.3. ^{bipy}Cb-Metal Complex Synthesis. 146

Scheme 4.4. Synthetic attempts for 1,2-bis(2,2';6',2''-terpyridyl)*o*-carborane. 156

Scheme 5.1. Synthesis of carboxylic acid derivatized *o*-carboranes. 174

Scheme 5.2. Synthesis of amido-derivatized *o*-carboranes. 178

Scheme 5.3. Synthesis of sulfide and sulfoxyl *o*-carborane derivatives. 184

List of Tables

Table 2.1. Reported P–O and bond lengths, C-P-C angle summation, C–C bond length for carborane species. 27

Table 2.2. Reported bond lengths, IR stretch, $^{31}P\{^{1}H\}$ NMR resonances, reduction potentials, pK_{BH^+} and pK_{eq} for the modified carborane series.....33

Table 3.1. Log K binding values of ^{14C4}Cb with Li^+, Na^+, or K^+ determined through experimental, simulated, or calculated methods.....107

Table 4.1. Reported reduction potentials of ^{bipy}Cb with metals.....144

List of Symbols and Abbreviations

A	amp
AgOTf	silver triflate
bipy	2,2′-bipyridine
C	coulomb
Cb	*ortho*-carborane
Cb^*	Any modified carborane
CV	cyclic voltammetry
DCE	dichloroethane
DCM	dichloromethane
DME	1,2-dimethoxyethane
DMF	dimethylformamide
$E_{1/2}$	formal reduction potential
EDG	electron-donating group
E_{ox}	oxidation potential
equiv.	equivalents
E_{red}	reduction potential
EVs	electric vehicles
EWG	electron-withdrawing group
F	Faraday's constant
Fc	ferrocene
Fc^+	ferrocenium

FT-IR	Fourier transform infrared spectroscopy
FWHM	full width at half maximum
GBE	galvanostatic bulk electrolysis
GHG	greenhouse gases
GW	gigawatt
HBA	hydrogen bond acceptor
HBD	hydrogen bond donor
HER	hydrogen evolution reaction
HLW	high level waste
HOMO	highest occupied molecular orbital
ICP-OES	inductively coupled plasma optical emission spectroscopy
KHMDS	potassium bis(trimethylsilyl)amide
kt	kiloton
kWh	kilowatt hour
LUMO	lowest unoccupied molecular orbital
M	metal
*m*CPBA	*meta*-chloroperoxybenzoic acid
MO	molecular orbital
MeCN	acetonitrile
n	number of electrons transferred
n-BuLi	*n*-butyllithium
NaOAc	sodium acetate
NMR	nuclear magnetic resonance

PFBA	pentafluorobenzoic acid
pH	potential of hydrogen
pK_{BH^+}	proton transfer basicity
pK_{eq}	- Log K
PPN	bis(triphenylphosphine)iminium
ppm	parts per million
PUREX	plutonium and uranium reduction extraction
R	universal gas constant
RVC	reticulated vitreous carbon
S_NAr	nucleophilic aromatic substitution
SNF	spent nuclear fuel
SOC	state of charge
terpy	2,2';6',2''-terpyridine
TFAB	tetrakis(pentafluorophenyl)borate ethyl etherate
TPPO	triphenylphosphine oxide
T_1	relaxation time
THF	tetrahydrofuran
TTF	tetrathiafulvalene
UO_2^{2+}	uranyl
UV-vis	ultraviolet-visible
XRD	X-ray diffraction
ΔG	Gibb's free energy

Chapter 1 Introduction

1.1. Overview

Anthropogenic climate change is here, happening now and will not recuperate unless urgent and genuine innovation is implemented worldwide. At unprecedented rates, the world is experiencing global catastrophes, melting icebergs, ocean acidification and rising temperatures. Ecosystems and biodiversity are being destroyed. Greenhouse gas (GHG) emissions are the culprit. As humans burn coal, oil, or natural gas for energy, harmful GHGs are released – CO_2, CH_4, NOx. The enrichment of GHGs in the atmosphere prevents infrared heat from escaping into space, known as the greenhouse effect. The Paris Agreement, signed by 197 countries, aims to combat climate change by mitigating GHG emissions to prevent global temperatures from rising 1.5 ℃ above preindustrial temperatures.[1]

Renewable energy paired with energy storage is an effective strategy to decarbonize the energy and transportation sectors. The amount of CO_2 emitted from energy sources is acutely reduced with renewables compared to fossil fuels: wind (12 g/kWh), hydropower (24 g/kWh), solar (48 g/kWh) vs. natural gas (490 g/kWh), coal (820 g/kWh).[2] However, renewable energy is intermittent. It must be used in conjunction with batteries and reliable carbon-neutral fuel sources such as nuclear energy (12 g/kWh).[2] Photovoltaic cells, wind turbines, nuclear energy and batteries require critical minerals (Si, Cu, Al, U, Li, Co, Ni, etc.), sourced primarily from terrestrial mining, an environmentally destructive process.

The demand for these minerals is increasing rapidly because of the shift towards clean energy. The global renewable energy capacity grew by 230% from 2015 (150 GW) to 2022 (350 GW) and is projected to grow an additional 75% by 2027 (600 GW).[3] The rising mineral demand for clean energy technology will exacerbate the supply and cause more ecological devastation. Terrestrial mining is energy intensive, generates caustic waste and pollutes water

streams.[4] The metal mining industry accounts for 8% of global GHG emissions.[5] Accordingly, it is crucial that we develop new strategies for sourcing critical minerals used in clean energy technology. Advancements in selective electrochemical metal capture chemistry could expand critical mineral extraction technologies to unconventional sources – spent nuclear fuel, seawater, end-of-life batteries. Electrochemically switchable extractants could eliminate the need for stoichiometric reagents and reduce waste during metal extraction processes.

1.2. Molecular Switches

Advances in molecular switch chemistry may complement existing metal extraction technologies via host-guest applications. Molecular switches, stable between two or more states, switch back and forth when exposed to an external stimulus such as pH, light, temperature, or electric current. Molecular switches have great utility for drug delivery[6, 7], optoelectronics[8, 9], biosensors[10], artificial photosynthesis[11], and nanomachinery[12] because of their switchable properties.

Host-guest chemistry has taken inspiration from molecular switches prevalent throughout biology. For example, calmodulin is a protein which reversibly binds to Ca^{2+} in eukaryotic cells to regulate intracellular signaling.[13] It is a conformational switch, undergoing large structural changes upon metal complexation. Molecular tweezers, a subset of conformational switches, have two long appendages resembling a pair of tongs. Molecular tweezers are synthetically designed to encapsulate a guest molecule in its closed form and release it in its open form. A host molecule, terpyridine(Ni-salphen)$_2$, is in an open configuration until bound to guest, Zn (Figure 1.1a). Once bound, release of Zn from terpyridine(Ni-salphen)$_2$-Zn can be initiated by introducing a competing ligand, terpyridine.[14] Molecular tweezers with azobenzene or diarylethene photoswitch moieties have been tailored

with benzo 15-crown-5 appendages to target reversible 2:1 sandwich complex binding of K^+ (Figure 1.1b).[15, 16] Metal release can be initiated by the absence of UV-light.

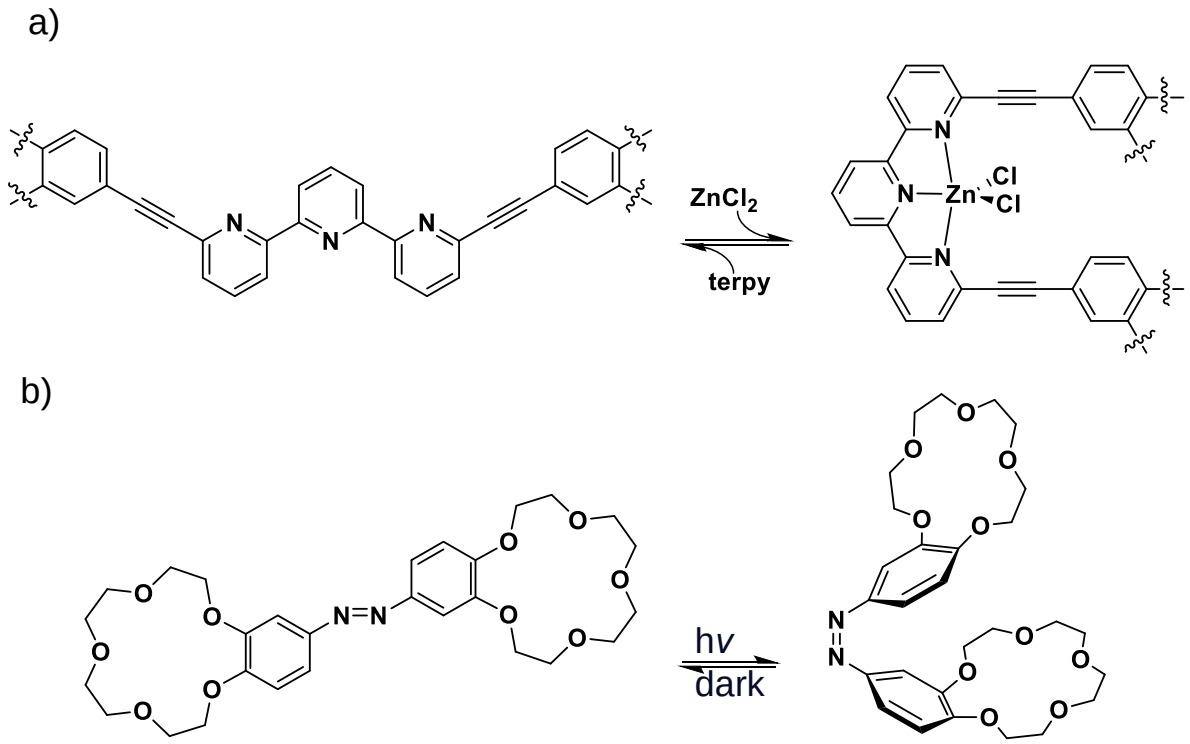

Figure 1.1. Confirmational Switches: Molecular Tweezers. a) terpyridine-based molecular tweezer. b) azobenzene molecular tweezers

Similarly, molecular grippers possess two or more states, one of which will "grip" the guest molecule through hydrogen bonding, π-π stacking or van der Waals forces. Cavitands, a type of molecular gripper, contain a cavity formed by aromatic rings that allows for encapsulation of small organic guest molecules.[17] Release is usually initiated by changes in pH, temperature, or concentration of Zn^{2+} ions.[18] Conformational switches offer an interesting approach to selective and reversible metal binding, though very limited research currently exists for targeted metal capture.

1.2.1. Redox Switches

Redox switches are reversibly interchangeable with applied electrical stimuli. Inducing redox switches with electricity is affordable, non-energy intensive, and eliminates stoichiometric reagents. Redox switches participate in reduction or oxidation reactions to switch between stable states. They usually contain ferrocene or organic redox-active molecules (tetrathiafulvalenes, quinones, viologens).

Ferrocene (Fc) has been adhered to various ligating groups for use as a redox switch. For example, Fc was cyclized with cyclopseudopeptides (Figure 1.2a).[19] The extractant displayed preferential binding towards Ca^{2+} in its neutral form (log K = 6.6). Upon electrochemical oxidation, the extractant still binds well to Ca^{2+} albeit, weaker than before (log K = 4.6). Similarly, Fc has been adhered to benzo-15-crown-5 and aza-crown ether moieties for applications as redox-active alkali metal sensors.[20, 21] In both cases, the crown will complex alkali metals in their neutral and oxidized states, though the formal reduction potential of the ferrocenyl group is sensitive to the bound metal. These redox switches are effective for electrochemical sensing applications but are not effective at releasing metals because they lack conformational changes and rely solely on electrostatic repulsion.

Tetrathiafulvalene (TTF) is a common redox-active subunit commonly used in redox switches. TTF can undergo two 1 e^- oxidations to form stable radical and dicationic species. In the neutral state, TTF usually takes a boat conformation. It becomes planar as a radical cation and twisted as a dication.[22] Sallé *et al.* adhered a polyether linkage to TTF affording a TTF-substituted 25-crown-5 complexing agent (Figure 1.2b).[23] It displayed strong binding to Ba^{2+} (log K = 4.3) in the neutral state and very weak binding as a dication ($K \approx 0$) due to electrostatic repulsions. Nielsen *et al.* synthesized bidentate TTF-pyridine ligands which

displayed strong affinity for Pb^{2+} (log K = 4) and Ag^{+} (log K = 4.3).[24] TTF is a fascinating redox-active subunit, but similar to Fc-based redox switches, metal expulsion arises from electrostatic repulsion with minimal structural changes.

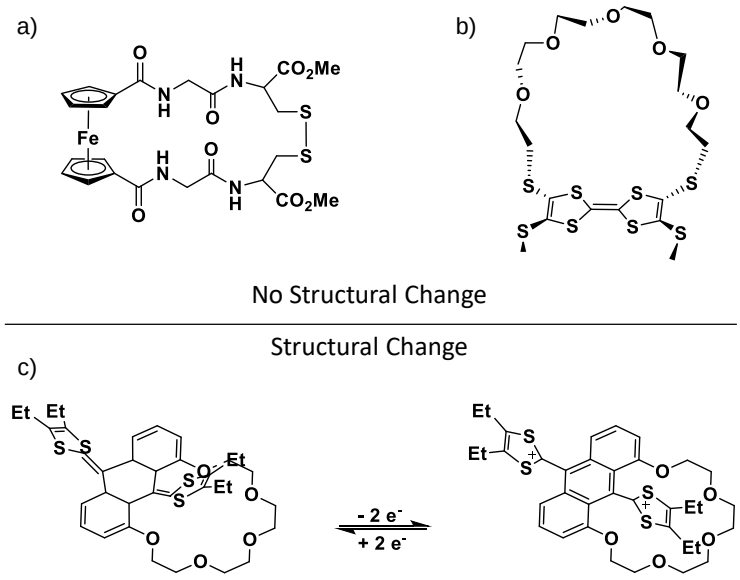

Figure 1.2. Reported Redox Switches. a) Fc-based redox switch. b) TTF-based redox switch. c) derivatized dihydroanthracene redox switch undergoing a structural change with twisting of 1,3-dithiolium rings

Very limited literature examples exist in which redox switches undergo conformational changes for reversible metal capture and release. Fujimori reported a redox-switchable 9,10-bis(1,3-dithiol-2ylidene)-9,10-dihydroanthracene moiety functionalized with a polyether linkage to afford an 18-crown-5 cavity (Figure 1.2c).[25] The neutral extractant has a butterfly shape and binds to K^{+} (log K = 3.4), Na^{+} (log K = 3.3), and Li^{+} (log K = 3.0) in the crown cavity. Upon 2 e^{-} oxidation, the alkali metal is expelled out of the cavity by electrostatic interactions and the twisting of 1,3-dithiolium rings which become orthogonal to the planar anthracene unit. Interestingly, the extractant displayed little difference in selectivity between

alkali metals. Conformational redox switch chemistry would greatly benefit from improved metal selectivity for real world applications.

1.3. Carboranes

Carboranes are icosahedral boron/carbon/hydrogen clusters ranging in size from 5 to 14 atoms. Each boron and carbon atom are bound to 5 neighboring atoms and a singular hydrogen ($C_xB_yH_{x+y}$). The carborane cage bonding follows Wade's rules instead of conventional 2 center 2 electron bonding.[26] Each B–H and C–H unit contains 2 electrons in the element–H σ bond and contributes the remaining 2 and 3 electrons, respectively, to delocalized $\sigma p_{x,y}$-bonding generating n cluster-based molecular orbitals (MO) with 2 e^- each. In the center of the cluster, overlapping hybrid sp_z orbitals create one additional bonding cluster MO for a total of n+1 cluster MOs. The geometry of the cluster is correlated to the n + 1 bonding MOs in that the total number of vertices corresponds to n. *Closo* carboranes have n vertices, whereas *nido* carboranes have n−1 vertices and *arachno* carboranes have n−2 vertices, yet the number of bonding MOs remains unchanged (n+1).[26]

Uniquely, carboranes are 3D-aromatic because they possess high symmetry with extensive electron delocalization across degenerate MOs.[27] Carboranes are hydrophobic, robust, luminescent, and have high thermal stability.[28] These special properties have attracted the interests of many researchers. Accordingly, carboranes have found applications in medicine[29, 30], coordination chemistry[31, 32], catalysis[33, 34], electronic devices[35, 36] and in new materials.[37, 38]

1.3.1. *Ortho*-carborane

1,2-*Ortho*-*closo*-dodecacarborane (Cb) ($C_2B_{10}H_{12}$), perhaps, is the most popular carborane derivative found in literature (Figure 1.3). Recent advances in the synthesis of derivatized Cb compounds have enabled new property exploration of Cb-based compounds.[26, 39-42] The C–H's on the cage are acidic which allows for 1,2- functionalization by deprotonation and subsequent reaction with electrophiles. The borons on the cage maintain some regioselectivity. The 9,12- positions are the most electron-rich and are susceptible to electrophilic substitution reactions. The 3,6- positions are electrophilic so functionalization at these positions is challenging and usually requires multi-step processes.[43] The 3,6- positions are susceptible to nucleophilic attack by strong Lewis bases such as halides, hydroxides, and coordinating solvents. Nucleophilic attack by two successive nucleophiles and subsequent protonation leads to deboronation, forming the *nido*-7,8-$[C_2B_9H_{12}]^-$ anion.[44] *nido*-7,8-$[C_2B_9H_{12}]^-$ cannot be electrochemically reverted back to Cb and instead requires a 2-step synthesis to restore the 12 vertex cage.[26]

Cb has very intriguing electrochemical properties. Functionalization of the 1,2-positions with bulky substituents enables some derivatized Cbs to behave as conformational redox switches. *Closo*-carborane cages are very electron deficient, and the carbons are more electropositive than boron. Upon 2 e^- reduction, the C–C bond cleaves and the cage rearranges to the *nido*-*meta*-7,9-$[C_2B_9H_{12}]^{2-}$ dianion (Figure 1.3).[45] C-substituted bulky substituents improve the stability of the *nido* dianion by hampering reactive sites and drastically shifting the redox potential more anodically.[46] The 2 e^- reduction, in a cyclic voltammogram, can occur simultaneously or step-wise depending on solvent, cage rearrangement, and substituents. The *closo/nido* redox couple is considered chemically reversible because in many cases the *nido*

dianion can be oxidized to reform *closo*-Cbs (Figure 1.3). Alternatively, some *nido*-carboranes can be further reduced by 2 e^- to *arachno*-carboranes. Though, this rarely occurs because the *nido* dianion must have adjacent carbon atoms otherwise the *arachno* reduction is very reducing and difficult to access.[45]

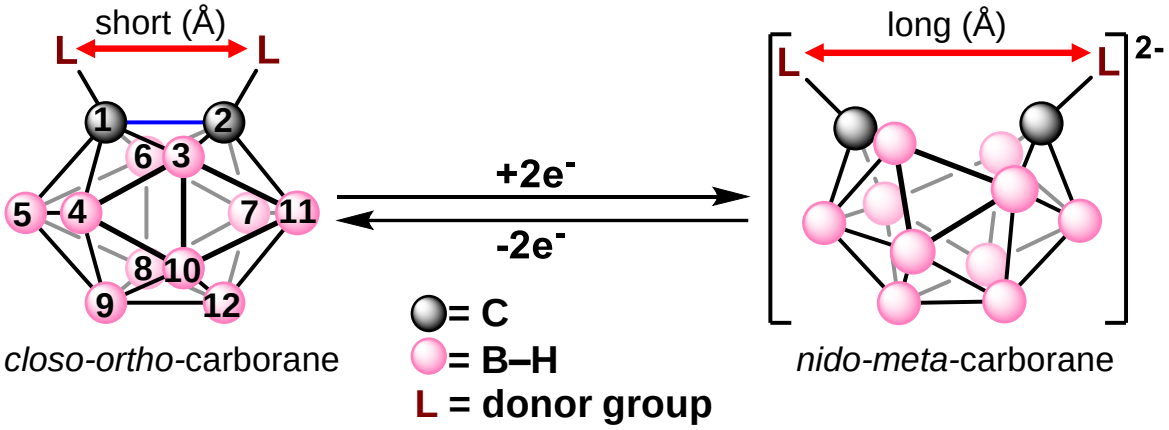

Figure 1.3. Derivatized *ortho*-carborane redox switching to *nido*-carborane.

1.3.2. 1,2-bis(diphenylphosphine oxide)-*o*-carborane

Previous work in our group has utilized the redox switching ability of *o*-carboranes for reversible uranyl (UO_2^{2+}) capture (Scheme 1.1).[47, 48] Diphenylphosphine oxide donor groups were appended to the 1,2- positions following literature procedures[49] to afford 1,2-bis(diphenylphosphine oxide)-*o*-carborane (**^{PO}Cb**). **^{PO}Cb** was chemically and electrochemically reduced by 2 e^- to *nido*-carborane dianion, **^{PO}Cb^{2-}**. Upon reduction, we observed C–C bond cleavage and a drastic increase in electron density funneled to the phosphine oxide moieties. The **^{PO}Cb^{2-}** extractant binds to UO_2^{2+} in both a 2:1 and 1:1 stoichiometry (Scheme 1.1). Upon oxidation to **^{PO}Cb**, UO_2^{2+} is released and prefers binding towards competitive ligands, such as triphenylphosphine oxide or water.[47] We suspected that the contracted bite angle and decreased electronic density of *closo*-carborane, **^{PO}Cb**, deactivated the extractant and shut off metal coordination. To the best of our knowledge, this

was the first example of derivatized Cbs being implemented as redox switches for reversible metal capture.

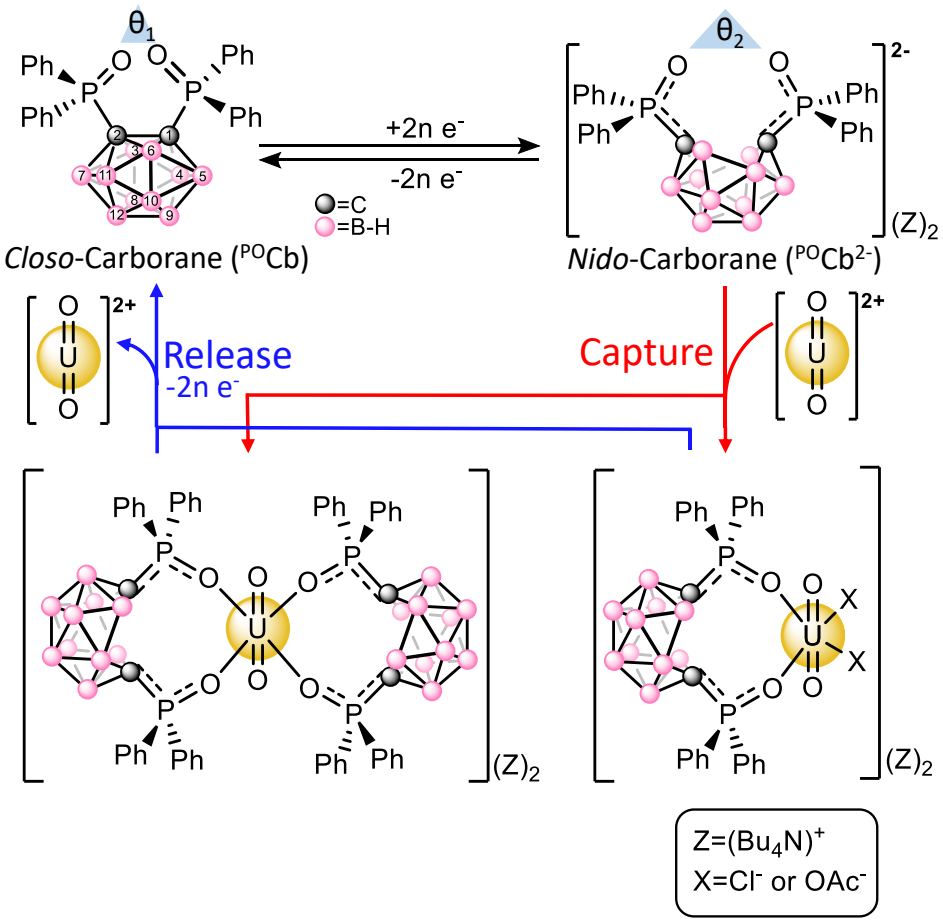

Scheme 1.1. Redox-switching UO_2^{2+} capture and release.

1.4. Scope of Thesis

The work detailed in this doctoral thesis expanded our fundamental understanding of main group carborane chemistry. In this thesis, we probed how carboranes can be tuned for improved redox switchable metal coordination. We combined the redox-switching property of Cb with an array of donor functional groups to target selective metal coordination of critical minerals used in clean energy technologies.

Chapter 2 deepened our understanding of phosphine oxide-substituted Cbs. We learned which intrinsic properties are most desirable in extractant design for biphasic capture and release of UO_2^{2+}. We benchmarked the effects of cage B-substitution on neighboring donor groups and carborane redox behavior. Hila Benhaim and I contributed equally to this work. We synthesized and characterized a library of phosphine oxide-substituted Cbs and performed cyclic voltammetry on the derivatives. Hila Benhaim carried out NMR basicity studies and I performed NMR competition experiments. We performed biphasic UO_2^{2+} capture and release studies using protocols developed by previous group members, Drs. Megan Keener, Camden Hunt, and Tim Carroll. Hila Benhaim obtained the UO_2^{2+} extraction and release efficiencies by ICP-OES using procedures developed by previous member, Dr. Maxwell Mattejat.

Chapter 3 expanded carborane redox switch chemistry to a new platform: crown ethers. We developed a methodology for electrochemical determination of metal binding constants using paired cyclic and simulated voltammetry. I would like to acknowledge that previous member, Dr. Zongheng Wang conceptualized the extractant design, chemically synthesized the *closo* and potassium *nido* crown-ether carboranes, and preformed preliminary NMR selectivity experiments. My role in the project was further probing the alkali metal selectivity of the *nido* crown-ether carborane via electrochemical methods. I implemented alkali metal titration experiments using cyclic and simulated voltammetry and I performed a Galvanostatic bulk electrolysis using a procedure developed by Dr. Camden Hunt. We demonstrated that the *nido* crown-ether carborane has preferential binding towards Li^+ over Na^+ and K^+ while the *closo* crown-ether carborane weakly interacts with alkali metals.

In Chapter 4, we targeted selective transition metal binding using bipyridyl appendages on redox switchable Cb. We attempted to chemically synthesize and characterize metal-*nido*-complexes of Mn^{2+}, Fe^{2+}, Co^{2+} and Ni^{2+} and observed a preference for square pyramidal geometries. We performed cyclic voltammetry experiments to discern *nido* metal binding parameters and discovered that increasing Lewis acidity of the metal may correlate to stronger binding with bipyridyl *nido*-carborane species.

Chapter 5 explored the use of Cbs with various functional groups – carboxylic acids, amides, sulfides, and sulfoxides. We observed that the 1,2- ligating groups attached to the carborane have pronounced effects on formal reduction potentials of the *closo/nido* redox couple.

At the time of writing this thesis, portions of Chapter 2 have been accepted for publication and manuscripts of the work detailed in Chapters 3 and Chapter 4 are in preparation.

1.5. References

(1) *The Paris Agreement*. United Nations Climate Change, https://unfccc.int/process-and-meetings/the-paris-agreement (accessed 2023 7/25/23).

(2) *Carbon Dioxide Emissions From Electricity*. World Nuclear Association, 2022. https://www.world-nuclear.org/information-library/energy-and-the-environment/carbon-dioxide-emissions-from-electricity.aspx (accessed 2023 7/25/23).

(3) IEA. Renewables 2022. International Energy Agency: 2022.

(4) Rötzer, N.; Schmidt, M. Decreasing Metal Ore Grades—Is the Fear of Resource Depletion Justified? *Resources* **2018**, *7* (4), 88.

(5) Cox, B.; Innis, S.; Kunz, N. C.; Steen, J. The mining industry as a net beneficiary of a global tax on carbon emissions. *Communications Earth & Environment* **2022**, *3* (1), 17. DOI: 10.1038/s43247-022-00346-4.

(6) Fitzmaurice, O.; Bartkowski, M.; Giordani, S. Molecular Switches—Tools for Imparting Control in Drug Delivery Systems. *Frontiers in Chemistry* **2022**, *10*. DOI: 10.3389/fchem.2022.859450.

(7) Kim, J.; Singh, B.; Shukla, N.; Lee, J.; Kim, K.; Park, M.-H. On-Demand Drug-Delivery Platform Using Electrospun Nanofibers by Externally Triggered Glass Transition Switch. *ACS Mater. Lett.* **2022**, *4* (11), 2252-2260. DOI: 10.1021/acsmaterialslett.2c00610.

(8) Yu, S. H.; Hassan, S. Z.; So, C.; Kang, M.; Chung, D. S. Molecular-Switch-Embedded Solution-Processed Semiconductors. *Adv. Mater.* **2023**, *35* (4), 2203401. DOI: https://doi.org/10.1002/adma.202203401.

(9) Sun, J.; Wu, Y.; Wang, Y.; Liu, Z.; Cheng, C.; Hartlieb, K. J.; Wasielewski, M. R.; Stoddart, J. F. An Electrochromic Tristable Molecular Switch. *JACS* **2015**, *137* (42), 13484-13487. DOI: 10.1021/jacs.5b09274.

(10) Bagheri, E.; Abnous, K.; Alibolandi, M.; Ramezani, M.; Taghdisi, S. M. Triple-helix molecular switch-based aptasensors and DNA sensors. *Biosensors and Bioelectronics* **2018**, *111*, 1-9. DOI: https://doi.org/10.1016/j.bios.2018.03.070.

(11) Hirakawa, K.; Takai, S.; Horiuchi, H.; Okazaki, S. Photooxidation Activity Control of Dimethylaminophenyl-tris-(N-methyl-4-pridinio)porphyrin by pH. *ACS Omega* **2020**, *5* (42), 27702-27708. DOI: 10.1021/acsomega.0c04303.

(12) Xu, T.; Soto, F.; Gao, W.; Dong, R.; Garcia-Gradilla, V.; Magaña, E.; Zhang, X.; Wang, J. Reversible Swarming and Separation of Self-Propelled Chemically Powered Nanomotors under Acoustic Fields. *JACS* **2015**, *137* (6), 2163-2166. DOI: 10.1021/ja511012v.

(13) Vetter, S. W.; Leclerc, E. Novel aspects of calmodulin target recognition and activation. *Eur J Biochem* **2003**, *270* (3), 404-414. DOI: 10.1046/j.1432-1033.2003.03414.x.

(14) Doistau, B.; Benda, L.; Cantin, J.-L.; Chamoreau, L.-M.; Ruiz, E.; Marvaud, V.; Hasenknopf, B.; Vives, G. Six States Switching of Redox-Active Molecular Tweezers by Three Orthogonal Stimuli. *JACS* **2017**, *139* (27), 9213-9220. DOI: 10.1021/jacs.7b02945.

(15) Shinkai, S.; Nakaji, T.; Ogawa, T.; Shigematsu, K.; Manabe, O. Photoresponsive crown ethers. 2. Photocontrol of ion extraction and ion transport by a bis(crown ether) with a butterfly-like motion. *JACS* **1981**, *103* (1), 111-115. DOI: 10.1021/ja00391a021.

(16) Takeshita, M.; Soong, C. F.; Irie, M. Alkali metal ion effect on the photochromism of 1,2-bis(2,4-dimethylthien-3-yl)-perfluorocyclopentene having benzo-15-crown-5 moieties. *Tetrahedron Letters* **1998**, *39* (42), 7717-7720. DOI: https://doi.org/10.1016/S0040-4039(98)01681-5.

(17) Rahman, F.-U.; Li, Y.-s.; Petsalakis, I. D.; Theodorakopoulos, G.; Rebek, J.; Yu, Y. Recognition with metallo cavitands. *Proceedings of the National Academy of Sciences* **2019**, *116* (36), 17648-17653. DOI: doi:10.1073/pnas.1909154116.

(18) Pochorovski, I.; Diederich, F. Development of Redox-Switchable Resorcin[4]arene Cavitands. *Accounts of Chemical Research* **2014**, *47* (7), 2096-2105. DOI: 10.1021/ar500104k.

(19) Huang, H.; Mu, L.; He, J.; Cheng, J.-P. Ferrocenyl-Bearing Cyclopseudopeptides as Redox-Switchable Cation Receptors. *The Journal of Organic Chemistry* **2003**, *68* (20), 7605-7611. DOI: 10.1021/jo030105v.

(20) Beer, P. D.; Danks, J. P.; Hesek, D.; McAleer, J. F. A potassium-selective sulfide-linked redox-active ferrocene ionophore that exhibits extraordinary electrochemical recognition behaviour. *Journal of the Chemical Society, Chemical Communications* **1993**, (23), 1735-1737. DOI: 10.1039/C39930001735.

(21) C. Grossel, M.; G. Hamilton, D.; I. Fuller, J.; Millan-Barios, E. Alkali-metal binding properties of simple ferrocenyl- and ruthenocenyl-substituted aza-crown ethers. *Journal of the Chemical Society, Dalton Transactions* **1997**, (19), 3471-3477. DOI: 10.1039/A703597G.

(22) Schröder, H. V.; Schalley, C. A. Tetrathiafulvalene – a redox-switchable building block to control motion in mechanically interlocked molecules. *Beilstein Journal of Organic Chemistry* **2018**, *14*, 2163-2185. DOI: 10.3762/bjoc.14.190.

(23) Le Derf, F.; Mazari, M.; Mercier, N.; Levillain, E.; Richomme, P.; Becher, J.; Garín, J.; Orduna, J.; Gorgues, A.; Sallé, M. Electroregulated Metal-Binding with a Crown Ether Tetrathiafulvalene Derivative: Toward Electrochemically Addressed Metal Cation Sponges. *Inorg. Chem.* **1999**, *38* (26), 6096-6100. DOI: 10.1021/ic9907617.

(24) Broman, S. L.; Andersen, C. L.; Jevric, M.; Tortzen, C. G.; Hammerich, O.; Nielsen, M. B. Metal cation binding to acetylenic tetrathiafulvalene–pyridine conjugates: affinity tuned by preorganization and cavity size. *Tetrahedron* **2016**, *72* (39), 5831-5842. DOI: https://doi.org/10.1016/j.tet.2016.08.001.

(25) Ohta, A.; Numae, T.; Yamashita, Y.; Fujimori, K. Novel 9,10Bis(1,3-dithiol-2-ylidene)-9,10- dihydroanthracene Derivatives Bridged by a Crown Ether Unit at the 1,8-Positions: A

New Type of Redox-switchable Hosts Undergoing Reversible Structural Changes. *Heterocycles* **2006**, *67*. DOI: 10.3987/COM-05-S(T)55.

(26) Grimes, R. N. *Carboranes*; Academic Press, 2016.

(27) El Bakouri, O.; Szczepanik, D. W.; Jorner, K.; Ayub, R.; Bultinck, P.; Solà, M.; Ottosson, H. Three-Dimensional Fully π-Conjugated Macrocycles: When 3D-Aromatic and When 2D-Aromatic-in-3D? *JACS* **2022**, *144* (19), 8560-8575. DOI: 10.1021/jacs.1c13478.

(28) Eleazer, B. J.; Peryshkov, D. V. Coordination Chemistry of Carborane Clusters: Metal-Boron Bonds in Carborane, Carboranyl, and Carboryne Complexes. *Comments on Inorganic Chemistry* **2018**, *38* (3), 79-109. DOI: 10.1080/02603594.2018.1465939.

(29) Issa, F.; Kassiou, M.; Rendina, L. M. Boron in Drug Discovery: Carboranes as Unique Pharmacophores in Biologically Active Compounds. *Chem. Rev.* **2011**, *111* (9), 5701-5722. DOI: 10.1021/cr2000866.

(30) Alberti, D.; Michelotti, A.; Lanfranco, A.; Protti, N.; Altieri, S.; Deagostino, A.; Geninatti Crich, S. In vitro and in vivo BNCT investigations using a carborane containing sulfonamide targeting CAIX epitopes on malignant pleural mesothelioma and breast cancer cells. *Sci Rep* **2020**, *10* (1), 19274. DOI: 10.1038/s41598-020-76370-1.

(31) Spokoyny, A. M.; Machan, C. W.; Clingerman, D. J.; Rosen, M. S.; Wiester, M. J.; Kennedy, R. D.; Stern, C. L.; Sarjeant, A. A.; Mirkin, C. A. A coordination chemistry dichotomy for icosahedral carborane-based ligands. *Nat. Chem.* **2011**, *3* (8), 590-596. DOI: 10.1038/nchem.1088.

(32) Adams, R. D.; Kiprotich, J. Coordination chemistry of thioether-carboranes in polynuclear metal carbonyl cluster complexes. B-H activation of thioether-carboranes by

dirhenium carbonyl complexes. *J. Organomet. Chem.* **2018**, *865*, 23-28. DOI: https://doi.org/10.1016/j.jorganchem.2017.09.004.

(33) Zhou, Y.-P.; Raoufmoghaddam, S.; Szilvási, T.; Driess, M. A Bis(silylene)-Substituted ortho-Carborane as a Superior Ligand in the Nickel-Catalyzed Amination of Arenes. *Angewandte Chemie* **2016**, *128* (41), 13060-13064. DOI: https://doi.org/10.1002/ange.201606979.

(34) Benton, A.; Copeland, Z.; Mansell, S. M.; Rosair, G. M.; Welch, A. J. Exploiting the Electronic Tuneability of Carboranes as Supports for Frustrated Lewis Pairs. *Molecules* **2018**, *23* (12). DOI: 10.3390/molecules23123099.

(35) Wee, K.-R.; Cho, Y.-J.; Jeong, S.; Kwon, S.; Lee, J.-D.; Suh, I.-H.; Kang, S. O. Carborane-Based Optoelectronically Active Organic Molecules: Wide Band Gap Host Materials for Blue Phosphorescence. *JACS* **2012**, *134* (43), 17982-17990. DOI: 10.1021/ja3066623.

(36) Ferrer-Ugalde, A.; González-Campo, A.; Viñas, C.; Rodríguez-Romero, J.; Santillan, R.; Farfán, N.; Sillanpää, R.; Sousa-Pedrares, A.; Núñez, R.; Teixidor, F. Fluorescence of New o-Carborane Compounds with Different Fluorophores: Can it be Tuned? *Chem. Eur. J.* **2014**, *20* (32), 9940-9951. DOI: https://doi.org/10.1002/chem.201402396.

(37) Li, Z.; Núñez, R.; Light, M. E.; Ruiz, E.; Teixidor, F.; Viñas, C.; Ruiz-Molina, D.; Roscini, C.; Planas, J. G. Water-Stable Carborane-Based Eu3+/Tb3+ Metal–Organic Frameworks for Tunable Time-Dependent Emission Color and Their Application in Anticounterfeiting Bar-Coding. *Chem. Mater.* **2022**, *34* (10), 4795-4808. DOI: 10.1021/acs.chemmater.2c00323.

(38) Jana, A.; Jash, M.; Dar, W. A.; Roy, J.; Chakraborty, P.; Paramasivam, G.; Lebedkin, S.; Kirakci, K.; Manna, S.; Antharjanam, S.; et al. Carborane-thiol protected copper nanoclusters: stimuli-responsive materials with tunable phosphorescence. *Chem. Sci.* **2023**, *14* (6), 1613-1626. DOI: 10.1039/D2SC06578A.

(39) Anderson, K. P.; Mills, H. A.; Mao, C.; Kirlikovali, K. O.; Axtell, J. C.; Rheingold, A. L.; Spokoyny, A. M. Improved synthesis of icosahedral carboranes containing exopolyhedral BC and CC bonds. *Tetrahedron* **2019**, *75* (2), 187-191. DOI: https://doi.org/10.1016/j.tet.2018.11.040.

(40) Dziedzic, R. M.; Spokoyny, A. M. Metal-catalyzed cross-coupling chemistry with polyhedral boranes. *Chem. Commun.* **2019**, *55* (4), 430-442. DOI: 10.1039/C8CC08693A.

(41) Lu, W.; Wu, Y.; Ma, Y.-N.; Chen, F.; Chen, X. A Method for Highly Selective Halogenation of o-Carboranes and m-Carboranes. *Inorg. Chem.* **2023**, *62* (2), 885-892. DOI: 10.1021/acs.inorgchem.2c03694.

(42) Ren, H.; Zhang, P.; Xu, J.; Ma, W.; Tu, D.; Lu, C.-s.; Yan, H. Direct B–H Functionalization of Icosahedral Carboranes via Hydrogen Atom Transfer. *JACS* **2023**, *145* (13), 7638-7647. DOI: 10.1021/jacs.3c01314.

(43) Cheng, R.; Qiu, Z.; Xie, Z. Iridium-catalysed regioselective borylation of carboranes via direct B–H activation. *Nat. Commun.* **2017**, *8* (1), 14827. DOI: 10.1038/ncomms14827.

(44) Taoda, Y.; Sawabe, T.; Endo, Y.; Yamaguchi, K.; Fujii, S.; Kagechika, H. Identification of an intermediate in the deboronation of ortho-carborane: an adduct of ortho-carborane with two nucleophiles on one boron atom. *Chem. Commun.* **2008**, (17), 2049. DOI: 10.1039/b716079h.

(45) Zi, G.; Li, H.-W.; Xie, Z. Synthesis, Structural Characterization, and Reactivity of ‘Carbons-Adjacent' nido- and arachno-Carborane Anions of the C2B10 Systems and Their Metal Complexes. *Organometallics* **2002**, *21* (24), 5415-5427. DOI: 10.1021/om020809f.

(46) Núñez, R.; Tarrés, M.; Ferrer-Ugalde, A.; de Biani, F. F.; Teixidor, F. Electrochemistry and Photoluminescence of Icosahedral Carboranes, Boranes, Metallacarboranes, and Their Derivatives. *Chem. Rev.* **2016**, *116* (23), 14307-14378. DOI: 10.1021/acs.chemrev.6b00198.

(47) Keener, M.; Hunt, C.; Carroll, T. G.; Kampel, V.; Dobrovetsky, R.; Hayton, T. W.; Ménard, G. Redox-switchable carboranes for uranium capture and release. *Nature* **2020**, *577* (7792), 652-655. DOI: 10.1038/s41586-019-1926-4.

(48) Keener, M.; Mattejat, M.; Zheng, S.-L.; Wu, G.; Hayton, T. W.; Ménard, G. Selective electrochemical capture and release of uranyl from aqueous alkali, lanthanide, and actinide mixtures using redox-switchable carboranes. *Chem. Sci.* **2022**, *13* (12), 3369-3374. DOI: 10.1039/D1SC07070C.

(49) Popescu, A. R.; Laromaine, A.; Teixidor, F.; Sillanpää, R.; Kivekäs, R.; Llambias, J. I.; Viñas, C. Uncommon Coordination Behaviour of P(S) and P(Se) Units when Bonded to Carboranyl Clusters: Experimental and Computational Studies on the Oxidation of Carboranyl Phosphine Ligands. *Chem. Eur. J.* **2011**, *17* (16), 4429-4443. DOI: 10.1002/chem.201003330.

Chapter 2 Diaryl Phosphine Oxide-Substituted *o*-Carboranes

2.1. Introduction

2.1.1. Nuclear Energy

Nuclear energy currently supplies 11% of the world's electricity and is projected to increase partly in response to the need for decarbonizing the energy grid.[1] Nuclear power plants can operate continuously – essential for periods of the day when renewable energy sources (e.g., solar, wind) are intermittent. Contrary to fossil-fuel power plants, no air pollution is generated during operation.

Nuclear energy is powered by a series of transmutation steps. Bombardment of ^{235}U with a neutron can initiate its splitting into two separate nuclei simultaneously releasing 2-3 neutrons and energy. The released neutrons propagate the nuclear fission chain reaction. Two common reaction pathways involve formation of ^{140}Cs and ^{93}Rb, or various isotopes of Ba and Kr. The energy produced from the nuclear reactors, submerged in water, generates steam which spin large turbines to produce electricity for the grid.[2]

The output of nuclear power can be modulated to match dynamic needs of the energy grid. Controlling the flow rate of water/steam allows for flexible energy production that can parallel the demands of the grid during peak hours. Neutron-absorbing control rods, containing either boron, hafnium or cadmium, are placed inside of the reactor core to control the rate of the fission reaction.[3] The depth of insertion can be raised or lowered to speed up or slow down the reaction.

A nuclear fuel rod reaches its end of life when it can no longer sustain a controlled and efficient fission reaction as ^{235}U is depleted. At this point, the nuclear rod is regarded as spent nuclear fuel (SNF). SNF consists of U (95%), Pu (0.9%), the minor actinides (0.1% (Np, Am, Cm)), and other elements (4% (Tc, Mo, I, Cs, lanthanides, etc.)).[4] SNF is initially stored in

temporary concrete cooling pools (~5-10 years) until the emitted heat and radiation is safe for handling. Afterwards, SNF is either reprocessed or stored long-term in concrete dry cask storage at the nuclear powerplant facilities, or in geographic repositories. In the United States, all SNF is stored indefinitely – 2,000 kilotons a year, approximately the size of an Olympic swimming pool. Very little nuclear waste is generated due to the high energy density of U (3,900,000 MW/kg) vs. coal (24 MW/kg) or natural gas (55 MW/kg).[5] However, treatment of SNF could mitigate the volume of waste generated because once U is separated from other fission products, it can be reprocessed and reused in a nuclear reactor. Recycling U is a superb strategy for minimizing environmentally-taxing, terrestrial land mining of uranium ores.[6]

Extensive research has been conducted on separating U in SNF. The Plutonium Uranium Reduction Extraction (PUREX) process is the most common method for treating SNF. The SNF is dissolved in concentrated nitric acid. An immiscible, organic phase consisting of 20-40% tributylphosphate in kerosene extracts uranyl (UO_2^{2+}) and Pu from the other fission products leaving behind the other minor fission products, termed High Level Waste (HLW) (Figure 2.1).[7] The Pu is reductively stripped to the aqueous phase with stoichiometric reagents resulting in a pure Pu stream. UO_2^{2+} is subsequently isolated in dilute nitric acid and can be reprocessed for nuclear fuel.

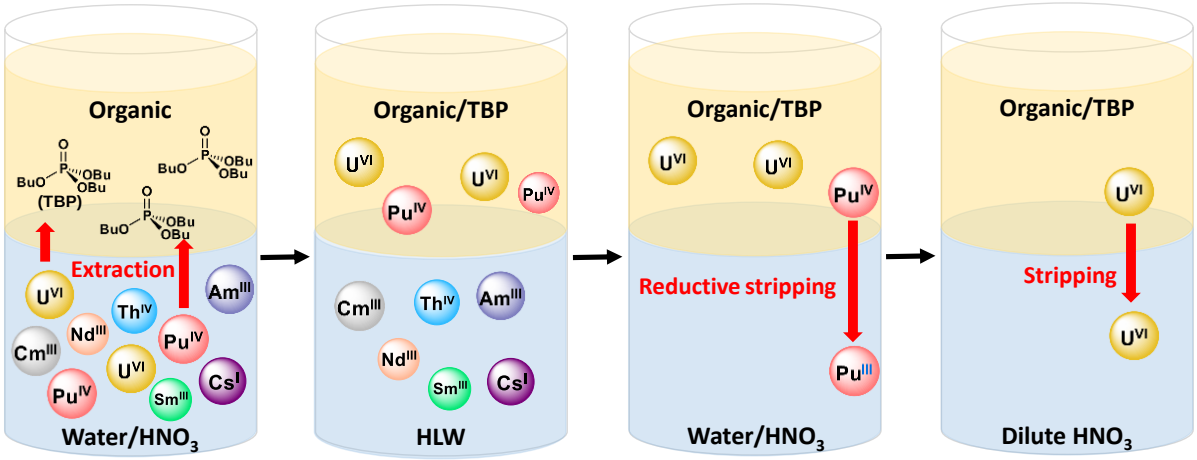

Figure 2.1. PUREX Process

The PUREX process is very effective at isolating UO_2^{2+}. However, the PUREX process is not implemented worldwide because of proliferation concerns regarding the unavoidable stockpiling of Pu.[7] Variations of the PUREX process have been developed such as the Uranium Extraction or Co-Extraction processes but are not yet economically viable for commercial scale applications in the United States.[8] Advances in the PUREX process that improve the monetary cost and eliminate Pu isolation could allow for widespread SNF treatment, curtailing the amount of nuclear waste and the need for terrestrial mining of uranium ores.

2.1.2. Biphasic UO_2^{2+} Extraction with Phosphine Oxide Carboranes

Previous work in our group has targeted a modified PUREX process incorporating redox-switches to eliminate stoichiometric reagents for cost effectiveness. Redox-switchable *ortho-closo*-carboranes bearing coordinating phosphine oxide donors, 1,2-(Ph_2PO)-1,2-$C_2B_{10}H_{10}$ (^{PO}**Cb**), could be electrochemically reduced to the *nido*-carborane, ^{PO}**Cb**$^{2-}$, an efficient extractant for biphasic uranyl (UO_2^{2+}) capture (Figure 2.2). Release of UO_2^{2+} was initiated by electrochemical oxidation of the captured *nido* product back to its *closo* (^{PO}**Cb**)

form.[9] With a solution of metals mimicking SNF (UO_2^{2+}, Cs^+, Th^{4+}, Sm^{3+}, Nd^{3+}), we observed up to 72% of selective capture of UO_2^{2+} relative to the other metals. While the extraction step performed well, the release step performed poorly with a maximum 38% release relative to extracted UO_2^{2+}.[10] This method provided a possible alternative approach to PUREX chemistry using non-stoichiometric, electrochemically-generated extractants.

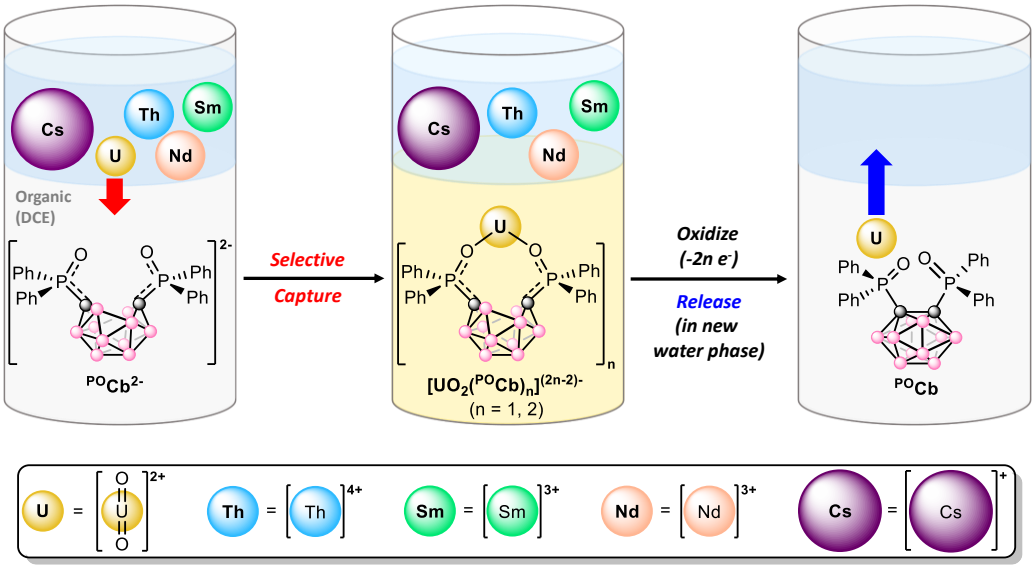

Figure 2.2. Selective Biphasic UO_2^{2+} Extraction

In this Chapter, we investigated how tuning the structural and electronic parameters of the starting **^{PO}Cb** extractant could alter the biphasic UO_2^{2+} capture and release efficiencies. While we have previously shown that the changing bite angle from the *closo* species, **^{PO}Cb**, to the *nido* species, **^{PO}Cb^{2-}**, likely played a dominant role in initiating biphasic capture, we also found that the drastically increasing Lewis basicity at the P=O moieties upon reduction may also play a key role.[9] Therefore, here we sought to determine how tuning this basicity through the installation of electron-withdrawing (EWG) or electron-donating groups (EDG) on the phenyl rings may alter the donicity (Figure 2.3). In addition, it is well known that

carboranyl cage substitution, such as with alkyls or halogens, leads to shifting carborane redox potentials.[11, 12] We further investigated these effects on ligation and capture/release chemistry.

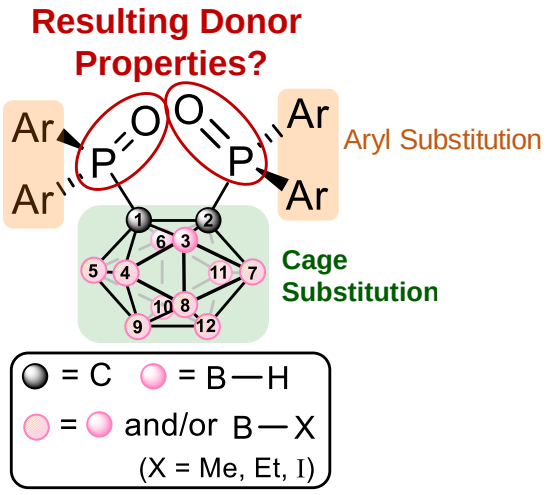

Figure 2.3. Phosphine Oxide Carborane Structure-Function Relationship.

Figure 2.4 outlines the series of seven new carboranes—derivatives of the original ^{PO}**Cb** structure—as well as the observed electron withdrawing or donating trends which were established through mixed spectroscopic, structural, and electrochemical experiments. Attempts to correlate these trends to biphasic UO_2^{2+} capture and release efficiencies, monitored using trace metal ICP-OES measurements, were also performed.

2.2. Results and Discussion

2.2.1. Synthesis and Characterization

Most B–H vertices on *ortho*-carborane (1,2-$C_2B_{10}H_{12}$, Cb) can be readily functionalized using standard Friedel-Crafts halogenation or alkylation chemistry. Incorporating halogens onto the cage is reported to lead to anodically shifted *closo*/*nido* reduction events and a concurrent increase in C–H acidity.[11] Conversely, the addition of methyl groups on boron vertices is reported to lead to cathodically shifted cage reduction

events with a concurrent decrease in C–H acidity (as also observed herein).[13-15] Interestingly, with few exceptions,[15] little is known about how altering the redox properties of the cage may affect the Lewis basic or acidic properties of substituents bound to the 1,2-carbon positions. Here, we sought to gain further insights into these effects by synthesizing a series of new cage- and aryl-substituted carboranes and monitoring the resulting effects on phosphine oxide donor properties (Figure 2.4).

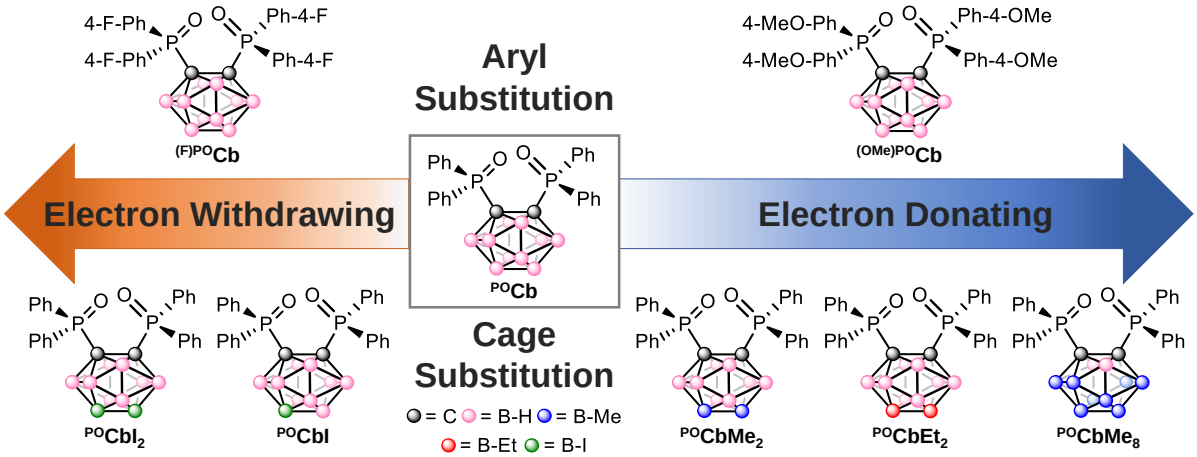

Figure 2.4. Library of 1,2-bis(diarylphosphine oxide)-*ortho*-carboranes with electron-withdrawing or electron-donating cage or aryl substituents.

The synthesized series of new cage-substituted **^{PO}Cb** compounds, including 9-I-^{PO}Cb (**^{PO}CbI**), 9,12-I_2-^{PO}Cb (**^{PO}CbI$_2$**), 9,12-Me_2-^{PO}Cb (**^{PO}CbMe$_2$**), 9,12-Et_2-^{PO}Cb (**^{PO}CbEt$_2$**), and 4,5,7,8,9,10,11,12-Me_8-^{PO}Cb (**^{PO}CbMe$_8$**) (Figure 2.4), were synthesized through initial Friedel-Crafts halogenation or alkylation of Cb to generate the cage precursors following reported procedures.[13,16-19] These precursors were then deprotonated with *n*-BuLi and treated with chlorodiphenylphosphine to obtain the P(III) precursors. Finally, treatment of these to *meta*-chloroperoxybenzoic acid (*m*CPBA) afforded the desired products in excellent yields (Scheme 2.1). The new aryl-substituted congeners, 1,2-((4-MeOPh)$_2$PO)$_2$-Cb (**$^{(OMe)PO}$Cb**) and

1,2-((4-FPh)$_2$PO)$_2$-Cb (**$^{(F)PO}$Cb**) were generated in an analogous fashion by initial deprotonation of Cb, followed by installation of the appropriate chlorodiarylphosphine precursor and oxidation with *m*CPBA (Scheme 2.1).

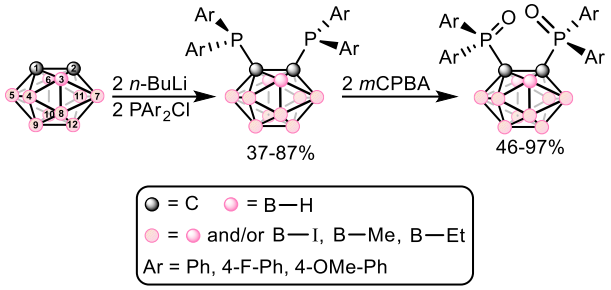

Scheme 2.1. Synthesis of 1,2-bis(diarylphosphine oxide)-*o*-carboranes

Each new carborane was structurally characterized via single-crystal X-ray diffraction (XRD) studies (Figure 2.5). A detailed analysis of the relevant bond metrics (e.g., P=O, C–C (on carborane), etc.) revealed few noticeable trends or significant differences between each species (Table 2.1), except for **^{PO}CbMe$_8$** which displayed more distorted pseudo-tetrahedral geometries around the P centers which we attribute to the increased steric bulk of the CbMe$_8$ cage.

Table 2.1. Reported P–O and bond lengths, C-P-C angle summation, C–C bond length for carborane species.

Compound	P=O Bond Length (Å)	C–P–C Angle Summation (°)	C–C Bond Length (Å)
^{PO}Cb	1.4716(17), 1.4767(19)	321.883, 320.676	1.689(3)
$^{(F)PO}$Cb	1.477(3), 1.471(4)	321.575, 320.113	1.711(6)
$^{(OMe)PO}$Cb	1.480(4), 1.490(4), 1.487(4), 1.483(4)	320.992, 321.187, 322.498, 322.561	1.728(9), 1.720(9)
^{PO}CbI$_2$	1.474(4), 1.465(4), 1.472(4), 1.472(4)	320.673, 321.246, 320.186, 320.697	1.690(9), 1.698(7)
^{PO}CbI	1.468(4), 1.474(3)	319.653, 322.275	1.690(5)
^{PO}CbMe$_2$	1.478(4), 1.469(4), 1.479(4), 1.476(4)	320.046, 321.243, 319.363, 321.157	1.706(7), 1.709(7)
^{PO}CbEt$_2$	1.474(3), 1.473(3)	322.804, 321.358	1.705(6)
^{PO}CbMe$_8$	1.4809(11), 1.4852(10)	326.939, 334.929	1.7841(19)

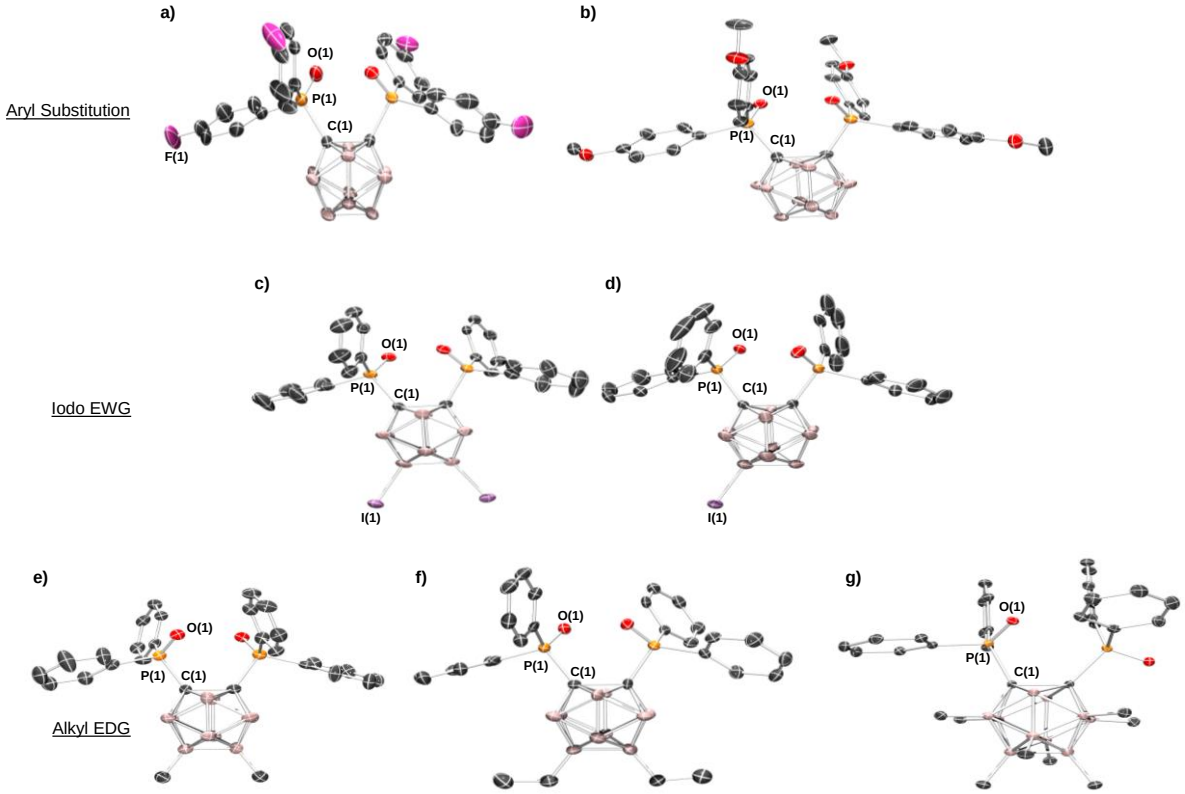

Figure 2.5. Solid-state molecular structures of Phosphine Oxide Carboranes obtained by single crystal XRD studies. H-atoms and co-crystallized solvent omitted for clarity. a) $^{(F)PO}$**Cb** b) $^{(OMe)PO}$**Cb** c) ^{PO}**CbI** d) ^{PO}**CbI$_2$** e) ^{PO}**CbMe$_2$** f) ^{PO}**CbEt$_2$** g) ^{PO}**CbMe$_8$**

Each new carborane species was also characterized by FT-IR and multi-nuclear NMR (^{31}P, ^{11}B, ^{19}F, ^{1}H, ^{13}C) spectroscopies. Given our interest in P=O donicity (*vide infra*, Figure 2.3) we were particularly interested in probing trends at the P centers. Surprisingly, the P=O stretching frequencies displayed no noticeable trends upon cage- or aryl-substitution. Similarly, no trends were observed in the ^{31}P NMR resonances upon substitution relative to ^{PO}**Cb**, except for ^{PO}**CbMe$_8$** which was again attributed to the more distorted geometry at these P centers (Table 2.2.).

2.2.2. Electrochemistry

The redox properties of each new species were probed by cyclic voltammetry (CV) taken in acetonitrile with $[Bu_4N][PF_6]$ (0.1 M) as supporting electrolyte and referenced to the ferrocene/ferrocenium (Fc/Fc^+) redox couple (Figure 2.6). With the exception of **^{PO}CbMe$_8$**, the CVs displayed quasi-reversible 2 e^- reduction events consistent with *closo→nido* reductions with concurrent C_1–C_2 bond cleavage (Figure 1.3).[9, 10] The CV of **^{PO}CbMe$_8$** instead displayed two separate quasi-reversible 1 e^- reductions ($E_{1/2}$ = -1.034, -1.314 V).

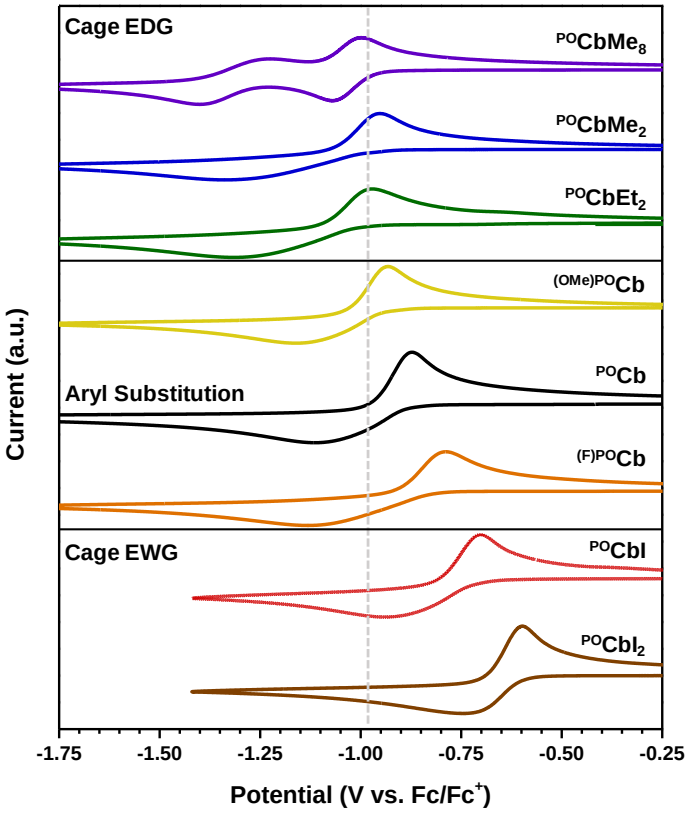

Figure 2.6. Stacked CVs of Phosphine Oxide Carboranes with 0.1 M $[Bu_4N][PF_6]$ in MeCN at 100 mV/s using a glassy carbon working electrode, Pt wire counter electrode, and $Ag/AgOTf_{(s)}$ reference electrode.

The addition of iodine to the carboranyl cage resulted in anodic shifts of the reduction potential by 163 mV ($E_{1/2}$ = -0.831 V) and 329 mV ($E_{1/2}$ = -0.665 V) for **^{PO}CbI** and **^{PO}CbI$_2$**, respectively, relative to **^{PO}Cb** ($E_{1/2}$ = -0.994 V), suggesting that these are electron-withdrawing to the cage.[11] Conversely, addition of two methyl (**^{PO}CbMe$_2$**) or two ethyl (**^{PO}CbEt$_2$**) groups caused a cathodic shift of 152 mV ($E_{1/2}$ = -1.146 V) and 146 mV ($E_{1/2}$ = -1.140 V), respectively, suggesting that these are electron-donating to the cage.[14, 15] In contrast to cage substitution, the addition of EDG or EWG to the aryl substituents only slightly shifted the reduction potentials. For instance, addition of a fluorine atom to each aryl group (4 total) in **$^{(F)PO}$Cb** resulted in only a minor anodic shift to the reduction potential by 35 mV ($E_{1/2}$ = -0.959 V). Similarly, addition of methoxy groups in **$^{(OMe)PO}$Cb** caused a cathodic shift of only 52 mV ($E_{1/2}$ = -1.046 V) (Table 2.2.)

A clear trend of redox properties for substituted carboranes was established. Accordingly, we were interested in studying the electrochemical redox behavior of **^{PO}Cb** in the presence of UO_2^{2+}. Control CVs were taken of $[UO_2Cl_2(THF)_2]_2$ and of $[UO_2Cl_2(THF)_2]_2$ with 4 equiv. of triphenylphosphine oxide (TPPO), generating *in situ* $UO_2Cl_2(TPPO)_2$ in 0.1 M $[Bu_4N][PF_6]$ in acetonitrile (Figure 2.7).

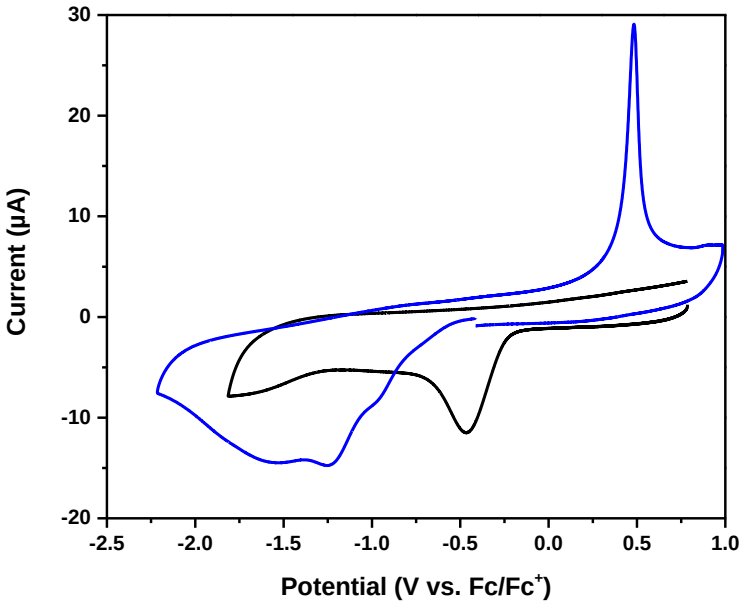

Figure 2.7. CV of $[UO_2Cl_2(THF)_2]_2$ and $UO_2Cl_2(TPPO)_2$. Black – 2 mM $[UO_2Cl_2(THF)_2]_2$. Blue – 2.2 mM $UO_2Cl_2(TPPO)_2$. CVs taken at 100 mV/s with a glassy carbon working electrode, Pt wire counter electrode and $Ag/AgOTf_{(s)}$ reference electrode in 0.1 M $[Bu_4N][PF_6]$ acetonitrile.

We observe the reduction of $U^{(VI)}$ (UO_2^{2+}) to $U^{(V)}$ (UO_2^{+}) at -0.469 V vs. Fc/Fc^+ when UO_2Cl_2 is bound to THF or acetonitrile. A disproportiation reaction subsequently occurs forming $UO_{2(s)}$ and UO_2^{2+}.[20] Adding TPPO to the UO_2^{2+} coordination sphere in place of coordinating solvents causes a cathodic shift in the reduction to approximately -1.2 V and an anodic stripping event at 0.48 V (Figure 2.7). The speciation of UO_2^{2+} has a pronounced effect on redox potential, wherein increasingly basic ligands shift the reduction cathodically.[21-23] Interestingly, the CV of ^{PO}**Cb** with $[UO_2Cl_2(THF)_2]_2$ displays an anodic shift in the *closo* reduction peak potential by 456 mV (E_{red} = -0.659 V) and a concurrent disappearance in the *nido* oxidation (Figure 2.8). The anodic shift in the reduction peak current suggests that *closo*-carborane species, ^{PO}**Cb** coordinates to UO_2Cl_2 . With TPPO in solution, the carborane

reduction remains anodically shifted, but the *nido* oxidation reemerges (Figure 2.8). No anodic stripping event is observed, as in Figure 2.7. Perhaps, this suggests that *closo*-carborane species may compete with TPPO for UO_2^{2+} binding. We will probe the binding competition between *closo*-carboranes and TPPO further in Section 2.2.4.

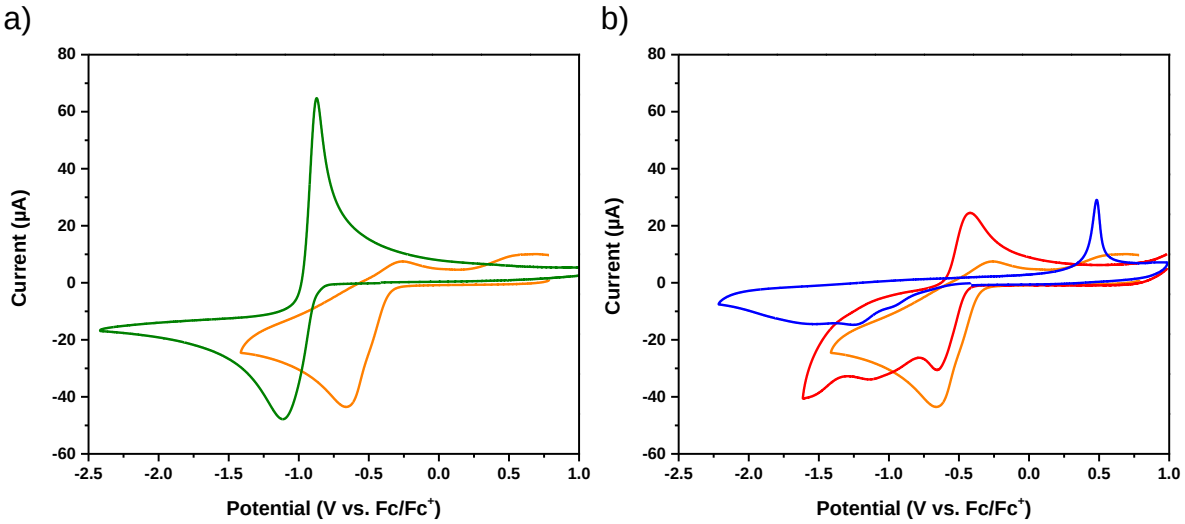

Figure 2.8. CVs of **^{PO}Cb** with $[UO_2Cl_2(THF)_2]_2$ and TPPO. a) Green – 2.1 mM **^{PO}Cb**. Orange – 2.1 mM **^{PO}Cb** with 2 mM $[UO_2Cl_2(THF)_2]_2$. b) Orange – 2.1 mM **^{PO}Cb** with 2 mM $[UO_2Cl_2(THF)_2]_2$. Blue – 2.2 mM $UO_2Cl_2(TPPO)_2$. Red – 2.1 mM **^{PO}Cb** with 2 mM $[UO_2Cl_2(THF)_2]_2$ and 7.9 mM TPPO. All CVs taken at 100 mV/s with a glassy carbon working electrode, Pt wire counter electrode and $Ag/AgOTf_{(s)}$ reference electrode in 0.1 M $[Bu_4N][PF_6]$ acetonitrile.

Table 2.2. Reported bond lengths, IR stretch, $^{31}P\{^{1}H\}$ NMR resonances, reduction potentials, pK_{BH^+} and pK_{eq} for the modified carborane series.

Substitution pattern		Compound	P=O stretch (cm^{-1})	P=O bond length (Å)	$^{31}P\{^{1}H\}$ NMR (ppm)	$E_{1/2}$ (V)	pK_{BH^+}	pK_{eq}
Aryl	**EWG**	$^{(F)PO}$Cb	1236	1.477(3), 1.471(4)	23.1	-0.959	-0.349 ± 0.010	-0.90 ± 0.14
	^{PO}Cb	**^{PO}Cb**	**1219**	**1.4716(17), 1.4767(19)**	**23.8**	**-0.994**	**0.457 ± 0.015**	**0.33 ± 0.05**
	EDG	$^{(OMe)PO}$Cb	1210	1.480(4), 1.490(4), 1.487(4), 1.483(4)	24.4	-1.046	0.701 ± 0.010	2.06 ± 0.05
Cage	**EWG**	^{PO}CbI$_2$	1222	1.474(4), 1.465(4), 1.472(4), 1.472(4)	25.9	-0.665	unstable	unstable
		^{PO}CbI	1217	1.468(4), 1.474(3)	25.97, 24.07 (d)	-0.831	0.052 ± 0.010	-0.46 ± 0.11
	^{PO}Cb	**^{PO}Cb**	**1219**	**1.4716(17), 1.4767(19)**	**23.8**	**-0.994**	**0.457 ± 0.015**	**0.33 ± 0.05**
	EDG	^{PO}CbEt$_2$	1214	1.474(3), 1.473(3)	23.7	-1.140	1.062 ± 0.010	0.78 ± 0.06
		^{PO}CbMe$_2$	1219	1.478(4), 1.469(4), 1.479(4), 1.476(4)	23.7	-1.146	1.191 ± 0.009	0.78 ± 0.11
		^{PO}CbMe$_8$	1200	1.4809(11), 1.4852(10)	31.1	-1.034, -1.314	1.373 ± 0.000	0.90 ± 0.06

2.2.3. NMR Basicity Studies

We next probed whether a correlation existed between the observed ligand redox properties and subsequent P=O Lewis basicity. We utilized an NMR technique developed by Franz and co-workers to probe these effects.[24] Here, pentafluorobenzoic acid (PFBA, pK_a = 1.48) acts as a highly sensitive ^{19}F NMR probe and hydrogen bond donor (HBD) forming an H-bond interaction with a hydrogen bond acceptor (HBA)—in our case corresponding to the

Lewis basic P=O moieties (Scheme 2.2)—which results in shifted (Δδ) PFBA ^{19}F NMR resonances.

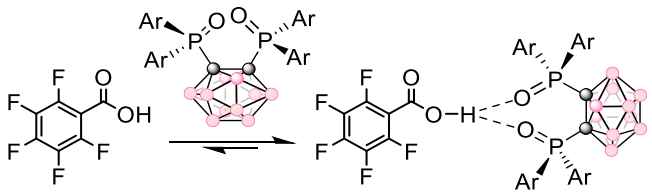

Scheme 2.2. Formation of HBA-HBD adduct between carboranes and PFBA.

The observed Δδ(^{19}F) may be correlated to the proton transfer basicity (pK_{BH^+}) of these Lewis bases using the linear equation established by Franz et. al. (Equation 2.1).[24-26]

$$pK_{BH^+} = 1.1795\left(\Delta\delta\left(^{19}F\right)\right) - 3.4079 \qquad (2.1)$$

The carborane species were loaded with PFBA in a 5:1 equivalent ratio in CD_2Cl_2, with the selected ratio derived from a saturation curve and the resulting ^{19}F NMR spectra were collected (Figure 2.9).

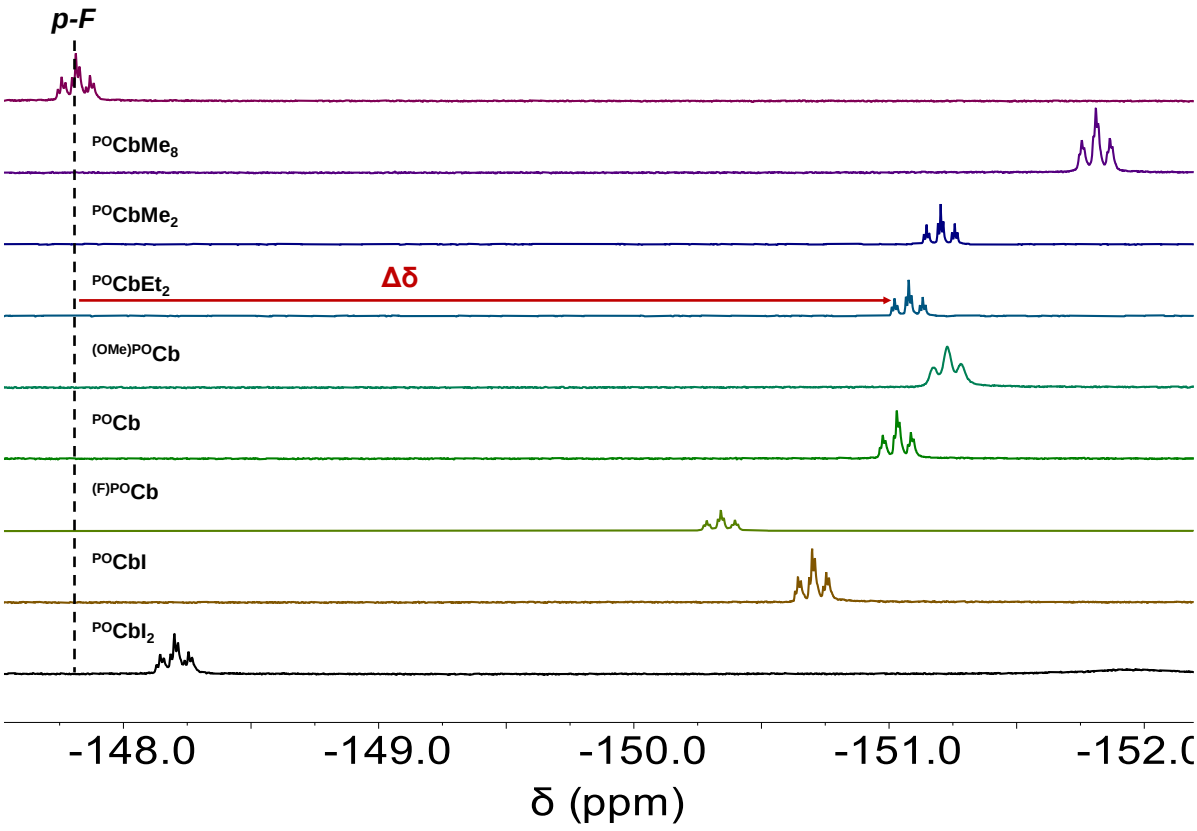

Figure 2.9. ^{19}F NMR spectra of PFBA-carborane adducts displaying the shift in *p*-F of PFBA.

^{PO}Cb had a measured pK_{BH^+} of 0.46. With EWG substituents in **$^{(F)PO}$Cb** and **^{PO}CbI**, we observed decreasing Lewis basicities with pK_{BH^+} values of -0.35 and 0.05, respectively. The pK_{BH^+} of **^{PO}CbI$_2$** could not be accurately measured due to observed degradation peaks in the ^{19}F NMR spectrum. Conversely, EDGs on the aryl and carboranyl cage positions resulted in increased basicities as evidenced by the following pK_{BH^+} values (in parentheses): **$^{(OMe)PO}$Cb** (0.701), **^{PO}CbEt$_2$** (1.06), **^{PO}CbMe$_2$** (1.19), and **^{PO}CbMe$_8$** (1.37). A general trend is observed wherein substituted carboranes with anodically shifted $E_{1/2}$ values relative to **^{PO}Cb** bear less Lewis basic P=O bonds, whereas those with cathodically shifted $E_{1/2}$ values bear more Lewis basic P=O bonds (Table 2.2).

2.2.4. NMR Competition Experiments

We next probed if the observed Lewis basic trends correlated to stronger UO_2^{2+} binding. We performed competition experiments comparing the relative binding affinities to UO_2^{2+} of triphenylphosphine oxide (TPPO) vs. our series of *closo*-carboranes (Figure 2.4) in dichloroethane (DCE) using $UO_2(NO_3)_2(THF)_2$ as the UO_2^{2+} source. These experiments were performed using unlocked $^{31}P\{^1H\}$ NMR spectroscopy. Experimental conditions and reagents were meticulously determined through optimization studies using various solvents (DCE, THF, MeCN, pyridine, DMF, DCM), different UO_2^{2+} sources (Cl vs. NO_3), and commercial phosphine oxides (TPPO) and methyldiphenylphosphine oxide. Coordinating solvents resulted in significant formation of two deboronated ($C_2B_9H_{10}^-$) phosphine oxide carborane units ($C_2B_9H_{10}^-$) bound to UO_2^{2+} appearing as a doublet at 47 ppm in the ^{31}P NMR spectrum because of asymmetric P environments with a 5-coordinate U in the equatorial plane (Figure 2.10). Non-coordinating solvents (DCE) minimize the deboronation byproduct, though it is still observed as a singlet in the NMR spectrum at 47 ppm. The identity of the byproduct was confirmed by a solid-state molecular structure obtained by single crystal X-ray diffraction studies (Figure 2.10).

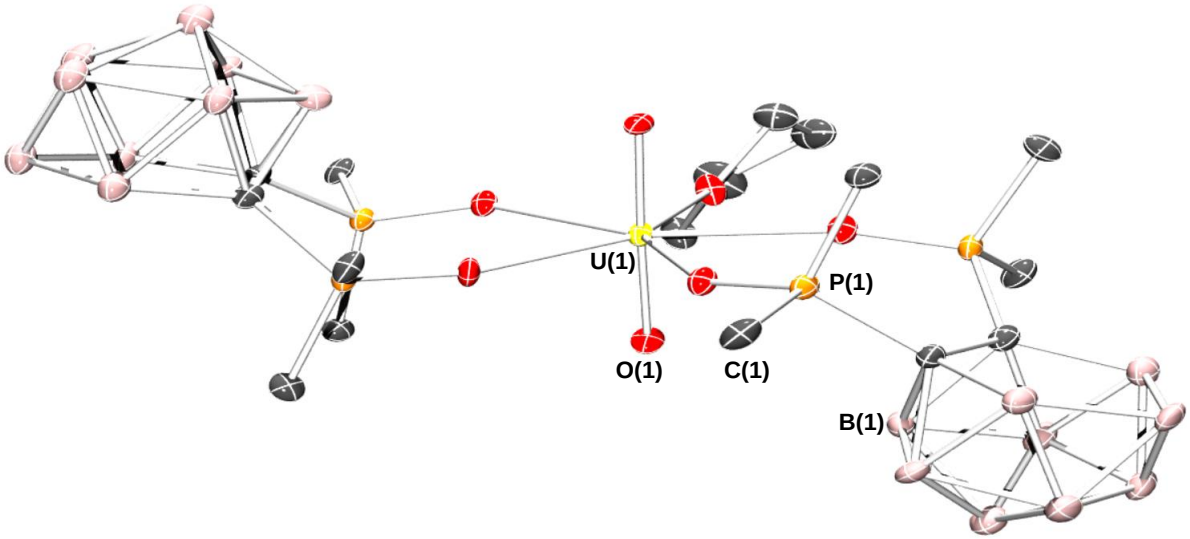

Figure 2.10. Solid-state molecular structure of 2 deboronated carboranes bound to UO_2^{2+} determined by single crystal XRD studies. H-atoms and phenyl rings omitted for clarity. A co-crystallized THF remains in the equatorial plane of UO_2^{2+} leading to asymmetry of the P environments.

We carefully selected reagents, DCE, $UO_2(NO_3)_2(THF)_2$, and TPPO to minimize byproducts. We cannot use reported $UO_2(NO_3)_2(TPPO)_2$ as the UO_2^{2+} source because of limited solubility in DCE.

With initial experimental parameters determined, we confirmed a bonding interaction exists between *closo* species, **^{PO}Cb**, and $(UO_2(NO_3)_2(THF)_2$, as observed by the emergence of a new singlet at 38 ppm in the $^{31}P\{^1H\}$ NMR spectrum. A saturation curve confirmed the 1:1 adduct ratio as addition of excess **^{PO}Cb** led to the sole reappearance of free ligand observed at 23 ppm (Figure 2.11). We assign the general formula, $UO_2(NO_3)_2(^{PO}Cb)$, to this complex as attempts to structurally characterize it have thus far failed. Attempts to obtain single crystals suitable for XRD studies failed and instead resulted in isolating degradation byproducts (Figure 2.10).

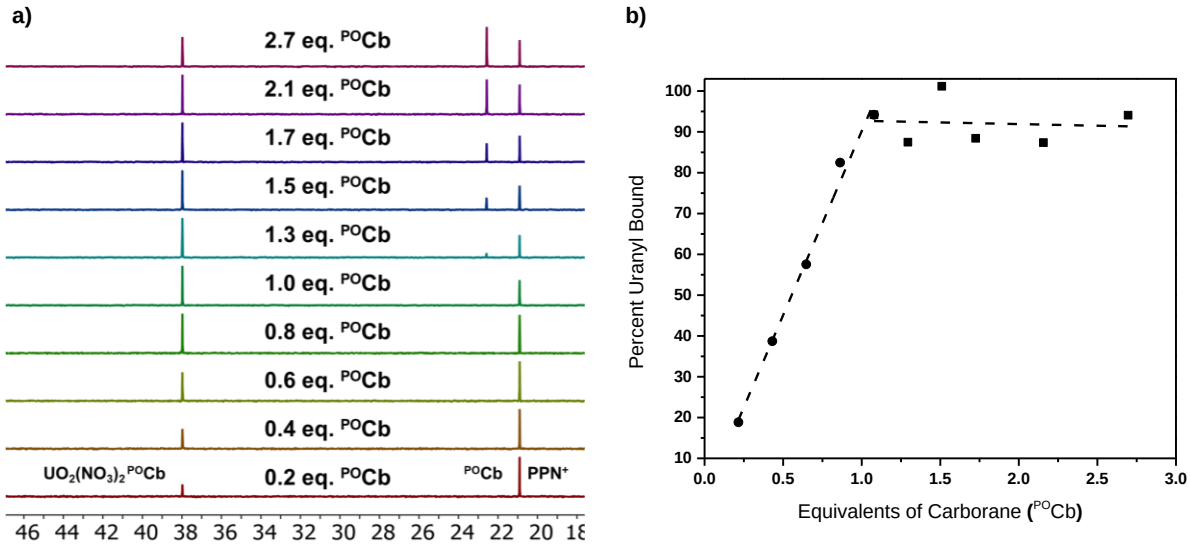

Figure 2.11. Established binding between *closo* carborane **^{PO}Cb** and UO_2^{2+}. a) Unlocked ^{31}P NMR spectra of $UO_2(NO_3)_2(THF)_2$ in DCE with increasing equivalents of **^{PO}Cb** and internal standard PPN^+. b) Corresponding UO_2^{2+} saturation curve with linear regressions intersecting at 1.03 equiv. **^{PO}Cb**.

Addition of TPPO to *in situ* generated $UO_2(NO_3)_2(^{PO}Cb)$ resulted in an equilibrium mixture of species identified as free **^{PO}Cb** and TPPO, as well as the complexes $UO_2(NO_3)_2(^{PO}Cb)$ and $UO_2(NO_3)_2(TPPO)_2$, the latter of which was identified by comparison to literature values.[27, 28] The chemical exchange between these four species occurred on a slow timescale such that sharp, distinct $^{31}P\{^1H\}$ NMR resonances were observable (Figure 2.12).[29, 30]

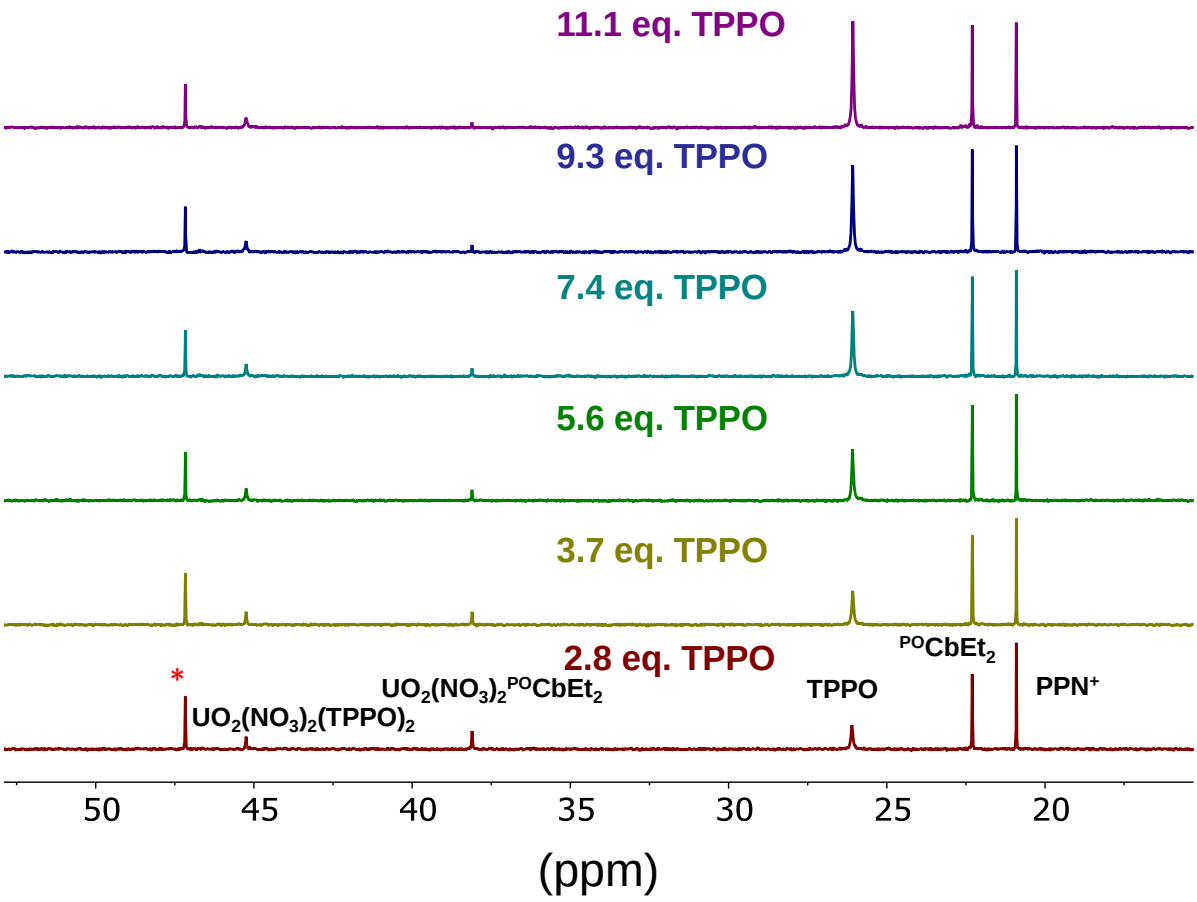

Figure 2.12. Example competition experiment of $^{PO}CbEt_2$, TPPO, and $UO_2(NO_3)_2$. The ^{31}P NMR displayed here demonstrates that as equivalents of TPPO are increased, the free **$^{PO}CbEt_2$** increases and *in situ* generated **$UO_2(NO_3)_2{}^{PO}CbEt_2$** decreases. The peak denoted with * is UO_2^{2+} bound to 2 deboronated carborane units.

The proposed equilibrium between these species is shown in Equation 2.2 with the corresponding equilibrium constant, *K*, expressed in Equation 2.3 (using **^{PO}Cb** as the example carborane). The relative binding strength of each carborane to UO_2^{2+} can then readily be represented by pK_{eq} values (Equation 2.4, Table 2.2). Bis(triphenylphosphine)iminium hexafluorophosphate ([PPN][PF_6]) was added to each solution as an internal standard and its

concentration was kept constant for quantitative determination of each equilibrium species by $^{31}P\{^{1}H\}$ NMR integration (e.g., Equation 2.5 for [^{PO}**Cb**]).[31, 32]

$$^{PO}Cb + UO_2(NO_3)_2(TPPO)_2 \;\rightleftarrows\; UO_2(NO_3)_2{}^{PO}Cb + 2\,TPPO \qquad (2.2)$$

$$K = \frac{\left[UO_2(NO_3)_2{}^{PO}Cb\right][TPPO]^2}{[^{PO}Cb][UO_2(NO_3)_2(TPPO)_2]} \qquad (2.3)$$

$$pK_{eq} = -\log K \qquad (2.4)$$

$$\left[^{PO}Cb\right] = \frac{Integration_{^{PO}Cb}}{Integration_{PPN}} \times \frac{\#Nuclei_{PPN}}{\#Nuclei_{^{PO}Cb}} \times [PPN] \qquad (2.5)$$

Average binding constants, pK_{eq}, were then determined for each carborane by holding the concentrations of each uranyl complex (e.g., $UO_2(NO_3)_2{}^{PO}Cb$) constant while adding different equivalents of TPPO (Figure 2.12). The measured pK_{eq} values generally mimicked the pK_{BH^+} trends determined as part of our basicity studies (*vide supra*, Table 2.2). For instance, addition of aryl or cage EWGs, such as in **$^{(F)PO}$Cb** and **^{PO}CbI**, resulted in lower pK_{eq} values of -0.89 and -0.46, respectively, relative to 0.33 for **^{PO}Cb**. Conversely, cage or aryl EDGs, such as in **^{PO}CbMe$_8$** and **$^{(OMe)PO}$Cb**, resulted in higher pK_{eq} values of 0.89 and 2.06, respectively, relative to **^{PO}Cb** (Table 2.2). Again here, the pK_{eq} value for **^{PO}CbI$_2$** could not be measured due to the formation of many unknown byproducts upon addition of TPPO.

Together, these results indicate that the relative donicity of the phosphine oxide groups to UO_2^{2+} can be controlled through judicious choice of aryl or cage substitution and almost linearly match the observed trends measured for relative basicities (Figure 2.13). The only

exception to this mostly linear trend was $^{(OMe)PO}$**Cb** which appeared to display the strongest affinity for UO_2^{2+}.

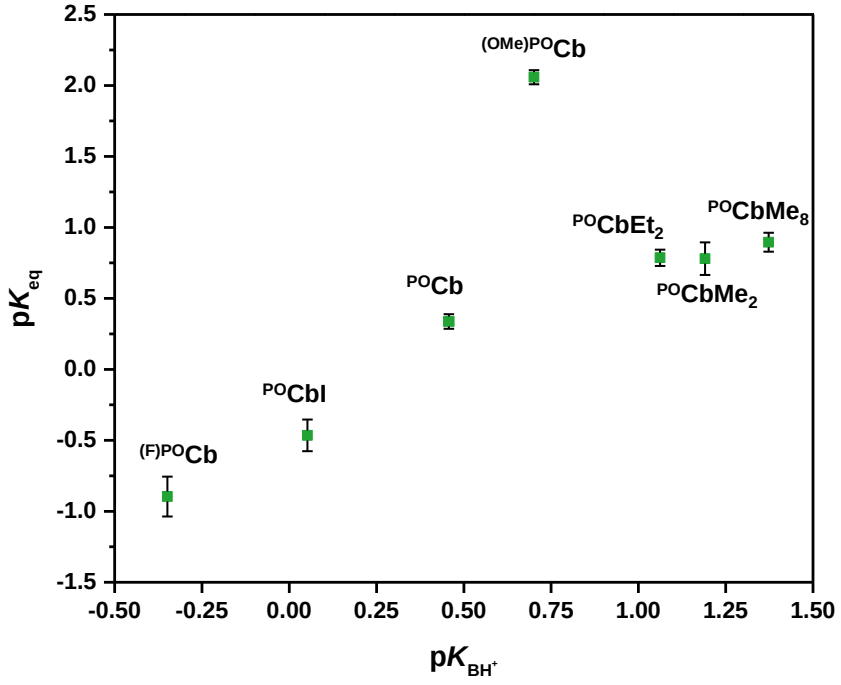

Figure 2.13. Graph of pK_{eq} vs. pK_{BH^+} for each carborane species.

2.2.5. Biphasic UO_2^{2+} Capture and Release

Having now experimentally established general donor trends for our new series of substituted carboranes (Figure 2.4), we next probed how these trends would impact biphasic UO_2^{2+} capture and release efficiencies (Figure 2.14).

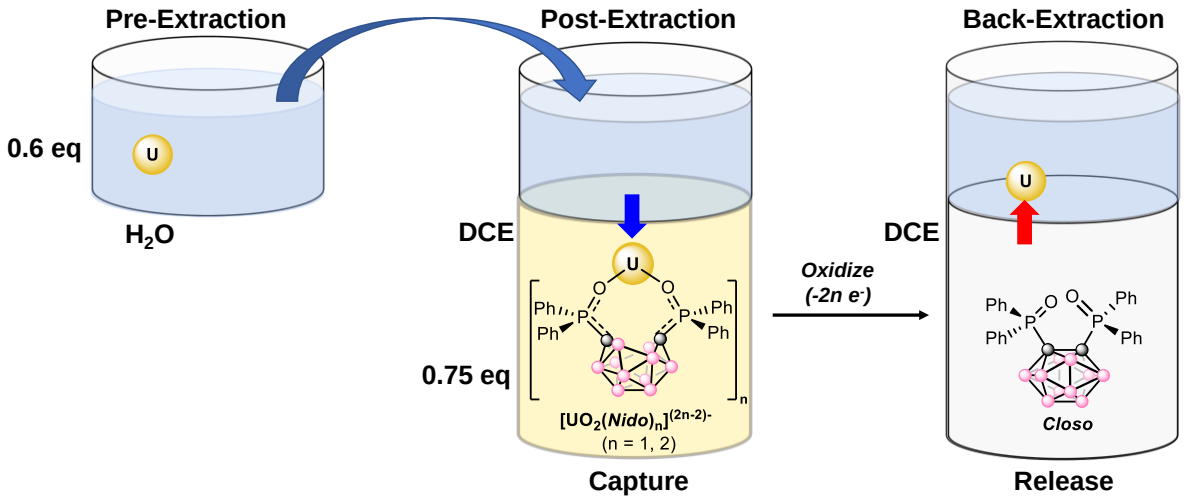

Figure 2.14. Biphasic Extraction Diagram. Labeled pre- post- and back-extraction phases monitored by ICP-OES. Pre-extraction aqueous phase contains 0.5 M NaOAc buffer and 0.6 equiv. of UO_2^{2+}. Back-extraction phase contains 0.1 M NaOAc buffer.

We electrochemically generated *nido*-carborane species through Galvanostatic bulk electrolysis (GBE) methods. Each modified carborane (1 equiv.) was dissolved in a 0.1 M $[Bu_4N][PF_6]$ DCE supporting electrolyte solution in the working compartment of an electrochemical H-cell. The auxiliary compartment, separated by a glass-frit, was loaded with a 0.1 M $[Bu_4N][PF_6]$ DCE solution with added Ketjenblack carbon additive serving as a capacitive buffer (Figure 2.15).[9]

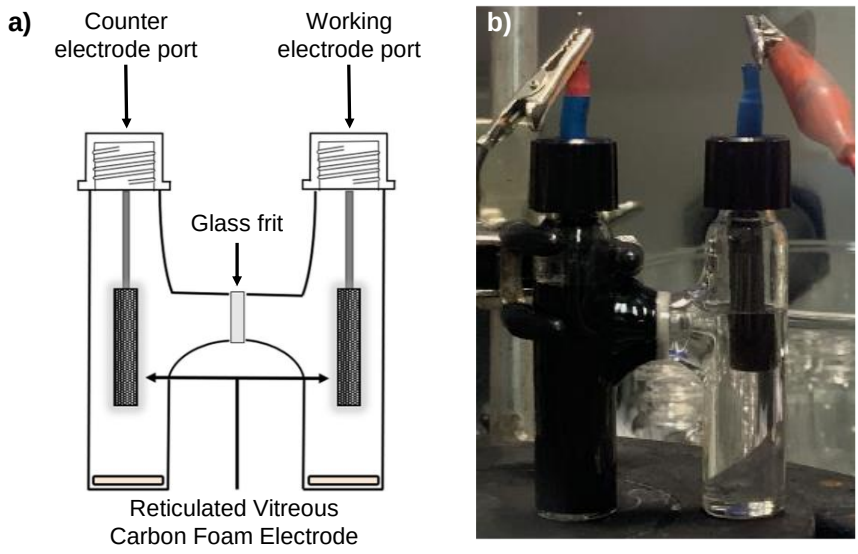

Figure 2.15. GBE H-cell design. a) Diagram of H-cell with its components labeled. b) Photograph of an H-cell set up with Ketjenblack addictive in the counter compartment and *closo*-carborane species in the working compartment.

The carborane solutions were galvanostatically charged to a ~75% theoretical state-of-charge (SOC) over 20 hours to form the respective reduced *nido*-carborane species (~0.75 equiv.) (Figure 2.16a).

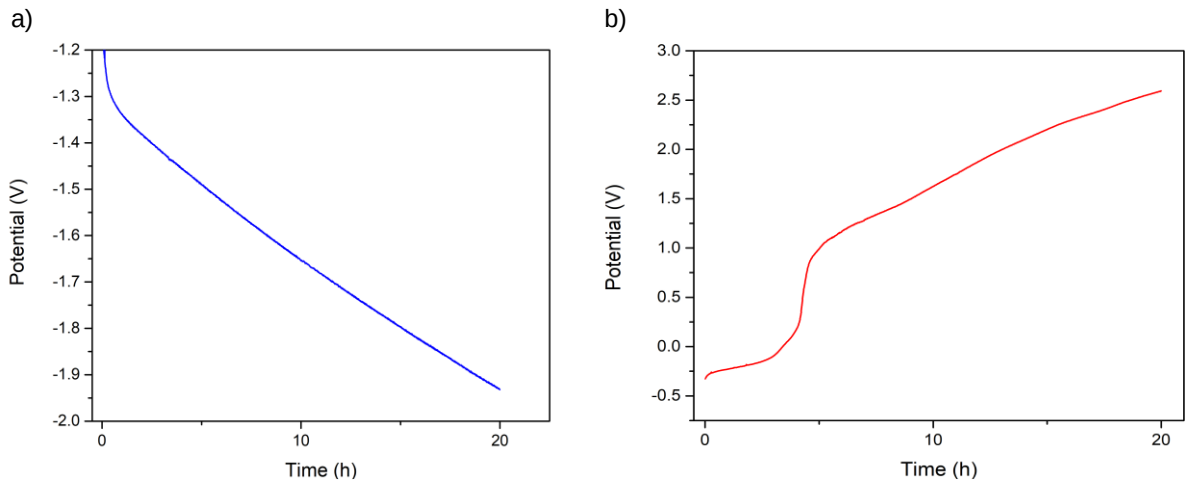

Figure 2.16. GBE Reduction (a) and Oxidation (b) Curves. a) A charging current of -127.6 μA was applied for a total of -9.20 C of charge transferred, resulting in a 75% SOC after 20 h assuming 100% columbic efficiency. b) A discharging current of 127.6 μA was applied for a total of 9.21 C of charge transferred, resulting in a 0% SOC after 20 h assuming 100% columbic efficiency.

Following ~75% conversion of *closo*-carborane species to *nido*-carborane, the working compartment DCE solution was removed from the H-cell and mixed with a 0.5 M NaOAc-buffered stock solution containing ca. 0.6 equiv. of $UO_2(NO_3)_2 \bullet 6H_2O$ (pre-extraction solution) for 1.5 hours (Figure 2.14). The aqueous phase was removed (post-extraction solution) and the DCE layer was galvanostatically discharged to a theoretical 0% SOC to regenerate the neutral *closo*-carborane species and initiate the release of UO_2^{2+} (Figure 2.16b).

Lastly, a fresh 0.1 M NaOAc-buffered aqueous solution was stirred with the DCE layer overnight for subsequent back-extraction of UO_2^{2+}(back-extraction solution) (Figure 2.14). Each of the cycling experiments were run in triplicate and formation of *nido*-carborane, uranyl carborane (e.g., $[UO_2(^{PO}Cb)_2]^{2-}$), and *closo*-carborane species in the organic phases were monitored via unlocked $^{31}P\{^1H\}$ NMR spectroscopy (Figure 2.17).

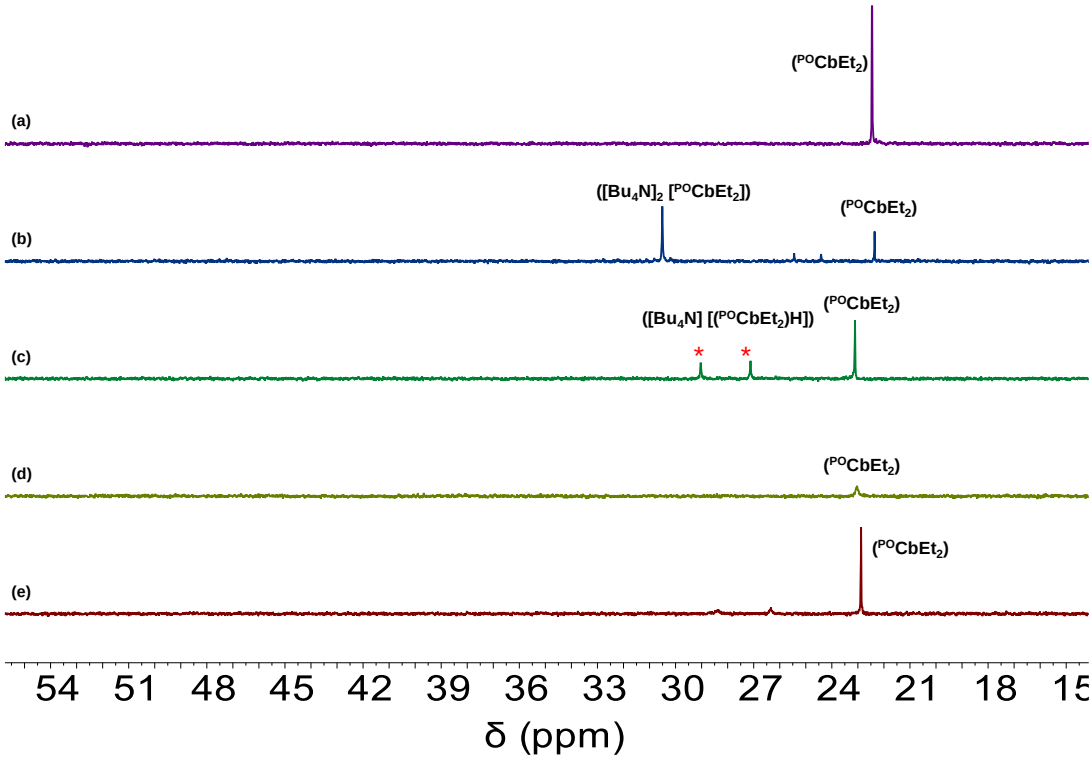

Figure 2.17. $^{31}P\{^{1}H\}$ NMR spectra of GBE cycling of **^{PO}CbEt$_2$** in DCE. a) Starting **^{PO}CbEt$_2$** solution. b) Reduced GBE solution. c) Organic phase after UO_2^{2+} capture. The $[UO_2(^{PO}CbEt_2)_2]^{2-}$ NMR resonance is not visible in the spectrum. * Denotes a protonated *nido*-species byproduct. d) Oxidized GBE solution. e) Organic phase following back-extraction of UO_2^{2+}.

The aqueous pre-, post-, and back-extraction solutions were analyzed via ICP-OES (Figure 2.14). Surprisingly, analyses of the aqueous phases by ICP-OES revealed high UO_2^{2+} percent extractions ranging from 78-88%, irrespective of aryl or cage substitution patterns (Figure 2.18). Back-extraction analyses revealed that **^{PO}Cb** released 38% of UO_2^{2+} relative to the percent extracted. Aryl substituted carboranes, **$^{(F)PO}$Cb** and **$^{(OMe)PO}$Cb**, released 49% and 45% of UO_2^{2+}, respectively, relative to the percent extracted. In contrast, the alkyl cage

substituted carboranes, **^{PO}CbEt$_2$** and **^{PO}CbMe$_8$**, yielded the highest percent back-extraction, with 68% and 59% of UO_2^{2+} released, respectively, relative to percent extracted (Figure 2.18).

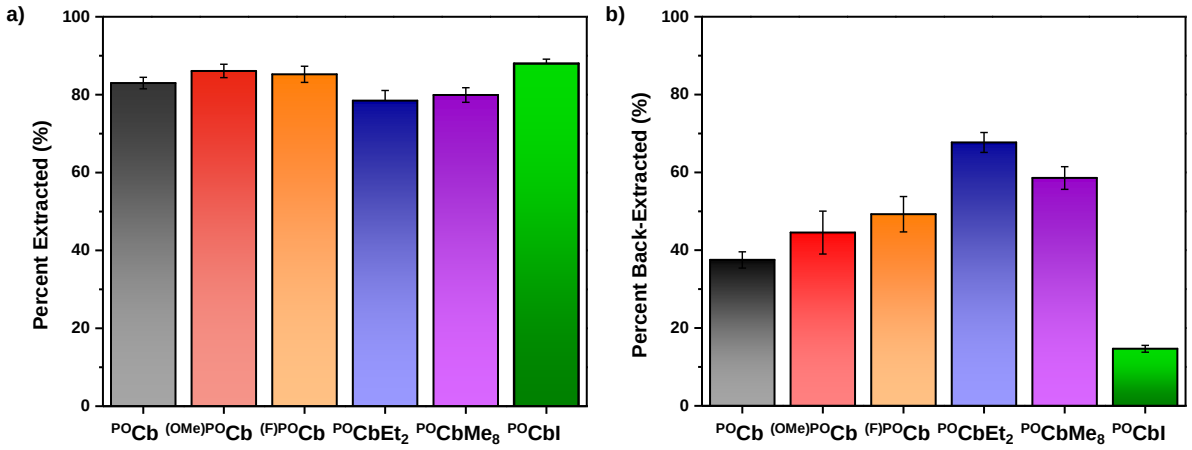

Figure 2.18. ICP-OES of UO_2^{2+} extraction and back-extraction. a) Average UO_2^{2+} percent extracted from the aqueous phase using electrochemically generated *nido*-carboranes. Percentages are relative to the initial 0.6 equiv. of UO_2^{2+} used (~0.75 equiv. of *nido*-carborane generated in DCE phase). b) Average UO_2^{2+} percent back-extracted from the DCE phase into the aqueous phase following electrochemical oxidation of *nido*-carboranes to *closo*-carboranes. Percentages are relative to the extracted amounts in (a).

The significant increase in UO_2^{2+} released for the alkyl substituted carboranes likely suggests that the hydrophobicity of the carborane plays a more important role in biphasic mass transport compared to the measured donor strength trends established in organic solvents (*vide supra*).[33, 34] **^{PO}CbI** and **^{PO}CbI$_2$** have shown consistent instability when in contact with Lewis bases and we suspected this degradation would carry on during biphasic cycling. **^{PO}CbI** maintained stability until discharge after which an unknown yellow precipitate was obtained. Consequently, **^{PO}CbI** only released 14% of UO_2^{2+} relative to the percentage extracted. Biphasic cycling of **^{PO}CbI$_2$** resulted in extensive, unidentifiable byproducts.

2.2.6. $UO_2(NO_3)_2{}^{PO}Cb$ displacement by H_2O

We were interested in further investigating the release of UO_2^{2+} from *closo*-carboranes. As detailed in section 2.2.4., *closo*-carboranes compete with known UO_2^{2+} extractant, TPPO.[35] Thus, it is peculiar that UO_2^{2+} is effectively back-extracted to the aqueous phase. $^{31}P\{^1H\}$ NMR spectra after the bulk oxidation step of biphasic cycling (Figure 2.17) appears to lack a peak corresponding to UO_2-*closo*-carborane species (e.g., $UO_2(NO_3)_2{}^{PO}Cb$)) as observed in anhydrous conditions (Figure 2.11). Admittedly, we are not aware of the speciation of UO_2^{2+} or transfer mechanism to and from the aqueous-organic interfaces. However, we were curious whether addition of H_2O to an anhydrous solution of $UO_2(NO_3)_2{}^{PO}Cb$ in DCE with internal standard PPN^+ would alter the $^{31}P\{^1H\}$ NMR resonances (Figure 2.19).

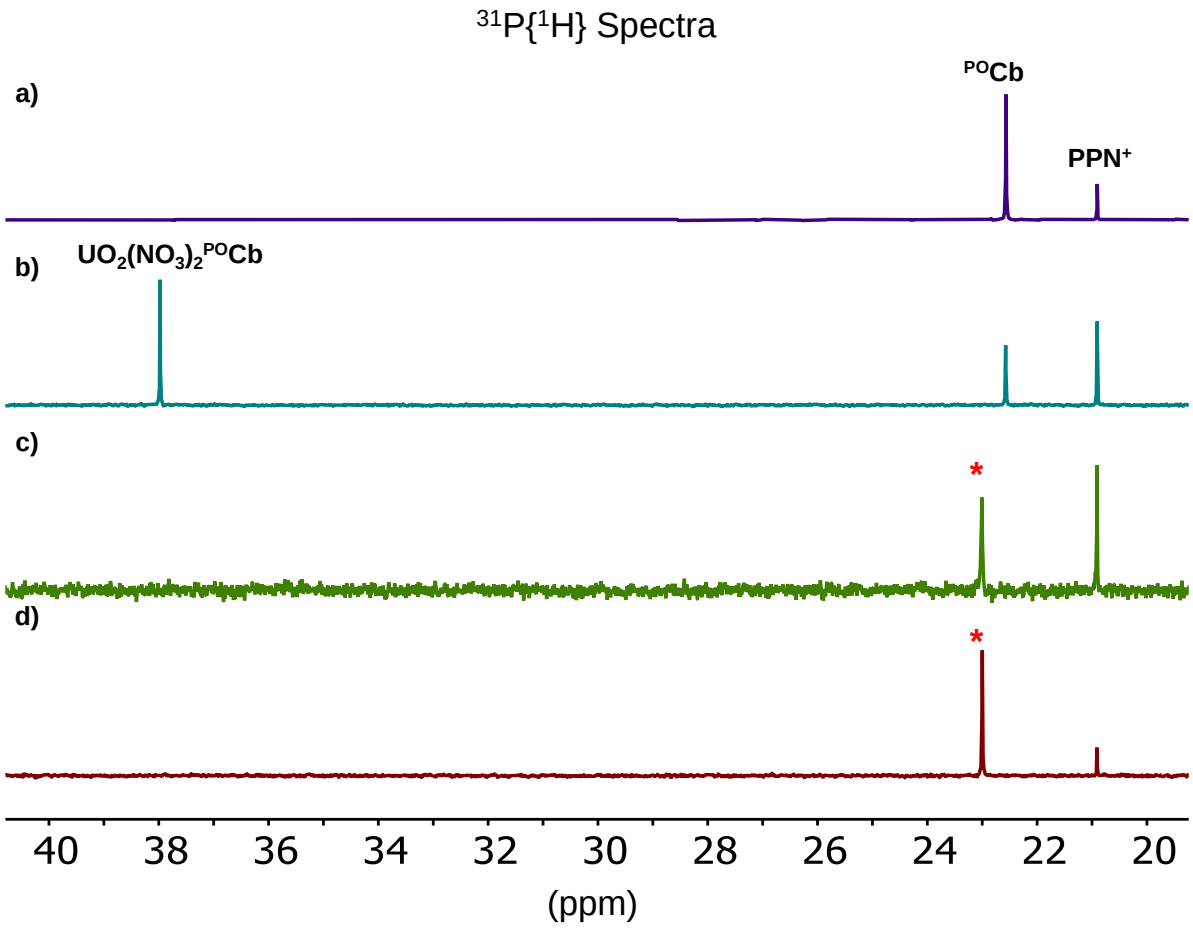

Figure 2.19. $^{31}P\{^{1}H\}$ NMR spectra of $UO_2(NO_3)_2{}^{PO}Cb$ / H_2O competition in DCE with internal standard PPN^+. a) Anhydrous **^{PO}Cb**. b) Anhydrous $UO_2(NO_3)_2{}^{PO}Cb$ with excess **^{PO}Cb**. c) H_2O added to the solution in (b). * Denotes an unidentified species that we tentatively assign to the ^{PO}Cb-H_2O adduct. d) H_2O added to the solution in (a).

We observed that addition of water to anhydrous $UO_2(NO_3)_2{}^{PO}Cb$ resulted in the disappearance of the $^{31}P\{^{1}H\}$ NMR resonance at 38 ppm and the peak for free **^{PO}Cb** shifted downfield by approximately 0.5 ppm. The downfield shift in the **^{PO}Cb** resonance mirrored the NMR spectrum of **^{PO}Cb** in wet DCE which we tentatively assign as a hydrogen-bonded **^{PO}Cb**-H_2O adduct (Figure 2.19). The integration of **^{PO}Cb** species increases upon addition of H_2O. Intriguingly, H_2O appears to outcompete **^{PO}Cb**-H_2O adduct for UO_2^{2+} coordination. We

suggest that further work be performed to further elucidate the effects of water on phosphine oxide carboranes and its role in biphasic UO_2^{2+} release.

2.2.7. Carborane Stability with EWGs and EDGs.

Carborane stability is a critical component for viability in a modified PUREX process. This work has enlightened us on important factors to consider when developing extractants. As mentioned throughout Chapter 2, addition of iodine onto the cage causes consistent instability. We suspect that iodine may be ejected from the cage during GBE. Unidentified byproducts are also observed with TPPO and PFBA – Lewis bases and Brønsted acids respectively. This hinders the viability of **^{PO}CbI** or **^{PO}CbI$_2$** as extractants. Generally, we have observed herein that EWGs decrease the stability of substituted *closo*-carboranes. Particularly, the electrophilic 3,6- boron positions are more susceptible to deboronation.[36] Alkyl or aryl protecting groups on the 3,6- positions may be an effective strategy to mitigate deboronation. However, with current synthetic carborane methodology, it is a laborious multi-step synthesis.[37] Recent advances in accessing cage-modified carboranes with chloro substituents may provide an alternative pathway to improving the redox behavior and cage stability.[38] We hypothesize that chloro derivatives may have enhanced stability over iodo analogs because of decreased leaving group reactivity and increased B–Cl bond strength.[39]

We attempted to improve *closo* stability by addition of EDGs (**^{PO}CbMe$_8$**, **^{PO}CbMe$_2$**, **^{PO}CbEt$_2$**). We have not performed experiments to quantify *closo* stability. Qualitatively, it is likely improved; however, deboronation is still a prominent byproduct with prolonged exposure to nucleophiles. Interestingly, *nido* stability declines with alkylated EDGs. The *nido*-carboranes bearing alkylated substituents become more susceptible to degradation by acids. Particularly, the 1,2- C positions are very basic in *nido* form and alkylated derivatives

accentuate this property.[10] We have isolated the protonated *nido* byproduct of **^{PO}CbMe$_8$**, **H-^{PO}CbMe$_8^-$**, obtained by chemical reduction of **^{PO}CbMe$_8$** with decamethylcobaltacene in benzene (Figure 2.20). **H-^{PO}CbMe$_8^-$** reacts with oxidant, ferrocenium hexafluorophosphate ($FcPF_6$) to reform **^{PO}CbMe$_8$**. Further mechanistic studies should be performed to investigate whether the evolution of hydrogen gas occurs.

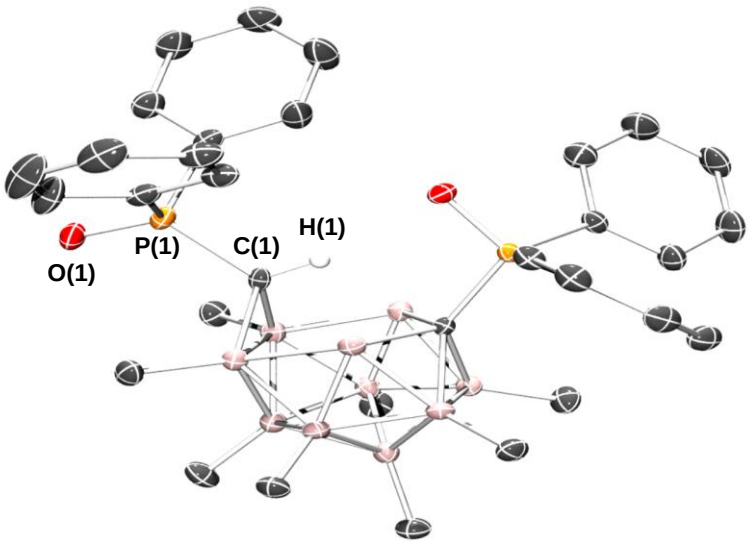

Figure 2.20. Solid-state molecular structure of **H-^{PO}CbMe$_8^-$** byproduct obtained by single crystal XRD studies. Irrelevant H-atoms and counter cation decamethylcobaltacenium omitted for clarity.

Given the decreased acid stability of *nido*-carboranes bearing alkyl substituents, they may be better suited for use as UO_2^{2+} extractants under basic conditions (seawater rather than SNF). Additional alkyl substituents (**^{PO}CbMe$_8$** vs. **^{PO}CbEt$_2$** and **^{PO}CbMe$_2$**) increase the basicity of the carborane (Section 2.2.3) but have minimal effect of UO_2^{2+} extraction efficiencies (Section 2.2.5.). We suggest increasing the chain length, rather than the number of alkyl chains for further optimization of carboranes for use as biphasic extractants.

2.3. Summary

We have described the synthesis and characterization of a series of substituted 1,2-bis(diarylphosphine oxide)-*ortho*-carboranes by addition of either electron-withdrawing or electron-donating groups to the aryl or carboranyl cage positions. As observed by CV, all modified carboranes maintained their redox-switchability between *closo* and *nido* forms; however, more pronounced shifts in redox potentials were observed in cage- vs. aryl-substituted variants. P=O Lewis basicities were further quantified in organic solution using empirical and competition-based NMR experiments and correlated to substituent effects. While the P=O Lewis basicities could be judiciously tuned through aryl and cage substitution, we observed no correlation between increased Lewis basicity and improved biphasic capture of UO_2^{2+} using the electrochemically-generated *nido*-carborane capture agents. While we suspected that biphasic UO_2^{2+} release from the organic to the aqueous phase may be promoted by weaker *closo*-carborane binding, we instead observed that release could be better controlled by increasing the overall hydrophobicity of the capture agent, suggesting that interfacial dynamics play a more prominent role here rather than electronically tuning the extractant. We suggest increasing the alkyl chain length for further optimization of carboranes as biphasic UO_2^{2+} extractants.

2.4. Experimental

2.4.1. Materials and Physical Measurements

General Considerations

All manipulations were performed under an atmosphere of dry, oxygen-free N_2 or Ar by means of standard Schlenk or glovebox techniques (MBraun equipped with a -38 °C freezer,

or VAC gloveboxes). Hexanes, pentane, DCM, THF, diethyl ether and benzene were dried on an MBraun solvent purification system. Acetonitrile and DCE were dried over CaH_2 for several days prior to distillation. *Ortho*-carborane was purchased from Boron Specialties and sublimed before use. $[Bu_4N][PF_6]$ was purchased from Oakwood Chemicals and purified by twice recrystallizing from hot ethanol. The recrystallized product was then washed with cold water, cold ethanol, and pentane prior to drying at 100 °C under vacuum for 24 h. Uranyl nitrate hexahydrate was purchased from International Bio-Analytical Industries Inc. and used as received.

Physical Measurements

NMR spectra were obtained in a Bruker Avance NEO 500 MHz or Agilent Technologies 400 MHz spectrometer. All NMR spectra were referenced to the residual ^1H resonance from the deuterated solvent in the ^1H spectrum according to IUPAC recommended method with the TMS ^1H resonance at 0 ppm. ^{19}F, ^{31}P, and ^{11}B NMR spectra were referenced indirectly using the ^1H NMR spectrum or externally (^{11}B: 85% $(Et_2O)BF_3$, ^{31}P: 85% H_3PO_4, ^{19}F: CCl_3F). Chemical shifts (δ) are recorded in ppm.

Elemental analyses (C, N, H) were recorded at the University of California, Santa Barbara using an Exeter Analytical CE440 elemental analyser.

X-ray crystallography data were collected at the University of California, Santa Barbara on a Bruker KAPPA APEX II diffractometer equipped with an APEX II CCD detector using a TRIUMPH monochromator with a Mo Kα X-ray source (wavelength α = 0.71073 Å). The crystals were mounted on a cryoloop under Paratone-N oil, and all data were collected at 100(2) K using an Oxford nitrogen-gas cryostream system. A hemisphere of data was collected using ω scans with 0.5° frame widths (ω, angle between the X-ray source and the sample). Data collection and cell-parameter determination were conducted using the SMART

program. Integration of the data frames and refinement of the final cell parameters were performed using SAINT software. Absorption correction of the data was carried out using SADABS. Structure determination was done using direct or Patterson methods and difference Fourier techniques. All hydrogen atom positions were idealized and rode on the atom of attachment. Structure solution, refinement, graphics, and creation of publication materials were performed using SHELXTL or OLEX.

Cyclic voltammetry was performed using a CH Instruments Electrochemical Analysis potentiostat, equipped with a 3-mm-diameter glassy carbon working electrode, 5 mM Ag/AgOTf reference electrode, and a Pt-wire counter electrode using a $[Bu_4N][PF_6]$ (0.1 M) solution as the supporting electrolyte and 2.1 mM analyte unless otherwise stated. Cyclic voltammograms were referenced to the Fc/Fc^+ redox couple.

Galvanostatic Bulk Electrolysis cycling experiments were carried out using a Metrohm Autolab PGSTAT128N potentiostat/galvanostat and carried out inside an Ar glovebox. The full experimental setup for biphasic cycling experiments is described in section 2.4.5.

Inductively Coupled Plasma-Optical Emission Spectroscopy (ICP-OES) was performed on an Agilent 5800 and used to determine the concentrations of U in aqueous solutions. Nitric acid (hps, ICP-OES grade for trace metal analysis, ACS testing specifications, LOT 2124406) and deionized water (Milli-Q, 18.2 MΩ.cm) were used for sample preparation and dilutions. A six-point calibration curve was made by serial dilution (100-0.1 ppm) of a custom multi-element certified reference material from High Purity Standards in 2% nitric acid. The emissions lines used were U (263.553 nm, 367.007 nm, 385.957 nm, 409.013 nm). The calibration curves for U all had $R^2 > 0.9999$.

2.4.2. Synthesis of Compounds

Precursor Synthesis: 9-I-1,2-dicarba-*closo*-dododecaborane (9-I-*o*-Cb), 9,12-I_2-1,2-dicarba-*closo*-dodecaborane (9,12-I_2-*o*-Cb), 9,12-$(CH_2CH_{3-})_2$-1,2-dicarba-*closo*-dodecaborane (9,12-$(CH_2CH_3)_2$-*o*-Cb), and 9,12-$(CH_3)_2$-1,2-dicarba-*closo*-dodecaborane (9,12-$(CH_3)_2$-*o*-Cb) were synthesized from previously reported literature procedures. 4,5,7,8,9,10,11,12-$(CH_3)_8$-1,2-dicarba-*closo*-dodecaborane was synthesized using modified literature procedures (see below).[13, 16-19] $[UO_2Cl_2(THF)_2]_2$ was synthesized following previously reported literature procedures and used as a precursor for anhydrous $UO_2(NO_3)_2(THF)_2$ synthesis.[40]

Synthesis of 4,5,7,8,9,10,11,12-$(CH_3)_8$-1,2-dicarba-*closo*-dodecaborane: Under an inert atmosphere, *o*-carborane (2.0 g, 13.9 mmol) was dissolved in methyl iodide (23 mL, 369 mmol). Aluminum chloride (13 g, 97.5 mmol) was added to the stirring solution. The reaction was heated at reflux for 4 days and monitored daily using ^{11}B NMR spectroscopy until completion. The reaction was cooled to room temperature and volatiles were removed *in vacuo*. The reaction was slowly redissolved in pentane (30 mL) at 0 ºC. The reaction was quenched with an aqueous solution of sodium thiosulfate. It was then filtered in a Buchner funnel and extracted with additional pentane. The organic phase was washed with water. It was dried over $MgSO_4$ and the volatiles were removed *in vacuo*. The solid was purified by column chromatography with 100% hexanes eluent. A white solid (2.38 g, 66% yield) was obtained. **^{1}H{^{11}B} NMR (400 MHz, $CDCl_3$)** δ 3.08 (t, *J* = 4.3 Hz, 2H), 1.83 (bs., 2H), 0.12 (s, 12H), -0.01 (s, 6H), -0.24 (s, 6H). **^{11}B{^{1}H} NMR (128 MHz, $CDCl_3$)** δ 6.08, -1.42, -8.75, -16.93.

Synthesis of $UO_2(NO_3)_2(THF)_2$: Under an inert atmosphere, $[UO_2Cl_2(THF)_2]_2$ (0.566 g, 0.584 mmol) was added to 15 mL of acetonitrile and stirred. Silver nitrate (0.397 g, 2.33

mmol) was dissolved in acetonitrile and added to the stirring uranyl solution. A white solid began precipitating out immediately. The reaction was stirred overnight. It was filtered over a Celite plug glass frit and the filtrate was taken to dryness. The solid was redissolved in diethyl ether and filtered through a Celite plug glass frit again. The filtrate was dried. The product was recrystallized from THF/hexanes at -40 ºC to afford yellow crystals matching the reported unit cell.[28]

General Procedure for Synthesis of Diphenyl Phosphine Oxide Carborane Derivatives

The synthesis of modified phosphine oxide carboranes was accomplished in two steps by modified literature procedures.[41, 42]

Step 1. Under an inert atmosphere, 2.1 equiv. of *n*-BuLi (2.5 M in hexane, 7.28 mmol) was added dropwise to a solution of cage modified *o*-carborane (1 equiv., 3.47 mmol) in dry diethyl ether at -78 °C resulting in a white precipitate. After 10 minutes, the solution was warmed to room temperature and stirred for an additional hour. After stirring, the mixture was cooled back to -78 °C. Ar_2PCl (Ar = Ph, 4-$(OMe)_2$-Ph, 4-F-Ph) (2 equiv., 6.92 mmol) was added dropwise producing a pale orange solution with a white precipitate. The mixture was warmed to room temperature and stirred for 1.5 h. The solvent was removed *in vacuo*. The residue was purified by recrystallization or column chromatography.

Step 2. In air, the product from *Step 1* (1 equiv., 0.53 mmol) was dissolved in DCM and stirred for 20 minutes at 0 °C. *Meta*-chloroperoxybenzoic acid (2 equiv., 1.06 mmol) was dissolved in minimal DCM and added dropwise. The reaction stirred for an additional 30 minutes at room temperature. The reaction was stopped by the addition of an aqueous solution of $NaHCO_3$. The organic phase was washed with water and brine, dried with $MgSO_4$ and

filtered. The solvent was removed, and the solid was purified by recrystallization or column chromatography.

Product Details

9-I-1,2-(Ph_2P)$_2$-1,2-$C_2B_{10}H_9$ ($^{P(III)}$CbI)

Synthesis modification: 2.0 equiv. of *n*-BuLi is added (2.5 M in hexanes, 6.95 mmols)

Purification: Recrystallization from DCM/hexanes

Yield: 82%; white solid

^{1}H NMR (500 MHz, $CDCl_3$): δ 7.90–7.81 (m, 8H), 7.56–7.42 (m, 12H), 3.34–1.53 (m, 9H). **^{11}B{^{1}H} NMR (160 MHz, $CDCl_3$):** δ 0.51, -4.65, -6.25, -10.48, -12.74, -14.50. **^{31}P{^{1}H} NMR (202 MHz, $CDCl_3$):** δ 8.56–5.35 (m).**^{13}C NMR (126 MHz, $CDCl_3$):** δ 135.83–135.70 (m), 135.66–135.48 (m), 132.80–132.45 (m), 132.87–134.1 (m), 132.08, 131.26, 131.00 (d, *J* = 11.0 Hz), 128.96–128.53 (m). *Anal. Calcd.* for $C_{26}B_{10}P_2H_{29}I$: C, 48.291; H, 4.58. *Found* C, 48.86; H, 4.45

9,12-I_2-1,2-(Ph_2P)$_2$-1,2-$C_2B_{10}H_8$ ($^{P(III)}$CbI$_2$)

Synthesis modification: 2.0 equiv. of *n*-BuLi is added (2.5 M in hexanes, 6.95 mmols)

Purification: Recrystallization from DCM/hexanes

Yield: 74%; white solid

^{1}H NMR (500 MHz, $CDCl_3$): δ 7.92–7.81 (m, 8H), 7.57–7.44 (m, 12H), 3.87–1.75 (broad, 8H). **^{11}B{^{1}H} NMR (160 MHz, $CDCl_3$):** δ -4.50, -10.33. **^{31}P{^{1}H} NMR (202 MHz, $CDCl_3$):** δ 6.86 **^{13}C NMR (126 MHz, $CDCl_3$):** δ 135.68 (dd, *J* = 14.2 Hz), 131.27, 128.86 (dd, *J* = 1.5 Hz).

9,12-(CH_3)$_2$-1,2-(Ph_2P)$_2$-1,2-$C_2B_{10}H_8$ ($^{P(III)}$CbMe$_2$)

Purification: Silica column; 100% hexanes

Yield: 40%; white solid

^{1}H NMR (500 MHz, $CDCl_3$): δ 7.81-7.89 (m, 8H), 7.51–7.39 (m, 12H), 2.76–1.38 (broad, 8H), 0.051 (s, 6H) **$^{11}B\{^{1}H\}$ NMR (160 MHz, $CDCl_3$):** δ 9.28, -5.41, -10.25. **$^{31}P\{^{1}H\}$ NMR (202 MHz, $CDCl_3$):** δ 5.11. **^{13}C NMR (126 MHz, $CDCl_3$):** δ 135.70 (dd, *J* = 14.1, 13.4 Hz), 133.66 (t, *J* = 5.3 Hz), 130.52, 128.43 (dd, *J* = 5.1, 4.6 Hz), 75.57–75.05 (m), 1.10. *Anal. Calcd.* for $C_{28}B_{10}P_2H_{34}$: C, 62.21; H, 6.34. *Found* C, 62.24; H, 6.32

9,12-$(CH_3CH_2)_2$-1,2-$(Ph_2P)_2$-1,2-$C_2B_{10}H_8$ ($^{P(III)}$CbEt$_2$)

Purification: Silica column; 100% hexanes

Yield: 52%; white solid

^{1}H NMR (500 MHz, $CDCl_3$): δ 7.89-7.84 (m, 8H), 7.49-7.41 (m, 12H), 2.97-1.57 (broad, 8H), 0.74 (t, J = 7.7 Hz, 6H), 0.58 (q, J = 7.6 Hz, 4H). **$^{11}B\{^{1}H\}$ NMR (160 MHz, $CDCl_3$):** δ 11.15, -6.68, -10.81. **$^{31}P\{^{1}H\}$ NMR (202 MHz, $CDCl_3$):** δ 5.23. **^{13}C NMR (126 MHz, $CDCl_3$):** δ 135.72 (dd, *J* = 13.7 Hz), 133.75 (td, *J* = 5.2 Hz), 130.52, 128.40 (dd, *J* = 4.9 Hz), 75.81–75.15 (m), 13.17, 9.06. *Anal. Calcd.* for $C_{30}B_{10}P_2H_{38}$: C, 63.36; H, 6.74. *Found* C, 63.41; H, 6.79

1,2-$((4\text{-}OCH_3\text{-}C_6H_5)_2P)_2$-$C_2B_{10}H_{10}$ ($^{(OMe)P(III)}$Cb)

Synthesis modification: Dropwise addition of $(4\text{-}(OMe)_2\text{-}Ph)_2PCl$ dissolved in THF and stirred overnight

Purification: Silica column, 15% ethyl acetate/hexanes

Yield: 87%; white solid

XRD: Single crystals suitable for XRD studies were grown from diethyl ether/isooctane via vapor diffusion at room temperature.

^{1}H NMR (500 MHz, $CDCl_3$): δ 7.81-7.75 (m, 8H), 7.00–6.93 (m, 8H), 3.86 (s, 12H), 2.92-1.38 (broad, 10H). **B{^{1}H} NMR (160 MHz, $CDCl_3$):** δ -0.65, -7.60, -9.77. **^{31}P{^{1}H} NMR (202 MHz, $CDCl_3$):** δ 4.06. **^{13}C NMR (126 MHz, $CDCl_3$):** δ 161.45, 137.29 (dd, J = 14.6 Hz), 124.76 (t, J = 3.7 Hz), 114.04 (dd, J = 5.4 Hz), 84.34–83.81 (m), 55.25. *Anal. Calcd.* for $C_{30}B_{10}P_2O_4H_{38}$: C, 56.95; H, 6.05. *Found* C, 56.97; H, 6.02

1,2-((4-F-C_6H_5)$_2$P)$_2$ -$C_2B_{10}H_{10}$ ($^{(F)P(III)}$Cb)

Purification: Silica column; 5% ethyl acetate/hexanes

Yield: 87%; white solid

XRD: Single crystals suitable for XRD studies were grown from 5% ethyl acetate/hexanes.

^{1}H NMR (500 MHz, $CDCl_3$) δ 7.81-7.75 (m, 8H), 7.22–7.12 (m, 8H), 2.72–0.49 (m, 10H). **^{11}B NMR (160 MHz, $CDCl_3$)** δ -0.14, -7.28, -9.90. **^{31}P NMR (202 MHz, $CDCl_3$)** δ 4.17. **^{19}F NMR (471 MHz, $CDCl_3$)** δ -108.82. **^{13}C NMR (126 MHz, $CDCl_3$)** δ 164.51 (d, J = 253.2 Hz), 137.73 (ddd, J = 18.6, 18.6, 13.2 Hz), 128.50 (td, J = 9.9, 8.9 Hz), 116.09 (ddd, J = 46.0, 12.0, 11.6 Hz), 82.97–82.28 (m). *Anal. Calcd.* for $C_{26}B_{10}P_2H_{26}F_4$: C, 53.42; H, 4.48. *Found* C, 53.45; H, 4.47

4,5,7,8,9,10,11,12-(CH_3)$_8$-1,2-(Ph_2P)$_2$-1,2-$C_2B_{10}H_2$ ($^{P(III)}$CbMe$_8$)

Synthesis modification: After *n*-BuLi addition at -78°C, stirred overnight at room temperature

Purification: Silica column; 100% hexanes followed by recrystallization from hot hexanes

Yield: 37%; pale yellow solid

XRD: Single crystals suitable for XRD studies were grown from hexanes at -40 °C.

^{1}H NMR (500 MHz, $CDCl_3$) δ 7.82-7.55 (broad m, 8H), 7.32-7,23 (m, 12H), 3.24–1.65 (broad, 2H), 0.01 (s, 6H), 0.04 (broad s, 12H), -0.25 (s, 6H).**^{11}B NMR (160 MHz, $CDCl_3$)** δ 10.69, 3.80, -2.04, -13.32. **^{31}P NMR (202 MHz, $CDCl_3$)** δ 26.93. **^{13}C NMR (126 MHz,**

$CDCl_3$) δ 136.34, 132.52, 129.45, 128.09–127.44 (m), -1.79. *Anal. Calcd.* for $C_{34}B_{10}P_2H_{46}$: C, 65.36; H, 7.42. *Found* C, 65.15; H, 7.40

9-I-1,2-$(Ph_2PO)_2$-1,2-$C_2B_{10}H_9$ (^{PO}CbI)

Purification: Recrystallization from DCM/hexanes

Yield: 46%; white solid

XRD: Single crystals suitable for XRD studies were grown from diethyl ether/isooctane via vapor diffusion at room temperature.

^{1}H NMR (500 MHz, $CDCl_3$): δ 7.87-7.81 (m, *J* = 18.7, 11.9, 7.8 Hz, 8H), 7.41–7.51 (m, 12H), 3.61–1.50 (broad, 9H). **^{11}B{^{1}H} NMR (160 MHz, $CDCl_3$):** δ 2.43, -6.35, -9.95, -12.63. **^{31}P{^{1}H} NMR (202 MHz, $CDCl_3$):** δ 25.97, 24.07. **^{13}C NMR (126 MHz, $CDCl_3$):** δ 132.76 (dd, *J* = 21.9, 3.0 Hz), 132.54 (dd, *J* = 11.9, 9.0 Hz), 130.75 , 130.35, 128.87, 129.46, 128.26 (dd, *J* = 13.0, 8.5 Hz), 81.44, 81.08. HRMS (ESI/Q-TOF) m/z: $[M + Na]^+$ Calcd for $C_{26}B_{10}H_{29}P_2O_2INa$: 694.1558; Found 694.1572

9,12-I_2 -1,2-$(Ph_2PO)_2$-1,2-$C_2B_{10}H_8$ (^{PO}CbI_2)

Purification: Recrystallization from DCM/hexanes

Yield: 80%; white solid

XRD: Single crystals suitable for XRD studies were grown from diethyl ether/isooctane via vapor diffusion at room temperature.

^{1}H NMR (500 MHz, $CDCl_3$): δ 7.88-7.81 (m, 8H), 7.62–7.49 (m, 12H), 2.89 (broad, 8H). **^{11}B{^{1}H} NMR (160 MHz, $CDCl_3$):** δ -4.70, -9.42, -10.65. **^{31}P{^{1}H} NMR (202 MHz, $CDCl_3$):** δ 25.86. **^{13}C NMR (126 MHz, $CDCl_3$):** δ 133.02 (d, *J* = 3.0 Hz), 132.50 (d, *J* = 9.1 Hz), 129.73 (d, *J* = 111.3 Hz), 128.40 (d, *J* = 13.1 Hz), 77.71 (d, *J* = 43.1 Hz). HRMS (ESI/Q-TOF) m/z: $[M + Na]^+$ Calcd for $C_{26}B_{10}H_{28}P_2O_2I_2Na$: 820.0519 ; Found 820.0521

9,12-(CH_3)$_2$-1,2-(Ph_2PO)$_2$-1,2-$C_2B_{10}H_8$ (^{PO}CbMe$_2$)

Purification: Silica column, 30% ethyl acetate/hexanes

Yield: 75%; white solid

XRD: Single crystals suitable for XRD studies were grown from diethyl ether/isooctane via vapor diffusion at room temperature.

^{1}H NMR (500 MHz, $CDCl_3$): δ 8.09-8.00 (m, 8H), 7.58–7.43 (m, 12H), 3.34–0.63 (broad, 8H), 0.08 (s, 6H)). **^{11}B{^{1}H} NMR (160 MHz, $CDCl_3$):** δ 11.58, -5.86, -12.42 (broad).**^{31}P{^{1}H} NMR (202 MHz, $CDCl_3$):** δ 23.72. **^{13}C NMR (126 MHz, $CDCl_3$):** δ 132.57 (d, *J* = 8.9 Hz), 132.31 (d, *J* = 2.9 Hz), 130.94 (d, *J* = 111.1 Hz) 128.02 (d, *J* = 12.9 Hz), 73.05 (d, *J* = 52.4 Hz). *Anal. Calcd.* for $C_{28}B_{10}H_{34}P_2O_2$: C, 58.73; H, 5.99. *Found* C, 58.25; H, 6.00

9,12-(CH_3CH_2)$_2$-1,2-(Ph_2PO)$_2$-1,2-$C_2B_{10}H_8$ (^{PO}CbEt$_2$)

Purification: Silica column; 40% ethyl acetate/hexanes

Yield: 87%; white solid

XRD: Single crystals suitable for XRD studies were grown from diethyl ether/isooctane via vapor diffusion at room temperature.

^{1}H NMR (500 MHz, $CDCl_3$): δ 8.09-7.99 (m, 8H), 7.57–7.44 (m, 12H), 3.50–0.92 (m, 8H), 0.66 (t, *J* = 7.3 Hz, 6H), 0.62 – 0.53 (m, 4H). **^{11}B{^{1}H} NMR (160 MHz, $CDCl_3$):** δ 13.65, -6.98, -10.29. **^{31}P{^{1}H} NMR (202 MHz, $CDCl_3$):** δ 23.73. **^{13}C NMR (126 MHz, $CDCl_3$):** δ 132.56 (d, *J* = 9.2 Hz), 132.31 (d, *J* = 2.9 Hz), 130.96 (d, *J* = 110.9 Hz), 128.00 (d, *J* = 12.9 Hz), 73.20 (d, *J* = 52.7 Hz), 12.96, 9.19. *Anal. Calcd.* for $C_{30}B_{10}P_2O_2H_{38}$: C, 59.99; H, 6.38. *Found* C, 60.10; H, 6.37

1,2-((4-$OCH_3C_6H_5$)$_2$PO)$_2$ -$C_2B_{10}H_{10}$ ($^{(OMe)PO}$Cb)

Purification: Silica column; 70% ethyl acetate/hexanes

Yield: 83%; white solid

XRD: Single crystals suitable for XRD studies were grown from diethyl ether/isooctane via vapor diffusion at room temperature.

^{1}H NMR (500 MHz, $CDCl_3$) δ 7.97–7.88 (m, 8H), 6.97 (m, 8H), 3.57–1.35 (broad, 10H). **^{11}B NMR (160 MHz, $CDCl_3$)** δ 1.18, -8.85. **^{31}P NMR (202 MHz, $CDCl_3$)** δ 24.41. **^{13}C NMR (126 MHz, $CDCl_3$)** δ 162.66 (d, *J* = 3.1 Hz), 134.55 (d, *J* = 10.3 Hz), 121.93 (d, *J* = 118.8 Hz), 113.56 (d, *J* = 14.1 Hz), 81.64 (d, *J* = 50.1 Hz), 55.31. *Anal. Calcd.* for $C_{30}B_{10}P_2O_6H_{38}$: C, 54.21; H, 5.76. *Found* C, 54.26; H, 5.84.

1,2-((4-F-C_6H_5)$_2$PO)$_2$ -$C_2B_{10}H_{10}$ ($^{(F)PO}$Cb)

Purification: Silica column; 20% ethyl acetate/hexanes

Yield: 86%; white solid

XRD: Single crystals suitable for XRD studies were grown from THF/isooctane via vapor diffusion at room temperature.

^{1}H NMR (500 MHz, $CDCl_3$) δ 7.99 (m, 8H), 7.20 (m, 8H), 3.55–1.36 (broad, 10H). **^{11}B NMR (160 MHz, $CDCl_3$)** δ 1.87, -7.70, -9.78. **^{31}P NMR (202 MHz, $CDCl_3$)** δ 23.13. **^{19}F NMR (471 MHz, $CDCl_3$)** δ -104.69– -104.82 (m). **^{13}C NMR (126 MHz, $CDCl_3$)** δ 165.43 (dd, *J* = 255.8, 3.5 Hz), 135.19–135.00 (m, 125.98 (dd, *J* = 115.7, 3.6 Hz), 115.77 (dd, *J* = 21.5, 14.3 Hz), 80.24 (d, *J* = 53.2 Hz). *Anal. Calcd.* for $C_{26}B_{10}P_2O_2H_{26}F_4$: C, 50.65; H, 4.25. *Found* C, 50.79; H, 4.32.

4,5,7,8,9,10,11,12-(CH_3)$_8$-1,2-(Ph_2PO)$_2$-1,2-$C_2B_{10}H_2$ (^{PO}CbMe$_8$)

Purification: Silica column; 40% ethyl acetate/hexanes

Yield: 97%; white solid

XRD: Single crystals suitable for XRD studies were grown from layering of DCM and hexanes at -40 °C.

^{1}H NMR (500 MHz, $CDCl_3$) δ 7.93 (m, 8H), 7.38-7.29 (m, 12H), 3.43–2.00 (broad m, 2H), 0.11 (s, 6H), 0.04 (s, 12H), -0.22 (s, 6H). **^{11}B NMR (160 MHz, $CDCl_3$)** δ 13.00, 8.86, -0.09, -14.68. **^{31}P NMR (202 MHz, $CDCl_3$)** δ 31.13. **^{13}C NMR (126 MHz, $CDCl_3$)** δ 133.89 (d, *J* = 9.9 Hz), 132.62–131.54 (m), 127.67 (d, *J* = 13.0 Hz), 86.18 (d, *J* = 50.7 Hz), 0.35–-2.58 (m). *Anal. Calcd.* for $C_{34}B_{10}P_2O_2H_{46}$: C, 62.18; H, 7.06. *Found* C, 61.80; H, 6.82

2.4.3. Procedure for NMR Basicity Studies

The example procedure here is given with **^{PO}Cb**. A stock solution of **^{PO}Cb** (36.93 mM, 1mL) and PFBA (22.28mM, 5mL) was made in *d*-DCM. A 300 µL aliquot of **^{PO}Cb** (11.08 mmol) was loaded in a borosilicate NMR tube with 100 µL PFBA (2.23 mmol) for a total volume of 400 µL. All volumes were measured using a 250 µL Hamilton syringe. All measurements were run in triplicate. Difference spectra ($\Delta\delta(^{19}F)$) were measured based on the shifting *para* resonances of pentafluorobenzoic acid (Figure S2).[24]

2.4.4. Procedure for NMR Competition Experiments

Saturation Curve: A stock solution of 2.58 mM $UO_2(NO_3)_2(THF)_2$ with 0.525 mM [PPN][PF_6] was made in DCE. A stock solution of 2.78 mM **^{PO}Cb** with 0.525 mM [PPN][PF_6] was made in DCE. To a glass vial, $UO_2(NO_3)_2(THF)_2$ stock (200 µL, 51.6 µmol) was added along with varied equivalents of stock **^{PO}Cb** (40–500 µL). [PPN][PF_6] stock was added to the vial such that a final volume between 0.5–0.7 mL was obtained. The contents of the vial were thoroughly mixed and then transferred to an NMR tube. ^{1}H and ^{31}P{^{1}H} NMR spectra were collected. ^{31}P{^{1}H} NMR spectra collected with 64 scans and 35 second T_1 relaxation time for

accurate integration of [PPN][PF_6] (T_1 = 7.1s).[9] Integration of NMR peaks were used to calculate the fraction of UO_2^{2+} bound as equivalents of **^{PO}Cb** were added. The data was modeled by two linear regressions (Figure 2.11). The linear regressions intersect precisely at 1.03 equivalents of **^{PO}Cb**.

NMR Competition Experiments: A stock solution of 0.5 mM bis(triphenylphosphine)iminium hexafluorophosphate ([PPN][PF_6]) in DCE was used to make stock solutions of 3 mM $UO_2(NO_3)_2$Cb* (Cb* = any modified carborane), 6 mM triphenylphosphine oxide (TPPO), and 20 mM TPPO. Modified carboranes with EWG required less concentrated, 6 mM TPPO solution for NMR competition experiments. Modified carboranes with EDG required more concentrated 20 mM TPPO solution. To a glass vial, $UO_2(NO_3)_2$Cb* (200 µL) was added along with specified TPPO stock (50–300 µL) and 0.5 mM [PPN][PF_6] stock solution to reach a total volume of 500 µL. The contents of the vial were thoroughly mixed then transferred to an NMR tube. ^{1}H and ^{31}P{^{1}H} NMR spectra were collected. ^{31}P{^{1}H} NMR spectra collected with 128 scans and 35 second T_1 relaxation time for accurate integration of [PPN][PF_6] (T1 = 7.1s).[9] NMR spectra of the stock solutions of $UO_2(NO_3)_2$Cb* and TPPO were taken and the peaks were integrated relative to $[PPN]^+$ to determine accurate concentration of the stock solutions. The reactants and products of the equilibria in each NMR spectrum were integrated relative to $[PPN]^+$ (PPN^+ concentration held constant at 0.5 mM) and fit into the K_{eq} (Equation 4) to obtain a pK_{eq} (Equation 5). The pK_{eq} values for each NMR spectrum at different equivalents of TPPO were then averaged. Additionally, all ligands displayed an additional degradation peak at 47 ppm during TPPO competition experiments which corresponded to two deboronated $(C_2B_9)^-$ phosphine oxide carboranes bound to uranyl ($UO_2(^{PO}C_2B_9)_2$) (denoted as *) wherein the binding is no longer

reversible (Figure 2.10). The byproduct remained relatively constant among all competition experiments.

2.4.5. Biphasic Electrochemical UO_2^{2+} Capture and Release

General Considerations: Two-electrode galvanostatic bulk electrolysis (GBE) was performed in an argon glovebox utilizing a two compartment H-cell with a glass frit separator, a stir bar in each compartment, and reticulated vitreous carbon (RVC) foam electrodes for both the working and counter electrodes. The RVC foam electrodes consisted of a ~5 cm steel rod inserted into 100 PPI Duocel® RVC foam core (length ~3 cm; diameter ~3mm), with a tap bore (length ~5 mm; diameter ~2 mm), which was filled with molten gallium to fuse the steel connector to the RVC foam. Each electrode has an end-to-tip resistance of < 30 Ω. The RVC electrodes were rinsed with acetone and dried. The Ketjenblack used was dried for 48 h in a 175 °C oven and ground in a glass mortar and pestle under inert atmosphere prior to use.[9]

Reduction (Charging): The counter compartment consisted of 300 mg of Ketjenblack suspended in 8 mL of a 0.1 M solution of $[Bu_4N][PF_6]$ in DCE. The working compartment consisted of the selected carborane (0.063 mmol, 1.0 equiv.) dissolved in 6 mL of a 0.1 M solution of $[Bu_4N][PF_6]$ in DCE. An initial $^{31}P\{^1H\}$ NMR spectrum was obtained of the DCE layer (Figure 2.17). A charging current of -127.6 μA with a -9.25 C charge cutoff was utilized, resulting in a ca. 76% SOC after 20 h (Figure 2.16; assuming 100% columbic efficiency). Upon completion, the working compartment solution was monitored by $^{31}P\{^1H\}$ NMR spectroscopy to reveal the formation of the reduced *nido* carborane (e.g., $^{PO}\mathbf{Cb}^{2-}$) with some uncharged carborane remaining (Figure 2.17). The working compartment solution was then removed from the H-cell and placed in a 20 mL vial for subsequent selective UO_2^{2+} capture chemistry.

UO_2^{2+} Capture: A 1 L plastic bottle was loaded with 0.19 mmols of $UO_2(NO_3)_2$*$6H_2O$ dissolved in 250 mL of a 0.5 M NaOAc aqueous buffered solution (pH = 5.4) resulting in a bright yellow stock solution. A 5 mL aliquot of the stock solution (0.6 equiv.) was added to the DCE solution containing the electrochemically reduced *nido*-carborane. After addition, the mixture was allowed to stir for 1.5 h, resulting in a bright yellow organic phase and a pale yellow-green aqueous phase. Stirring was discontinued and the organic and aqueous phases were separated using a small separatory funnel. A 0.5 mL aliquot was taken from the DCE layer and transferred to an NMR tube. An unlocked $^{31}P\{^1H\}$ NMR spectrum was collected indicating the formation of the uranyl-captured products ($[UO_2(^{PO}Cb^*)_2]^{2-}$), as well as some protonated carborane (denoted as *) (Figure 2.17).[10] The NMR solution was subsequently returned to the 20 mL vial.

Oxidation (Discharging): The DCE layer was returned to the H-cell and GBE was used to discharge (oxidize) the carborane. A discharging current of 127.6 μA with a 9.21 C charge cutoff was utilized resulting in a final SOC of ca. 0 % (**Error! Reference source not found.**; a ssuming 100% coulombic efficiency). Upon completion, a 0.5 mL aliquot was taken from the pale yellow DCE layer and transferred to an NMR tube. An unlocked $^{31}P\{^1H\}$ NMR spectrum was collected indicating a broad signal between 22–25 ppm which we attribute to an adduct of UO_2^{2+} with the carborane (Figures S13d-S18d). The NMR sample and working compartment solutions were combined and placed in a 20 mL vial for subsequent release chemistry.

UO_2^{2+} recovery: The 20 mL vial containing the electrochemically discharged DCE solution was equipped with a stir bar and a 5 mL solution of a 0.1 M NaOAc aqueous buffer solution was added. The mixture was allowed to stir for 15 h, resulting in a bright-yellow aqueous

phase and a colorless organic layer. A 0.5 mL aliquot was taken from the colorless DCE layer and transferred to an NMR tube. An unlocked $^{31}P\{^{1}H\}$ NMR spectrum was collected indicating the clean formation of the *closo* carborane.

Control: Performed in triplicate, 5 mL of the UO_2^{2+} stock solution was stirred with 6 mL of a 0.5 M solution of $[Bu_4N][PF_6]$ in DCE for 1.5 hours. The aqueous solution was isolated from the DCE layer and saved for analysis by ICP-OES. The DCE layer was then stirred with 0.1 M NaOAc buffer for 15 h. The aqueous solution was isolated from the DCE layer and saved for analysis by ICP-OES. Triplicate runs of the control indicate a low 2.35% extraction of UO_2^{2+} and released 50% of UO_2^{2+} relative to percent extracted.

2.5. References

(1) *IAEA Nuclear Power and the Paris Agreement*. https://www.iaea.org/sites/default/files/16/11/np-parisagreement.pdf (accessed 2021 2/5/2021).

(2) Administration, U. S. E. I. *Nuclear explained*. https://www.eia.gov/energyexplained/nuclear/nuclear-power-plants.php (accessed 2023 07/08/2023).

(3) Bodansky, D. *Nuclear Energy: Principles, Practices, and Prospects*; Springer, 2004. DOI: https://doi.org/10.1007/b138326.

(4) Kumari, I.; Kumar, B. V. R.; Khanna, A. A review on UREX processes for nuclear spent fuel reprocessing. *Nucl. Eng. Des.* **2020**, *358*, 110410. DOI: https://doi.org/10.1016/j.nucengdes.2019.110410.

(5) Hore-Lacy, I. *Nuclear Energy in the 21st Century*; World Nuclear University Press, 2006.

(6) Srivastava, R. R.; Pathak, P.; Perween, M. Environmental and Health Impact Due to Uranium Mining. In *Uranium in Plants and the Environment*, Gupta, D. K., Walther, C. Eds.; Springer International Publishing, 2020; pp 69-89.

(7) Law, J. D. *Aqueous Reprocessing of Used Nuclear Fuel*; Idaho National Laboratory, 2018.

(8) Finan, A.; Foss, A.; Goff, M.; King, C.; Lohse, C. *Nuclear Energy: Supply Chain Deep Dive Assessment*; Office of Scientific and Technical Information (OSTI), 2022. https://dx.doi.org/10.2172/1871579DOI: 10.2172/1871579.

(9) Keener, M.; Hunt, C.; Carroll, T. G.; Kampel, V.; Dobrovetsky, R.; Hayton, T. W.; Ménard, G. Redox-switchable carboranes for uranium capture and release. *Nature* **2020**, *577* (7792), 652-655. DOI: 10.1038/s41586-019-1926-4.

(10) Keener, M.; Mattejat, M.; Zheng, S.-L.; Wu, G.; Hayton, T. W.; Ménard, G. Selective electrochemical capture and release of uranyl from aqueous alkali, lanthanide, and actinide mixtures using redox-switchable carboranes. *Chem. Sci.* **2022**, *13* (12), 3369-3374. DOI: 10.1039/D1SC07070C.

(11) Núñez, R.; Tarrés, M.; Ferrer-Ugalde, A.; de Biani, F. F.; Teixidor, F. Electrochemistry and Photoluminescence of Icosahedral Carboranes, Boranes, Metallacarboranes, and Their Derivatives. *Chem. Rev.* **2016**, *116* (23), 14307-14378. DOI: 10.1021/acs.chemrev.6b00198.

(12) Morris, J. H.; Gysling, H. J.; Reed, D. Electrochemistry of boron compounds. *Chem. Rev.* **1985**, *85* (1), 51-76. DOI: 10.1021/cr00065a003.

(13) Herzog, A.; Maderna, A.; Harakas, G. N.; Knobler, C. B.; Hawthorne, M. F. A Camouflaged nido-Carborane Anion: Facile Synthesis of Octa-B-methyl-1,2-dicarba-closo-dodecaborane(12) and Its Deboration Reaction. *Chem. Eur. J.* **1999**, *5* (4), 1212-1217. DOI:

https://doi.org/10.1002/(SICI)1521-3765(19990401)5:4<1212::AID-CHEM1212>3.0.CO;2-W.

(14) Teixidor, F.; Barberà, G.; Vaca, A.; Kivekäs, R.; Sillanpää, R.; Oliva, J.; Viñas, C. Are Methyl Groups Electron-Donating or Electron-Withdrawing in Boron Clusters? Permethylation of o-Carborane. *JACS* **2005**, *127* (29), 10158-10159. DOI: 10.1021/ja052981r.

(15) Yruegas, S.; Axtell, J. C.; Kirlikovali, K. O.; Spokoyny, A. M.; Martin, C. D. Synthesis of 9-borafluorene analogues featuring a three-dimensional 1,1′-bis(o-carborane) backbone. *Chem. Commun.* **2019**, *55* (20), 2892-2895. DOI: 10.1039/C8CC10087J.

(16) Andrews, J. S.; Zayas, J.; Jones, M. 9-Iodo-o-carborane. *Inorg. Chem.* **1985**, *24* (22), 3715-3716. DOI: 10.1021/ic00216a053.

(17) Zheng, Z.; Jiang, W.; Zinn, A. A.; Knobler, C. B.; Hawthorne, M. F. Facile Electrophilic Iodination of Icosahedral Carboranes. Synthesis of Carborane Derivatives with Boron-Carbon Bonds via the Palladium-Catalyzed Reaction of Diiodocarboranes with Grignard Reagents. *Inorg. Chem.* **1995**, *34* (8), 2095-2100. DOI: 10.1021/ic00112a023.

(18) Anderson, K. P.; Mills, H. A.; Mao, C.; Kirlikovali, K. O.; Axtell, J. C.; Rheingold, A. L.; Spokoyny, A. M. Improved synthesis of icosahedral carboranes containing exopolyhedral BC and CC bonds. *Tetrahedron* **2019**, *75* (2), 187-191. DOI: https://doi.org/10.1016/j.tet.2018.11.040.

(19) Li, J.; Logan, C. F.; Jones, M., Jr. Simple syntheses and alkylation reactions of 3-iodo-o-carborane and 9,12-diiodo-o-carborane. *Inorg. Chem.* **1991**, *30* (25), 4866-4868. DOI: 10.1021/ic00025a037.

(20) Burn, A. G.; Nash, K. L. Electrochemical behavior of uranyl in anhydrous polar organic media. *Radiochimica Acta* **2017**, *105* (7), 513-522. DOI: doi:10.1515/ract-2016-2684.

(21) Fortier, S.; Hayton, T. W. Oxo ligand functionalization in the uranyl ion (UO22+). *Coordination Chemistry Reviews* **2010**, *254* (3), 197-214. DOI: https://doi.org/10.1016/j.ccr.2009.06.003.

(22) Kim, S.-Y.; Tomiyasu, H.; Ikeda, Y. Electrochemical Studies on [UO2(DMF)5](ClO4)2, UO2(acac)2DMF, and UO2(salen)DMF (DMF=N, N-dimethylformamide, acac=acetylacetonate, salen=N, N′-disalicylideneethylenediaminate) Complexes in DMF. *J. Nucl. Sci. Technol.* **2002**, *39* (2), 160-165. DOI: 10.1080/18811248.2002.9715170.

(23) Mizuoka, K.; Kim, S.-Y.; Hasegawa, M.; Hoshi, T.; Uchiyama, G.; Ikeda, Y. Electrochemical and Spectroelectrochemical Studies on UO2(saloph)L (saloph = N,N‘-Disalicylidene-o-phenylenediaminate, L = Dimethyl Sulfoxide or N,N-Dimethylformamide). *Inorg. Chem.* **2003**, *42* (4), 1031-1038. DOI: 10.1021/ic0260926.

(24) Milic, M.; Targos, K.; Tellez Chavez, M.; Thompson, M. A. M.; Jennings, J. J.; Franz, A. K. NMR Quantification of Hydrogen-Bond-Accepting Ability for Organic Molecules. *The Journal of Organic Chemistry* **2021**, *86* (9), 6031-6043. DOI: 10.1021/acs.joc.0c02876.

(25) Laurence, C.; Brameld, K. A.; Graton, J.; Le Questel, J.-Y.; Renault, E. The pKBHX Database: Toward a Better Understanding of Hydrogen-Bond Basicity for Medicinal Chemists. *Journal of Medicinal Chemistry* **2009**, *52* (14), 4073-4086. DOI: 10.1021/jm801331y.

(26) Laurence, C.; Graton, J.; Berthelot, M.; Besseau, F.; Le Questel, J. Y.; Lucon, M.; Ouvrard, C.; Planchat, A.; Renault, E. An enthalpic scale of hydrogen-bond basicity. 4. Carbon pi bases, oxygen bases, and miscellaneous second-row, third-row, and fourth-row

bases and a survey of the 4-fluorophenol affinity scale. *J Org Chem* **2010**, *75* (12), 4105-4123. DOI: 10.1021/jo100461z.

(27) Breshears, A. T.; Barnes, C. L.; Wagle, D. V.; Baker, G. A.; Takase, M. K.; Walensky, J. R. Structure and spectroscopy of uranyl and thorium complexes with substituted phosphine oxide ligands. *Radiochimica Acta* **2015**, *103* (1), 49-56. DOI: doi:10.1515/ract-2014-2295.

(28) Alcock, N. W.; Roberts, M. M.; Brown, D. Actinide structural studies. Part 1. Crystal and molecular structures of dinitratodioxobis(triphenylphosphine oxide)neptunium(VI), dinitratodioxobis(triphenylphosphine oxide)uranium(VI), and dichlorodioxo-(triphenylphosphine oxide)neptunium(VI). *Journal of the Chemical Society, Dalton Transactions* **1982**, (1), 25-31. DOI: 10.1039/DT9820000025.

(29) Kleckner, I. R.; Foster, M. P. An introduction to NMR-based approaches for measuring protein dynamics. *Biochimica et Biophysica Acta (BBA) - Proteins and Proteomics* **2011**, *1814* (8), 942-968. DOI: https://doi.org/10.1016/j.bbapap.2010.10.012.

(30) Hirose, K. A Practical Guide for the Determination of Binding Constants. *Journal of Inclusion Phenomena* **2001**, *39*, 193-209. DOI: 10.1023/A:1011117412693.

(31) Delius, J.; Frank, O.; Hofmann, T. Label-free quantitative 1H NMR spectroscopy to study low-affinity ligand–protein interactions in solution: A contribution to the mechanism of polyphenol-mediated astringency. *PLOS ONE* **2017**, *12* (9), e0184487. DOI: 10.1371/journal.pone.0184487.

(32) Wallace, M.; Holroyd, J.; Kuraite, A.; Hussain, H. Does It Bind? A Method to Determine the Affinity of Calcium and Magnesium Ions for Polymers Using 1H NMR Spectroscopy. *Anal. Chem.* **2022**, *94* (31), 10976-10983. DOI: 10.1021/acs.analchem.2c01166.

(33) Špadina, M.; Dufrêche, J.-F.; Pellet-Rostaing, S.; Marčelja, S.; Zemb, T. Molecular Forces in Liquid–Liquid Extraction. *Langmuir* **2021**, *37* (36), 10637-10656. DOI: 10.1021/acs.langmuir.1c00673.

(34) Stamberga, D.; Healy, M. R.; Bryantsev, V. S.; Albisser, C.; Karslyan, Y.; Reinhart, B.; Paulenova, A.; Foster, M.; Popovs, I.; Lyon, K.; et al. Structure Activity Relationship Approach toward the Improved Separation of Rare-Earth Elements Using Diglycolamides. *Inorg. Chem.* **2020**, *59* (23), 17620-17630. DOI: 10.1021/acs.inorgchem.0c02861.

(35) Sahu, S. K.; Chakravortty, V. Extraction of uranium(VI) with binary mixtures of a quadridentate Schiff base and various neutral donors. *J. Radioanal. Nucl. Chem.* **1998**, *227* (1), 163-165. DOI: 10.1007/BF02386452.

(36) Taoda, Y.; Sawabe, T.; Endo, Y.; Yamaguchi, K.; Fujii, S.; Kagechika, H. Identification of an intermediate in the deboronation of ortho-carborane: an adduct of ortho-carborane with two nucleophiles on one boron atom. *Chem. Commun.* **2008**, (17), 2049. DOI: 10.1039/b716079h.

(37) Yamazaki, H.; Ohta, K.; Endo, Y. Regioselective synthesis of triiodo-o-carboranes and tetraiodo-o-carborane. *Tetrahedron Letters* **2005**, *46* (17), 3119-3122. DOI: https://doi.org/10.1016/j.tetlet.2005.02.163.

(38) Lu, W.; Wu, Y.; Ma, Y.-N.; Chen, F.; Chen, X. A Method for Highly Selective Halogenation of o-Carboranes and m-Carboranes. *Inorg. Chem.* **2023**, *62* (2), 885-892. DOI: 10.1021/acs.inorgchem.2c03694.

(39) Dziedzic, R. M.; Spokoyny, A. M. Metal-catalyzed cross-coupling chemistry with polyhedral boranes. *Chem. Commun.* **2019**, *55* (4), 430-442. DOI: 10.1039/C8CC08693A.

(40) Wilkerson, M. P.; Burns, C. J.; Paine, R. T.; Scott, B. L. Synthesis and Crystal Structure of UO2Cl2(THF)3: A Simple Preparation of an Anhydrous Uranyl Reagent. *Inorg. Chem.* **1999**, *38* (18), 4156-4158. DOI: 10.1021/ic990159g.

(41) Popescu, A. R.; Laromaine, A.; Teixidor, F.; Sillanpää, R.; Kivekäs, R.; Llambias, J. I.; Viñas, C. Uncommon Coordination Behaviour of P(S) and P(Se) Units when Bonded to Carboranyl Clusters: Experimental and Computational Studies on the Oxidation of Carboranyl Phosphine Ligands. *Chem. Eur. J.* **2011**, *17* (16), 4429-4443. DOI: 10.1002/chem.201003330.

(42) Maaliki, C.; Canac, Y.; Lepetit, C.; Duhayon, C.; Chauvin, R. P-oxidation of gem-dicationic phosphines. *RSC Adv.* **2013**, *3* (43), 20391-20398. DOI: 10.1039/C3RA43563F.

Chapter 3 Crown Ether *o*-Carboranes for High Li^+ Selectivity

3.1. Introduction

3.1.1. Lithium Extraction

Lithium is a critical mineral for the transition from fossil fuels to renewable energy and battery energy storage. Lithium is a vital component in battery technology. Li-ion batteries are lightweight, have a high energy density and great long-term stability. They are used in an array of modern technology such as electric vehicles and energy storage systems. The demand for Li is rapidly rising (150 kt Li in 2022 to 700 kt by 2030) and current production capacities are struggling to keep pace.[1] Li is primarily extracted from brine salt lakes (62.6%) and the remaining amount (37.4%) is extracted from high-grade ores.[2] Extracting Li from ore generates extensive pollution and is 30-50% more expensive than extracting from concentrated salt lakes.[2] To extract Li from salt lakes, the brine beneath the salt flat is pumped into large evaporation basins which rely on the sun to slowly evaporate and concentrate the Li. The process is water intensive, losing 100–800 m^3 of water per metric ton of Li_2CO_3 over a slow 10-24 month period.[3] The evaporitic production of Li is also geographically limited to South America and not easily scalable.[3] Alternative Li sources are needed to emulate the increasing demand.

Extracting Li and other critical elements from seawater has garnered considerable attention.[4] The oceans contain ~ 180 billion tons of Li metal – the largest reservoir of the element, albeit at a lower concentration of ~ 0.2 ppm. The abundance of other cationic species in seawater[5] – Na^+ (11,000 ppm), K^+ (400 ppm), Mg^{2+} (1300 ppm), Ca^{2+} (400 ppm)[6] to list a few – makes Li^+ capture from seawater challenging. Direct lithium extraction (DLE) processes aim to extract Li from dilute brine or seawater using ion exchange, adsorption, solvent extraction, or electrochemical techniques.[7] Ion exchange and adsorption processes use

materials with high affinities for selective Li^+ extraction. Electrochemical techniques often couple a selective cationic membrane with a cathode suitable for Li^+ intercalation.[8, 9]

3.1.2. Materials for Li^+ Seawater Extraction

Materials for Li^+ capture exist in two broad classes – inorganic adsorbents and macrocyclic-ligand based materials. Inorganic adsorbents include zeolites, metal-organic frameworks (MOFs), titanium oxides and manganese oxides.[10-13] These materials possess high affinity for Li^+ but suffer from slow chemisorption processes. The high affinity for Li^+ compromises the durability of these adsorbents, requiring harsh acid elution processes for desorption. In particular, the durability of MnO_2-based adsorbents is exacerbated as the solid adsorbent dissociates into Mn^{2+} ions.[14]

Macrocyclic ligands with size-selective cation-binding pockets provide excellent control over Li^+ capture selectivity. Crown-ethers, cryptands, and spherands bind to Lewis acidic metals via the oxygen and/or nitrogen donor atoms in the macrocycle with electrostatic σ-hole interactions. Tuning the selectivity for Li^+ over Na^+ and K^+ by varying the pocket-size of the macrocycle is well established, and cavity sizes of 0.6–0.75 Å in crown-ethers lead to Li^+ binding affinity log K values of 2.14 ± 0.03 and 2.34 ± 0.06 for 12-crown-4 and 14-crown-4, respectively.[15] The cavity sizes of 14-crown-4 variants are optimal for Li^+ binding and result in 1:1 Li^+ to crown binding stoichiometry compared to 12-crown-4 derivatives which form 2:1 metal sandwich complexes.[16] Spherands are very rigid macrocycles with negligible reorganization energy resulting in even higher log K values of 16.8.[17] Removal of Li^+ often requires heating to 100 °C and the irreversible destruction of covalent bonds.[18] Crown-ethers, while they possess weaker Li^+ binding than spherands, are synthetically more accessible and offer flexibility enabling their use in Li^+ selective ion-exchange resins and membranes.[19]

Both these classes of materials suffer from sluggish Li^+ capture, especially from dilute feedstocks. Electrochemical methods enhance Li^+ capture kinetics.[20] For instance, while MnO_2-based adsorbents have slow adsorption kinetics requiring many days to reach saturation, electrochemical Li^+ intercalation in MnO_2 results in rapid Li^+ extraction within hours.[21] Electrochemical methods for Li^+ extraction may provide a pathway towards speedy Li^+ production to match rising demand. However, improvements are needed in the selectivity and robustness of working electrodes from competing metals in seawater.[22] Current electrodialysis methods struggle with separating monovalent cations: Li^+, Na^+, and K^+.[23]

In this Chapter, we integrate metal-binding selectivity offered by crown ethers with a redox-active framework – the *ortho*-carborane moiety ($C_2B_{10}H_{12}$). As described in Chapter 1 and demonstrated throughout Chapter 2, the unique redox-switching property of derivatized *ortho*-carboranes between *closo* and *nido* forms (Figure 1.3) offers a new approach for reversible metal capture and release. Herein, we targeted Li selectivity by adhering a size-selective binding pocket to *o*-carborane which closely emulates the Li^+ cationic size (Scheme 3.1). In the *closo* form, we suspected that the electron-deficient carborane cage may induce weak binding between the crown and Li^+, while in the *nido* form, an electron-rich, expanded crown cavity may promote stronger Li^+ binding. We synthesized the first *o*-carborane crown-ether, specifically 1,2-((6,6,7,7-Me_4)14-crown-4)-*o*-carborane (**^{14C4}Cb**). We then scrutinized structural and spectroscopic differences that accompany the chemical and electrochemical reduction of the *closo* (**^{14C4}Cb**) to the *nido* (**^{14C4}Cb^{2-}**) state. We then estimated the binding affinity of **^{14C4}Cb** and **^{14C4}Cb^{2-}** to Li^+, Na^+ and K^+ through a combination of spectroscopic and electrochemical techniques.

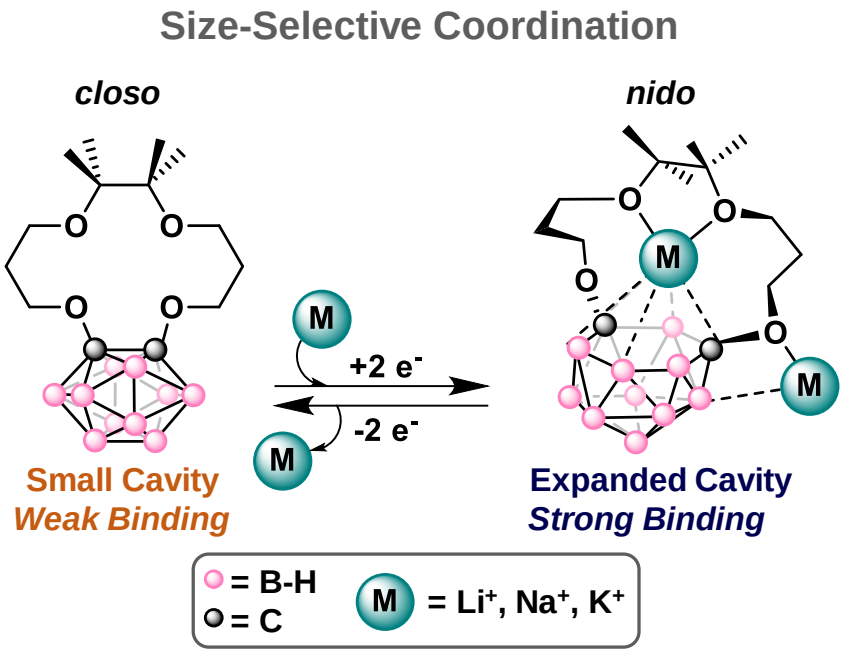

Scheme 3.1. Size-selective *closo/nido* Li^+ capture and release.

3.2. Results and Discussion

3.2.1. Synthesis and Characterization

We identified **^{14C4}Cb** as the target *o*-carborane crown-ether from two considerations – cavity size and macrocycle flexibility. The first factor narrows the choice of crown to a 14-crown-4 due to stronger and more selective Li^+ binding (log K of 2.34 ± 0.06) compared to 12-crown-4 (log K of 2.14 ± 0.03).[15] We further raised the Li^+ selectivity over Na^+ and K^+ by replacing the ethylene bridge distal to the *o*-carborane with a bulkier pinacol bridge (Scheme 3.1). The increased steric repulsion of a pinacol bridge favors smaller cations, Li^+ over Na^+. Additionally, we suspected that a pinacol bridge may promote metal release in *closo* form because additional reorganization energy is required for binding due to increased torsion angles.[24,25, 26]

Dr. Zongheng Wang determined that *p*-tosyl terminated bis(ether) linker, (2,3-Bis(3-[*p*-toluenesulfonyloxy]propoxy)-2,3-dimethylbutane)[27] (referred to as *p*-tosyl linker) prepared using modified literature procedures and purified by column chromatography after each step[28, 29] (Scheme 3.2a), enabled the synthesis of **^{14C4}Cb**. **^{14C4}Cb** can be prepared in a 1-step cyclization reaction from reported precursor 1,2-diol-*o*-carobrane[30] with *p*-tosyl linker (Scheme 3.2b). Specifically, the 1,2-diol-*o*-carborane was deprotonated with potassium hydride in THF and heated overnight with the *p*-tosyl linker (Scheme 3.2b) in DMF to afford the desired *closo*-1,2-((6,6,7,7-Me_4)14-crown-4)-*o*-carborane (**^{14C4}Cb**) as a pure white solid after purification by column chromatography.

We obtained the solid-state molecular structure of **^{14C4}Cb** from crystals suitable for single crystal X-ray diffraction studies grown from a saturated solution of diethyl ether at −25 °C (Figure 3.1a). The O–O distances in **^{14C4}Cb** are slightly elongated with nearest neighbor O–O distances of ~ 2.9 Å (d(O_1–O_2) = 2.931 Å) and diagonally opposed O–O distances of 4.5-4.9 Å (d(O_1–O_3) = 4.567 Å, d(O_2–O_4) = 4.840 Å) compared to dibenzo-14-crown-4.[31] The O_4–C_6–C_7–O_3 dihedral torsion angle is 78.008°. The C–C bond length in the carborane moiety (1.767 Å) and the C–O bond lengths (1.345 Å and 1.351 Å) are unremarkable.

We next investigated the reduction of **^{14C4}Cb**. To a frozen solution of **^{14C4}Cb** in THF, a solution of potassium naphthalenide in THF was added dropwise, and then allowed to warm to room temperature (Scheme 3.2b). After recrystallization from acetonitrile, we isolated the reduced species, K_2[*nido*-1,2-((6,6,7,7-Me_4)14-crown-4)-*o*-carborane] (**K_2^{14C4}Cb**).

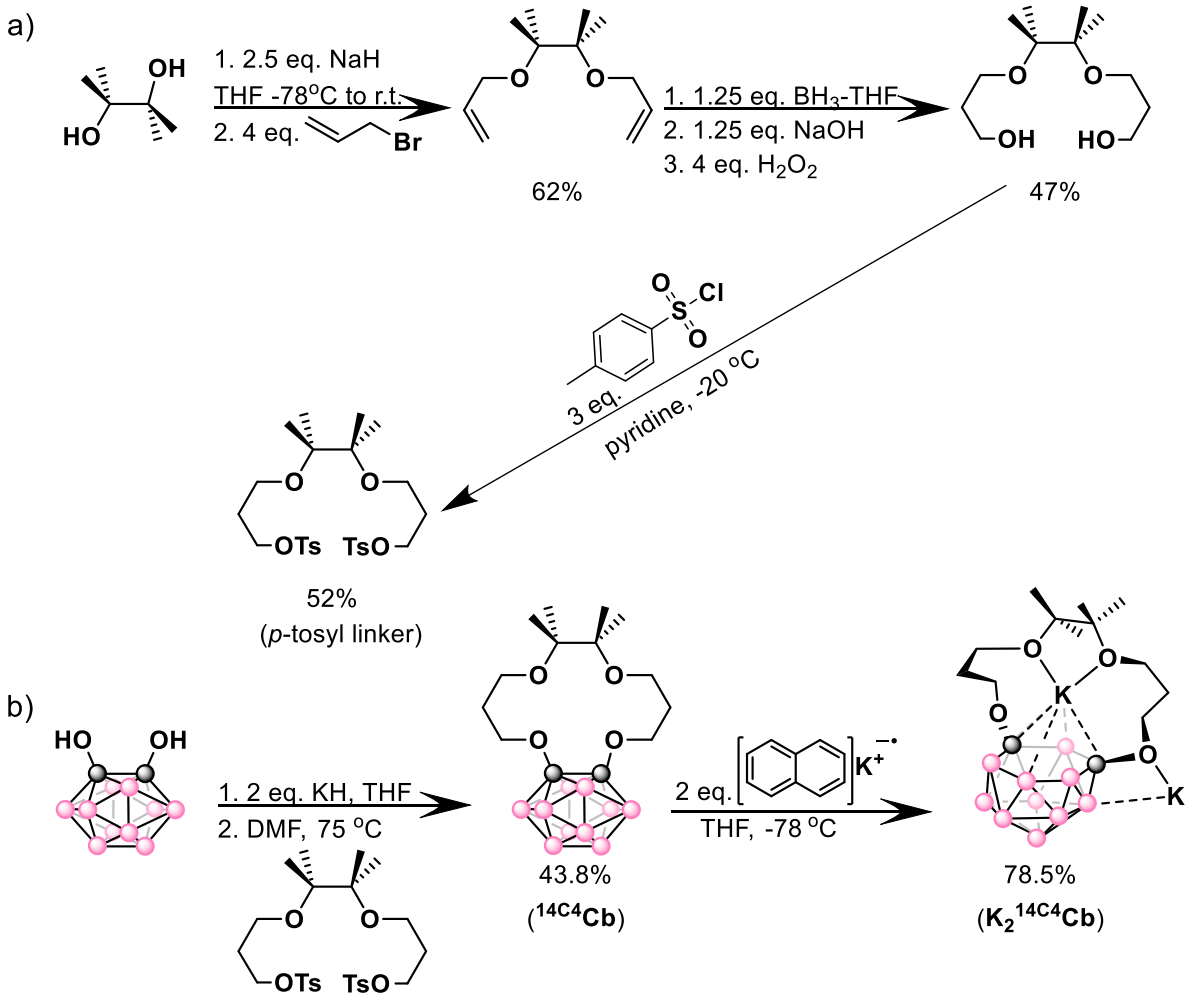

Scheme 3.2. Synthesis of a) Precursor *p*-tosyl linker b) *closo*- and *nido*- 1,2-((6,6,7,7-Me_4)14-crown-4)-*o*-carborane. Coordinating solvents and an additional carborane bound to the outer sphere K were omitted from the pictorial representation of **K_2^{14C4}Cb** for clarity.The solid-state molecular structure of **K_2^{14C4}Cb** was obtained from crystals suitable for single crystal X-ray diffraction studies grown from a concentrated acetonitrile solution at −25 °C (Figure 3.1b). We observed dramatic structural changes to both the crown and the carborane polyhedron upon the $2e^-$ reduction to the *nido* form. In the crown ring of **K_2^{14C4}Cb**, the oxygen-oxygen distances increase: O_1–O_3 (5.252 Å), O_2–O_4 distance (5.103 Å), O_1–O_2 (5.039 Å) while the O_4–C_6–C_7–O_3 dihedral torsion angle lowers to 52.477°. The O_3 and O_4 lone pair

orbitals point toward the expanded cavity as the ring flexes to permit for donation to the K^+ center.

The C_1–C_2 bond is cleaved (2.737 Å), the C–O bonds elongate (1.411 Å and 1.448 Å), and the boron centers rearrange to form the planar 6-membered η^6 donating ring, consisting of C_1, C_2 and four boron centers (Figure 3.1b). The η^6 6-membered ring observed here is reminiscent of dicarbollide sandwich clusters formed with η^5 5-membered rings.[32, 33] The distance between this 6-membered ring and the K^+ center in the cavity is ~3 Å, similar to cation-π bonding observed in potassium metallocene-crown complexes[34] and $[C_6H_6\text{-}M]^+$ adducts.[35] The second K^+ is located between two *nido*-carboranes, binding with one crown oxygen from each and forming weak agnostic B–H interactions with the cage (3.490 Å and 3.292 Å). The structure displayed K−H distances of 3.163 Å and 3.431 Å.

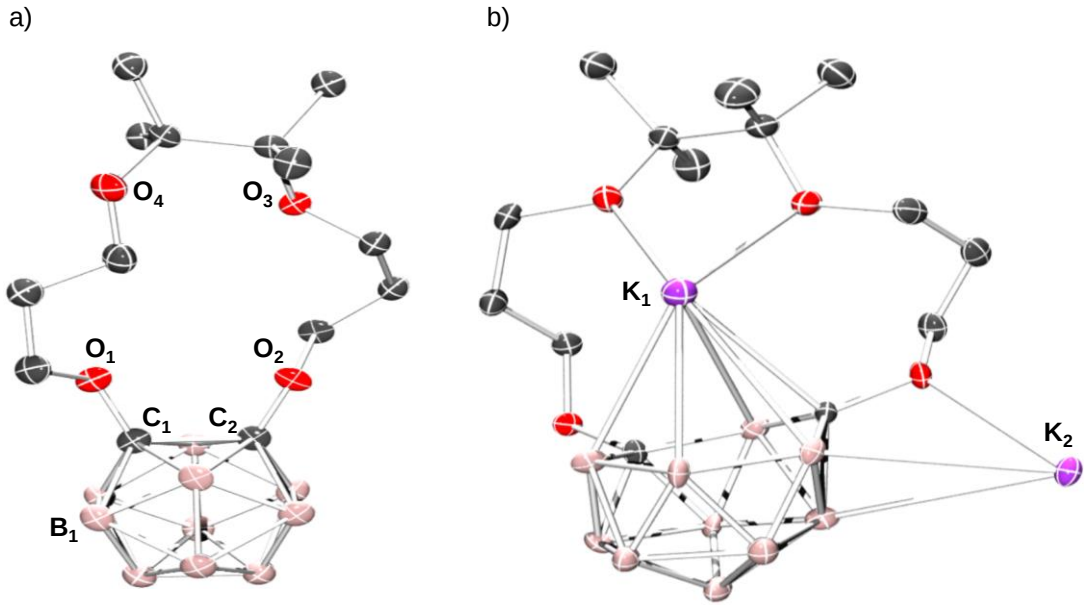

Figure 3.1. Solid-state molecular structures of a) **^{14C4}Cb** b) **$K_2{}^{14C4}$Cb** obtained by single crystal XRD studies. Hydrogen atoms, co-crystallized solvents and repeating units omitted for clarity.

We were unsuccessful at isolating Li_2[*nido*-1,2-((6,6,7,7-Me_4)14-crown-4)-*o*-carborane] (**Li_2^{14C4}Cb**) via the analogous reduction using Li naphthalenide. The stoichiometry was more difficult to control given that Li naphthalenide forms a mixture of mono- and di-anionic species and we observed many peaks in the ^{7}Li and ^{11}B NMR spectra.[36] Instead, we performed a salt swap by stirring 1 equiv. of **K_2^{14C4}Cb** with 2 equiv. of lithium tetrakis(pentafluorophenyl)borate ethyl etherate ([Li(OEt_2)][TFAB]) at room temperature in acetonitrile to afford the putative species, **Li_2^{14C4}Cb** (Scheme 3.3). We observed that a white solid partially precipitated out which we suspected may be KTFAB.

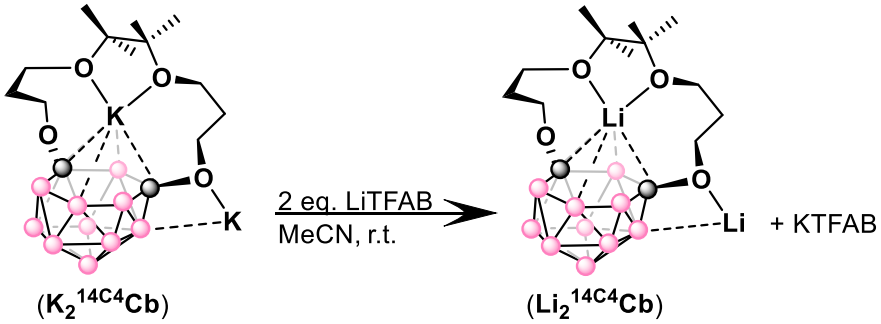

Scheme 3.3. Salt swap of **K_2^{14C4}Cb** with LiTFAB.

Monitoring the reaction by ^{11}B{^{1}H} NMR spectroscopy, we observed an intermediate product formed immediately that contained 12 distinct peaks (Figure 3.2). We attempted to obtain a ^{11}B–^{11}B COSY of the intermediate product; however, it rapidly converted to a thermodynamic product with 5 different ^{11}B{^{1}H} resonances (Figure 3.3). The ^{11}B–^{11}B COSY indicated strong correlation between these 5 resonances in this thermodynamic product (Figure 3.4). The ^{1}H NMR displayed chemically inequivalent diastereotopic methylene C–H resonances (6 total integrating to 2H each) and 2 chemically inequivalent methyl resonances. This is in contrast to the resonances in **K_2^{14C4}Cb** which displayed chemically equivalent methylene resonances (3 resonances total integrating to 4H each) and chemically equivalent

methyl resonances (1 single resonance integrating to 12H) which likely indicates a more fluxional system. The ^{7}Li NMR spectrum in **Li_2^{14C4}Cb** displayed one broadened peak downfield relative to free LiTFAB (Figure 3.3). We note that diethyl ether from the [Li(OEt_2)][TFAB] reagent and a sharp B resonance from TFAB are present within the ^{1}H and ^{11}B{^{1}H} NMR spectra, respectively. The ^{1}H–^{1}H COSY confirms that one carborane species is present in solution, and an additional crown peak is hidden underneath the large diethyl ether signal (Figure 3.4). We suspect that the asymmetry of the ^{1}H resonances is likely due to stronger, rigid binding between Li^+ and the crown cavity. Comparatively, the ^{1}H NMR spectrum of **K_2^{14C4}Cb**, displayed symmetric resonances which we attribute to weaker, flexible K^+ binding by the crown moiety. Attempts to grow single crystals of **Li_2^{14C4}Cb** suitable for X-ray diffraction studies have thus far failed. Solvent combinations of carborane dissolved in THF with hexane/pentane/diethyl ether as well as carborane dissolved in acetonitrile and diethyl ether, all grown by vapor diffusion, have not yet produced viable crystals for a solid-state molecular structure.

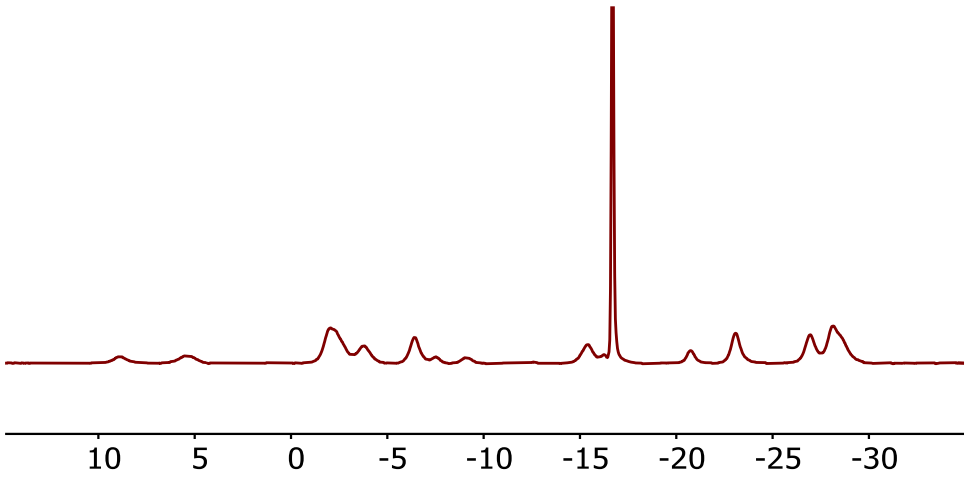

Figure 3.2. ^{11}B{^{1}H} NMR of kinetic **Li_2^{14C4}Cb** product acquired immediately in CD_3CN.

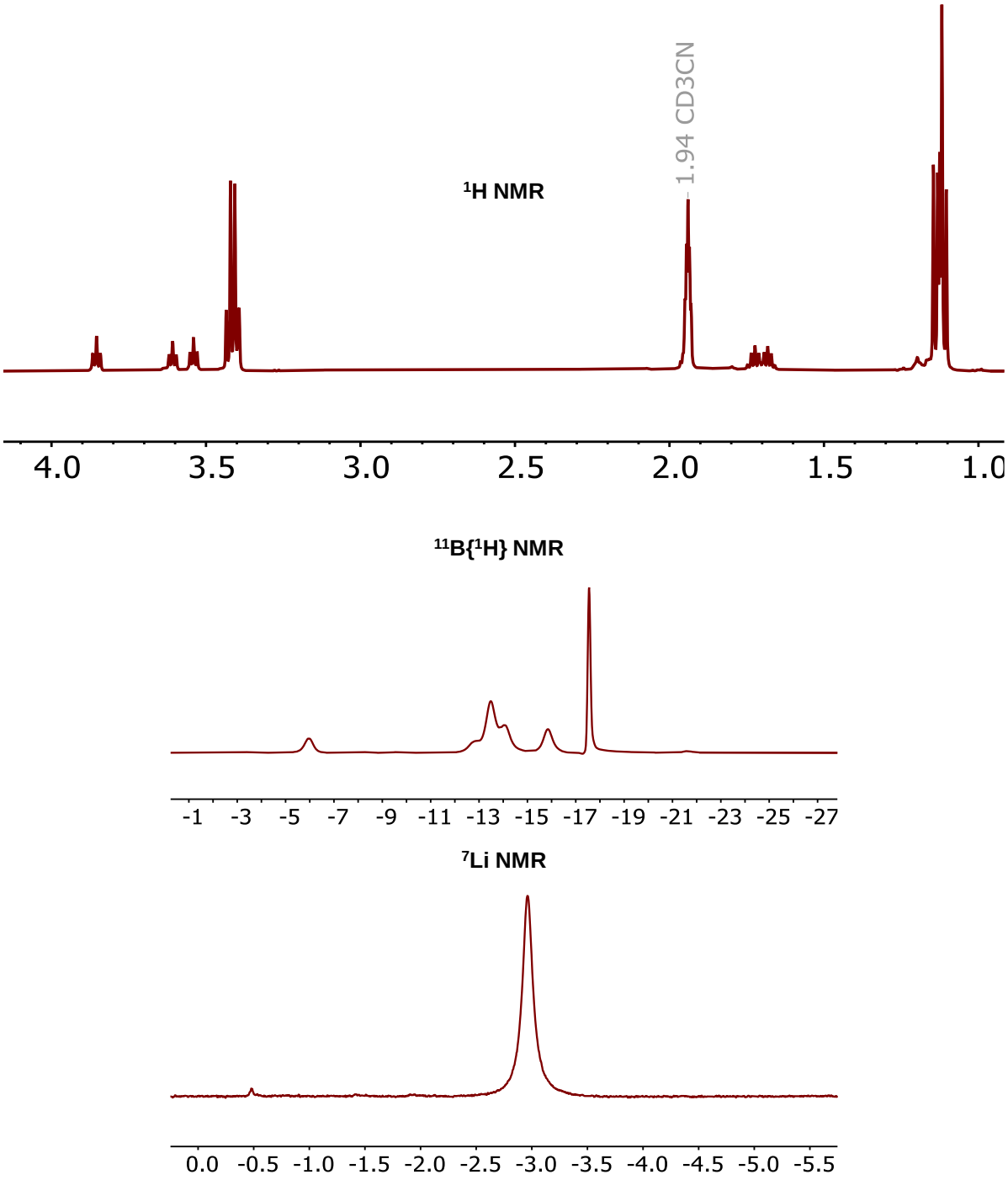

Figure 3.3. ^{1}H, $^{11}B\{^{1}H\}$ and ^{7}Li NMR spectra of **$Li_2^{14C4}Cb$** taken in CD_3CN.

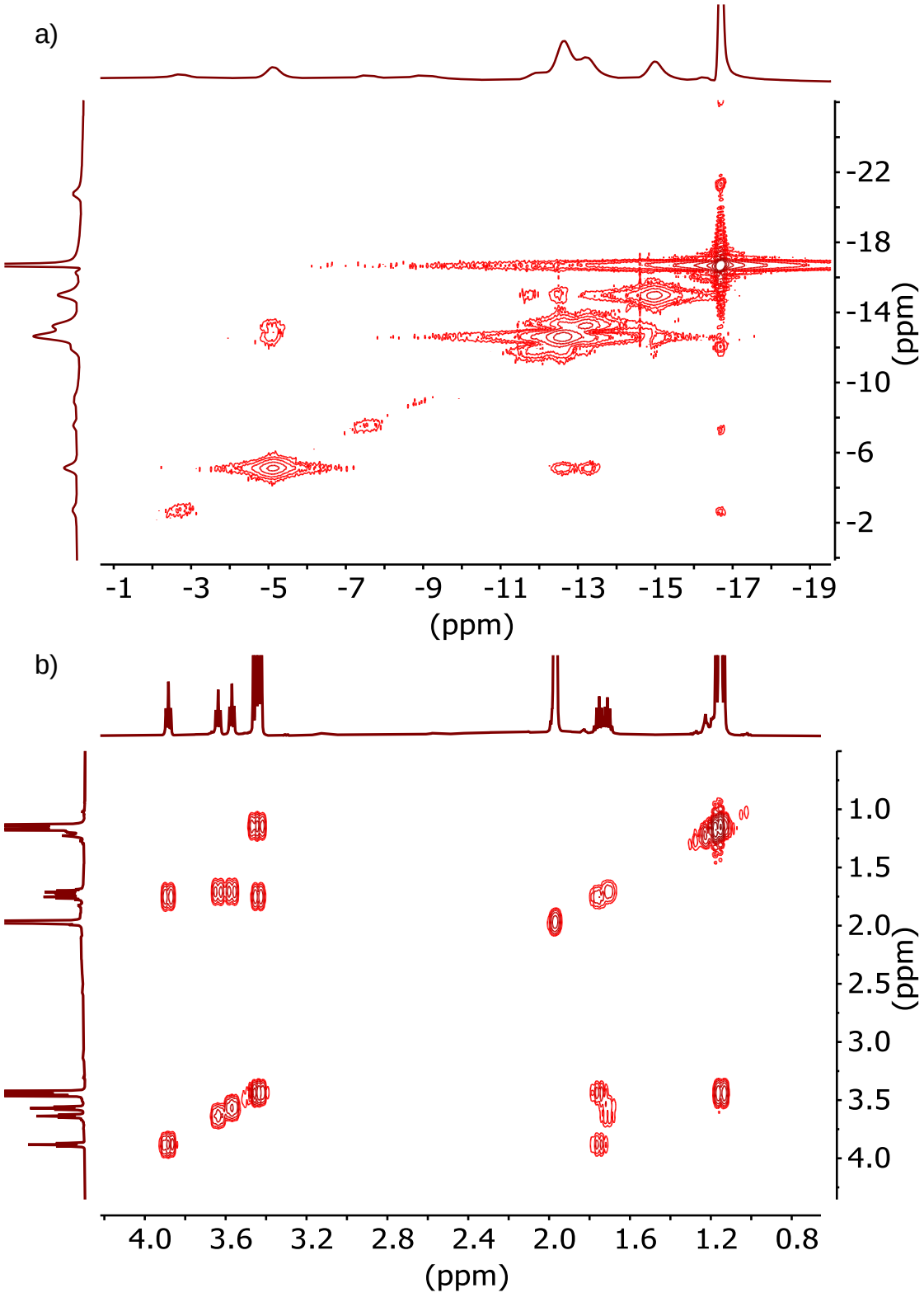

Figure 3.4. 2D NMR spectra of **Li_2^{14C4}Cb** taken in CD_3CN. a) ^{11}B–^{11}B COSY b) ^{1}H–^{1}H COSY

We wanted to verify whether **$Li_2^{14C4}Cb$** is redox-switchable from *nido*-carborane species to *closo*-carborane, **^{14C4}Cb**. To a solution of **$Li_2^{14C4}Cb$** in CD_3CN, 2 equiv. of freshly prepared $[(C_6H_4Br)_3N][PF_6]$ "magic blue" was added.[37] No color change occurred and the $^{11}B\{^1H\}$ NMR spectrum remained unaltered. Though, new downfield ^1H NMR resonances emerged, perhaps suggesting decomposition of the crown. In the ^7Li NMR spectrum, the Li peak sharpened and shifted upfield (more upfield than free LiTFAB). Similarly, we tried to oxidize **$Li_2^{14C4}Cb$** again, but this time with immediately prepared **$Li_2^{14C4}Cb$** (intermediate product) and 2 equiv. of magic blue. The color changed from blue to light yellow and a white precipitate formed. We tried to isolate the white precipitate by filtering and subsequently extracting it into $CDCl_3$; though, this only contained LiTFAB and tris(4-bromophenyl)amine and no carborane species. The yellow filtrate contained the carborane products. Specifically, the ^1H NMR spectrum of the filtrate displayed a festival of peaks that do not match the spectral data for **^{14C4}Cb** or **$Li_2^{14C4}Cb$**. Additionally, we observed the formation of tris(4-bromophenyl)amine. The $^{11}B\{^1H\}$ NMR also suggests that the reaction did not revert to *closo*-carborane **^{14C4}Cb**, though the ^7Li NMR peak also sharpened and shifted upfield. The data seems to suggest that **$Li_2^{14C4}Cb$** might be getting oxidized, but it is not reforming **^{14C4}Cb** as a true redox switch. A solid-state molecular structure of **$Li_2^{14C4}Cb$** would help with discerning what structural changes might be happening upon forming a Li-*nido*-carborane species. Possibly, using a stronger oxidant, such as $[(C_6H_3Br_2)_3N]^+$ "magic green", may help with the oxidation (Figure 3.10).[38]

3.2.2. NMR Binding Studies

We used two parallel approaches to evaluate the metal binding behavior of **^{14C4}Cb** and metal-free *nido*-carborane species, **$^{14C4}Cb^{2-}$**. We acquired the ^1H NMR spectrum of **^{14C4}Cb** in

d_8-THF with varying concentrations of Li^+ added as $LiPF_6$ (Figure 3.5a). We found the ^1H NMR resonances corresponding to **^{14C4}Cb** remained unaltered with up to 4 equivalents of added Li^+ (Figure 3.5a). In a complementary experiment where a solution of **^{14C4}Cb** was added to a solution of $LiPF_6$ in d_8-THF, the ^7Li NMR resonance corresponding to the solvated Li^+ shifted marginally (Δ = 0.03 ppm) from δ_{Li} = -1.10 in absence of **^{14C4}Cb** to δ_{Li} = -1.07 with 13.3 equivalents of **^{14C4}Cb** (Figure 3.5b). The peak full width at half maximum (FWHM) broadened from 0.80 Hz to 1.19 Hz as **^{14C4}Cb** was added. The fast exchange between bound and unbound Li^+ states displayed a minimal downfield shift in the ^7Li NMR spectrum which confirmed the presence of a very weak interaction between Li^+ and **^{14C4}Cb**. We attributed this weak coordination to the electron-withdrawing effects of the *ortho*-carborane cage which deactivates the oxygens in the macrocycle, especially O1 and O2 (Figure 3.3a). The decreased electronic density of the **^{14C4}Cb** cavity is observable by upfield shifted ^1H NMR resonances compared to reported 14-crown-4 derivatives.[27] We unfortunately could not determine this minute Li^+ binding constant using standard NMR techniques because the shift in resonances was too small to accurately compute a binding constant.

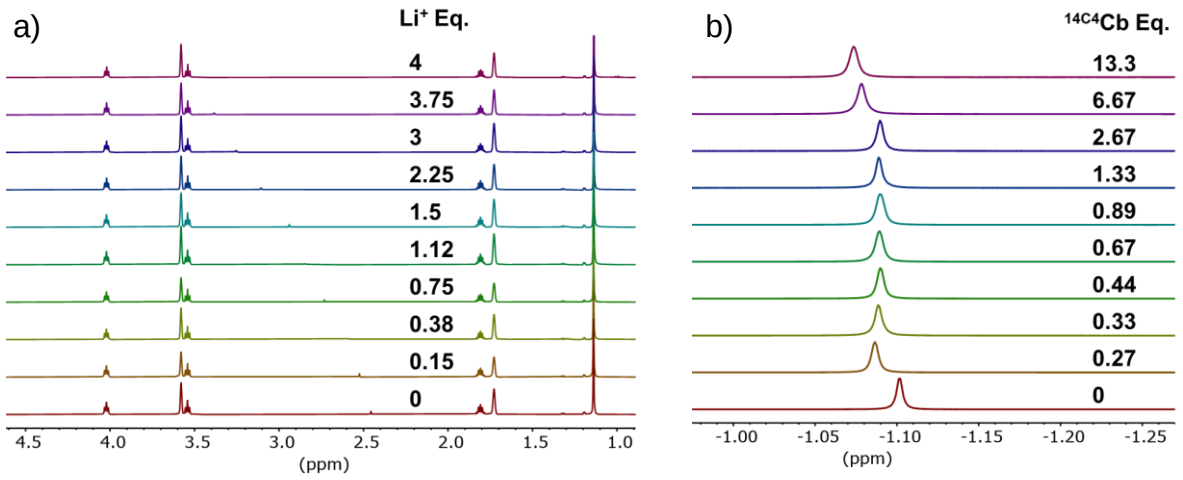

Figure 3.5. NMR binding studies **^{14C4}Cb** and $LiPF_6$ in d_8-THF.a) ^1H NMR spectrum b) ^7Li NMR spectrum

In lieu of using **$K_2{}^{14C4}$Cb** to study the binding properties of the *nido*-carborane, we instead electrochemically generated the metal-free variant, **^{14C4}Cb^{2-}**, for ^7Li NMR binding studies. We performed a bulk electrolysis of **^{14C4}Cb** in the presence of $[Bu_4N][PF_6]$ supporting electrolyte to *in situ* generate the metal-free *nido*-carborane, $[Bu_4N]_2[$**^{14C4}Cb**$]$. In a two-compartment H-cell separated by a fine glass frit, we added a 10.5 mM solution of **^{14C4}Cb** in 0.1 M $[Bu_4N][PF_6]$ DME to the working compartment and a Ketjenblack slurry in 0.1 M $[Bu_4N][PF_6]$ DME to the counter compartment serving as a sacrificial oxidant. We then reduced the **^{14C4}Cb** galvanostatically until complete conversion to **^{14C4}Cb^{2-}** after 2 mol equiv. of electrons were passed. Conversion to **^{14C4}Cb^{2-}** was confirmed by the disappearance of **^{14C4}Cb** and the emergence of 5 new resonances in the $^{11}B\{^1H\}$ NMR spectrum at 9.69, -2.13, -7.65, -16.22, and -20.66 ppm (Figure 3.6). We also confirmed the identity of metal-free electrochemically-generated **^{14C4}Cb^{2-}** by adding 2 equiv. of KPF_6. We observed the formation of peaks in the $^{11}B\{^1H\}$ NMR spectrum that match the chemically isolated **$K_2{}^{14C4}$Cb**.

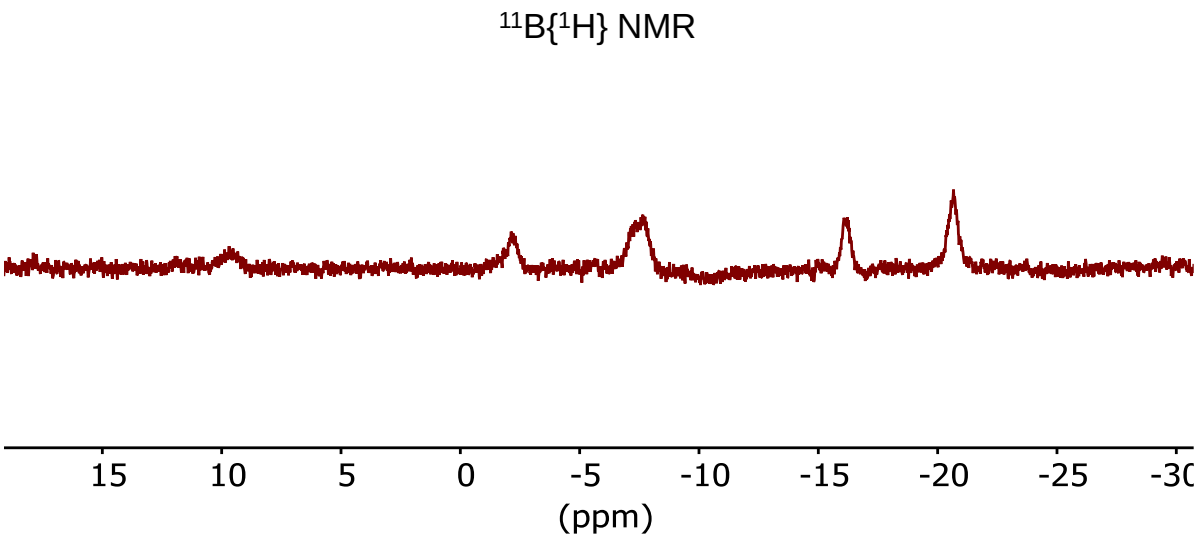

Figure 3.6. Unlocked $^{11}B\{^{1}H\}$ NMR spectrum of electrochemically-generated $[Bu_4N]_2[$**^{14C4}Cb**$]$ in 0.1 M $[Bu_4N][PF_6]$ DME.

During a GBE, a loss in theoretical yield is expected due to crossover across the glass frit in the H-cell, adsorption onto the RVC electrodes, and/or analyte degradation. Accordingly, we determined the concentration of [**^{14C4}Cb^{2-}**] to be 7.64 mM by performing a UV-vis back-titration using a standardized solution of ferrocenium hexafluorophosphate ($[Fc][PF_6]$) and a UV-Vis calibration curve of the absorbance of $[Fc][PF_6]$ at 620 nm (Figure 3.7). 1 equiv. of **^{14C4}Cb^{2-}** reacts with 2 equiv. of Fc^+ to regenerate **^{14C4}Cb** and Fc both of which do not absorb visible light at 620 nm.

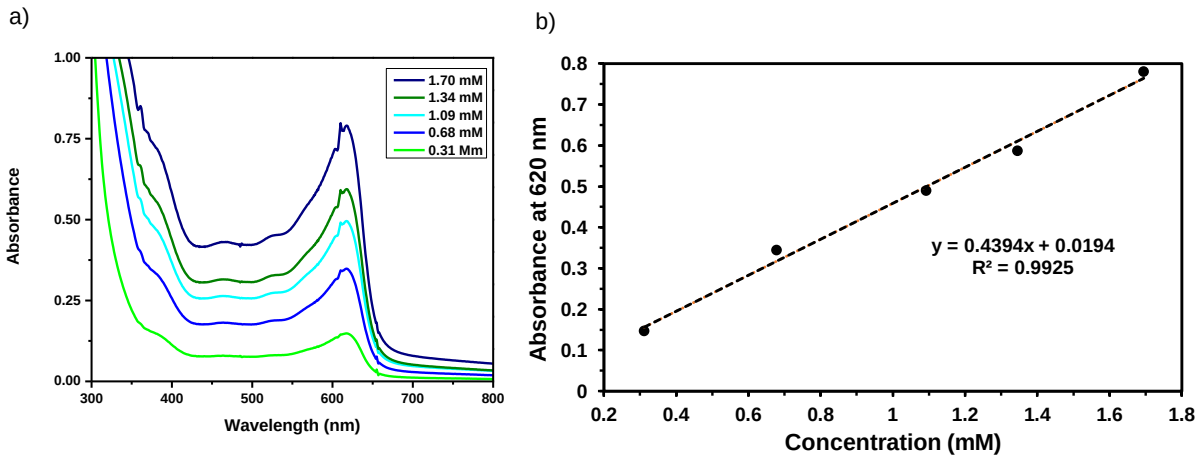

Figure 3.7. UV-Vis calibration curve of $FcPF_6$.a) UV-visible spectra of various concentrations of Fc^+ in 0.1 M $[Bu_4N][PF_6]$ DME. b) Corresponding calibration curve of the UV-Vis spectra presented in (a).

We next turned to ^{7}Li NMR titrations using the electro-generated ^{14C4}**Cb**$^{2-}$ solution and LiTFAB in DME as the Li^+ source. The unlocked ^{7}Li NMR spectra of these solutions are shown in Figure 3.8. In absence of any ^{14C4}**Cb**$^{2-}$, we observed the sharp resonance of solvated Li^+ at -1.42 ppm (FWHM = 1.07 Hz). When < 1 equiv. of ^{14C4}**Cb**$^{2-}$ was added relative to Li^+, we observed an extremely broad ^{7}Li resonance (**A**) between 0–2 ppm hidden in the baseline (Figure 3.8) and a broadening resonance, **B**. With increasing equivalents of ^{14C4}**Cb**$^{2-}$, resonance **B** shifted downfield from -1.35 ppm (0.4 equiv., FWHM = 5.70 Hz)) to -0.8 (0.9 equiv.) with maximal broadening (FWHM = 16.33 Hz). Once > 1 equiv. of ^{14C4}**Cb**$^{2-}$ is added, the resonance of **B** disappears favoring **A**. The very different chemical shift of **A** may suggest complete encapsulation of Li^+ by the crown pocket whereas resonance **B** (< 1 equiv. of ^{14C4}**Cb**$^{2-}$) is likely indicative of rapidly interchanging crown-encapsulated and weakly cage-bound exogenous Li^+ centers (similar to Figure 3.1b, but with Li). We attempted to perform variable temperature ^{7}Li NMR of ^{14C4}**Cb**$^{2-}$ with 1 equiv. of Li^+. However, at cold temperatures

the electrolyte precipitated out, impeding the attainment of higher resolution spectra. While the ^{7}Li NMR spectra qualitatively suggest near complete Li^{+} binding by **^{14C4}Cb^{2-}**, the signal broadness of the quadrupolar Li^{+} bound to the asymmetric coordination shell of the crown pocket precludes the use of ^{7}Li NMR spectroscopy to determine the binding constant in the Li^{+} – **^{14C4}Cb^{2-}** system. ^{1}H and ^{7}Li NMR binding experiments are limited by a requirement to know the binding stoichiometry and are only applicable for simple 1:1 or 1:2 binding.[39]

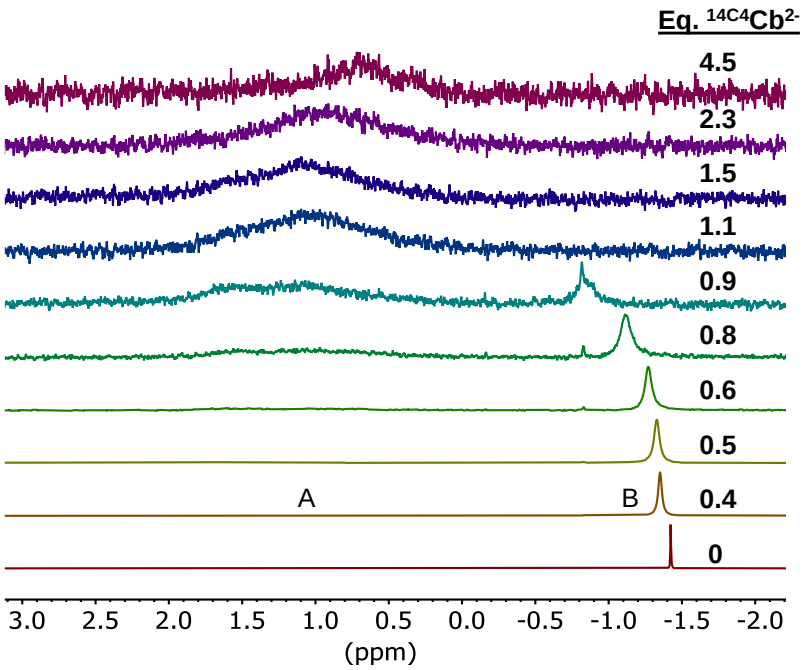

Figure 3.8. Unlocked ^{7}Li NMR spectra of LiTFAB with increasing equivalents of **^{14C4}Cb^{2-}** in 0.1 M $[Bu_4N][PF_6]$ DME.

The unlocked $^{11}B\{^{1}H\}$ NMR spectra of the Li^{+}/**^{14C4}Cb^{2-}** solutions closely resembled the spectrum displayed in Figure 3.2 after immediate salt swap of **K_2^{14C4}Cb** with LiTFAB. Here, we observed 9 distinct (-0.44, -2.28, -5.24, -7.79, -16.23, -20.65, -25.02, -29.39 ppm) in the $^{11}B\{^{1}H\}$ NMR spectrum (Figure 3.9). After a few days, the spectrum appeared to match the NMR spectrum of the thermodynamic **Li_2^{14C4}Cb** species (Figure 3.3). We observed that

the conversion to the thermodynamic product occurred at a slower timescale using dilute electrogenerated solutions. Adding 2 equiv. of 12-crown-4 to thermodynamic, electrogenerated **$Li_2^{14C4}Cb$** had no effect on these resonances suggesting that 12-crown-4 does not outcompete the *nido*-carborane species for Li^+ binding.

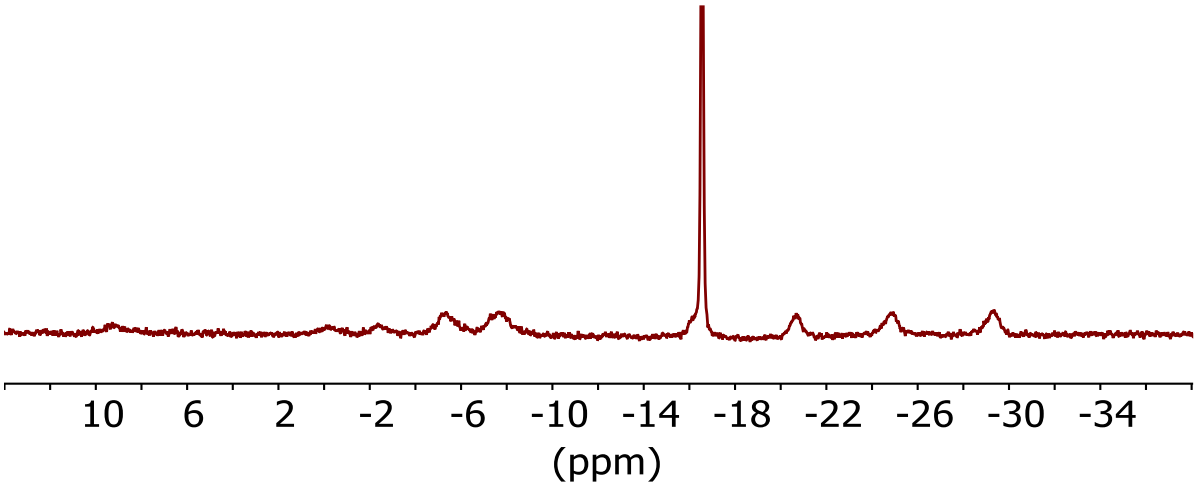

Figure 3.9. Example $^{11}B\{^1H\}$ NMR spectrum of **$^{14C4}Cb^{2-}$** with 2 equiv. of Li^+.

3.2.3. Electrochemistry

Electrochemistry is a powerful tool for probing binding interactions. For example, d-block or f-block metal complexes bearing crown moieties may experience anodic shifts in metal reduction potentials upon alkali metal complexation.[34, 40-42] Similarly, redox-active drugs have been shown to become redox-inactive once bound to DNA.[43, 44] The CVs of **^{14C4}Cb** with alkali metal solutions offered an alternative method to measure the **^{14C4}Cb** – alkali metal binding constant. In a 0.1 M $[Bu_4N][PF_6]$ DME solution devoid of any metal species, we observed a chemically reversible 2 e^- redox with a formal potential of $E_{1/2}$ = -2.20 V vs $Fc^{+|0}$ (Figure 3.10a). The large difference between the peak reductive potential (E_{red} = -2.86 V) and the peak oxidative potential (E_{ox} = -1.54 V) suggests significant structural and solvation shell reorganization which may be explained by C–C bond scission and cage rearrangement.

Next, we acquired the CVs of solutions containing **^{14C4}Cb** with 2 equivalents of alkali metals, Li^+, Na^+, and K^+ (Figure 3.10b). The CV of **^{14C4}Cb** with KPF_6 displayed a shift in the peak oxidative potential by 70 mV to E_{ox} = -1.47 V while the peak oxidative current decreased by 10% compared to the metal-free CV. In a solution with 2 equiv. of Na^+ instead of K^+, we observed an even larger anodic shift by 200 mV to E_{ox} = -1.34 V accompanied by an even greater, 31% decrease in the anodic current. With 2 equiv. of Li^+ instead of Na^+ or K^+, the *nido*- to *closo*- oxidation around -1.54 V disappeared entirely. The CV of **^{14C4}Cb** with a mixed metal $Li^+/Na^+/K^+$ solution (2 equiv. each) was similar to the CV with only Li^+ present, lacking the *nido*- to *closo*- oxidation.

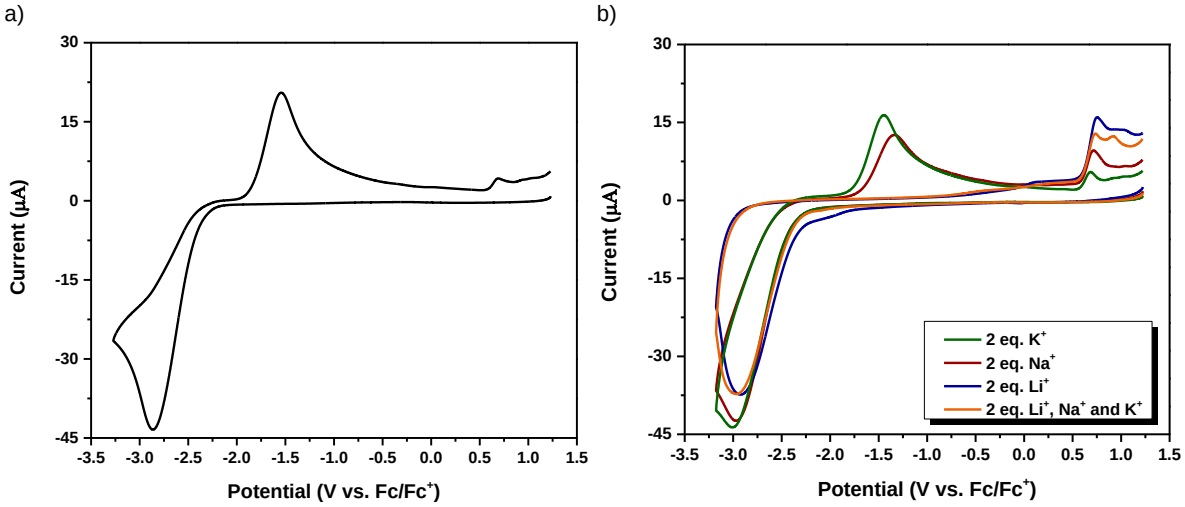

Figure 3.10. CVs of 2.9 mM **^{14C4}Cb** in 0.1 M $[Bu_4N][PF_6]$ DME. 50 mV/s scan rate, glassy carbon working electrode, Pt wire counter electrode, $Ag_{(s)}$/AgOTf reference electrode a) **^{14C4}Cb** with no metal b) **^{14C4}Cb** with 2 equivalents of alkali metals (5.8 mM)

In addition to the loss in return current observed upon metal addition, we observed a new oxidative event emerge at ~ 0.7 V. While faintly observed in the absence of metal (Figure 3.10a), it is not present when scanning anodically first. In addition, we do not believe that it is a carborane- nor metal-based adsorption event. This was confirmed by testing whether the

nido peak oxidation current (~ -1.5 V) and the oxidation at ~0.7 V scale proportionally with incremental cathodic sweeps with and without Li^+ present (Figure 3.11). In a metal-free solution of **^{14C4}Cb**, we observed that the *nido* oxidation peak current increases as the CV is scanned more cathodically (Figure 3.11a), consistent with the increased generation of the *nido* carborane. Additionally, we saw that intentionally scanning beyond the solvent window does not cause the *nido* oxidation to diminish, nor does the oxidation at ~0.7 V increase dramatically, thus negating carborane-based adsorption. With 0.87 mM of Li^+ (0.3 equiv.) in solution, we observed similar redox behavior where the *nido* oxidation increases with increasingly cathodic sweeps (Figure 3.11b); however, here we see a marked increase in the oxidation event at ~0.7 V when scanning cathodically. Scanning beyond the solvent window does diminish the *nido* oxidation in favor of the ~0.7 V oxidation event. Interestingly, when the CV scan is reversed at -2.57 V (Figure 3.11b, orange trace), no *nido* oxidation is observed but the anodic event at ~0.7 V is visible. Together, these data strongly suggest that the emerging oxidation at ~0.7 V is due to metal-bound *nido*-carborane species reforming *closo*-carborane (metal release).

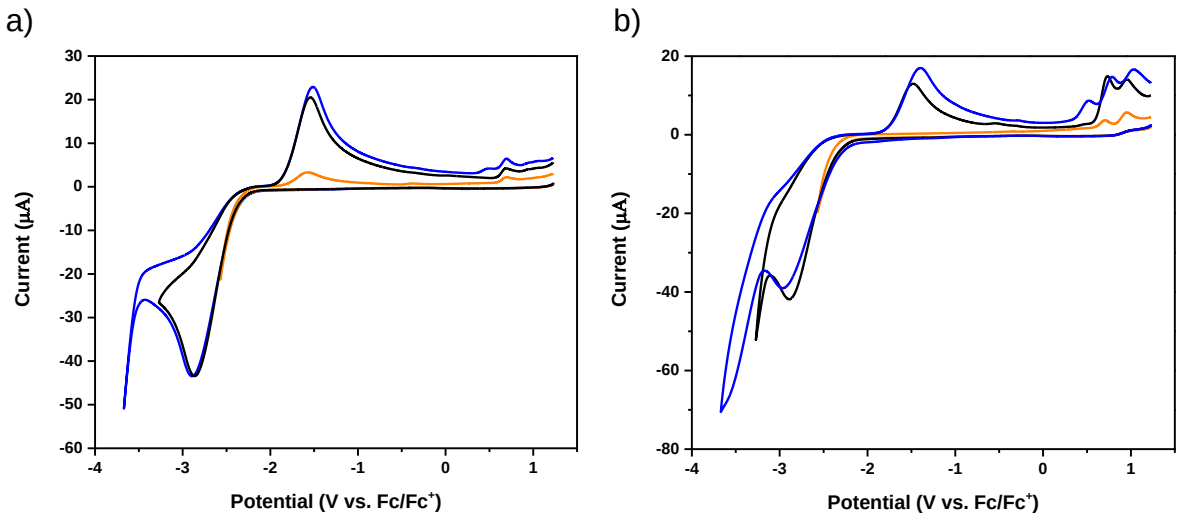

Figure 3.11. Varied cut off cathodic sweeps of **^{14C4}Cb** without (a) and with (b) 0.87 mM LiTFAB (0.3 equiv.).Cutoff potentials: Orange – -2.57. Black – -3.27 V. Blue – -3.67 V. Data collected using a 0.1 M $[Bu_4N][PF_6]$ DME electrolyte solution with a glassy carbon working electrode, Pt wire counter electrode, and $Ag_{(s)}$/AgOTf reference electrode.

We postulate that *in situ*-generated **^{14C4}Cb^{2-}** binds to alkali metal cations generating the putative $[M_n(\mathbf{^{14C4}Cb^{2-}})]$ species which becomes electrochemically inactive to oxidation near ~ -1.54 V and instead oxidizes at ~0.7 V. Combining the metal-**^{14C4}Cb^{2-}** binding equilibrium and experimentally measured loss of *nido*- to *closo*- peak oxidation current at varying metal concentrations then offers an approach to determining binding constant of *nido*-carborane **^{14C4}Cb^{2-}** to Li^+, Na^+ and K^+. Denoting **^{14C4}Cb^{2-}** as Cb and the alkali metal cations as M, we have a general binding equilibrium where x metal centers bind to each Cb center to generate the bound metal–*nido*-carborane species, denoted as $[Cb\ xM]$. We thus have the equilibrium,

$$Cb + x\,M \rightleftarrows [Cb\ xM] \qquad (3.1)$$

$$K = \frac{[Cb\ \ xM]}{[Cb][M]^x} \qquad (3.2)$$

Rearranging Equation 3.2, we have

$$\frac{[Cb\ xM]}{[Cb]} = K[M]^x \qquad (3.3)$$

Applying a logarithm function on both sides of this equation leads to

$$log\ \frac{[Cb\ xM]}{[Cb]} = x\ log[M] + \log K \qquad (3.4)$$

$[Cb\ x\ M]$, $[Cb]$ and $[M]$ are local concentrations in close proximity to the electrode surface, changing with the applied electrode potential. However, the sum of $[Cb\ xM]$ and $[Cb]$ is constant, equal to the initial bulk concentration of **^{14C4}Cb**, denoted as $[Cb]_o$ in the electrochemical cell as expressed in Equation 3.5.

$$[Cb]_o = [Cb\ xM] + [Cb] \qquad (3.5)$$

which can be rearranged and substituted in Equation 3.4 to obtain

$$log\ \frac{[Cb]_o - [Cb]}{[Cb]} = x\ log[M] + \log K \qquad (3.6)$$

The peak *nido*- to *closo*- current $I_{p,a}$ in the CVs of **^{14C4}Cb** has a linear dependence on the concentration of *nido*-**^{14C4}Cb** at the electrode surface and thus enables measuring the $[Cb]$ that remains unbound to alkali cations. We further note that the *nido*- to *closo*- peak oxidation current is diffusion-limited and adheres to the Randles-Ševčík equation (Equation 3.7, Figure 3.23): where n is the number of electrons transferred, F is Faraday's constant, A is the area of the electrode, D is the diffusion coefficient, *v* is the scan rate, R is the gas constant, T is temperature and C is concentration of the redox probe.

We held all the terms in the Randles-Ševčík equation constant besides the changing concentration of the *nido*-carborane in the CVs we have acquired; hence, the peak oxidation current is directly proportional to $[Cb]$ ($C = [Cb]$)

$$i_p = 0.4463nFA\left(\frac{nFvD}{RT}\right)^{\frac{1}{2}} C = p \cdot [Cb] \qquad (3.7)$$

where p is constant. Substituting Equation 3.7 into Equation 3.6, we find

$$log\ \frac{I_o - I}{I} = log\ \frac{\Delta I}{I} = \ x\ log[M] + \log K \qquad (3.8)$$

where I_o is the peak oxidation current in absence of any metals, and I is the oxidation current once metal is added, and ΔI is the magnitude of current decrease upon addition of Li^+, Na^+ or K^+.[44-47] Plotting the logarithm of the relative current change $\log(\frac{\Delta I}{I})$ with respect to the concentration of metal, the y-intercept would be equal to log K, while the number of the metal ions binding to each **^{14C4}Cb^{2-}** constitutes the slope (Equation 3.8). The obtained log K is the summation of the alkali metals binding (e.g., log K_1 + log K_2) to **^{14C4}Cb^{2-}** (Scheme 3.4).

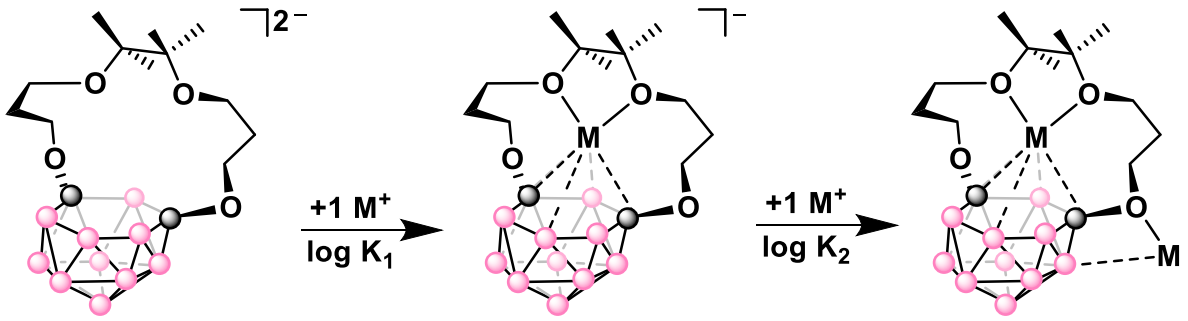

Scheme 3.4. Stepwise metal binding for 2 metals binding to **^{14C4}Cb^{2-}**.

We performed CV metal titrations in triplicate using a 2.9 mM solution of **^{14C4}Cb** with varied equivalents of either LiTFAB, $NaPF_6$, or KPF_6 in DME alongside 0.1 M $[Bu_4N][PF_6]$ electrolyte (Figure 3.12a-i).

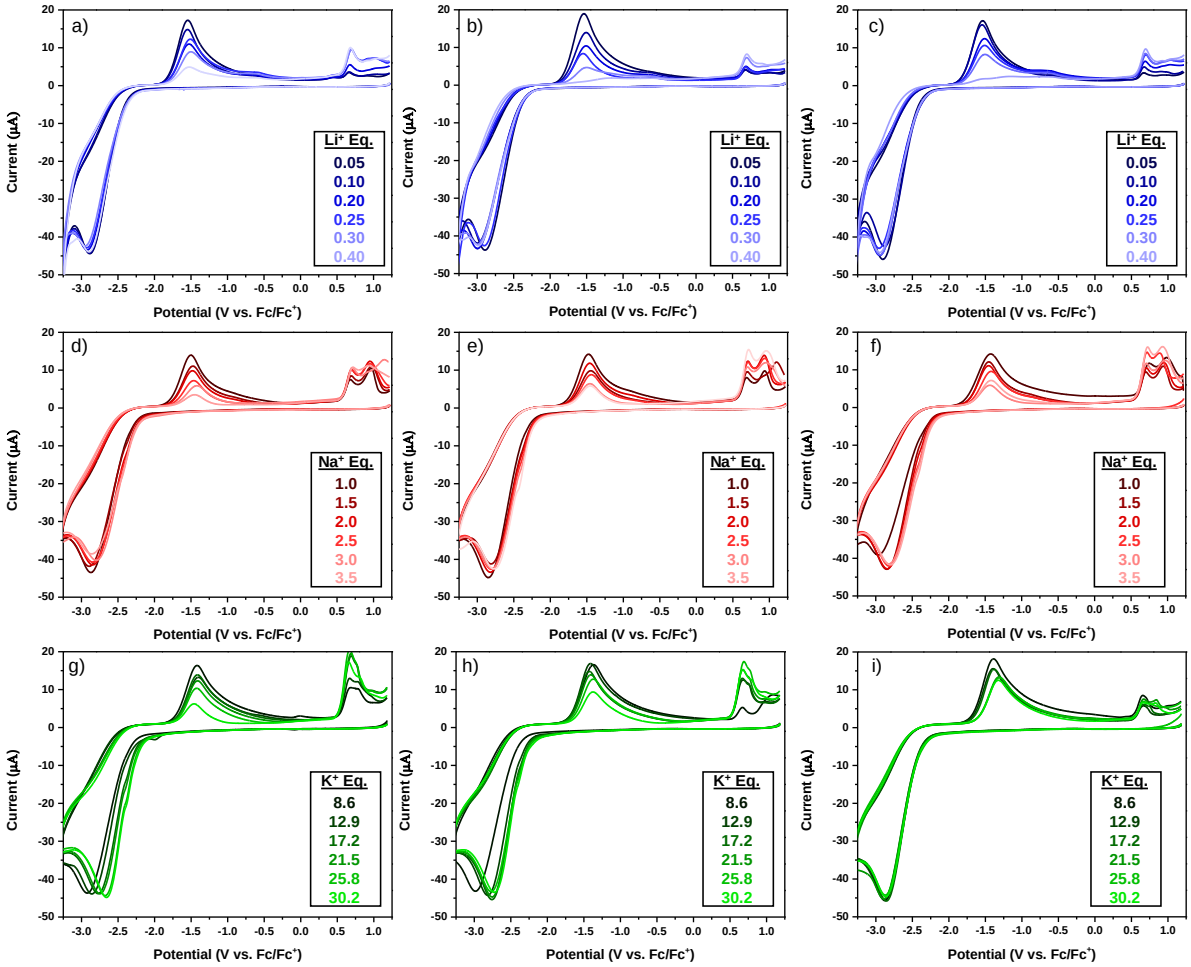

Figure 3.12. CV of 2.9 mM **^{14C4}Cb** with alkali metal titrations. a-c) Concentrations of Li^+ added: 0.145 mM, 0.29 mM, 0.58 mM, 0.725 mM, 0.87 mM, 1.16 mM. a) Li^+ Trial 1 b) Li^+ Trial 2 c) Li^+ Trial 3 d-f) Concentrations of Na^+ added: 2.9 mM, 4.35 mM, 5.8 mM, 7.25 mM, 8.7 mM, 10.15 mM. d) Na^+ Trial 1 e) Na^+ Trial 2 f) Na^+ Trial 3 g-i) Concentrations of K^+ added: 25 mM, 37.5 mM, 50 mM, 62.5 mM, 75 mM, 87.5 mM. g) K^+ Trial 1 h) K^+ Trial 2 i) K^+ Trial 3

Mixing Li^+ with **^{14C4}Cb** rapidly diminished the oxidation of **^{14C4}Cb^{2-}** at -1.56 V (Figure 3.12a-c), becoming almost non-existent once 0.40 equivalents of Li^+ are added. Only 0.40 equivalents were needed to suppress the *nido* oxidation because Li^+ mass transport towards the working electrode occurred. Fitting the CV data with Li^+ to Equation 3.8 yielded a log K of 6.8 ± 0.6 with a stoichiometry of 2.1 ± 0.2 (Figure 3.13). Similarly, mixing Na^+ with **^{14C4}Cb**

also resulted in a decreased oxidation of ^{14C4}**Cb**$^{2-}$ (Figure 3.12d-f), albeit at much higher concentrations, requiring 3.5 equivalents of Na^+ to substantially suppress the oxidation. Fitting the CV data with Na^+ to Equation 3.8, we determined a log K of 3.7 ± 0.2 with 1.6 ± 0.1 Na^+ ions binding to ^{14C4}**Cb**$^{2-}$ (Figure 3.13). We observed much weaker binding with K^+ (Figure 3.12g-i) and a prominent *nido*-carborane oxidation peak still exists even with 30.2 equivalents of K^+. The CV data with K^+ was fit to Equation 3.8 which resulted in a log K of 1.7 ± 0.2 and a stoichiometry of 1.6 ± 0.1(Figure 3.13).

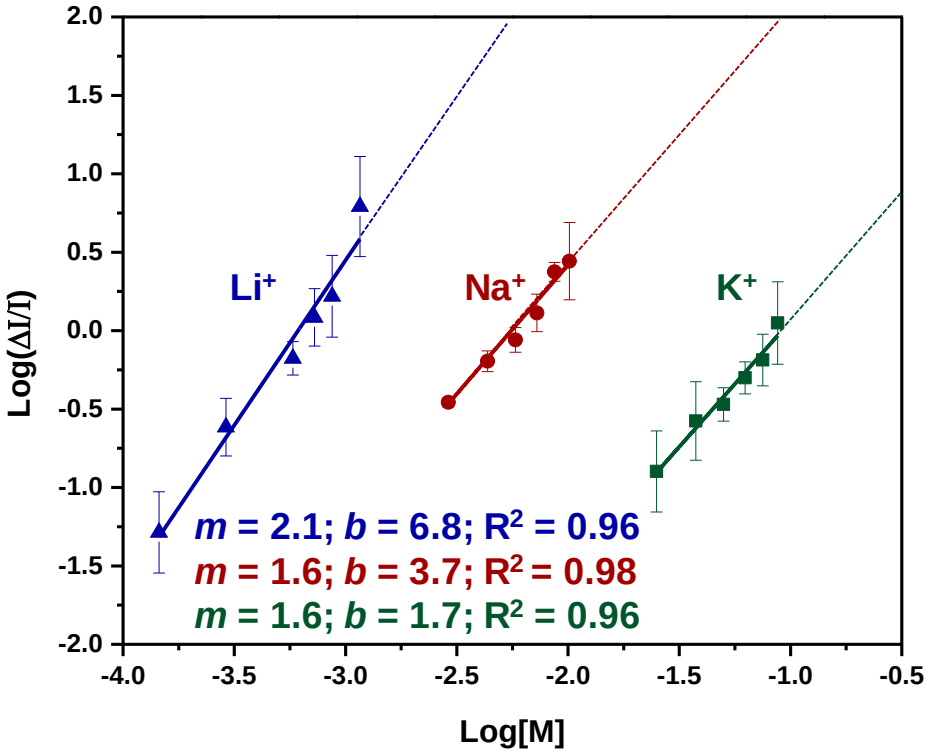

Figure 3.13. Linear Regressions for determination of Log K. Blue triangle – Li+. Red circle – Na+. Green square – K+.

From the binding constant measurements presented herein, ^{14C4}**Cb**$^{2-}$ appears to bind to 2 Li^+ compared to only 1.5 Na^+ and 1.5 K^+, likely due to the smaller ionic radius of Li^+. A stoichiometry of 1.5 suggests that the first metal binds in the crown cavity and the second

metal is bound between two ^{14C4}**Cb**$^{2-}$ units, as depicted in the solid-state crystal structure of **K**$_2$^{14C4}**Cb** (Figure 3.1). While we suspect that the binding of the first alkali metal is much more exergonic than the second binding event, the timescale of our experiments made deconvoluting the multiple binding events difficult.

We benchmarked the proposed binding constant values by addition of competing commercial complexing agents – 12-crown-4 or 18-crown-6. A CV of ^{14C4}**Cb** with 0.3 equivalents of Li^+ and 0.7 equivalents of 12-crown-4 demonstrate that the diminished peak oxidation current of ^{14C4}**Cb**$^{2-}$ does not recover (Figure 3.14a). This suggests that ^{14C4}**Cb**$^{2-}$ outcompetes 12-crown-4 for Li^+ complexation which is consistent with the obtained log K value. Similarly, a CV of ^{14C4}**Cb** with 30 equivalents of K^+ and 30 equivalents of 18-crown-6 shows that the peak oxidation current of ^{14C4}**Cb**$^{2-}$ is restored (Figure 3.14b). Affirmatively, 18-crown-6 (log K = 4.21)[48] complexes K^+ more strongly than ^{14C4}**Cb**$^{2-}$. Notably, using 2.2.2 cryptand instead of 18-crown-6 interferes with the observed carborane redox behavior. We advise against performing electrochemical competition experiments with cryptands.

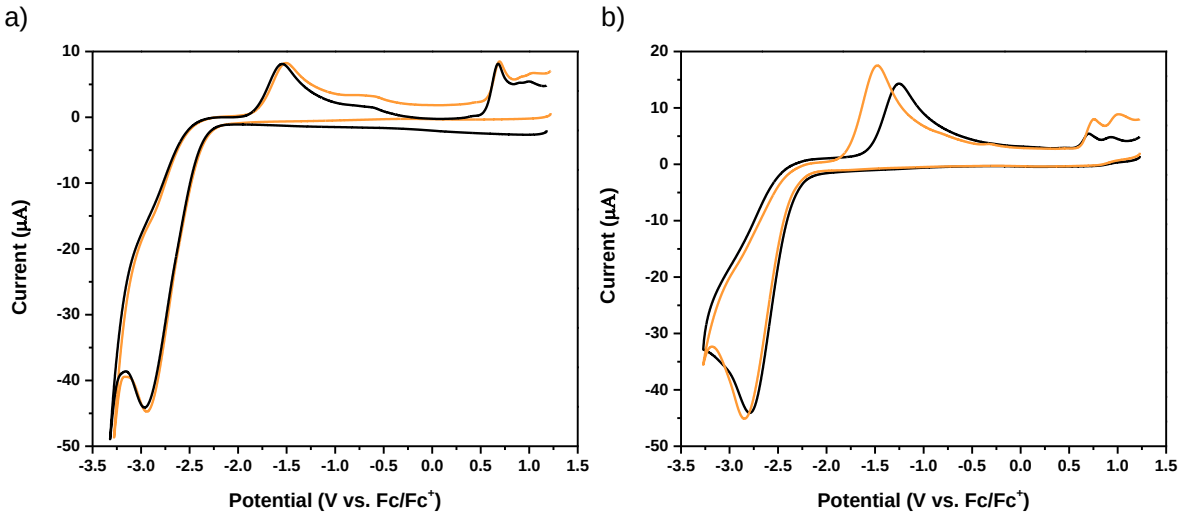

Figure 3.14. CVs of 2.9 mM ^{14C4}**Cb** with competing commercial crown-ethers and alkali metals. a) Black – 0.87 mM Li^+. Orange – 0.87 mM Li^+ and 1.74 mM 12-crown-4. b) Black

– 87 mM K^+. Orange – 87 mM K^+ and 87 mM 18-crown-6. Data collected using a 0.1 M $[Bu_4N][PF_6]$ DME electrolyte solution with a glassy carbon working electrode, Pt wire counter electrode, and $Ag_{(s)}$/AgOTf reference electrode.

3.2.4. Electrochemical Simulations

Parallel to the analytical equilibrium binding model, we analyzed the voltammetry data from the **^{14C4}Cb-**alkali metal solutions by simulating these CVs and determined the log K values independent of Equation 3.8. DigiSim version 3.03b was used to simulate voltammetry experiments.[49] We first simulated the CVs of **^{14C4}Cb** in absence of alkali metals at variable scan rates to converge to the electrochemical parameters of the **^{14C4}Cb**-**^{14C4}Cb^{2-}** redox (Figure 3.15a). Interestingly, we found the very broad reduction and oxidation events of **^{14C4}Cb** are best modeled by an ECEC mechanism (Figure 3.15b). In this mechanism, the neutral *closo* species is reduced to a *closo*$^{2-}$ dianion that undergoes rapid C–C bond scission to generate the *nido*$^{2-}$ dianion. During the reverse sweep, the *nido*$^{2-}$ dianion oxidizes to a short-lived neutral *nido*^{0} species that rapidly reforms the cage C–C bond to revert into the *closo* species.

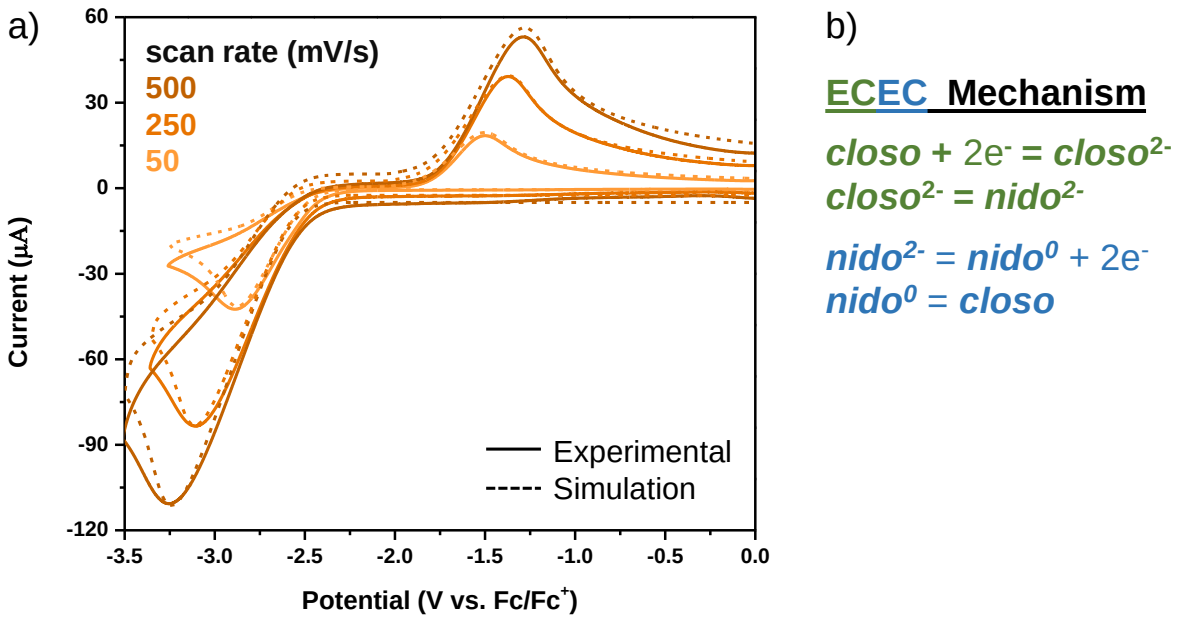

Figure 3.15. Simulated CVs of metal-free ^{14C4}**Cb**. a) Simulated (dashed) and experimental CVs of 2.9 mM ^{14C4}**Cb** (solid) at 50 mV/s, 250 mV/s, and 500 mV/s. b) The ECEC mechanism for modeling metal-free CVs of ^{14C4}**Cb**.

We determined the fitting parameters – the heterogenous electron transfer rates (k_o), charge transfer coefficients (α), diffusion coefficients (D) etc. and input these parameters for further CV simulations, now in presence of varying equivalents of alkali metals (Section 3.4.7). Simulations suggest that ^{14C4}**Cb**$^{2-}$ undergoes stepwise complexation reactions with alkali metals (M^+), adding two chemical steps to the ECEC mechanism to create an ECCCEC mechanism (Figure 3.16).

EC CC EC Mechanism

$$closo + 2e^- = closo^{2-}$$

$$closo^{2-} = nido^{2-}$$

$$nido^{2-} + M^+ = Mnido^-$$

$$Mnido^- + M^+ = M_2nido$$

$$nido^{2-} = nido^0 + 2e^-$$

$$nido^0 = closo$$

Figure 3.16. Proposed ECCCEC mechanism for simulations with metal binding.

We entered the bulk solution concentrations of Li^+, Na^+ or K^+ used experimentally, alongside diffusion coefficients for each cation reported from literature.[50-52] Accordingly, the equilibrium of the forward versus backwards chemical reaction (k_f/k_b) was optimized and the binding constant (K) for each metal was obtained by fitting simulated voltammetry to experimental voltammetry. From these CV simulations, we determined log K values of $^{14C4}\mathbf{Cb}^{2-}$ for Li^+ (log K = 8, Figure 3.17), Na^+ (log K = 4.9, Figure 3.18), and K^+ (log K = 2.2, Figure 3.19). The simulations model two binding events (the **CC** in EC**CC**EC); thus, the overall log K is the summation of **CC**. The simulated values follow the same trend as the analytical binding model with a binding preference for Li^+ over Na^+ and K^+. Additionally, the simulated log K values per metal cation match well with experimental values (Table 3.1).

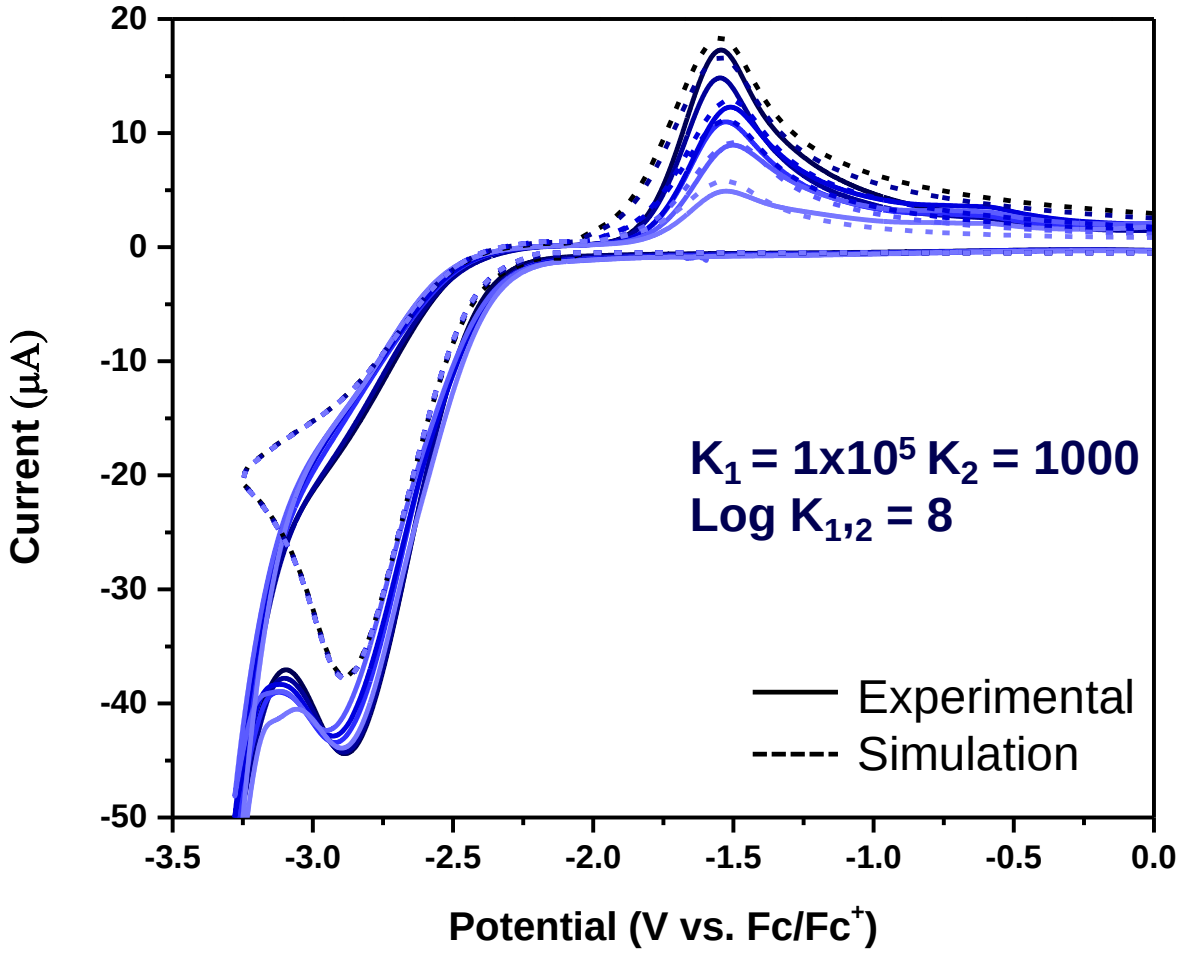

Figure 3.17. Simulated voltammetry of **^{14C4}Cb** with Li^+ (0.145 mM, 0.29 mM, 0.58 mM, 0.725 mM, 0.87 mM, 1.16 mM). Simulated using a k_f of 300 and 1, and $K_1 = 1 \times 10^5$ and $K_2 = 1000$.

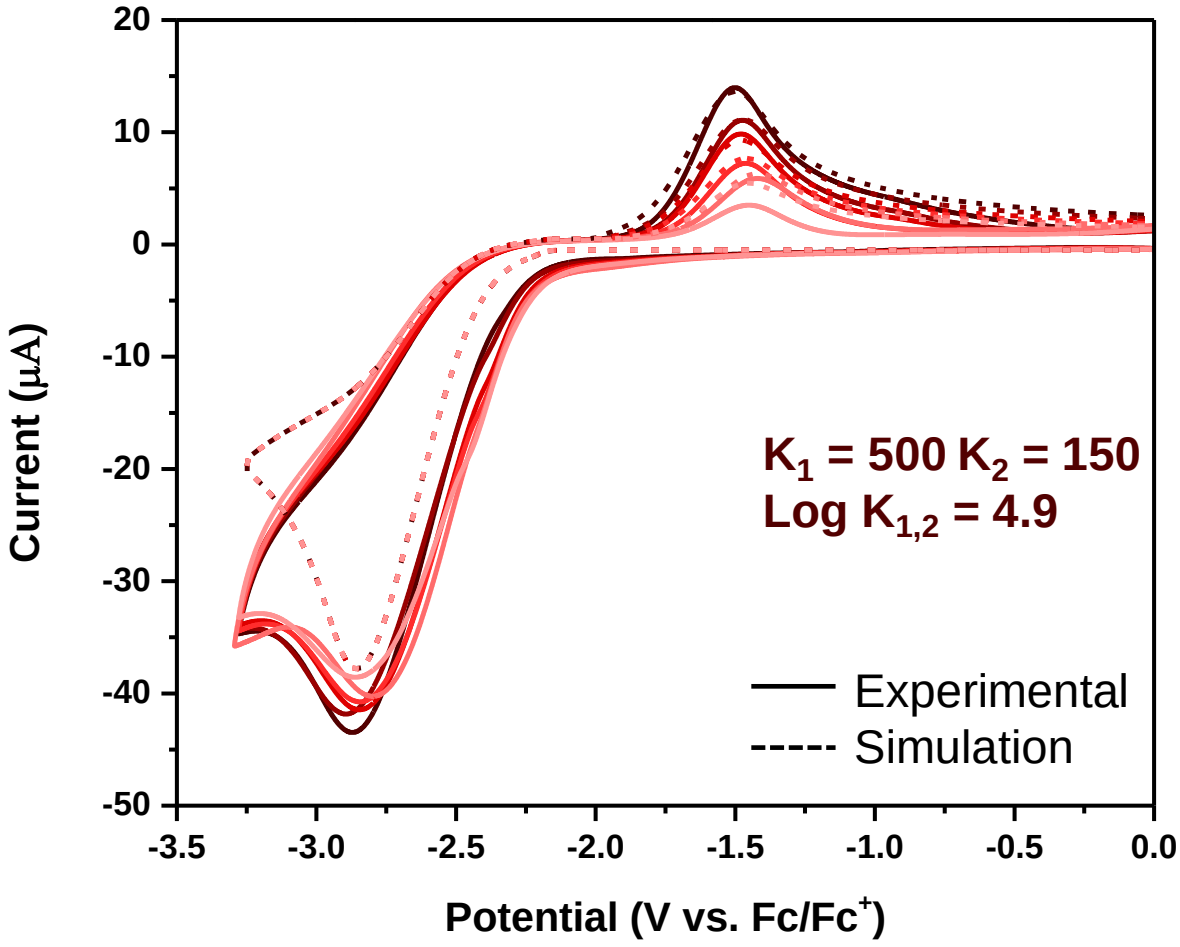

Figure 3.18. Simulated voltammetry of **^{14C4}Cb** with Na^+. (2.9 mM, 4.35 mM, 5.8 mM, 7.25 mM, 8.7 mM, 10.15 mM). Simulated using a k_f of 5 and 1.5, and K_1 = 500 and K_2 = 150.

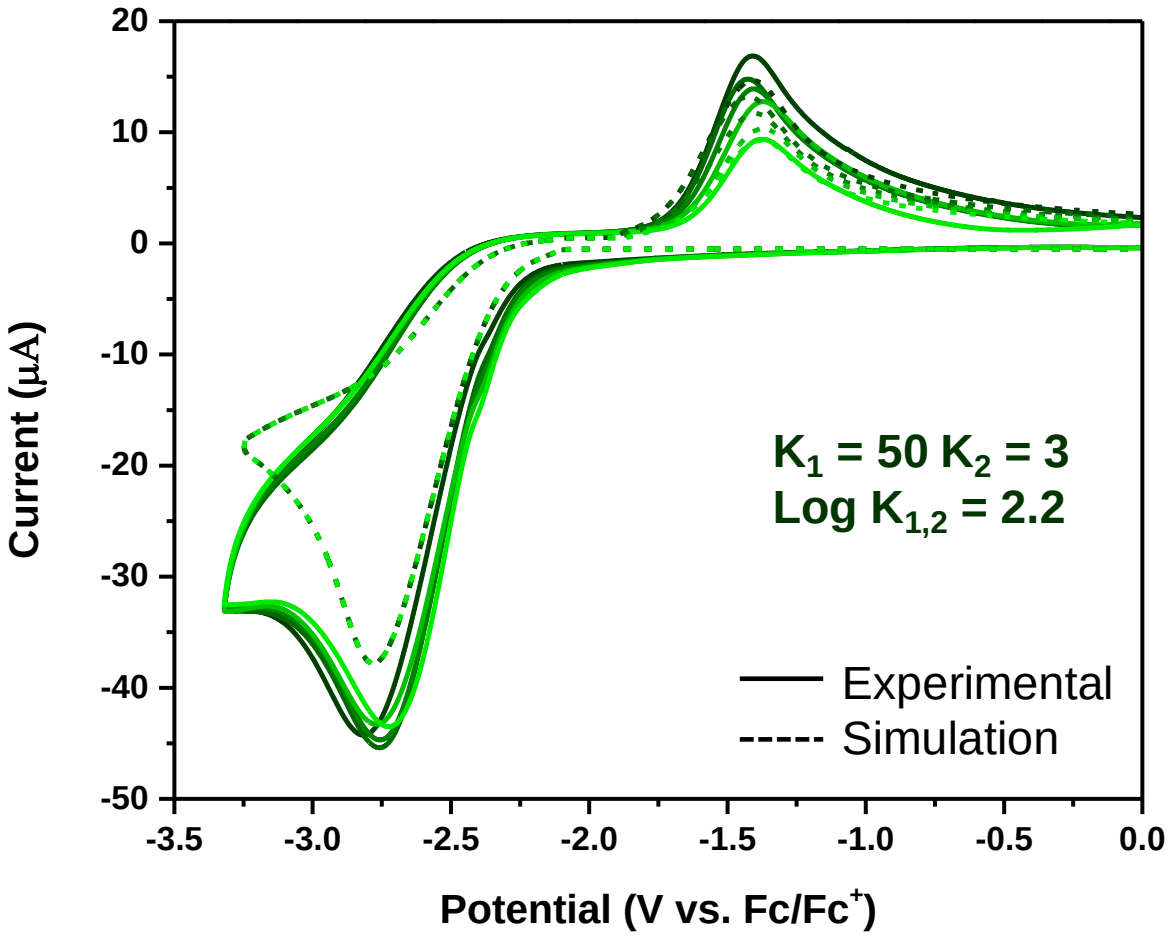

Figure 3.19. Simulated voltammetry of ^{14C4}**Cb** with K^+. (37.5 mM, 50 mM, 62.5 mM, 75 mM, 87.5 mM). Simulated using a k_f of 0.3 and 0.1, and $K_1 = 50$ and $K_2 = 3$.

Looking into the concentration profiles of each chemical species as a function of time and position using Digisim at this juncture informed us about the limitations of the equilibrium binding model described earlier (Equation 3.8). Under the simulated model, the electrogenerated ^{14C4}**Cb**$^{2-}$ rapidly binds to Li^+, depleting nearly all the free Li^+ proximate to the electrode surface under the bulk solution Li^+ concentrations used (~0.4 eq). This led to significant mass transport of free Li^+ to the electrode where it was coordinated by the ^{14C4}**Cb**$^{2-}$ generated at the electrode.

This concentration gradient explained several observations with the CVs of the **^{14C4}Cb**-Li^+ system. The *nido* to *closo* oxidative current is entirely suppressed by the time just 0.5 eq of bulk Li^+ is present in solution; this is possible because additional free Li^+ away from the electrode rapidly diffuses towards the electrode**.** In simulations where we hypothetically assumed that Li^+ diffusion coefficient was more rapid by a factor of 10, we found merely 0.25 equiv. of Li^+ would eliminate the *nido* to *closo* oxidation wave (Figure 3.20). Thus, the Li^+ to **^{14C4}Cb^{2-}** binding constant is too large to compute accurately. The obtained value here is a lower limit for log K because the diffusion of Li^+ dictates the relative loss of *nido* to *closo* oxidative current instead of the precise value of the Li^+-**^{14C4}Cb^{2-}** binding constant.

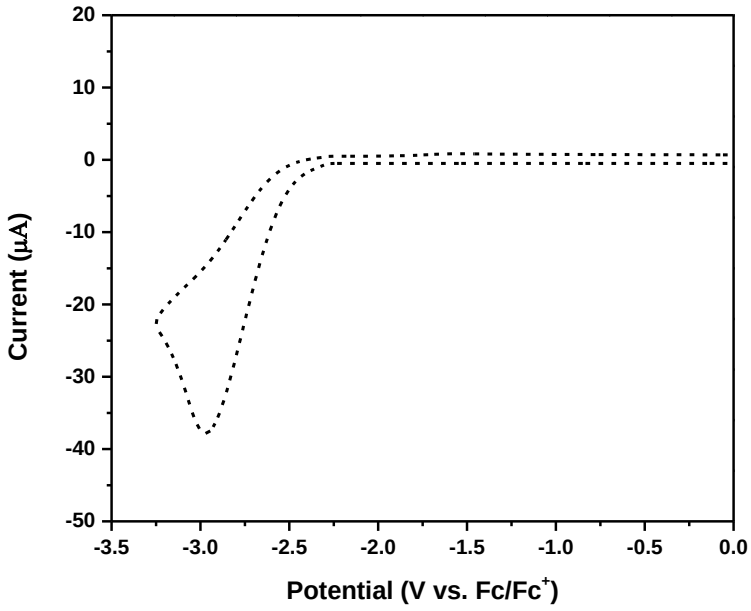

Figure 3.20. Simulated (dashed) CV of **^{14C4}Cb** with 0.725 mM of Li^+ with a hypothetical increased Li^+ diffusion coefficient of 1.5 x 10^{-4} cm^2/s (10-fold increase).

For the cases of Na^+ and K^+, the concentrations of the alkali metals were significantly greater than the concentrations of the **^{14C4}Cb^{2-}**, hence the simulations show negligible changes

in the concentration of these cations, and the loss of *nido*- to *closo*- oxidation current is reflective of the values of the binding constant to these metals.

Table 3.1. Log K binding values of **^{14C4}Cb** with Li^+, Na^+, or K^+ determined through experimental, simulated, or calculated methods.

Alkali Metal	Experimental Method			Simulated Method	
M^+	Total Log K	Stoichiometry	Log K per M^+	Total Log K	Log K per M^+
Li^+	6.8 ± 0.6	2.1 ± 0.2	3.4[a]	8	4
Na^+	3.7 ± 0.2	1.6 ± 0.1	2.4[b]	4.9	2.45
K^+	1.7 ± 0.2	1.6 ± 0.1	1.1[b]	2.2	1.1

[a]Calculated assuming metal binding stoichiometry rounded to 2. [b]Calculated assuming metal binding stoichiometry rounded to 1.5.

Using the same simulation parameters as reported in Section 3.4.7. unless otherwise stated, we simulated **^{14C4}Cb** with 0.87 mM LiTFAB at fast scan rates of 1V/s and 2V/s where Li^+ is no longer fully depleted near the electrode. The increased peak to peak separation at fast scan rates was better modeled by a heterogenous charge transfer rate k_o of $1x10^{-4}$ for the *closo* and *nido* redox events. The CV was scanned from 1.25 V to -3.87 V or -3.93 V and back with a potential step of 0.001 V and a scan rate of 1 V/s or 2 V/s respectively. The simulations at 1 V/s and 2 V/s demonstrated that at faster scan rates, the mass transport of Li^+ no longer hinders the chemical reaction with **^{14C4}Cb^{2-}**. We paired these simulations with experimental CVs and obtained a log K of 8, consistent with the value obtained at slower scan rate, 50 mV/s (Figure 3.21).

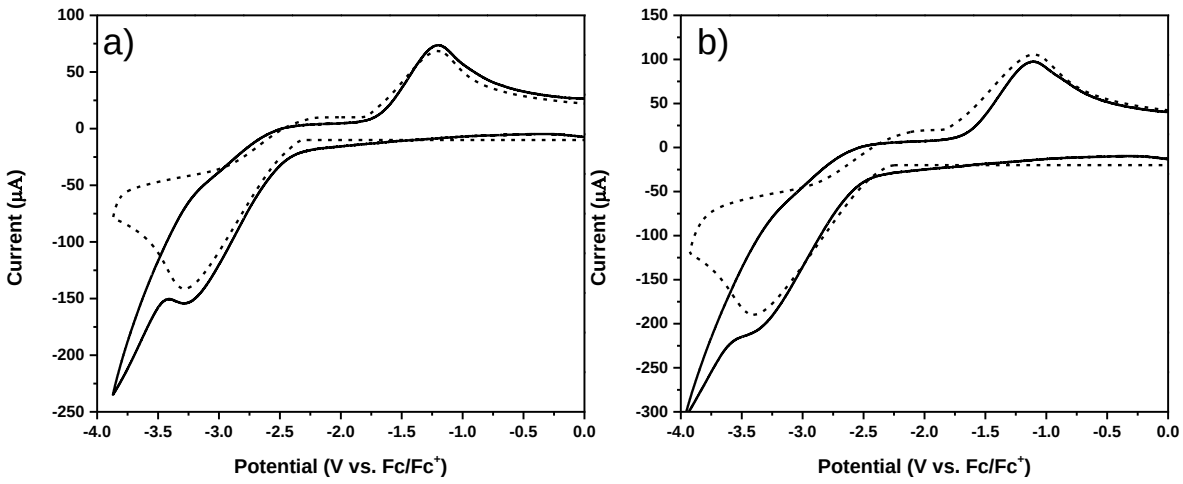

Figure 3.21. Simulated CVs of **^{14C4}Cb** with 0.87 mM Li^+ at fast scan rates. Simulated (dashed). Experimental (solid). a) 1 V/s b) 2 V/s

3.2.5. Limitations to Method

We have derived a binding model (Equation 3.8) for redox-active complexing agents undergoing an EC or ECE mechanism. The experimental method, performed in triplicate, suggests an error of approximately 10% of the true value. The accuracy of this does not compete with traditional ^{1}H NMR binding methods. However, it allows for obtaining log K values that would be otherwise unattainable due to synthetic challenges and complexities of multiple coordination environments. The experimental binding model does not account for mass transport of the cations, an integral component on the timescale of a CV. We suggest that the experimental method be paired with simulated CVs for obtaining a modeled concentration gradient to verify that the reagent is not fully depleted at the electrode surface. Furthermore, we advise performing the CV titration experiments in triplicate because the peak oxidation currents obtained herein vary with each scan. The simulated voltammetry method using DigiSim 3.0b is limited by stepwise chemical reactions which increases the complexity

of the modelled system. Additionally, the simulations are limited by the sensitivity of the software and its ability to converge on values.

3.2.6. 18-crown-6-*o*-carborane

We expanded alkali metal selectivity experiments to a different crown-ether carborane, 18-crown-6-*o*-carborane (**^{18C6}Cb**). **^{18C6}Cb** was prepared analogously to **^{14C4}Cb** by deprotonating diol-*o*-carborane with potassium hydride in THF (Scheme 3.5). The reaction was subsequently filtered over celite and taken to dryness. It was then redissolved in DMF and heated at 75 °C with commercial pentaethylene glycol di(*p*-toluenesulfonate) overnight to afford **^{18C6}Cb** (Scheme 3.5).

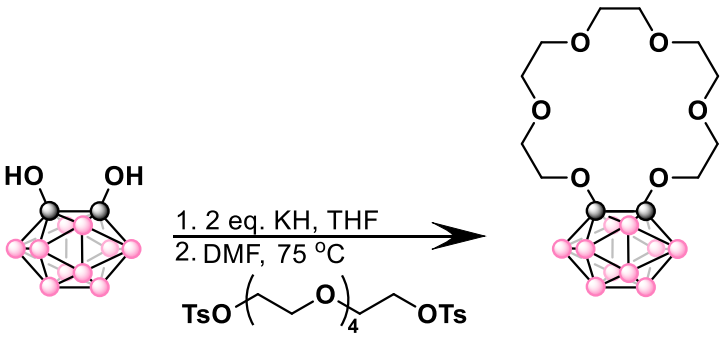

Scheme 3.5. Synthesis of 18-crown-6-*o*-carborane.

We acquired a CV of 2.9 mM **^{18C6}Cb** in 0.1 M [Bu_4][PF_6] DME and observed a chemically reversible 2 e^- redox with a formal potential of $E_{1/2}$ = -2.09 V vs $Fc^{+|0}$ (Figure 3.22a). Similar to **^{14C4}Cb**, the large difference between the peak reductive potential (E_{red} = -2.80 V) and the peak oxidative potential (E_{ox} = -1.39 V) suggests significant structural and solvation shell reorganization which may be explained in part by *nido* cage rearrangement.

Next, we acquired the CVs of solutions containing **^{18C6}Cb** with 2 equivalents of alkali metals, K^+, Na^+, and Li^+ (Figure 3.22b). The CV of **^{18C6}Cb** with KPF_6 displayed an anodic

shift in peak reductive potential E_{red} by 516 mV (E_{red} = -2.28 V) and a cathodic shift in peak oxidative potential E_{ox} by 36 mV (E_{ox} = -1.43 V), becoming more reversible (Figure 3.22b). The *nido* peak oxidation current increased in current response by 20% compared to the metal-free CV. In totality, this likely indicates that *closo* **^{18C6}Cb** binds strongly towards K^+ and the preferred conformation for K^+ binding is *closo*-carborane instead of *nido*-carborane **^{18C6}Cb^{2-}**. With 2 equivalents of Na^+, we observed an anodic shift in peak reductive potential E_{red} by 172 mV (E_{red} = -2.63 V) and an anodic shift in peak oxidative potential by 26 mV (E_{ox} = -1.36 V) (Figure 3.22b). The peak oxidative current decreased by 68% which suggests that *nido*-carborane, **^{18C6}Cb^{2-}** binds more strongly towards Na^+ than its counterpart, **^{14C4}Cb^{2-}**, which only had a 31% decrease in anodic current under the same conditions (Figure 3.10b). Affirmatively, commercial 18-crown-6 coordinates Na^+ more strongly than 14-crown-4.[25, 53] The CV of **^{18C6}Cb** with 2 equiv. of LiTFAB displayed a similar anodic shift in peak reductive current E_{red} by 140 mV (E_{red} = -2.66 V) (Figure 3.22b). Shockingly, the *nido* oxidation near -1.39 V completely vanishes with 2 equivalents of Li^+. This implies that **^{18C6}Cb^{2-}** also binds very strongly to Li^+, similar to the redox behavior observed for **^{14C4}Cb^{2-}**. A mixed-metal CV with 2 equivalents of Li^+, Na^+, and K^+ displayed a large anodic shift in the peak reductive current E_{red} by 571 mV (E_{red} = -2.23 V) and the complete disappearance of the *nido* oxidation. This suggests that **^{18C6}Cb** first binds to K^+ in *closo* form but upon electrochemically forming *nido*-carborane species, the K^+ is likely displaced by Li^+ and Na^+ to become electrochemically inactive in the selected electrochemical window. We suggest that smaller crown sizes (12-crown-4 and 14-crown-4) be utilized for selective Li^+ capture and release since *closo*-carborane **^{18C6}Cb** binds exceedingly well towards K^+.

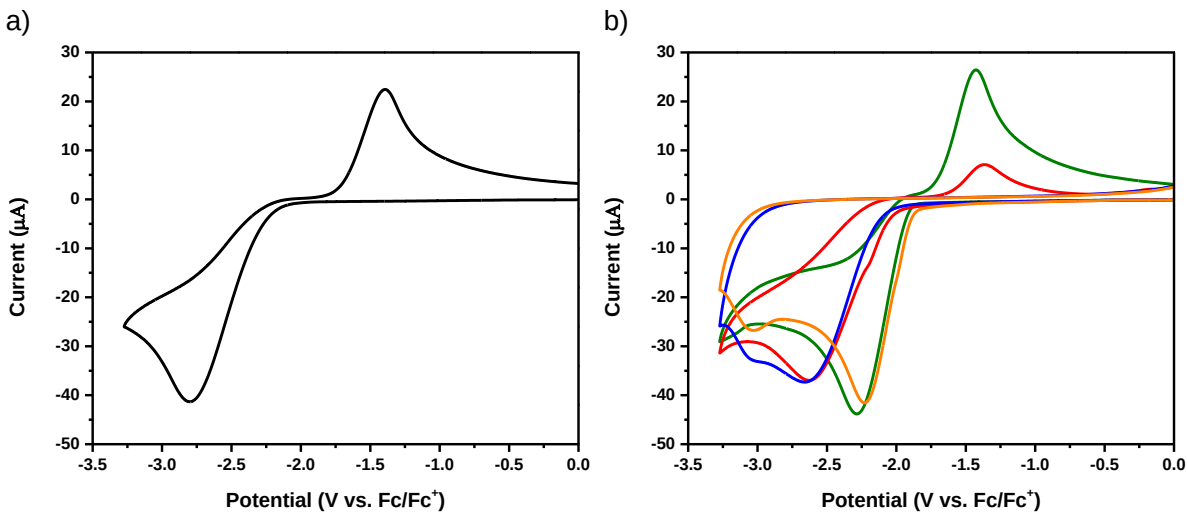

Figure 3.22. CV of 2.9 mM **^{18C6}Cb** with 2 equiv. of alkali metals. a) metal-free b) with 2 equiv. metals. K^+ – Green. Na^+ – Red. Li^+ – Blue. Orange – K^+, Na^+ and Li^+. A glassy carbon working electrode, Pt wire counter electrode, and $Ag_{(s)}$/AgOTf reference electrode were used.

3.3. Summary

We have described the synthesis of a new, size-selective redox-switchable crown-ether complexing agent – 1,2-((6,6,7,7-Me_4)14-crown-4)-*o*-carborane. The structural change from **^{14C4}Cb** to **K_2^{14C4}Cb** upon chemical reduction demonstrated C–C bond cleavage and cage rearrangement. Structural studies revealed that K^+ inside of the crown cavity further interacts with the carboranyl cage via cation-π interactions. The binding of **^{14C4}Cb** towards Li^+ was probed through standard ^{1}H and ^{7}Li NMR techniques. Only negligible shifts were observed in the presence of Li^+, indicating very weak binding. **^{14C4}Cb^{2-}** was electrochemically generated via bulk electrolysis and ^{7}Li NMR binding studies revealed extreme quadrupolar broadening and multiple coordination environments, qualitatively suggesting a strong Li^+ interaction.

Alkali metal binding with **^{14C4}Cb** was further studied by electrochemical methods. The CV of **^{14C4}Cb** demonstrated a chemically reversible $2e^-$ redox event with a formal reduction

potential of $E_{1/2}$ = -2.20 V. With increasing equivalents of alkali metal (Li^+, Na^+, K^+), the peak anodic current was suppressed suggesting that *in situ* $^{14C4}\mathbf{Cb}^{2-}$ undergoes a competing chemical reaction with alkali metals. We have derived a new binding model (Equation 3.8) for redox-active complexing agents undergoing an EC or ECE mechanism through observed experimental phenomena paired with simulated voltammetry. The binding affinity of $^{14C4}\mathbf{Cb}^{2-}$ suggests a size-selective preference for smaller cations following the trend: Li^+ (log K = 3.4 – 4) > Na^+ (log K = 2.4) > K^+ (log K = 1.1). Simulated voltammetry revealed that mass transport of Li^+ limits the derived binding constants via experimental methods which neglect diffusion towards the electrode surface.

3.4. Experimental

3.4.1. Materials and Physical Measurements

All manipulations were performed under an atmosphere of dry, oxygen-free N_2 or Ar by means of standard Schlenk or glovebox techniques (MBraun equipped with a -38 °C freezer, or VAC gloveboxes). Molecular sieves (3Å, Fisher) were activated by heating (~200 °C) under a dynamic vacuum (<40 mtorr) overnight and brought into the glovebox. Hexanes, pentane, DCM, diethyl ether, THF and benzene were dried on an MBraun solvent purification system. Glyme, DMF, and acetonitrile were dried over CaH_2 for several days prior to distillation. All solvents were stored over molecular sieves (3Å, Fisher). All deionized water was obtained from a MilliQ purifier with a resistivity of 18.2 MΩ.cm.

Ortho-carborane was purchased from Boron Specialties and sublimed before use. Potassium hydride was purchased from Sigma Aldrich and washed with hexanes prior to use. Tetrabutylammonium hexafluorophosphate was purchased from Oakwood Chemicals and purified twice by dissolving in hot ethanol and precipitating out with deionized water and

washed with additional deionized water then dried at 100°C under vacuum for 24 h. Lithium hexafluorophosphate was purchased from TCI Chemicals and recrystallized before use. Potassium hexafluorophosphate was purchased from Matrix Scientific and recrystallized prior to use. Sodium hexafluorophosphate was purchased from Acros Organics and used as received. Lithium tetrakis(pentafluorophenyl)borate ethyl etherate (LiTFAB) was purchased from Sigma Aldrich and used as received.

Physical Measurements

NMR spectra were obtained in a Bruker Avance NEO 500 MHz or Agilent Technologies 400 MHz spectrometer, and referenced to residual solvent resonances of chloroform ($CDCl_3$), tetrahydrofuran (C_4D_8O), DME ($C_4H_{10}O_2$) or externally (^{11}B: 85% $(Et_2O)BF_3$, ^{7}Li: 9.7 M $LiCl/D_2O$). Chemical shifts (δ) are recorded in ppm.

Elemental analyses (C, N, H) were recorded at the University of California, Santa Barbara using an Exeter Analytical CE440 elemental analyser for air stable compounds. Elemental analyses (C, N, H) for air-sensitive compounds were recorded at University of California, Berkeley using a ThermoFisher Flash Smart Elemental analyzer.

X-ray crystallography data were collected at the University of California, Santa Barbara on a Bruker KAPPA APEX II diffractometer equipped with an APEX II CCD detector using a TRIUMPH monochromator with a Mo Kα X-ray source (wavelength α = 0.71073 Å). The crystals were mounted on a cryoloop under Paratone-N oil, and all data were collected at 100(2) K using an Oxford nitrogen-gas cryostream system. A hemisphere of data was collected using ω scans with 0.5° frame widths (ω, angle between the X-ray source and the sample). Data collection and cell-parameter determination were conducted using the SMART program. Integration of the data frames and refinement of the final cell parameters were

performed using SAINT software. Absorption correction of the data was carried out using SADABS. Structure determination was done using direct or Patterson methods and difference Fourier techniques. All hydrogen atom positions were idealized and rode on the atom of attachment. Structure solution, refinement, graphics, and creation of publication materials were performed using SHELXTL or OLEX.

Cyclic voltammetry was performed using a CH Instruments Electrochemical Analysis potentiostat, equipped with a 3-mm-diameter glassy carbon working electrode, 5 mM Ag/AgOTf reference electrode (BASi, non-aqueous reference electrode kit) and a Pt-wire counter electrode using a $[Bu_4N][PF_6]$ (0.1 M) solution as the supporting electrolyte. Cyclic voltammograms were referenced to Fc/Fc^+ redox couple. The glassy carbon working electrode was polished between each scan with diamond slurry (3 µm, 1 µm, 0.25 µm and 0.05 µm, Buehler MetaDiTM Supreme) on polishing pads (Buehler MasterTex) for 2 minutes per pad and sonicated in DI water for ~ 5 s. The Pt-wire counter electrode was rinsed with acetone and heated until bright red with a propane flame.

Galvanostatic Bulk Electrolysis cycling experiments were carried out using a Biologic VMP3 potentiostat/galvanostat and carried out inside a nitrogen glovebox. The full experimental setup for electrolysis experiments is described in section 3.

UV-Visible Spectroscopy was performed using an Agilent 8543 UV-Visible Spectrophotometer with screw top quartz cuvettes supplied from Starna Cells Inc.

3.4.2. Synthesis of Compounds

Precursor 1,2-diol-*o*-carborane was prepared using literature methods.[30] The precursor tosyl linker, 2,3-bis(3-[p-toluenesulfonyloxy]propoxy)-2,3-dimethylbutane was prepared using literature procedures.[27]

1,2-((6,6,7,7-Me$_4$)14-crown-4)-*o*-carborane (^{14C4}**Cb)**

Under inert atmosphere, $CbOH_2$ (0.360 g, 2.05 mmol, 1 eq.) dissolved in 5 ml THF and cooled to -25°C. To this, a suspension of KH (0.168 g, 4.2 mmol, 2.05 eq.) in THF was added and the resulting pale, yellow solution was stirred for 0.5 h at RT. All volatiles were removed under reduced pressure and then the reaction was redissolved in minimal DMF. To this, 2,3-bis(3-[p-toluenesulfonyloxy]propoxy)-2,3-dimethylbutane (1.11 g, 2.05 mmol, 1 eq.) in 10 mL of DMF was added dropwise. The solution stirred overnight at 80°C. Then, the volatiles were removed under reduced pressure. The residue was redissolved in DCM and washed with water and brine. It was dried over anhydrous $MgSO_4$ and filtered. The solvent was removed and the residue was purified by column chromatography (5% ethyl acetate / 95% hexanes). Yield: (0.250 g, 32.8%) Single crystals suitable for XRD studies were obtained by recrystallization from saturated diethyl ether solution at −25 °C.

^{1}H NMR (500 MHz, $CDCl_3$) δ 3.96 (t, *J* = 5.4 Hz, 4H), 3.54 (t, *J* = 6.3 Hz, 4H), 1.83 (p, *J* = 6.1 Hz, 4H), 1.14 (s, 12H). **^{1}H NMR (500 MHz, $CDCl_3$)** δ 3.96 (t, *J* = 5.3 Hz, 4H), 3.54 (t, *J* = 6.3 Hz, 4H), 2.50 (s, 1H), 2.33 (s, 2H), 1.90 (s, 1H), 1.83 (p, *J* = 6.1 Hz, 4H), 1.77 (s, 1H), 1.14 (s, 12H). **^{11}B{^{1}H} NMR (160 MHz, CD_3CN)** δ -13.08, -13.95, -15.10, -17.80. **^{11}B NMR (160 MHz, CD_3CN)** δ -12.65, -13.57, -14.60, -15.59, -17.31, -18.26. **^{13}C NMR (126 MHz, CD_3CN)** δ 109.26, 80.56, 73.02, 58.14, 30.60, 21.50. *Anal. Calcd.* for $B_{10}C_{14}O_4H_{34}$: C, 44.90; H, 9.15. *Found*: C, 45.27; H, 9.26.

K_2[1,2-((6,6,7,7-Me$_4$)14-crown-4)-*o*-carborane] ($K_2{}^{14C4}$**Cb)**

Naphthalene (0.16 g, 0.13 mmol, 2 eq.) was dissolved in dry THF and cooled to -78°C. Excess solid K was added and the reaction stirred at RT for 0.5 h. The deep green solution was filtered over a celite plug, and extracted with additional THF. *closo*-(14-crown-4)*o*-carborane was

cooled to -78°C and the potassium naphthalenide solution was added dropwise. The reaction stirred for an hour at RT. The volatiles were removed in vacuo. Then, the reaction was stirred with diethyl ether (5 ml x 3) and decanted. The reaction was dissolved in acetonitrile and filtered through a celite plug. The solution was saturated then recrystallized at -25 °C producing colorless crystals suitable for XRD studies. Yield: (0.023 g, 78%).

^{1}H NMR (500 MHz, CD_3CN) δ 3.96 (t, *J* = 7.6 Hz, 4H), 3.42 (t, *J* = 5.6 Hz, 4H), 1.75 (p, *J* = 6.8 Hz, 4H), 1.10 (s, 12H**).** **^{11}B{^{1}H} NMR (160 MHz, CD_3CN)** δ -8.06, -23.59. **^{11}B NMR (160 MHz, CD_3CN)** δ -8.14, -23.30. **^{13}C NMR (126 MHz, CD_3CN)** δ 81.36, 70.09, 68.23, 58.99, 31.42, 20.39. *Anal. Calcd.* for $K_2B_{10}C_{14}O_4H_{34}$: C, 37.14; H, 7.57. *Found*: C, 37.09; H, 7.28.

Li_2[1,2-((6,6,7,7-Me_4)14-crown-4)-*o*-carborane] (**Li_2^{14C4}Cb**)

K_2^{14C4}Cb (0.0215 g, 0.046 mmol) was dissolved in 1 mL of acetonitrile. LiTFAB (0.0829 g, 0.092 mmol) was dissolved in 1 mL of acetonitrile. It was added to the stirring carborane and stirred for 48 hours. Afterwards, the stirring was discontinued. The reaction was filtered through a celite plug and then taken to dryness, yielding a white powder.

^{1}H NMR (500 MHz, CD_3CN) δ 3.85 (t, *J* = 6.1 Hz, 2H), 3.61 (t, *J* = 5.9 Hz, 2H), 3.54 (t, *J* = 5.6 Hz, 2H), 1.72 (p, *J* = 6.0 Hz, 2H), 1.68 (p, *J* = 5.8 Hz, 2H), 1.15 (s, 6H), 1.13 (s, 6H). **^{11}B{^{1}H} NMR (160 MHz, CD_3CN)** δ -5.91, -12.80, -13.45, -14.03, -15.80. **^{7}Li NMR (194 MHz, CD_3CN)** δ -2.96.

3.4.3. *Closo* NMR binding procedure

Stock solutions of 20 mM **^{14C4}Cb** and 60 mM of lithium hexafluorophosphate ($LiPF_6$) in deuterated THF were prepared. To a glass vial, the desired amount of each stock solution was dispensed using a Hamilton syringe. The sample was then diluted to a final volume of

0.50 mL with deuterated THF. The contents of the vial were thoroughly mixed and transferred to an NMR tube. ^{1}H and ^{7}Li NMR spectra collected on a Bruker Avance NEO 500 MHz. ^{7}Li NMR spectra collected with 128 scans and a 1 second T_1 relaxation delay. The ^{1}H NMR and ^{7}Li spectra were referenced to the residual solvent d-THF peak. The amount of carborane was kept constant for ^{1}H NMR K determination with varied equivalents of Li^{+}.

3.4.4. Galvanostatic Bulk Electrolysis Procedure

Galvanostatic Bulk Electrolysis experiments were carried out using a Biologic VMP3 potentiostat/galvanostat under inert atmosphere. Two-electrode galvanostatic bulk electrolysis (GBE) was performed in a nitrogen glovebox utilizing a two compartment H-cell with a glass frit separator, a stir bar in each compartment, and reticulated vitreous carbon (RVC) foam electrodes for both the working and counter electrodes. The RVC foam electrodes consisted of a ~5 cm steel rod inserted into 100 PPI Duocel® RVC foam core (length ~3 cm; diameter ~3mm), with a tap bore (length ~5 mm; diameter ~2 mm), which was filled with molten gallium to fuse the steel connector to the RVC foam. Each electrode has an end-to-tip resistance of <30 Ω. The RVC electrodes were rinsed with acetone and dried. The Ketjenblack used was dried for 48 h in a 175 °C oven and ground in a glass mortar and pestle under inert atmosphere prior to use.[54]

Reduction (Charging): The counter compartment consisted of 300 mg of Ketjenblack suspended in 8 mL of a 0.1 M solution of $[Bu_4N][PF_6]$ in DME. The working compartment consisted of **^{14C4}Cb** (0.063 mmol, 1.0 equiv) dissolved in 6 mL of a 0.1 M solution of $[Bu_4N][PF_6]$ in DME. A charging current of -140 μA with a -12 C charge cutoff was utilized, resulting in a ca. 100% SOC after 24 h assuming 100% columbic efficiency. Upon completion,

the working compartment solution was monitored by $^{11}B\{^{1}H\}$ NMR spectroscopy to reveal full conversion to [Bu_4N][1,2-((8,9-Me_2)14-crown-4)-*o*-carborane] (**^{14C4}Cb^{2-}**) (Figure 3.6).

UV-Vis Calibration Curve: A 3 mM stock solution of ferrocenium hexafluorophosphate ($FcPF_6$) in 0.1 M [Bu_4N][PF_6] in DME was prepared. Stepwise dilutions were prepared by mass using the density of the solution 0.1 M [Bu_4N][PF_6] in DME, 0.8816 g/mL. The UV-Vis spectra were recorded for 5 different concentrations of $FcPF_6$ with absorbance at 620 nm ranging between 0.1 – 1 for linearity adhering to Beer-Lambert's law (Figure 3.7a). A calibration curve was constructed plotting absorbance at 620 nm versus concentration of $FcPF_6$ and a linear regression analysis was employed (Figure 3.7b). An aliquot of the working compartment solution was then added to a known volume and concentration of ferrocenium hexafluorophosphate in 0.1 M [Bu_4N][PF_6] DME. The absorbance of the solution was measured by UV-Vis. The concentration of $FcPF_6$ remaining was found from the calibration curve and the amount of $FcPF_6$ that reacted with **^{14C4}Cb^{2-}** was used to determine the concentration of **^{14C4}Cb^{2-}** in the working compartment solution. The remaining **^{14C4}Cb^{2-}** solution was utilized for subsequent NMR binding studies.

3.4.5. *Nido* NMR Binding Procedure

A stock solution of 7.64 mM **^{14C4}Cb^{2-}** was prepared with 0.1 M [Bu_4N][PF_6] in DME by bulk electrolysis of **^{14C4}Cb**. A stock solution of 8.3 mM LiTFAB with 0.1 M [Bu_4N][PF_6] in DME was prepared. The desired ratio of **^{14C4}Cb^{2-}** and LiTFAB were dispensed into small vials using Hamilton syringes. Extra solvent, 0.1 M [Bu_4N][PF_6] DME was dispensed so that the total volume equated to 0.50 mL or above. The contents of the vial were mixed thoroughly and transferred to an NMR tube. ^{1}H, ^{7}Li and $^{11}B\{^{1}H\}$ NMR spectra collected on a Bruker Avance NEO 500 MHz. ^{7}Li NMR spectra collected with 128 scans and a 1 second T_1

relaxation delay. The ^{1}H, ^{7}Li, $^{11}B\{^{1}H\}$ NMR spectra were referenced to the residual solvent d_8-THF peak.

3.4.6. Electrochemical Procedures

Randles-Ševčík: CVs of a 2.9 mM solution of **^{14C4}Cb** in 0.1 M $[Bu_4N][PF_6]$ DME was taken at scan rates: 50 mV/s, 100 mV/s, 250 mV/s, 350 mV/s, 500 mV/s. The electrodes consisted of a glassy carbon working electrode, Pt wire counter electrode, and Ag/AgOTf reference electrode. The working electrode was polished between each scan. The peak current, $I_{p,c}$, and $I_{p,a}$, was taken at each scan rate after subtracting a straight line prior to the redox event on OriginPro 9 software. The peak current was plotted versus square root of scan rate. The data was fit to linear regressions and the corresponding slope was used to calculate diffusion coefficients through the Randles-Ševčík equation (Equation 3.7). The corresponding diffusion coefficients are 7.02 x 10^{-7} cm^2s^{-1} and 1.77 x10^{-7} cm^2s^{-1} for **^{14C4}Cb** and **^{14C4}Cb^{2-}** respectively.

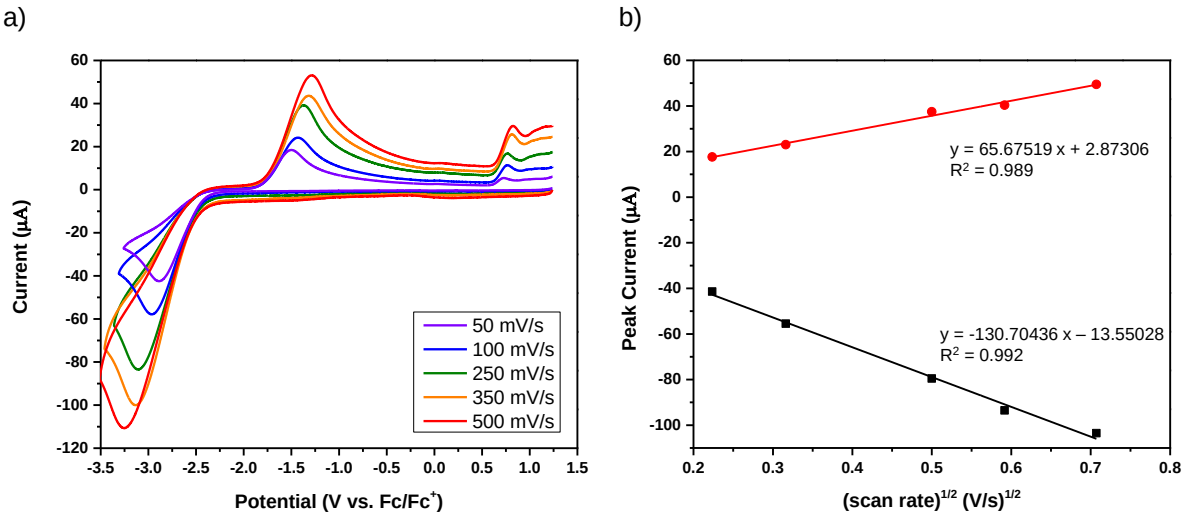

Figure 3.23. Randles-Ševčík of **^{14C4}Cb**. a) CVs of ^{14C4}Cb with variable scan rates b) Randles-Ševčík of the cathodic (black) and anodic (red) events.

Alkali Metal Titrations: Stock solutions of 5.8 mM **^{14C4}Cb**, 2.9 mM LiTFAB, 29 mM $NaPF_6$, and 250 mM KPF_6 were prepared in volumetric flasks with 0.1 M $[Bu_4N][PF_6]$ in DME in a nitrogen glovebox. Using a 500 µL Hamilton syringe, 500 µL of **^{14C4}Cb** was dispensed into the electrochemical cell. Then, the corresponding metal solution was dispensed into the cell using a Hamilton syringe. Electrolyte solution was dispensed into the cell so that the final volume of solution had a total volume of 1 mL. Each solution was thoroughly stirred for 30 minutes. Stirring was discontinued and then the CV was taken at 50 mV/s using the same freshly polished glassy carbon working electrode. All stock solutions, cell mixtures, and corresponding CV measurements were performed in triplicate. The peak current of each oxidation, $I_{p,a}$, was recorded after a straight line subtraction on OriginPro 9 software. The peak current of 2.9 mM **^{14C4}Cb** with no metal, 17.69 µA, was determined by CV with 6 trial averages and was used for all ΔI calculations. The average log(ΔI/I) versus metal concentration was plotted for each alkali metal with the standard deviation shown as error bars. A linear regression with no weighting was used on OriginPro 9. The y-intercept and error correspond to the log K for each metal. The slope and error of each linear regression corresponds to the stoichiometry.

3.4.7. Simulated Voltammetry Procedures

All simulations were performed using DigiSim version 3.03b. Pre-equilibration was enabled. A semi-infinite model for diffusion was used. A planar electrode with surface area 0.07071 cm^2 was used. The capacitance double layer set to $1x10^{-5}$ F. The temperature was set to the same temperature as the lab, 295 K. The resistance in the cell with 0.1 M $[Bu_4N][PF_6]$ DME was measured by the peak to peak separation of the ferrocene/ferrocenium redox couple at 500 mV/s (3600 Ω) and used for all simulations. The concentration of **^{14C4}Cb** was set to

2.9 mM. The CV was scanned from 1.25 to -3.25 and back with a potential step of 0.001 V and a scan rate of 50 mV/s unless otherwise stated.

CVs of **^{14C4}Cb** were simulated at 50 mV/s, 250 mV/s, and 500 mV/s to obtain fits for the remaining parameters (Figure S27). To simulate the metal-free carborane species, an ECEC mechanism was implemented to account for the chemical changes (i.e., cage rearrangement) of carborane between its *closo* and *nido* forms (Figure S27). **^{14C4}Cb** is represented by *closo, closo*$^{2-}$ is the reduced species before bond cleavage and cage rearrangement, **^{14C4}Cb^{2-}** is denoted as *nido*$^{2-}$, and *nido*^{0} is the neutral species before C–C bond and carborane cage reformation.

A diffusion coefficient of 8 x 10^{-6} cm^2/s was used for *closo* and *closo*$^{2-}$. A diffusion coefficient of 1 x 10^{-6} cm^2/s was used for *nido*$^{2-}$ and *nido*^{0}. We note that the diffusion coefficients were experimentally determined in section S5.1, but the values used here provided a better fit to the experimental data. For the first electron transfer step, (*closo* + $2e^-$ = *closo*$^{2-}$) a heterogenous electron transfer rate, k_o, 5 x 10^{-5} (cm/s), heterogenous charge transfer coefficient, α, of 0.20, and an initial reduction potential, E_o, of -2.48 V were used. For the second electron transfer step, (*nido*$^{2-}$ = *nido*^{0} + $2e^-$) a heterogenous electron transfer rate, k_o, 5 x 10^{-5} (cm/s), heterogenous charge transfer coefficient, α, of 0.85, and an initial reduction potential, E_o, of -1.78 V were implemented. For the chemical changes, (*closo*$^{2-}$ = *nido*$^{2-}$) and (*nido*^{0} = *closo*), we assumed fast kinetics with a k_f of 1 x 10^5 and favorable thermodynamics with a K_{eq} of 1 x 10^{10} to ensure complete chemical conversion.

For the metal CV simulations, the parameters as described above were used, with the exception of reduction potentials E_o which were optimized for each scan, and the cathodic heterogenous charge transfer coefficient α was kept constant at 0.15. Literature values for

diffusion coefficients of Li^+ (1.5 x 10^{-5} cm^2/s)[51], Na^+ (1.0 x 10^{-5} cm^2/s)[50], and K^+ (9.0 x 10^{-6} cm^2/s)[52] were used. An ECCCEC mechanism was implemented with two additional competing chemical reaction occurring between *nido*$^{2-}$ and the alkali metal, M^+ to form M*nido*$^-$ and M_2*nido* (Figure S28). The metal binding events must occur sequentially as DigiSim 3.03b is not capable of having two concurrent binding events. The diffusion coefficient of *nido*, 1 x 10^{-6} cm^2/s was used for the metal-carborane species. The voltammetry was then simulated with different concentrations of Li^+, Na^+ or K^+ and fit to experimental data (Figures S29-S31). The voltammetry was fit to experimental data to obtain K_{eq} values for each metal binding to ^{14C4}**Cb**$^{2-}$. Note: The simulated cathodic event does not vary with different equivalents of metal resulting in superimposed dashed lines for the observed reduction. We note that via simulations, we cannot converge on separate log K values with confidence and have higher regard for the summed total log K.

3.5. References

(1) IEA. Critical Minerals Market Review 2023. IEA: 2023.

(2) Ding, T.; Zheng, M.; Peng, S.; Lin, Y.; Zhang, X.; Li, M. Lithium extraction from salt lakes with different hydrochemical types in the Tibet Plateau. *Geoscience Frontiers* **2023**, *14* (1), 101485. DOI: https://doi.org/10.1016/j.gsf.2022.101485.

(3) Vera, M. L.; Torres, W. R.; Galli, C. I.; Chagnes, A.; Flexer, V. Environmental impact of direct lithium extraction from brines. *Nature Reviews Earth & Environment* **2023**, *4* (3), 149-165. DOI: 10.1038/s43017-022-00387-5.

(4) Diallo, M. S.; Kotte, M. R.; Cho, M. Mining Critical Metals and Elements from Seawater: Opportunities and Challenges. *Environmental Science & Technology* **2015**, *49* (16), 9390-9399. DOI: 10.1021/acs.est.5b00463.

(5) Turekian, K. K. *Oceans*; Prentice-Hall, 1976.

(6) Loganathan, P.; Naidu, G.; Vigneswaran, S. Mining valuable minerals from seawater: a critical review. *Environmental Science: Water Research & Technology* **2017**, *3* (1), 37-53. DOI: 10.1039/C6EW00268D.

(7) Murphy, O.; Haji, M. N. A review of technologies for direct lithium extraction from low Li+ concentration aqueous solutions. *Frontiers in Chemical Engineering* **2022**, *4*. DOI: 10.3389/fceng.2022.1008680.

(8) Calvo, E. J. Direct Lithium Recovery from Aqueous Electrolytes with Electrochemical Ion Pumping and Lithium Intercalation. *ACS Omega* **2021**, *6* (51), 35213-35220. DOI: 10.1021/acsomega.1c05516.

(9) Liu, D.; Zhao, Z.; Xu, W.; Xiong, J.; He, L. A closed-loop process for selective lithium recovery from brines via electrochemical and precipitation. *Desalination* **2021**, *519*, 115302. DOI: https://doi.org/10.1016/j.desal.2021.115302.

(10) Xing, P.; Wang, C.; Zeng, L.; Ma, B.; Wang, L.; Chen, Y.; Yang, C. Lithium Extraction and Hydroxysodalite Zeolite Synthesis by Hydrothermal Conversion of α-Spodumene. *ACS Sustainable Chemistry & Engineering* **2019**, *7* (10), 9498-9505. DOI: 10.1021/acssuschemeng.9b00923.

(11) Bian, W.; Chen, J.; Chen, Y.; Xu, W.; Jia, J. A novel waste paper cellulose-based Cu-MOF hybrid material threaded by PSS for lithium extraction with high adsorption capacity and selectivity. *Cellulose* **2021**, *28* (5), 3041-3054. DOI: 10.1007/s10570-021-03707-y.

(12) Rozhdestvenska, L. M.; Chaban, M. O.; Dzyazko, Y. S.; Palchik, O. V.; Dzyazko, O. G. Formation of lithium-selective sorbent in nanoreactors of the support based on titanium dioxide. *Applied Nanoscience* **2022**, *12* (4), 1113-1122. DOI: 10.1007/s13204-021-01832-5.

(13) Bao, L.-R.; Zhang, J.-Z.; Tang, W.-P.; Sun, S.-Y. Synthesis and adsorption properties of metal oxide-coated lithium ion-sieve from salt lake brine. *Desalination* **2023**, *546*, 116196. DOI: https://doi.org/10.1016/j.desal.2022.116196.

(14) Xiao, G.; Tong, K.; Zhou, L.; Xiao, J.; Sun, S.; Li, P.; Yu, J. Adsorption and Desorption Behavior of Lithium Ion in Spherical PVC–MnO2 Ion Sieve. *Industrial & Engineering Chemistry Research* **2012**, *51* (33), 10921-10929. DOI: 10.1021/ie300087s.

(15) Inoue, Y.; Hakushi, T.; Liu, Y.; Tong, L. H. Molecular design of crown ethers. 12. Complexation thermodynamics of 12- to 16-crown-4: thermodynamic origin of high lithium selectivity of 14-crown-4. *The Journal of Organic Chemistry* **1993**, *58* (20), 5411-5413. DOI: 10.1021/jo00072a024.

(16) Buschmann, H.-J. Stability constants and thermodynamic data for complexes of 12-crown-4 with alkali metal and alkaline-earth cations in methanol solutions. *Journal of Solution Chemistry* **1987**, *16* (3), 181-190. DOI: 10.1007/BF00646985.

(17) Cram, D. J.; Lein, G. M. Host-guest complexation. 36. Spherand and lithium and sodium ion complexation rates and equilibria. *JACS* **1985**, *107* (12), 3657-3668. DOI: 10.1021/ja00298a041.

(18) Lindoy, L. F.; Park, K.-M.; Sung Lee, S. Cryptands and Spherands. In *Supramolecular Chemistry*, 2012.

(19) Warnock, S. J.; Sujanani, R.; Zofchak, E. S.; Zhao, S.; Dilenschneider, T. J.; Hanson, K. G.; Mukherjee, S.; Ganesan, V.; Freeman, B. D.; Abu-Omar, M. M.; et al. Engineering Li/Na selectivity in 12-Crown-4–functionalized polymer membranes. *Proceedings of the National Academy of Sciences* **2021**, *118* (37), e2022197118. DOI: doi:10.1073/pnas.2022197118.

(20) Battistel, A.; Palagonia, M. S.; Brogioli, D.; La Mantia, F.; Trócoli, R. Electrochemical Methods for Lithium Recovery: A Comprehensive and Critical Review. *Adv. Mater.* **2020**, *32* (23), 1905440. DOI: https://doi.org/10.1002/adma.201905440.

(21) Lawagon, C. P.; Nisola, G. M.; Cuevas, R. A. I.; Torrejos, R. E. C.; Kim, H.; Lee, S.-P.; Chung, W.-J. Li1−xNi0.5Mn1.5O4/Ag for electrochemical lithium recovery from brine and its optimized performance via response surface methodology. *Separation and Purification Technology* **2019**, *212*, 416-426. DOI: https://doi.org/10.1016/j.seppur.2018.11.046.

(22) Sun, J.; Liang, D.; Meng, X.; Li, Z. Recent Advances in Lithium Extraction Using Electrode Materials of Li-Ion Battery from Brine/Seawater. *Processes* **2022**, *10* (12), 2654.

(23) Chen, Q.-B.; Ji, Z.-Y.; Liu, J.; Zhao, Y.-Y.; Wang, S.-Z.; Yuan, J.-S. Development of recovering lithium from brines by selective-electrodialysis: Effect of coexisting cations on the migration of lithium. *Journal of Membrane Science* **2018**, *548*, 408-420. DOI: https://doi.org/10.1016/j.memsci.2017.11.040.

(24) Czech, B. P.; Babb, D. A.; Son, B.; Bartsch, R. A. Functionalized 13-crown-4, 14-crown-4, 15-crown-4, and 16-crown-4 compounds: synthesis and lithium ion complexation. *The Journal of Organic Chemistry* **1984**, *49* (25), 4805-4810. DOI: 10.1021/jo00199a011.

(25) Tian, Y.; Chen, W.; Zhao, Z.; Xu, L.; Tong, B. Interaction and selectivity of 14-crown-4 derivatives with Li+, Na+, and Mg2+ metal ions. *J. Mol. Model.* **2020**, *26* (4). DOI: 10.1007/s00894-020-4325-8.

(26) Sachleben, R. A.; Davis, M. C.; Bruce, J. J.; Ripple, E. S.; Driver, J. L.; Moyer, B. A. An efficient synthesis of lithium-selective extractants: Tertiary-alkyl-14-crown-4 ethers. *Tetrahedron Letters* **1993**, *34* (34), 5373-5376. DOI: https://doi.org/10.1016/S0040-4039(00)73912-8.

(27) Zong, K.; Reynolds, J. R. 3,4-Alkylenedioxypyrroles: Functionalized Derivatives as Monomers for New Electron-Rich Conducting and Electroactive Polymers. *The Journal of Organic Chemistry* **2001**, *66* (21), 6873-6882. DOI: 10.1021/jo001620l.

(28) Citterio, D.; Takeda, J.; Kosugi, M.; Hisamoto, H.; Sasaki, S.-i.; Komatsu, H.; Suzuki, K. pH-Independent Fluorescent Chemosensor for Highly Selective Lithium Ion Sensing. *Anal. Chem.* **2007**, *79* (3), 1237-1242. DOI: 10.1021/ac061674g.

(29) Alston, D. R.; Stoddart, J. F.; Wolstenholme, J. B.; Allwood, B. L.; Williams, D. J. Synthesis of an octamethyl-18-crown-6 derivative and the X-ray crystal structure of its 2:1 complex with borane-ammonia. *Tetrahedron* **1985**, *41* (14), 2923-2926. DOI: https://doi.org/10.1016/S0040-4020(01)96617-7.

(30) Ohta, K.; Goto, T.; Yamazaki, H.; Pichierri, F.; Endo, Y. Facile and Efficient Synthesis of C-Hydroxycarboranes and C,C‘-Dihydroxycarboranes. *Inorg. Chem.* **2007**, *46* (10), 3966-3970. DOI: 10.1021/ic062025q.

(31) Dalley, N. K.; Jiang, W.; Olsher, U. The crystal structure of dibenzo-14-crown-4, a preorganized basis of square pyramid coordination for lithium ions. *Journal of inclusion phenomena and molecular recognition in chemistry* **1992**, *12* (1), 305-312. DOI: 10.1007/BF01053870.

(32) Zhang, T.; Zhu, L.; Tian, Z.; Wang, J. Structural, Electronic, and Magnetic Properties of Neutral and Charged Transition Metal–Bis(dicarbollide) Sandwich Clusters. *The Journal of Physical Chemistry C* **2011**, *115* (30), 14542-14547. DOI: 10.1021/jp202531c.

(33) Hata, M.; Kautz, J. A.; Lu, X. L.; McGrath, T. D.; Stone, F. G. A. Revisiting [Mn(CO)3(η5-nido-7,8-C2B9H11)]-, the Dicarbollide Analogue of [(η5-C5H5)Mn(CO)3]:

Reactivity Studies Leading to Boron Atom Functionalization. *Organometallics* **2004**, *23* (15), 3590-3602. DOI: 10.1021/om049822l.

(34) C. Grossel, M.; G. Hamilton, D.; I. Fuller, J.; Millan-Barios, E. Alkali-metal binding properties of simple ferrocenyl- and ruthenocenyl-substituted aza-crown ethers. *Journal of the Chemical Society, Dalton Transactions* **1997**, (19), 3471-3477. DOI: 10.1039/A703597G.

(35) López, E.; Lucas, J. M.; de Andrés, J.; Albertí, M.; Bofill, J. M.; Bassi, D.; Aguilar, A. Cross-section energy dependence of the [C6H6–M]+ adduct formation between benzene molecules and alkali ions (M = Li, Na, K). *Physical Chemistry Chemical Physics* **2011**, *13* (35), 15977-15984. DOI: 10.1039/C1CP21889A.

(36) Melero, C.; Guijarro, A.; Yus, M. Structural characterization and bonding properties of lithium naphthalene radical anion, [Li+(TMEDA)2][C10H8˙−], and lithium naphthalene dianion [(Li+TMEDA)2C10H8−2]. *Dalton Trans.* **2009**, (8), 1286-1289. DOI: 10.1039/B821119C.

(37) Connor, G. P.; Mercado, B. Q.; Lant, H. M. C.; Mayer, J. M.; Holland, P. L. Chemical Oxidation of a Coordinated PNP-Pincer Ligand Forms Unexpected Re–Nitroxide Complexes with Reversal of Nitride Reactivity. *Inorg. Chem.* **2019**, *58* (16), 10791-10801. DOI: 10.1021/acs.inorgchem.9b01075.

(38) Connelly, N. G.; Geiger, W. E. Chemical Redox Agents for Organometallic Chemistry. *Chem. Rev.* **1996**, *96* (2), 877-910. DOI: 10.1021/cr940053x.

(39) Hirose, K. A Practical Guide for the Determination of Binding Constants. *Journal of Inclusion Phenomena* **2001**, *39*, 193-209. DOI: 10.1023/A:1011117412693.

(40) Barlow, J. M.; Ziller, J. W.; Yang, J. Y. Inhibiting the Hydrogen Evolution Reaction (HER) with Proximal Cations: A Strategy for Promoting Selective Electrocatalytic Reduction. *ACS Catal.* **2021**, *11* (13), 8155-8164. DOI: 10.1021/acscatal.1c01527.

(41) Reath, A. H.; Ziller, J. W.; Tsay, C.; Ryan, A. J.; Yang, J. Y. Redox Potential and Electronic Structure Effects of Proximal Nonredox Active Cations in Cobalt Schiff Base Complexes. *Inorg. Chem.* **2017**, *56* (6), 3713-3718. DOI: 10.1021/acs.inorgchem.6b03098.

(42) Ghosh, T. K.; Maity, S.; Ghosh, S.; Gomila, R. M.; Frontera, A.; Ghosh, A. Role of Redox-Inactive Metal Ions in Modulating the Reduction Potential of Uranyl Schiff Base Complexes: Detailed Experimental and Theoretical Studies. *Inorg. Chem.* **2022**, *61* (18), 7130-7142. DOI: 10.1021/acs.inorgchem.2c00645.

(43) Shah, A.; Nosheen, E.; Munir, S.; Badshah, A.; Qureshi, R.; Rehman, Z.-u.; Muhammad, N.; Hussain, H. Characterization and DNA binding studies of unexplored imidazolidines by electronic absorption spectroscopy and cyclic voltammetry. *J. Photochem. Photobiol., B* **2013**, *120*, 90-97. DOI: https://doi.org/10.1016/j.jphotobiol.2012.12.015.

(44) Ramotowska, S.; Ciesielska, A.; Makowski, M. What Can Electrochemical Methods Offer in Determining DNA–Drug Interactions? *Molecules* **2021**, *26* (11), 3478.

(45) Guin, P. S.; Das, S. Exploration of Electrochemical Intermediates of the Anticancer Drug Doxorubicin Hydrochloride Using Cyclic Voltammetry and Simulation Studies with an Evaluation for Its Interaction with DNA. *International Journal of Electrochemistry* **2014**, *2014*, 517371. DOI: 10.1155/2014/517371.

(46) Harit, A.; Das, R.; Bose, P. Interaction study of Glutamic Acid with double-stranded calf thymus DNA by using Cyclic Voltammetric, Ultraviolet-visible and Fluorescence spectroscopy. *Journal for Foundations and Applications of Physics* **2017**, *4*, 62-73.

(47) Feng, X.-Z.; Lin, Z.; Yang, L.-J.; Wang, C.; Bai, C.-l. Investigation of the interaction between acridine orange and bovine serum albumin. *Talanta* **1998**, *47* (5), 1223-1229. DOI: https://doi.org/10.1016/S0039-9140(98)00198-2.

(48) Ozutsumi, K.; Ohtsu, K.; Kawashima, T. Thermodynamics of complexation of 18-crown-6 with sodium, potassium, rubidium, caesium and ammonium ions in N,N-dimethylformamide. *Journal of the Chemical Society, Faraday Transactions* **1994**, *90* (1), 127-131. DOI: 10.1039/FT9949000127.

(49) Feldberg, M. R. S. W. DigiSim Version 3.03b. Bioanalytical System: West Lafayette, 2004.

(50) Morales, D.; Ruther, R. E.; Nanda, J.; Greenbaum, S. Ion transport and association study of glyme-based electrolytes with lithium and sodium salts. *Electrochim. Acta* **2019**, *304*, 239-245. DOI: https://doi.org/10.1016/j.electacta.2019.02.110.

(51) Yoshida, K.; Tsuchiya, M.; Tachikawa, N.; Dokko, K.; Watanabe, M. Change from Glyme Solutions to Quasi-ionic Liquids for Binary Mixtures Consisting of Lithium Bis(trifluoromethanesulfonyl)amide and Glymes. *The Journal of Physical Chemistry C* **2011**, *115* (37), 18384-18394. DOI: 10.1021/jp206881t.

(52) Popovic, J. Insights into Cationic Transference Number Values and Solid Electrolyte Interphase Growth in Liquid/Solid Electrolytes for Potassium Metal Batteries. *ACS Physical Chemistry Au* **2022**, *2* (6), 490-495. DOI: 10.1021/acsphyschemau.2c00024.

(53) Ohtsu, K.; Ozutsumi, K.; Kurihara, M.; Kawashima, T. Thermodynamics of Complexation of Sodium Ion with 12-Crown-4 and 18-Crown-6 in Pyridine. *Zeitschrift für Naturforschung B* **1995**, *50* (4), 529-535. DOI: doi:10.1515/znb-1995-0410.

(54) Keener, M.; Hunt, C.; Carroll, T. G.; Kampel, V.; Dobrovetsky, R.; Hayton, T. W.; Ménard, G. Redox-switchable carboranes for uranium capture and release. *Nature* **2020**, *577* (7792), 652-655. DOI: 10.1038/s41586-019-1926-4.

Chapter 4 Bipyridyl *o*-Carborane for Transition Metal Capture

4.1. Introduction

4.1.1. The Rise of Electric Vehicles

As an alternative to fossil-fuel powered cars, electric vehicles (EVs), can alleviate GHG emissions when paired with an electric grid powered by renewable energy. EVs are becoming exponentially popular. In 2022, 762,000 EVs were sold in the United States compared to merely 230,000 in 2019.[1] Globally, there were 26 million EVs on the roads in 2022, and this is projected to increase to 200–350 million by 2030.[2] At the 2021 United Nations Climate Change Conference, Ford, General Motors, Mercedes-Benz, Volvo, Jaguar and Land Rover pledged to stop internal combustion engine vehicle sales by 2040.[3] EVs will decidedly dominate the car market; however, the transition could encounter significant delays because of inadequate sourcing of critical minerals used in the batteries.[4]

4.1.2. Batteries & Critical Minerals

EVs operate using Li-ion batteries. The battery components consist of a graphite anode adhered to Cu, Li electrolyte, a porous separator, and a crystalline transition metal-based cathode supported on Al. Lithium nickel manganese cobalt oxide (NMC) cathodes are the most prevalent because they provide a high operating voltage and energy density.[5] As a result, the use of NMCs has placed significant pressure on Co and Ni supply chains. From 2017 to 2022, the demand for Co and Ni grew by 70% and 40%, respectively.[4] The global production of these critical minerals must be expanded; however, Co and Ni are sourced by terrestrial mining. Co is primarily extracted as a byproduct of Cu mining (55%) and Ni mining (29%) thus increasing the global supply is challenging and unscrupulous.[6] Terrestrial mining causes extensive environmental harm by polluting soil, water and air while releasing more GHG

emissions. In the Democratic Republic of the Congo, where Co is primarily sourced from, work conditions are exploitive. Miners suffer from poor health and safety protocols and, abhorrently, child labor is used.[7] An ethical and sustainable alternative for sourcing Co and Ni could arise from battery recycling.

4.1.3. Battery Recycling

In 2019, only 5% of all end-of-life Li-ion batteries were recycled in the United States.[8] Battery recycling can play a pivotal role in reducing waste and creating a circular supply chain for EVs. To recycle batteries, the cathode is mechanically shred into a powder termed "black mass." The metals in the black mass are then separated through either pyrometallurgy or hydrometallurgy and subsequently reprocessed into new batteries.

Pyrometallurgy smelters battery components at extremely high temperatures (>1200 ^{o}C) with an oxidizing agent to obtain Co and Ni as a molten alloy. The other metals (Mn, Li, Cu, Al) form a slag which is discarded.[9] Co and Ni are further separated using hydrometallurgical techniques. Most current industrial processes are opting to skip the pyrometallurgy phase because it is very energy intensive and produces toxic fluorinated gases and GHG emissions. In contrast, hydrometallurgy leaches the metals from the black mass using strong acids or bases. The metals are then separated using a combination of precipitation, solvent-extraction, or selective adsorption techniques.[10] Hydrometallurgy is not energy intensive and can be scaled for industrial purposes. However, it generates large volumes of caustic waste and consumes stoichiometric reagents.[10]

Electrochemical methods, such as electrodeposition, use redox-active materials to separate metals. By applying a potential, the metals are selectively electrodeposited onto the electrode. Electrochemical metal separation reduces the volume of caustic waste and has low

energy consumption.[11] However, obtaining selectivity between Co and Ni is challenging because they possess similar reduction potentials and physical properties.[12] Electrochemical metal separation could provide a more sustainable pathway towards a circular supply chain for EVs, but it is not yet scalable for commercial applications. More research is needed to improve the scalability and selectivity for industrial battery recycling.

4.1.4. Pyridyl Carboranes for Metal Selectivity

Solvent-extraction processes used in hydrometallurgy have incorporated amine-based extractants for targeting Co and Ni selectivity. Using Alamine 336, a mixture of tertiary amines with varied alkyl chain lengths (6–8 carbons), 80% of Co was extracted from leached Li-ion batteries, though 60% of the Cu was also co-extracted.[13] Similarly, trioctylamine in kerosene extracts Co (94%) and Ni (40%) from the aqueous phase. The metals can then can be stripped using 1 M H_2SO_4.[14] Notably, it is difficult to obtain selective metal capture, as seen with monodentate extractants, because transition metals have similar ionic sizes, cationic charges, and binding modalities with d-orbitals. Perhaps, multidentate chelators, as opposed to monodentate amines, may provide optimized selectivity for Co or Ni. Specifically, 2,2'-bipyridine (bipy) is a bidentate chelator which forms stable 1st row transition metal complexes.[15-17]

In this chapter, we combined the redox-switchable properties of carboranes with bidentate, bipy appendages for a new platform to target transition metal capture. We suspected that sterically encumbered bipyridyl moieties may promote metal release in *closo* form and have strong metal binding in *nido* form (Figure 4.1). We optimized the synthesis of new polypyridyl carborane derivatives through a nucleophilic aromatic substitution reaction paired with a Stille-cross coupling reaction. The metal binding properties of 1,2-bis(2,2'-bipyridyl)*o*-

carborane (**^{bipy}Cb**) were probed through electrochemical and structural studies. We explore whether the coordination geometry of the extractant may be a tunable property for selective Co or Ni recycling.

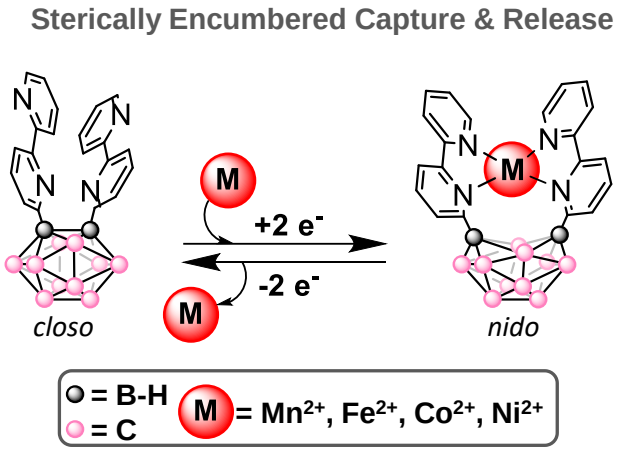

Figure 4.1. Proposed transition metal capture and release with bipyridyl *o*-carboranes.

4.2. Results and Discussion

4.2.1. Ligand Synthesis and Characterization

We targeted the synthesis of 1,2-bis(2,2'-bipyridyl)*o*-carborane (**^{bipy}Cb**) for use as a redox-switchable, biphasic extractant for transition metal capture. However, **^{bipy}Cb** is not a suitable extractant for biphasic capture which we will discuss in further depth throughout the chapter. We initially approached the synthesis of **^{bipy}Cb** via Route 1 (Scheme 4.1) utilizing a modified 1-step nucleophilic aromatic substitution (S_NAr) procedure developed by Spokoyny et. al.[18] Three equivalents of potassium bis(trimethylsilyl)amide (KHMDS) were used to deprotonate Cb followed by addition of 2 equivalents of 6-chloro-2,2'-bipyridine. **^{bipy}Cb** was obtained in a meager 3% yield after refluxing for 4 days. The reaction was drastically improved to a 70% yield by swapping the chloro leaving group for fluoro (Scheme 4.1).

However, 6-fluoro-2,2'-bipyridine is not commercially available and we proceeded to synthesize it. The compound was synthesized using a reported Suzuki-Miyaura reaction in a 2-step procedure, but the yield was very low (4% yield).[19] Synthesis of ^{bipy}**Cb** via Route 1 with 6-fluoro-2,2'-bipyridine required a linear 3-step reaction with a poor overall yield of 3%, mostly due to the poor precursor yield.

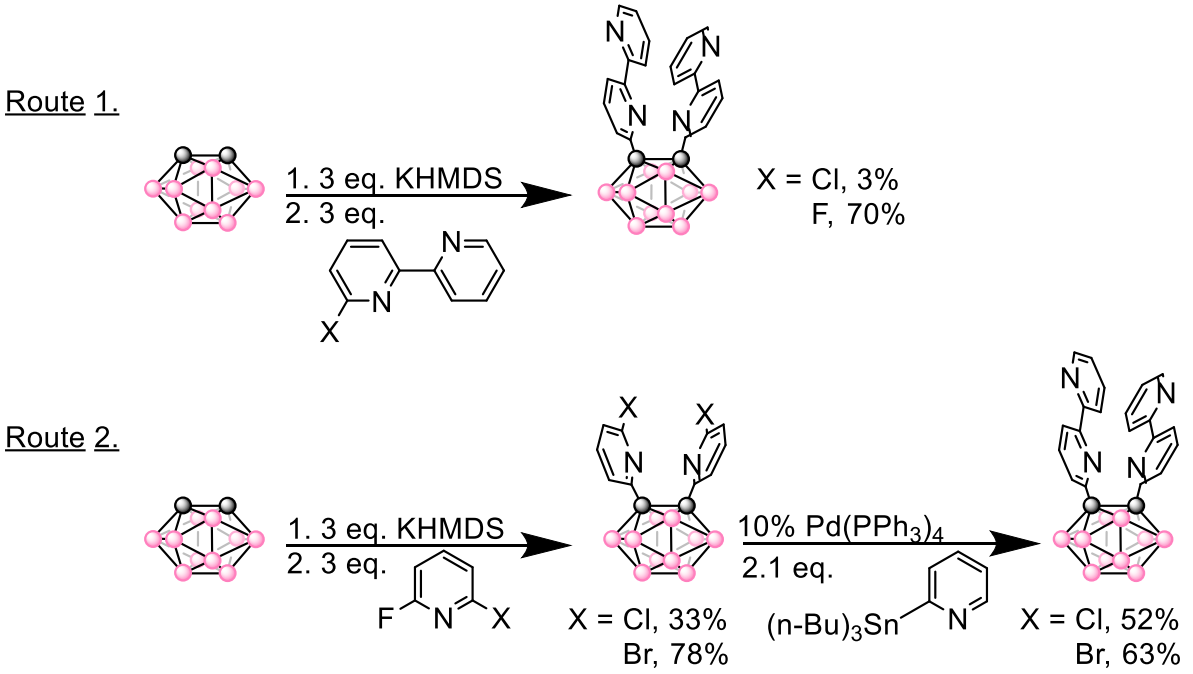

Scheme 4.1. Synthesis of 1,2-bis(2,2'-bipyridyl)*o*-carborane.

We next tried an alternative synthesis via Route 2 (Scheme 4.1), wherein we add the pyridyl moieties step-wise onto *o*-carborane using commercially available reagents. Similar to Route 1, we first performed an S_NAr reaction using commercial 2-chloro-6-fluoropyridine or 2-bromo-6-fluoropyridine, affording 1,2-bis(2-chloropyridyl)*o*-carborane ($^{(Cl)Py}$**Cb**) and 1,2-bis(2-bromopyridyl)*o*-carborane ($^{(Br)Py}$**Cb**) respectively. Interestingly, the yield for $^{(Br)Py}$**Cb** (78%) is significantly higher than $^{(Cl)Py}$**Cb** (33%) which we suspect is due to the decreased reactivity of bromo leaving groups in S_NAr reactions leading to less byproducts.

Subsequently, ^{bipy}**Cb** is obtained from $^{(X)Py}$**Cb** via a Stille cross coupling reaction with 2-(tributylstannyl)pyridine and tetrakis(triphenylphosphine)palladium(0) as catalyst (Scheme 4.1).[20] The overall yields for the 2-step reaction are 17% and 49% using the $^{(Cl)Py}$**Cb** and $^{(Br)Py}$**Cb** intermediates, respectively. We emphasize that the selected leaving group for S_NAr and Stille cross coupling reactions has an immense role in reaction optimization.

X-ray diffraction studies of single crystals of $^{(Cl)Py}$**Cb** and $^{(Br)Py}$**Cb** show that the carborane cages possess unremarkable C–C bond distances of 1.693(4) Å and 1.703(3) Å respectively (Figure 4.2) An expected longer C–Br bond (1.908 Å) than C–Cl bond (1.736 Å) is also observed. The N–N distances for $^{(Cl)Py}$**Cb** (3.415 Å) and $^{(Br)Py}$**Cb** (3.055 Å) suggest that pyridyl-derivatized *closo*-carboranes may be too sterically encumbered for metal coordination (Figure 4.2).

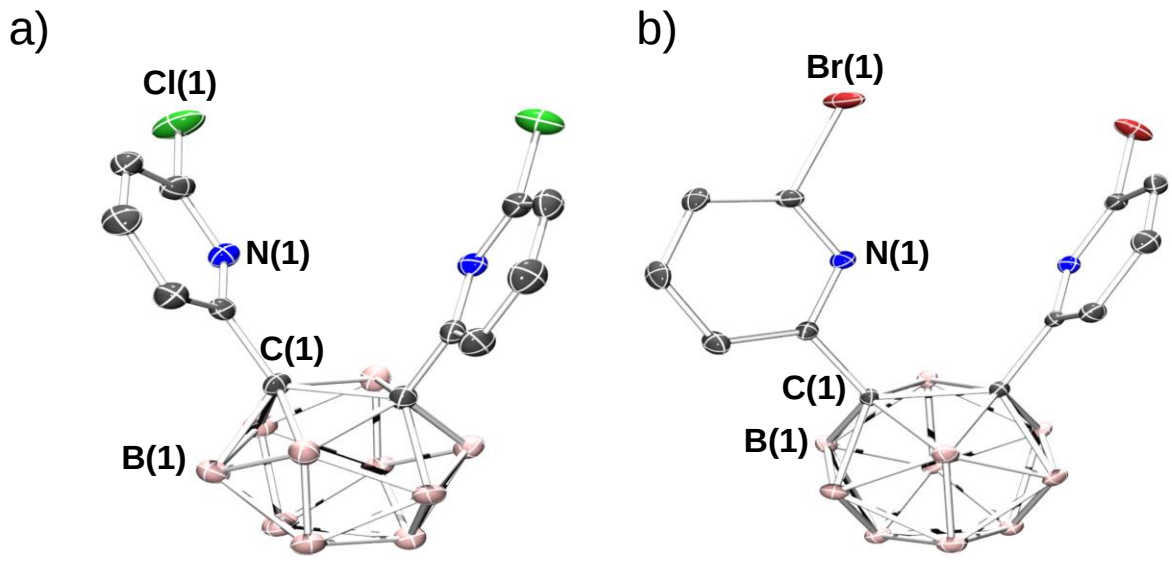

Figure 4.2. Solid-state molecular structures of $^{(Cl)Py}$**Cb** and $^{(Br)Py}$**Cb** obtained by single crystal XRD studies. a) $^{(Cl)Py}$**Cb** b) $^{(Br)Py}$**Cb**. H atoms omitted for clarity.

Chemically reducing ^{bipy}**Cb** with excess potassium graphite (KC_8) in THF afforded the *nido*-carborane species, potassium 1,2-bis(2,2'-bipyridyl)*o*-carborane (**K$_2$**^{bipy}**Cb**) in near

quantitative yield (Scheme 4.2). Single crystals suitable for XRD studies were obtained from vapor diffusion of hexanes into a concentrated solution of THF with 18-crown-6 (Figure 4.3).

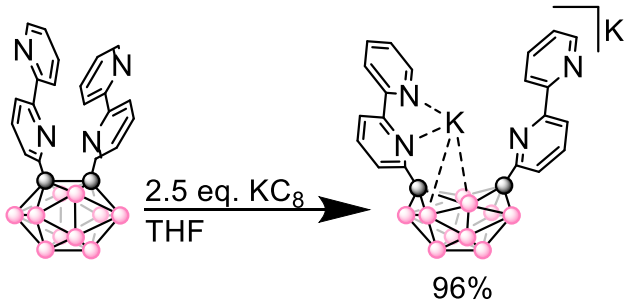

Scheme 4.2. Synthesis of potassium 1,2-bis(2,2'-bipyridyl)*o*-carborane

The solid-state structure of **^{bipy}Cb** displays a C_2 rotational axis wherein the bipy appendages are inverted to one another but remain chemically equivalent via NMR spectroscopy. The carborane cage maintains a C–C bond of 1.675(3) Å (Figure 4.3). Similar to the structures of the monopyridyl-based carboranes (Figure 4.2), N_1 and N_3 in the **^{bipy}Cb** structure are a mere 3.204 Å apart. N_2 and N_4 are separated by 5.889 Å; perhaps, still too constricted for a metal to fit within the cavity. Reducing **^{bipy}Cb** by 2 e^- to the *nido* form results in dramatic structural changes. The **$K_2{}^{bipy}$Cb** structure displays one K^+ coordinated to a bipy moiety, and one K^+ encapsulated by 18-crown-6 (not pictured) (Figure 4.3b). The structure reveals C–C bond scission with a resulting distance of 2.546 Å. The nitrogen–nitrogen distances elongate considerably: N_1–N_3 (5.302 Å) and N_2–N_4 (8.451 Å). **$K_2{}^{bipy}$Cb** packs in the solid-state such that coordinated K^+ forms weak agostic bonds to the borons (3.094(5) Å – 3.4.12(5) Å) of two carborane cage units. Interestingly, the *nido* cage rearranges here to form the face of a 4-membered ring, quite different than the 6-membered ring observed with **$K_2{}^{14C4}$Cb** (Figure 3.1) or 5-membered rings observed with deboronated *nido*-carborane species (Figure 2.10, Figure 4.10).

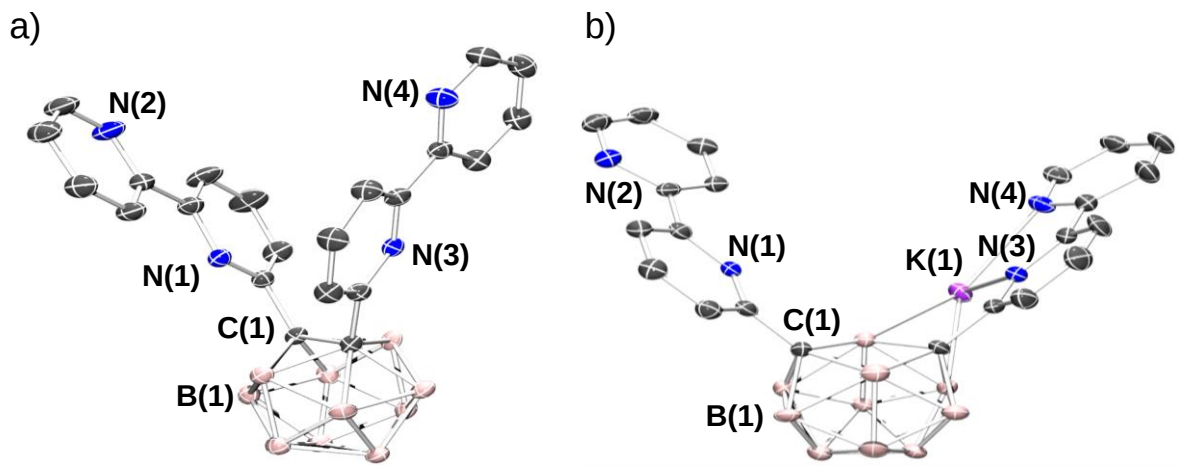

Figure 4.3. Solid-state molecular structures of *closo* and *nido* 1,2-bis(2,2'-bipyridyl)*o*-carborane obtained by single crystal XRD studies. a) ^{bipy}**Cb** b) **K$_2$^{bipy}Cb**. H atoms, cocrystallized solvent, and K-18-crown-6 omitted for clarity.**4.2.2. Electrochemistry**

We next proceeded to study the electrochemical redox-switching and metal binding properties of ^{bipy}**Cb** using cyclic voltammetry. Frequently *closo*/*nido* carborane-based redox occurs as 2 e^- process; though, here we observed 1 e^- stepwise redox as seen with ^{PO}**CbMe$_8$** (Figure 2.6). In a 0.1 M [Bu_4N][PF_6] DMF solution, we observed two close electrochemically reversible 1 e^- redox events which we assign together as the carborane redox couple (^{bipy}**Cb**/^{bipy}**Cb^{2-}**) with formal potentials of $E_{1/2}$ = -1.51 V and -1.67 V vs $Fc^{+|0}$ (Figure 4.4). Notably, the formal reduction potential is quite reductive which leads to air instability and inhibits its viability as a biphasic extractant. Interestingly, bipyridyl substituents are redox non-innocent and at more negative potentials, we observed a reversible 2 e^- event which we tentatively assign as a bipyridyl redox event with formal potential of $E_{1/2}$ = -2.99 V (Figure 4.4). We suspect that the bipyridyl redox are two degenerate bipy→monoanion ($bipy^{\cdot-}$) redox couples.[15, 21, 22]

Subsequently, we studied the CVs of ^{bipy}**Cb** with various metal hexafluorophosphate salts in solution. Initially we performed a control CV experiment with alkali metal Li^+ because of its abundance in NMC cathodes. The CV of ^{bipy}**Cb** with 2 equivalents of $LiPF_6$ shows that the carborane-redox is unaltered while the bipy reductions subtly split and shift anodically with potential shifts of 150 mV and 340 mV ($E_{1/2}$ = -2.84 V, $E_{1/2}$ = -2.65 V) compared to the metal-free CV (Figure 4.4). Similarly, the CV with 1 equivalent of Ca^{2+} displays stationary carborane-redox and an anodic shift in the bipy redox events by 460 mV and 630 mV ($E_{1/2}$ = -2.53 V, $E_{1/2}$ = -2.36 V) (Figure 4.4) (Table 4.1).

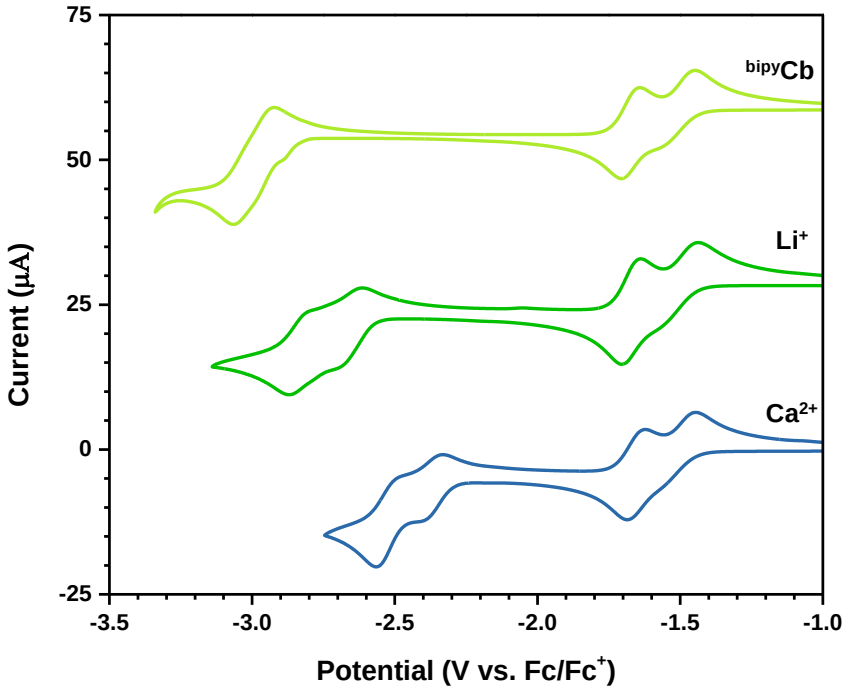

Figure 4.4. CVs of ^{bipy}**Cb** with Li^+ and Ca^{2+} with 0.1 M $[Bu_4N][PF_6]$ in DMF at 10 mV/s using a glassy carbon working electrode, Pt wire counter electrode, and $Ag/AgOTf_{(s)}$ reference electrode.

The CVs with Li^+ and Ca^{2+} suggest that *in situ* electrochemically generated *nido*-carborane species, ^{bipy}**Cb**$^{2-}$, interacts with Lewis acidic metals. Upon binding, the delocalized

negative charge on the carborane-species is stabilized via strong σ-donation onto the metal center. Concurrently, the lowest unoccupied molecular orbital (LUMO), centered on bipy, decreases in energy. Notably, the unperturbed *closo* reduction in Figure 4.4 suggests that ^{bipy}**Cb** does not participate in binding with Li^+ nor Ca^{2+} while the unperturbed *nido* oxidation suggests that the metal-*nido*-carborane binding is weak. Instead, we would expect a large shift in the *nido* oxidation if the metal-*nido*-carborane species was strongly bound.

We next studied the CVs of ^{bipy}**Cb** with 1 equivalent of 1st row transition metals (Mn^{2+}, Fe^{2+}, Co^{2+}, Ni^{2+}) using synthesized PF_6 salts as the transition metal sources (See Section 4.4.2 for synthetic procedure). The redox behavior of ^{bipy}**Cb**/^{bipy}**Cb**$^{2-}$ was previously observed as electrochemically reversible 1 e^- stepwise events, but with transition metals in solution it is remarkably different. Instead, the carborane redox couple appears as electrochemically irreversible 2 e^- events with a tremendous anodic shift in the 2 e^- *nido* oxidation (Figure 4.5).

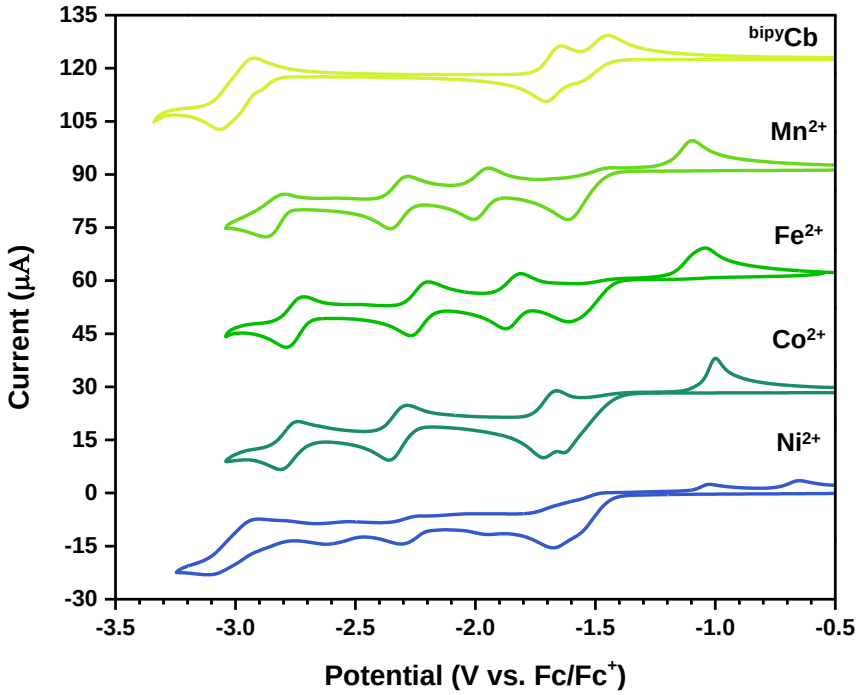

Figure 4.5. CVs of 2 mM **^{bipy}Cb** with 2 mM 1st row transition metals in 0.1 M $[Bu_4N][PF_6]$ DMF at 10 mV/s using a glassy carbon working electrode, Pt wire counter electrode, and $Ag/AgOTf_{(s)}$ reference electrode.

The CV of **^{bipy}Cb** with 1 equivalent of Mn^{2+} displayed a 2 e^- *closo* reduction (E_{red} = -1.61 V) instead of successive 1 e^- reductions (E_{red} = -1.56 V, -1.70 V) observed without transition metals (Figure 4.5). The *nido* oxidation shifts anodically by ~350 mV (E_{ox} = -1.10 V) compared to the metal-free *nido* oxidations (E_{ox} = -1.45, -1.64 V). We also observed a new reversible redox event ($E_{1/2}$ = -1.98 V) which we suspect is **$Mn^{2+/+}$**. The **bipy/bipy$^-$** redox couples are also anodically shifted by 670 mV and 160 mV ($E_{1/2}$ = -2.32 V, $E_{1/2}$ = -2.83 V) (Table 4.1). We observed a similar trend with Fe^{2+} in solution wherein a 2 e^- *closo* reduction is observed (E_{red} = -1.61 V) and the 2 e^- *nido* oxidation is anodically shifted by ~410 mV (E_{ox} = -1.04 V) (Figure 4.5). We observed a new reversible redox event which we suspect is the **$Fe^{2+/+}$** redox couple ($E_{1/2}$ = -1.84 V) (Table 4.1). The **bipy/bipy$^-$** redox couples are also

anodically shifted by 760 mV and 200 mV ($E_{1/2}$ = -2.23 V, $E_{1/2}$ = - 2.79 V). With 1 equivalent of Co^{2+}, we detected a 2 e^- *closo* reduction (E_{red} = -1.63 V) and a shift in the *nido* peak oxidation current by ~450 mV (E_{ox} = -1.00 V) (Figure 4.5). A new reversible redox event emerges which we tentatively assign as $\mathbf{Co^{2+/+}}$ ($E_{1/2}$ = -1.69 V). The **bipy**/**bipy**$^-$ redox couples are anodically shifted by 670 mV and 210 mV ($E_{1/2}$ = -2.32 V, $E_{1/2}$ = -2.78 V) (Table 4.1). Lastly, the CV of $^{\mathbf{bipy}}$**Cb** with 1 equivalent of Ni^{2+} displayed additional, irreversible redox events that are perhaps either metal-based events or byproducts (Figure 4.5). Ni^+ metal species are thermodynamically and kinetically unstable and irreversible redox events are common because the Ni^+ species may disproportionate into Ni^0 and Ni^{2+}.[23, 24] The **bipy**/**bipy**$^-$ also appears less reversible and assignment of individual redox events is challenging. Though, we clearly observed the 2 e^- *closo* reduction (E_{red} = -1.68 V) and the *nido* oxidation appeared anodically shifted and occurred in two 1 e^- steps (E_{ox} = -1.02 V, -0.65 V).

We suspect that *in situ* generated $^{\mathbf{bipy}}\mathbf{Cb^{2-}}$ binds to the transition metals strongly. The **bipy**/**bipy**$^-$ redox couples are all anodically shifted, signaling significant stabilization of the LUMO. Interestingly, the transition metals are all redox-active and we observe that the redox couple assigned to each metal species becomes easier to reduce as Lewis acidity increases: Co^{2+} > Fe^{2+} > Mn^{2+}. Similarly, we notice greater anodic shifts in *nido* oxidation which seemingly correlate to greater Lewis acidity. The shift in the *nido* peak oxidation current and resulting formal reduction potential ($E_{1/2}$) corresponds to binding constant log K through Equation 4.1 and Equation 4.2. The shift in formal reduction potential is denoted by E (V), n is the number of electrons transferred, F is Faraday's constant (C mol^{-1}), and ΔG is Gibb's free energy (J). R is the universal gas constant (J mol^{-1} K^{-1}), and T is temperature (K). The natural log (ln) of K was then converted to log K through mathematical operations.

$$\Delta G = -nFE \qquad (4.1)$$

$$\Delta G = -RT\,lnK \qquad (4.2)$$

The metal-free ^{bipy}**Cb**/^{bipy}**Cb**$^{2-}$ redox couple occurs as two successive 1 e$^-$ events. We calculated the shift in formal reduction potential by using the average of the ^{bipy}**Cb**/^{bipy}**Cb**$^{2-}$ $E_{1/2}$ values ($E_{1/2}$ = -1.58 V). Similarly, with Ni^{2+} in solution, the *nido* oxidation appeared as two 1 e$^-$ anodic events which were averaged to obtain the formal reduction potential. We observed anodic shifts in the formal reduction potential of the ^{bipy}**Cb**/^{bipy}**Cb**$^{2-}$ redox couple when transition metals Mn^{2+} (ΔE = 0.225 V), Fe^{2+} (ΔE = 0.255 V), Co^{2+} (ΔE = 0.265 V) and Ni^{2+} (ΔE = 0.322 V) are present in solution. Accordingly, we obtained preliminary log K values of ^{bipy}**Cb**$^{2-}$ binding to Mn^{2+} (log K = 7.6), Fe^{2+} (log K = 8.6), Co^{2+} (log K = 9.0) and Ni^{2+} (log K = 11.3) (Table 4.1). These log K values are remarkably high and demonstrate that ^{bipy}**Cb**$^{2-}$ is an effective complexing agent for transition metal sequestration. However, there does not appear to be a high selectivity preference for Mn^{2+}, Fe^{2+}, or Co^{2+}. The log K for Ni^{2+} is extraordinarily high, perhaps due to the formation of a 4-coordinate square planar geometry. Though, attempts at structurally characterizing this metal complex have thus far failed (*vida infra*). We suggest that CVs be performed with varied concentrations of metals to extrapolate the log K value from a linear regression of a modified Nernst equation.[25, 26]

Table 4.1. Reported reduction potentials of ^{bipy}**Cb** with metals.

Metal	^{bipy}Cb/^{bipy}Cb^{2-} $E_{1/2}$ (V)	$M^{2+/+}$ $E_{1/2}$ (V)	bipy/(bipy$^{\bullet-}$)$^-$ $E_{1/2}$ (V)	Log K
no metal	-1.51, -1.67	N/A	-2.99	N/A
Li^+	-1.50, -1.67	not observed	-2.65, -2.84	N/A
Ca^{2+}	-1.50, -1.65	not observed	-2.36, -2.53	N/A
Mn^{2+}	-1.355	-1.98	-2.32, -2.83	7.6
Fe^{2+}	-1.325	-1.84	-2.23, -2.79	8.6
Co^{2+}	-1.315	-1.69	-2.32, -2.78	9.0
Ni^{2+}	-1.258	unidentifiable	unidentifiable	11.3

We performed control CVs of the synthesized transition metal PF_6 salts to verify that the metals do not become reduced and/or plate out before binding to $^{bipy}\mathbf{Cb}^{2-}$ (Figure 4.6). The CV of $Mn(PF_6)_2$ displays negligible redox activity in the potential window from 0 V to -2 V. With $Fe(PF_6)_2$, we observed a reduction at -1.86 V and possible stripping events at -0.799 V and -0.581 V, as well as the tentatively assigned $\mathbf{Fe}^{2+/3+}$ redox couple ($E_{1/2}$ = -0.46 V) (Figure 4.6). The CV of $Co(PF_6)_2$ showed a reduction at -1.69 V and a stripping event at -0.32 V. Similarly, the CV of $Ni(PF_6)_2$ displayed a reduction at -1.71 V and a subsequent stripping event at -0.31 V (Figure 4.6). The metal reduction events are suspiciously close to the formal reduction potential of $^{bipy}\mathbf{Cb}/^{bipy}\mathbf{Cb}^{2-}$ but we do not observe the associated stripping oxidations with $^{bipy}\mathbf{Cb}$ in solution (Figure 4.5). We propose that the chemical reactions between $^{bipy}\mathbf{Cb}^{2-}$ and the transition metals proceed before metal deposition can occur.

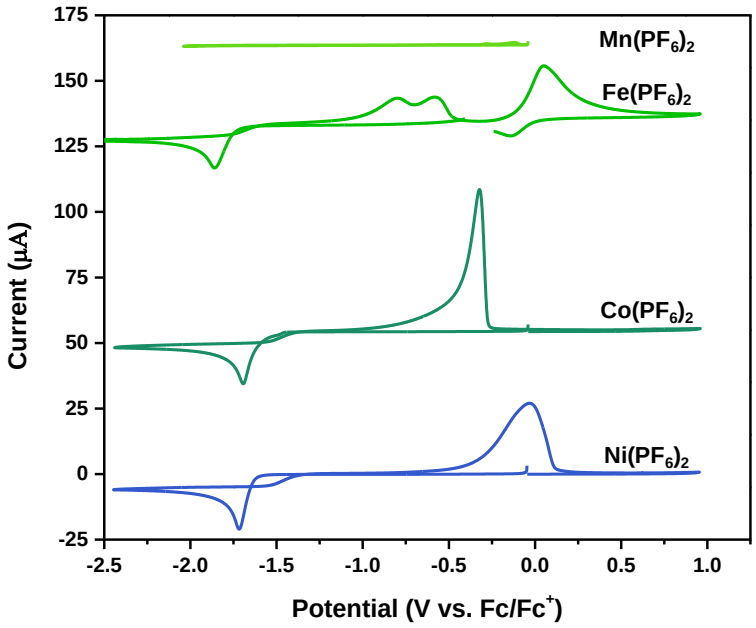

Figure 4.6. CVs of 2 mM transition metal PF_6 salts in 0.1 M $[Bu_4N][PF_6]$ DMF at 10 mV/s using a glassy carbon working electrode, Pt wire counter electrode, and $Ag/AgOTf_{(s)}$ reference electrode.

4.2.3. Metal Complex Synthesis and Characterization

We attempted to synthesize and isolate the series of transition metal complexes (Mn^{2+}, Fe^{2+}, Co^{2+}, Ni^{2+}) bound to the *nido*-carborane species. Under inert atmosphere, stirring 1 equivalent of the metal halide salts with **K_2^{bipy}Cb** overnight in THF resulted in a slurry of deeply colored solids (Scheme 4.3) (Section 4.4.2.). For workup, the reactions were taken to dryness and then washed with THF, filtered over a celite plug and extracted with acetonitrile and/or pyridine. Great care was taken to ensure that the metal complexes were not dissolved in pyridine for prolonged periods unless during recrystallization because pyridine is quite nucleophilic and can cause carborane cage deboronation (Figure 4.7, Figure 4.10).

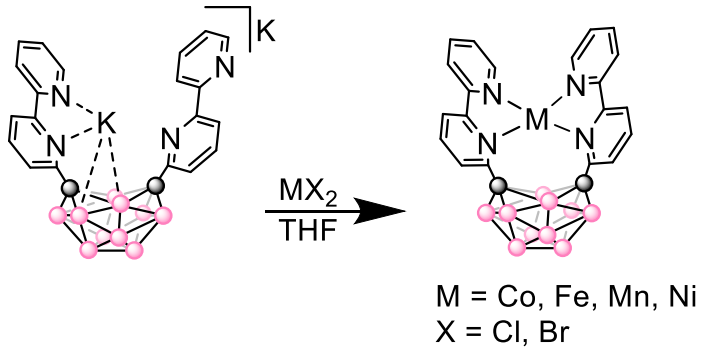

Scheme 4.3. **^{bipy}Cb**-Metal Complex Synthesis.

We attempted to structurally characterize the series with XRD studies (Figure 4.7). Using $MnCl_2$ as the manganese source and stirring with **K_2^{bipy}Cb** overnight, we observed a color change from sunset red to maroon. We found difficulties in obtaining a solid-state structure of the Mn^{2+} *nido*-1,2-bis(2,2'-bipyridyl)*o*-carborane (**Mn^{bipy}Cb**). Orange block single crystals suitable for XRD studies were grown from THF and toluene via vapor diffusion. The solid-state molecular structure corresponded to a bimetallic Mn^{3+} structure with a bridging oxo and bridging Cl and Br with mixed occupancies and co-crystallized THF (Figure 4.7c). Red single crystals suitable for XRD studies were grown from pyridine and

diethyl ether. The solid-state molecular structure corresponded to a trimetallic mixed valance Mn structure with two deboronated carborane units and carbonate (Figure 4.7d) Red block single crystals grown from acetonitrile and ether at -40 ^{o}C via vapor diffusion produced extremely air sensitive crystals which did not diffract well enough for a partial structure, but perhaps indicate that the Mn^{2+} oxidation state and carborane cage were intact. We suggest attempting this solvent combination again for growing single crystals. We note that the equivalents of metal halide should be judiciously controlled, the solvents must be pristinely degassed and dried, and the glovebox atmosphere needs to be immaculate owing to the extreme sensitivity of Mn^{2+} complexes.[27, 28]

Reacting **K_2^{bipy}Cb** with $FeBr_2$ overnight caused a color change from sunset red to brown. Single crystals suitable for XRD studies were grown from vapor diffusion of pyridine and diethyl ether at room temperature. Brown block crystals corresponded to the solid-state molecular structure of Fe^{2+} *nido*-1,2-bis(2,2'-bipyridyl)*o*-carborane) (**Fe^{bipy}Cb**) (Figure 4.7a). **Fe^{bipy}Cb** has a distorted square pyramidal geometry with co-crystallized pyridine coordinating in the equatorial plane. The carborane cage rearranges to a distorted 5-membered ring. The Fe^{2+} center forms Fe–N_{bipy} bonds with bond lengths: 2.153(1) Å, 2.201(1) Å, 2.262(9) Å, 2.122(1) Å. Comparatively, the Fe–N_{py} bond length is 2.171(1) Å. The ^{1}H and ^{11}B NMR spectra in d_5-pyridine was NMR silent.

We stirred $CoBr_2$·DME with **K_2^{bipy}Cb** overnight and observed a color change from sunset red to dark brown. After workup, the ^{1}H NMR was silent, but the ^{11}B{^{1}H} NMR displayed two resonances (-2.14, -9.73 ppm). Single crystals suitable for XRD studies were grown from vapor diffusion of hexanes into a concentrated solution of THF at room temperature. We obtained a partial solid-state structure of a dimeric Co species, bis(cobalt(II)

nido-1,2-bis(2,2'-bipyridyl)*o*-carborane) (**Co$_2^{bipy}$Cb$_2$**) (Figure 4.7b). Surprisingly, **Co$_2^{bipy}$Cb$_2$** is a bimetallic dimer with each Co^{2+} center in a nominally square pyramidal configuration complexed by two bipyridyl appendages from opposing carboranes and bound directly to a deprotonated boron. We suspect that a hydrogen transfer reaction occurred from the borons onto the carbons of the carborane cages. The Co–B distances (1.986 Å and 2.032 Å) are comparable to distances reported in Co^{2+}-boryl complexes.[29] Also, the puckering of the carbons out of the plane of the cage is analogous to the geometry observed with protonated-*nido* species (Figure 2.20). We suggest that further XRD studies be performed to obtain a higher quality crystal structure of **Co$_2^{bipy}$Cb$_2$**.

Mixing 1 equivalent of $NiBr_2$ with **K$_2^{bipy}$Cb** overnight afforded a color change from sunset red to steel blue. The $^{11}B\{^1H\}$ NMR spectrum in d_8-THF displayed two resonances (0.63, -8.27 ppm). The ^1H NMR spectrum contained broad peaks in the aromatic region (8.50, 8.23, 8.14, 7.78, 7.71, 7.27 ppm). We were unsuccessful in obtaining a solid-state structure of Ni^{2+} *nido*-1,2-bis(2,2'-bipyridyl)*o*-carborane (**Ni^{bipy}Cb**), though we do assume that the reaction progresses into a nickel-carborane species, possibly with a square planar geometry. We attempted to grow single crystals suitable for XRD studies using THF, DME, acetonitrile, and pyridine as the polar solvent combined with nonpolar solvents (e.g., hexanes, isooctane, diethyl ether, benzene) with vapor diffusion at room temperature and in the freezer. All solvent combinations attempted thus far resulted in a steel-blue solid powdering out.

Interestingly, **Fe^{bipy}Cb**, **Co$_2^{bipy}$Cb$_2$** and the manganese-carborane species all possess 5-coordinate geometries (Figure 4.7). This suggests that a *nido* polypyridyl-carborane containing 5 or 6 donor atoms may adapt preferable configuration for transition metal capture compared to **^{bipy}Cb^{2-}**.

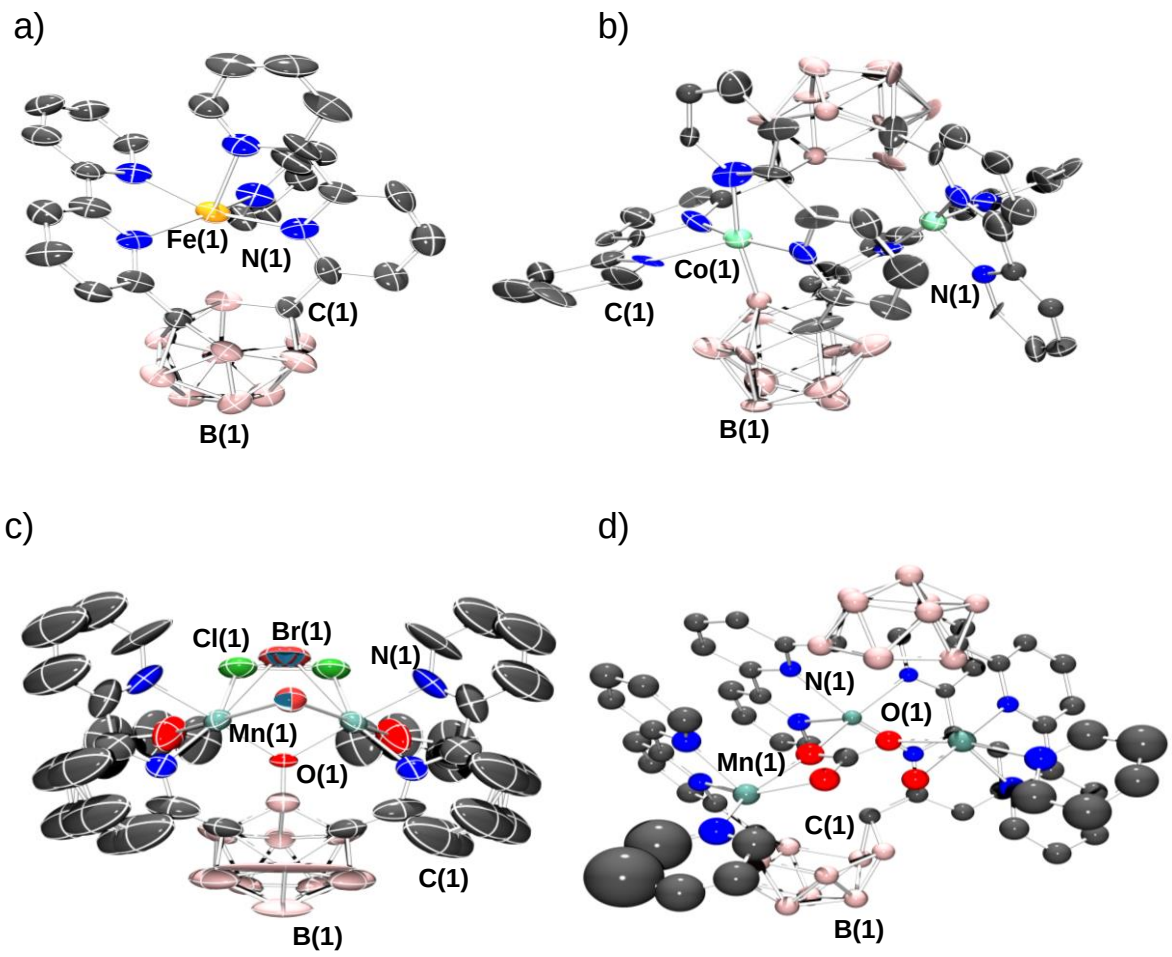

Figure 4.7. Solid-state molecular structures of metal-^{bipy}Cb complexes obtained by single crystal XRD studies. a) **Fe^{bipy}Cb** b) **Co$_2$^{bipy}Cb$_2$** c) bimetallic Mn^{III} carborane species d) trimetallic mixed-valence-Mn deboronated carborane species.

Bipyridyl-based metal complexes are traditional photosensitizers with excellent light absorbing properties for use in photocatalysis, photodynamic therapy, and in dye-sensitized solar cells.[16, 30-34] Carboranes are also well known for their luminescent properties with use in organic light emitting diodes.[35] As such, we performed UV-Visible spectroscopy with **^{bipy}Cb**, **K$_2$^{bipy}Cb**, and **Co$_2$^{bipy}Cb$_2$** (Figure 4.8). Unremarkably, we observed that **^{bipy}Cb** does not absorb visible light. We see the bipyridyl $\pi \rightarrow \pi^*$ transition in the UV region at 283 nm.[36, 37]

Upon 2 e^- reduction to *nido*-carborane, **$K_2^{bipy}Cb$**, the conjugation increases with charge delocalization across the 3D-aromatic carborane cage and bipyridyl moieties. The increased conjugation in **$K_2^{bipy}Cb$** is evident as two new absorbance bands emerge at 392 nm and 432 nm (Figure 4.8).[38] The UV-Visible spectrum of **$Co_2^{bipy}Cb_2$** displays a decrease in molar absorptivity in the visible-light region upon metal complexation (Figure 4.8). We observe no metal to ligand charge transfer or ligand to metal charge transfer, but weak spin forbidden d→d transitions likely arise. The molar absorptivity of the $\pi \rightarrow \pi^*$ is nearly double the absorptivity of **^{bipy}Cb** which confirms the dimeric structure of **$Co_2^{bipy}Cb_2$** in the solution-state.

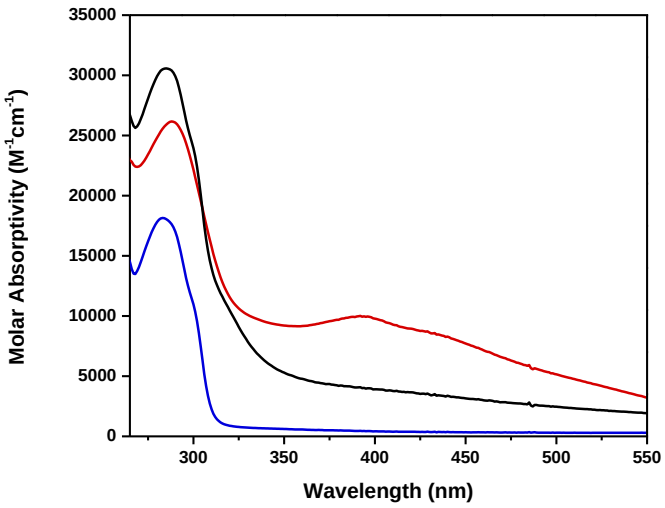

Figure 4.8. UV-Visible Spectroscopy of **^{bipy}Cb**, **$K_2^{bipy}Cb$**, and **$Co_2^{bipy}Cb_2$** in DMF. Blue – **^{bipy}Cb**. Red – **$K_2^{bipy}Cb$**. Black – **$Co_2^{bipy}Cb_2$**.

A CV of **$Co_2^{bipy}Cb_2$** in 0.1 M $[Bu_4][PF_6]$ DMF reveals an irreversible anodic peak (E_{ox} = 0.21 V) which we suspect corresponds to the oxidation of *nido*-carborane species (Figure 4.9). On the reverse sweep, we observe a reduction (E_{red} = -1.52 V) with broadness that resembles the *closo*- oxidation and a reversible redox event ($E_{1/2}$ = -1.687 V), possibly the **$Co^{2+/+}$** redox couple. The CV of chemically synthesized **$Co_2^{bipy}Cb_2$** (Figure 4.9) seems to be in agreement with the CV of **^{bipy}Cb** with 1 equivalent of Co^{2+} (Figure 4.5). The only

discrepancy is the peak oxidation potential of *nido*-species (0.21 V vs -1.00 V). Perhaps kinetics plays a role wherein electrogenerated ^{bipy}**Cb**$^{2-}$ coordinates to Co^{2+} but has not yet reached the thermodynamic product, **Co**$_2$^{bipy}**Cb**$_2$.

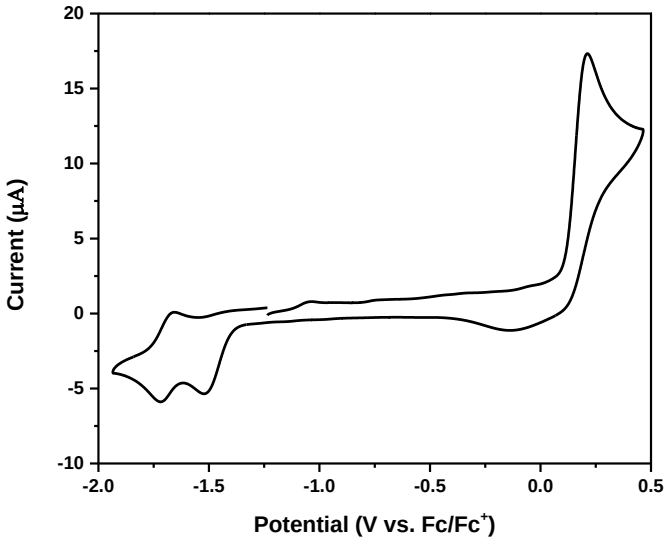

Figure 4.9. CV of 1 mM **Co**$_2$**(**^{bipy}**Cb)**$_2$ in 0.1 M $[Bu_4N][PF_6]$ DMF at 10 mV/s using a glassy carbon working electrode, Pt wire counter electrode, and $Ag/AgOTf_{(s)}$ reference electrode.

We attempted to synthesize *closo*-carborane, **metal-**^{bipy}**Cb**$^{2+}$ compounds to verify whether the *closo* form will interact with transition metals. Mixing ^{bipy}**Cb** with $CoBr_2$·DME in d_8-THF, no immediate reaction occurred, and we only observed sharp resonances that correspond to ^{bipy}**Cb** in the NMR spectrum. After 16 hours, very broad and downfield shifted paramagnetic peaks arise in the $^{11}B\{^1H\}$ NMR spectrum (86.32, 42.90, 29.8, 3.89 ppm). Over a couple of weeks in the NMR tube, long dark blue needle-like single crystals emerged that were suitable for XRD studies. The solid-state molecular structure revealed the identity of the compound to be deboronated-*nido*-carborane metal complex (**CoBr**^{bipy}**Cb**) (Figure 4.10). We observe a charge-balanced Co(II) metal complex adopting a distorted square pyramidal geometry with bromine in the axial plane. Interestingly, we also observe similar deboronation

starting from **Co$_2$^{bipy}Cb$_2$** if dissolved in pyridine for prolonged periods (Figure 4.10). The deboronated-species (**CoPy^{bipy}Cb**) is monomeric and charge-balanced with a proposed Co(I) metal center adopting a square pyramidal configuration with pyridine in the axial plane.

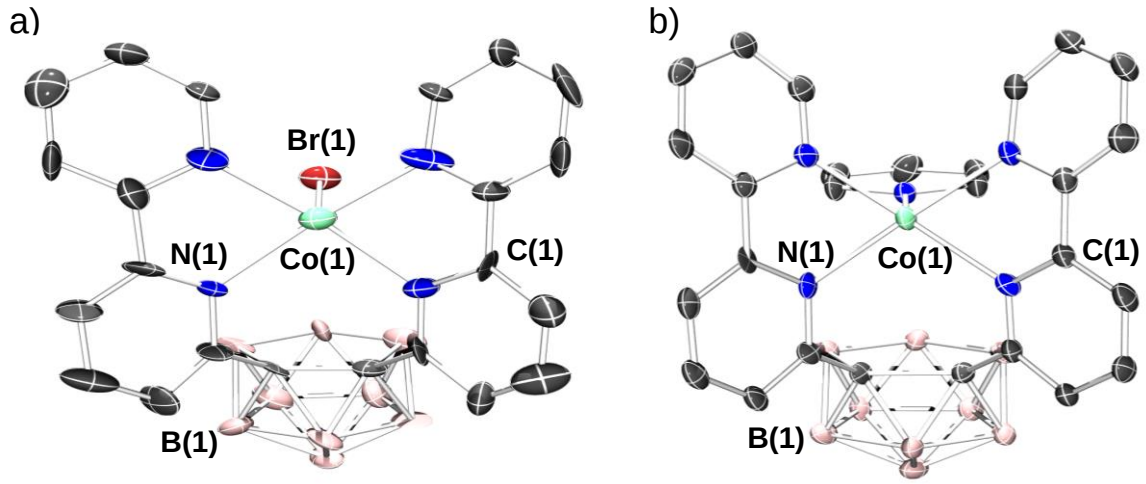

Figure 4.10. Solid-state molecular structures of deboronated **Co-^{bipy}Cb** complexes obtained by single crystal XRD studies. a) **CoBr^{bipy}Cb** generated from **^{bipy}Cb** with $CoBr_2$ b) **CoPy^{bipy}Cb** generated from **Co$_2$^{bipy}Cb$_2$** in pyridine.Since the carborane cage is prone to deboronation by halogens, we attempted to synthesize the *closo* metal complexes using the metal PF_6 salts as the transition metal sources. The syntheses were as yet unsuccessful – **^{bipy}Cb** had limited solubility in acetonitrile whereas $M(PF_6)_2$ salts (M = Mn, Co, Fe) had minimal solubility in THF. Stirring 1 equivalent of each reagent together in either THF or acetonitrile resulted in a slurry which appeared unchanged overnight. Similarly, we tried reacting **^{bipy}Cb** with 1 equivalent of $Ni(PF_6)_2$ in THF overnight. Both reagents possessed excellent solubility in the selected solvent, but the corresponding NMR spectrum displayed solely unreacted **^{bipy}Cb**. We suspect that *closo*-carborane, **^{bipy}Cb**, does not coordinate well to transition metals found in NMCs.

4.2.4. DFT Calculations

DFT calculations were performed by our collaborator, Prof. Roman Dobrovetsky at Tel Aviv University, using the **Fe^{bipy}Cb** solid-state structure (Figure 4.7). We assumed a charge of 0 and a multiplicity of 3 using a BP86-D3/def2SVP basis set. The occupied molecular orbitals are on the metal center, except for the highest occupied molecular orbital (HOMO) (MO 147a) which is delocalized between the carborane cage and the metal center (Figure 4.11) The LUMO (MO 146b) is also carborane and metal-based which agrees with the redox events and assignments in Section 4.2.2. The next unoccupied molecular orbitals (MO), after the LUMO, are MO 147b and 148a/148b which are bipyridyl-based. This further supports the bipyridyl redox assignments observed in the CVs.

a) Occupied Molecular Orbitals

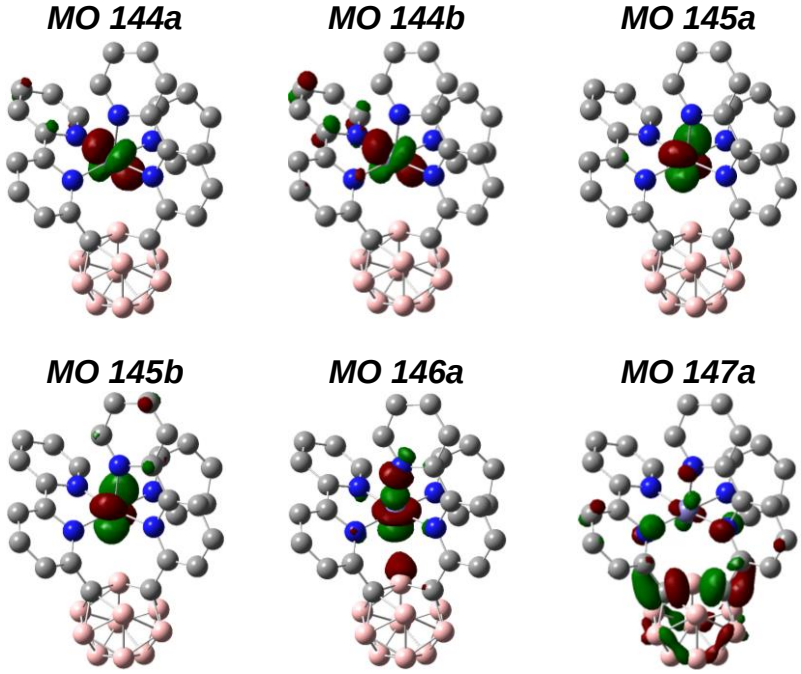

b) Unoccupied Molecular Orbitals

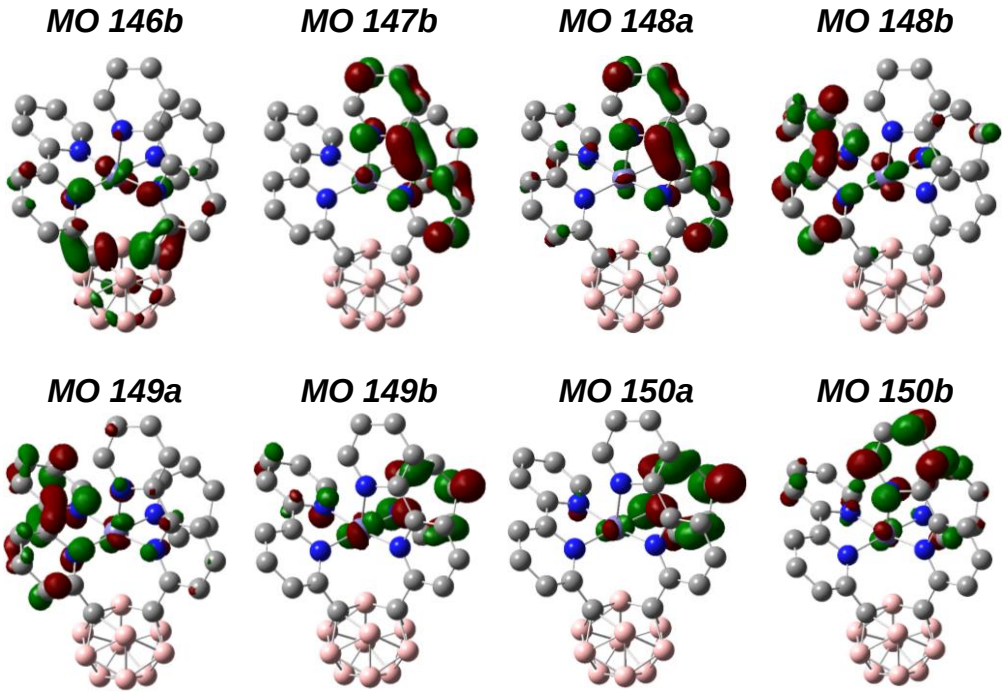

Figure 4.11. DFT Molecular Orbitals of **Fe^{bipy}Cb**. a) Occupied Molecular Orbitals. b) Unoccupied molecular orbitals.

4.2.5. Alternative Pyridine Syntheses

As described throughout Section 4.2.3., the transition metal-complexes with bipyridyl-based carboranes consistently adapt a 5-coordinate square planar geometry. We suspect that that with only 4 donor atoms in the bipyridyl analog, metal coordination is debilitated and an optimized extractant may contain 5 or 6 donor atoms, perhaps with terpyridine (terpy) moieties.

We attempted to synthesize the 1,2-bis(2,2';6',2''-terpyridyl)*o*-carborane (**^{tpy}Cb**) analog containing 6 donor atoms. We approached this synthetic challenge via two routes. In route 1, we tried a Stille-cross coupling reaction with **$^{Py(Cl)}$Cb** and reported 2-(tributylstannyl)bipyridine[39] (Scheme 4.4). However, the reaction did not proceed, and the starting materials were isolated. In route 2, a Stille cross-coupling between 2-chloro-6-fluoropyridine and 2-(tributylstannyl)bipyridine afforded 6-fluoro-2,2';6',2''-terpyridine, surprisingly a new molecule (Scheme 4.4).[40] Then, a S_NAr reaction between Cb and 6-fluoro-2,2';6',2''-terpyridine yielded exclusively the mono-substituted terpyridine derivative, 1-(2,2';6',2''-terpyridyl)*o*-carborane (**$^{mono\text{-}tpy}$Cb**) in a 32% yield.

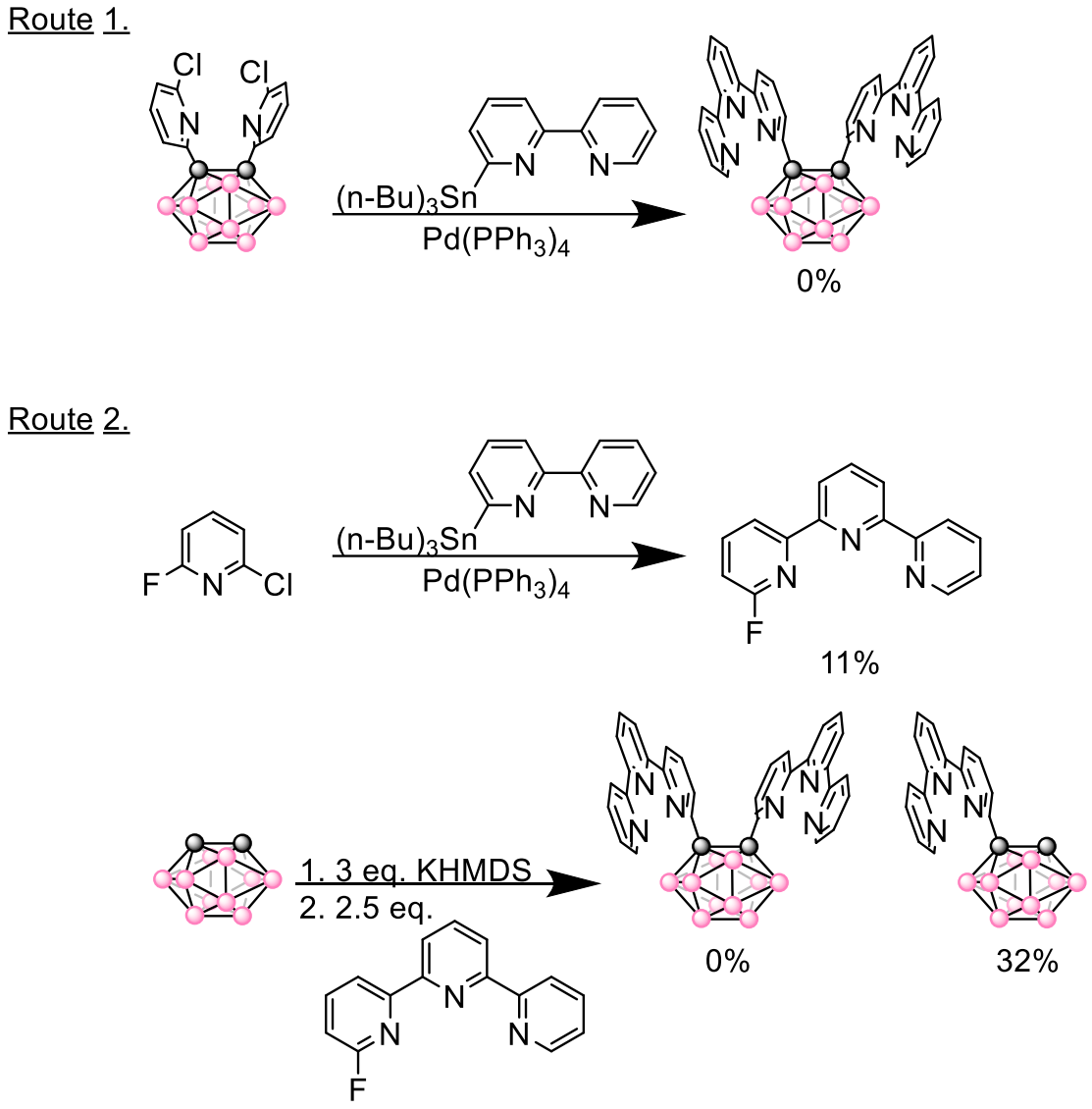

Scheme 4.4. Synthetic attempts for 1,2-bis(2,2';6',2''-terpyridyl)*o*-carborane.

We suggest that the synthetic approach via route 1 be repeated using $^{Py(Br)}$**Cb** as the starting carborane analog. We suspect that swapping a chloro substituent for bromo may increase reactivity. The synthetic approach via route 2 may be optimized to produce ^{tpy}**Cb** perhaps with excess 6-fluoro-2,2';6',2''-terpyridine and more concentrated reaction conditions.

Alternatively, an asymmetric carborane with terpy and bipy (1-(2,2'-bipyridyl)-2-(2,2';6',2''-terpyridyl)*o*-carborane could be an interesting, and also challenging synthetic target that likely has superb metal-coordinating abilities.

In summary, we believe that ligand design needs optimization in 3 key aspects: number of donor atoms, solubility, and formal reduction potential. We propose improving solubility by installing methyl substituents onto the bipyridyl rings. We suggest increasing the number of donor atoms and anodically shifting the *closo/nido* reduction potential for water stability by incorporating an electron-withdrawing ketone onto the bipyridyl appendages. Deprotonated Cb is known to react with acyl chlorides to form ketones.[41] The 6-(acylchloride)-2,2'-bipyridine can be retroactively synthesized in a high yielding 4-step procedure from 2,2'-bipyridine.[42] We suggest swapping 2,2'-bipyridine for the methylated analog, 3,3',4,4'-tetramethyl-2,2'-bipyridine.

4.3. Summary

We have described and optimized the synthesis of new 1,2-bis(polypyridyl)-substituted carboranes. We find that the leaving group plays a critical role in reaction success while steric factors of polypyridyl reagents may impede reaction progression. We have studied the electrochemical behavior of 1,2-bis(2,2'-bipyridyl)*o*-carborane with transition metals and group one and group two metals. We observed that the *nido*-carborane coordinates to Li^+ and Ca^{2+}, evidenced by stabilization of the LUMOs, but the *nido* oxidation remained unchanged. However, with transition metals (Mn^{2+}, Fe^{2+}, Co^{2+}, Ni^{2+}) a considerable anodic shift in *nido* oxidation was observed which we correlated to the binding affinity, log K. $^{\mathbf{bipy}}\mathbf{Cb}^{\mathbf{2-}}$ coordinates most strongly to increasingly Lewis acidic metals: $Ni^{2+} > Co^{2+} > Fe^{2+} > Mn^{2+} >> Ca^{2+} > Li^+$. We have structurally characterized the Co-carborane and Fe-carborane derivatives and in both

cases note a square pyramidal geometry. We propose optimizing the transition metal capture agent with improved selectivity and stability by incorporating carbonyl moieties onto the bipyridyl appendages and boosting solubility with methyl substituents.

4.4. Experimental

4.4.1. General Methods and Considerations

General Considerations

All manipulations were performed under an atmosphere of dry, oxygen-free N_2 or Ar by means of standard Schlenk or glovebox techniques (MBraun equipped with a -38 °C freezer, or VAC gloveboxes). Hexanes, pentane, DCM, THF, diethyl ether and benzene were dried on an MBraun solvent purification system. All solvents were stored over molecular sieves (3Å, Fisher). *Ortho*-carborane was purchased from Boron Specialties and sublimed before use. $[Bu_4N][PF_6]$ was purchased from Oakwood Chemicals and purified by twice recrystallizing from hot ethanol. The recrystallized product was then washed with cold water, cold ethanol, and pentane prior to drying at 100 °C under vacuum for 24 h. KC_8 was prepared using literature methods.[43] Cobalt(II)bromide dimethoxyethane, iron(II)bromide dimethoxyethane, and nickel(II) bromide were purchased and used as received from Strem Chemicals. Solid potassium bis(trimethylsilyl)amide and 85% 2-(tributylstannyl)pyridine were purchased and used as received from Sigma Aldrich. 2-chloro-6-fluoropyridine and 2-bromo-6-fluoropyridine were purchased from Oakwood Chemical and used as received.

Physical Measurements

NMR spectra were obtained in a Bruker Avance NEO 500 MHz or Agilent Technologies 400 MHz spectrometer. All NMR spectra were referenced to the residual ^1H resonance from the deuterated solvent in the ^1H spectrum according to IUPAC recommended method with the

TMS ^{1}H resonance at 0 ppm. ^{19}F, ^{31}P and ^{11}B NMR spectra were referenced indirectly using the ^{1}H NMR spectrum or externally (^{11}B: 85% $(Et_2O)BF_3$, ^{31}P: 85% H_3PO_4, ^{19}F: CCl_3F). Chemical shifts (δ) are recorded in ppm.

Elemental analyses (C, N, H) were recorded at the University of California, Santa Barbara using an Exeter Analytical CE440 elemental analyser.

X-ray crystallography data were collected at the University of California, Santa Barbara on a Bruker KAPPA APEX II diffractometer equipped with an APEX II CCD detector using a TRIUMPH monochromator with a Mo Kα X-ray source (wavelength α = 0.71073 Å). The crystals were mounted on a cryoloop under Paratone-N oil, and all data were collected at 100(2) K using an Oxford nitrogen-gas cryostream system. A hemisphere of data was collected using ω scans with 0.5° frame widths (ω, angle between the X-ray source and the sample). Data collection and cell-parameter determination were conducted using the SMART program. Integration of the data frames and refinement of the final cell parameters were performed using SAINT software. Absorption correction of the data was carried out using SADABS. Structure determination was done using direct or Patterson methods and difference Fourier techniques. All hydrogen atom positions were idealized and rode on the atom of attachment. Structure solution, refinement, graphics, and creation of publication materials were performed using SHELXTL or OLEX.

Cyclic voltammetry was performed using a CH Instruments Electrochemical Analysis potentiostat, equipped with a 3-mm-diameter glassy carbon working electrode, 5 mM Ag/AgOTf reference electrode (BASi, non-aqueous reference electrode kit), and a Pt-wire counter electrode using a $[Bu_4N][PF_6]$ (0.1 M) solution as the supporting electrolyte in DMF. CVs were taken with 2.0 mM analyte unless otherwise stated. Cyclic voltammograms were

referenced to the Fc/Fc^+ redox couple. The glassy carbon working electrode was polished between each scan with diamond slurry (3 µm, 1 µm, 0.25 µm and 0.05 µm, Buehler MetaDiTM Supreme) on polishing pads (Buehler MasterTex) for 2 minutes per pad and sonicated in DI water for ~ 5 s. The Pt-wire counter electrode was rinsed with acetone and heated until bright red with a propane flame.

UV-Visible Spectroscopy was performed using an Agilent 8543 or a Shimadzu UV-2401PC spectrophotometer with screw top quartz cuvettes supplied from Starna Cells Inc. Stepwise dilutions were prepared by mass in DMF.

4.4.2. Synthesis of Compounds

Precursor Synthesis: 6-fluoro-2,2'-bipyryidine was synthesized using reported literature methods.[19] 6-Tributylstannyl-2,2'-bipyridine was synthesized using literature procedures.[39]

General Procedure for Synthesis of $M(PF_6)_2$ Salts: A slurry of the MX_2 salt ($MnCl_2$, $NiBr_2$, $CoCl_2$, or $FeCl_2$) (1 equiv., 1.28 mmol) was stirred in 2 ml of MeCN. $AgPF_6$ (2 equiv., 2.57 mmol) dissolved in acetonitrile was added to the slurry. A white solid began precipitating out. The stirring was discontinued after 16 hours. The reaction was vacuum filtered over a celite plug and the filtrate was taken to dryness. The $M(PF_6)_2$ salts were purified by bulk recrystallizations at -40 ^oC by layering with MeCN ($Mn(PF_6)_2$, $Fe(PF_6)_2$, $Co(PF_6)_2$) or THF ($Ni(PF_6)_2$) and diethyl ether.

Synthesis of Compounds:

1,2-bis(2-chloropyridyl)*o*-carborane ($^{(Cl)Py}$Cb)

Under inert atmosphere, *o*-carborane (1.0 g, 6.9 mmol) was dissolved in minimal diethyl ether (5 mL) and stirred. Solid KHDMS (4.12 g, 20.7 mmol) was dissolved in minimal diethyl ether (7 mL) and added to the stirring carborane solution. The reaction stirred for an hour. The

reaction was cooled to 0 ^{o}C and the 2-chloro-6-fluoropyridine (2.72 g, 20.7 mmol) was added. It was allowed to stir at room temperature for 16 hours as it became dark brown. The pH was neutralized (pH ≈ 7-8) with an aqueous ammonium chloride solution. The reaction was extracted with ethyl acetate (3 x 20 mL) and washed with brine (1 x 30 mL). It was dried over $MgSO_4$, filtered and the volatiles were removed in vacuo. The product was purified by column chromatography using an eluent mixture of 15% DCM/hexanes. A white solid was obtained. (0.85 g, 33.5% yield). Crystals suitable for XRD were obtained via vapor diffusion of a DCM/iso-octane mixture. **^{1}H NMR (400 MHz, $CDCl_3$)** δ 7.66 (d, J = 7.7 Hz, 1H), 7.60 (t, J = 7.8 Hz, 1H), 7.20 (d, J = 7.7 Hz, 1H). **^{11}B{^{1}H} NMR (128 MHz, $CDCl_3$)** δ -2.14, -9.81. *Anal. Calcd.* for $B_{10}C_{12}N_2Cl_2H_{16}$: C, 39.24; H, 4.39; N, 7.63. *Found*: C, 38.85; H, 4.42; N, 7.39.

1,2-bis(2-bromopyridyl)*o*-carborane ($^{(Br)Py}$Cb)

Under inert atmosphere, *o*-carborane (1.0 g, 6.9 mmol) was dissolved in minimal diethyl ether (5 mL) and stirred. Solid KHDMS (4.12 g, 20.7 mmol) was dissolved in minimal diethyl ether (7 mL) and added to the stirring carborane solution. The reaction stirred for an hour. The reaction was cooled to 0 ^{o}C and the 2-bromo-6-fluoropyridine (3.64 g, 20.7 mmol) was added. it was allowed to stir at room temperature for 16 hours as it became dark brown. The pH was neutralized (pH ≈ 7-8) with an aqueous ammonium chloride solution. The reaction was extracted with ethyl acetate (3 x 20 mL) and washed with brine (1 x 30 mL). It was dried over $MgSO_4$, filtered and the volatiles were removed in vacuo. The product was purified by column chromatography using an eluent mixture of 10% DCM/hexanes. A white solid was obtained. (2.47 g, 78.5% yield). Crystals suitable for XRD were obtained via slow evaporation from a concentrated ethyl acetate solution. **^{1}H{^{11}B} NMR (500 MHz, $CDCl_3$)** δ 7.69 (d, J = 7.8 Hz,

2H), 7.50 (t, J = 7.9 Hz, 2H), 7.36 (d, J = 7.9 Hz, 2H), 3.30 (s, 2 H), 2.56-2.41 (m, 8 H). **^{11}B{^{1}H} NMR (160 MHz, $CDCl_3$)** δ -2.13, -9.88.

1,2-bis(2,2'-bipyryidyl)*o*-carborane (^{bipy}Cb)

In a Schlenk flask, **$^{(Br)Py}$Cb** (0.75 g, 1.64 mmol) and $Pd(PPh_3)_4$ (0.189 g, 0.164 mmol) were dissolved in 15 mL of toluene. 85% 2-(tributylstannyl)pyridine (1.32 mL, 3.45 mmol) was added to the stirring solution. The reaction was heated to reflux and stirred for 2 days. Afterwards, it was cooled to room temperature and the volatiles were removed in vacuo. A brown sludge was obtained and purified by column chromatography (10% ethyl acetate/hexanes) on alumina. Then, it was recrystallized in hot DCM with hexanes layered on top at -40 ^{o}C. A white solid was obtained (0.47 g, 63.1% yield). Crystals suitable for XRD were obtained via vapor diffusion of DCM and hexanes. **^{1}H{^{11}B} NMR (400 MHz, $CDCl_3$)** δ 8.54 (d, *J* = 5.0 Hz, 2H), 8.15 (d, *J* = 7.7 Hz, 2H), 8.07 (d, *J* = 8.0 Hz, 2H), 7.68 (d, *J* = 8.9 Hz, 2H), 7.60 (dd, *J* = 7.9, 7.9 Hz, 4H), 7.23 (d, *J* = 5.8 Hz, 2H) 3.65 (s, 2 H), 2.65-2.45 (m, 8 H). **^{11}B NMR{^{1}H} (128 MHz, $CDCl_3$)** δ -2.30, -10.09. *Anal. Calcd.* for $B_{10}C_{22}N_4H_{24}$: C, 58.39; H, 5.35; N, 12.38. *Found*: C, 58.19; H, 5.44; N, 11.93.

Potassium 1,2-bis(2,2'-bipyryidyl)*o*-carborane MeCN (K_2^{bipy}Cb)

KC_8 (0.154 g, 1.14 mmol) submerged in 2 ml of THF was cooled with liquid N_2 in the cold well until frozen. **^{bipy}Cb** (0.207 g, 0.455 mmol) was dissolved in THF and added dropwise to the KC_8 portion in the cold well. Once the addition was complete, it was cooled until frozen solid. Then, it was allowed to warm to room temperature and stirred for an hour and a half. It was filtered over a celite plug and extracted with acetonitrile. The reaction was taken to dryness and rinsed with diethyl ether (2 x 5mL). It was purified by recrystallization from layered acetonitrile and diethyl ether at -40 ^{o}C. An orange-red solid was obtained (0.25 g,

96.5% yield). Crystals suitable for XRD studies were obtained via vapor diffusion of THF and hexanes with 18-crown-6. **^{1}H NMR (500 MHz, CD_3CN)** δ 8.58 (s, 2H), 8.11 (d, *J* = 8.1 Hz, 2H), 7.80 (dd, *J* = 7.8, 7.8 Hz, 2H), 7.42 (d, *J* = 7.5 Hz, 2H), 7.35 (dd, *J* = 7.6, 7.6 Hz, 2H), 7.31 – 7.24 (m, 4H). **^{11}B{^{1}H} NMR (160 MHz, CD_3CN)** δ 5.27, -8.70, -17.71, -29.58. **^{11}B NMR (160 MHz, CD_3CN)** δ -8.70 (d, *J* = 124.6 Hz), -17.71 (d, *J* = 129.3 Hz), -29.58 (d, *J* = 121.7 Hz).

General Procedure for Synthesis of metal-^{bipy}Cb complexes: K_2^{bipy}Cb•MeCN (0.030 g, 0.052 mmol) was cooled to -78 ºC in 2 ml of THF. The metal halide ($MnCl_2$, $FeBr_2$•DME, $CoBr_2$•DME, $NiBr_2$) (1 equiv., 0.052 mmol) was partially dissolved in 2 mL of THF and added to the carborane. It stirred at room temperature overnight. It was taken to dryness and washed with diethyl ether (3x 5 ml). It was then filtered through a celite plug with THF, then acetonitrile, and then pyridine. The extracts were collected and dried down.

Fe^{2+} *nido*-1,2-bis(2,2'-bipyryidyl)*o*-carborane (**Fe^{bipy}Cb**)

Brown solid: (0.028 g, 92% yield). Crystals suitable for XRD studies were obtained by vapor diffusion of pyridine and diethyl ether. **^{1}H NMR (400 MHz, C_5D_5N)** NMR silent. **^{11}B{^{1}H} NMR (128 MHz, C_5D_5N)** NMR silent.

Bis(cobalt(II) *nido*-1,2-bis(2,2'-bipyryidyl)*o*-carborane) (**$Co_2^{bipy}Cb_2$**)

Brown solid: (0.025 g, 93% yield). Crystals suitable for XRD studies were obtained by vapor diffusion of THF and hexanes. **^{1}H NMR (400 MHz, C_5D_5N)** δ 4.30 – 0.13 (m, 10H). NMR silent. **^{11}B{^{1}H} NMR (128 MHz, C_5D_5N)** δ -2.14, -9.73.

Ni^{2+} *nido*-1,2-bis(2,2'-bipyryidyl)*o*-carborane (**Ni^{bipy}Cb**)

Steel-blue solid: (0.015 g, 56% yield). **^{1}H NMR (400 MHz, C_4D_8O)** (δ 8.50 (bs, 2H), δ 8.23 (bs, 2H), δ 8.14 (bs, 2H), δ 7.78–7.71 (m, 6H), δ 7.27 (bs, 2H),) **^{11}B{^{1}H} NMR (128 MHz, C_4D_8O)** δ -0.63, -8.27.

6-fluoro-2,2';6',2"-terpyridine

A Schlenk flask was charged with 2-chloro-6-fluoropyridine (0.200 g, 1.52 mmol) along with 90% purity 2-(tributylstannyl)pyridine (0.750 g, 1.52 mmol) and $Pd(PPh_3)_4$ (0.105 g, 0.15 mmol) dissolved in 20 mL of toluene. The reaction was heated to reflux and stirred for 24 hours. The reaction was cooled and stirred with saturated aqueous NH_4Cl for an hour. Following workup with organic extractions (ethyl acetate 3 x 10 mL) and brine wash (1 x 10 mL), the reaction was dried over $MgSO_4$ and taken to dryness. A brown solid was obtained which was purified by column chromatography (60% DCM / hexanes) on alumina. It was then further purified by recrystallizing from hot hexanes at -40 ^{o}C. A white solid was obtained (0.043 g, 11.2% yield). **^{1}H NMR (400 MHz, $CDCl_3$)** δ 8.70 (d, *J* = 4.9 Hz, 1H), 8.59 (d, *J* = 8.0 Hz, 1H), 8.52 (d, *J* = 7.4 Hz, 1H), 8.46 (d, *J* = 7.8 Hz, 1H), 8.39 (d, *J* = 7.8 Hz, 1H), 7.96 (dd, *J* = 7.9, 2.2 Hz, 2H), 7.86 (dd, *J* = 7.7, 7.7 Hz, 1H), 7.34 (dd, *J* = 6.2, 6.2 Hz, 1H), 6.97 (d, *J* = 8.1 Hz, 1H). **^{19}F NMR (376 MHz, $CDCl_3$)** δ -67.52.

1-(2,2';6',2"-terpyridyl)*o*-carborane ($^{mono\text{-}tpy}$Cb)

The *o*-carborane (0.010 g, 0.068 mmol) and KHMDS (0.042 g, 0.21 mmol) were dissolved in 1 mL of diethyl ether and stirred for an hour. 6-fluoro-2,2';6',2"-terpyridine (0.043 g, 0.171 mmol) was added and rinsed with 1 mL of diethyl ether. The reaction stirred overnight. The pH was neutralized (pH ≈ 7-8) with an aqueous ammonium chloride solution. The reaction was extracted with ethyl acetate (3 x 10 mL) and washed with brine (1 x 10 mL). It was dried over $MgSO_4$, filtered and the volatiles were removed in vacuo. The product was purified by

column chromatography (30% DCM/hexanes) on alumina. A white solid was obtained (0.009 g, 32% yield). **^{1}H NMR (400 MHz, $CDCl_3$)** δ 8.71 (d, *J* = 4.8 Hz, 1H), 8.64 (d, *J* = 7.9 Hz, 3H), 8.57 (d, *J* = 7.9 Hz, 2H), 8.50 (d, *J* = 7.8 Hz, 2H), 8.29 (d, *J* = 7.8 Hz, 3H), 7.98 (dd, *J* = 7.8, 7.8 Hz, 4H), 7.92 – 7.82 (m, 5H), 7.59 (d, *J* = 7.8 Hz, 3H), 7.35 (dd, *J* = 6.3, 4.7 Hz, 2H). **^{11}B NMR (128 MHz, $CDCl_3$)** δ -3.06, -3.94, -8.42, -11.33, -13.19.

4.5. References

(1) Shahan, Z. *US Electric Car Sales Increased 65% In 2022*. CleanTechnica, 2023. https://cleantechnica.com/2023/02/25/us-electric-car-sales-increased-65-in-2022/#:~:text=Here%20are%20the%20BEV%20totals,2020%20%E2%80%94%20245%2C586 (accessed 2023 7/16/23).

(2) IEA. Global EV Outlook 2022. IEA, Ed.; 2022.

(3) Simon Jessop, D. S., Jonathan Saul. *UN climate summit lands pledges to slash emissions from cars, planes and ships*. 2021. https://www.reuters.com/business/cop/un-climate-summit-lands-pledges-slash-emissions-cars-planes-ships-2021-11-10/ (accessed 2023 7/16/23).

(4) IEA. Critical Minerals Market Review 2023. IEA: 2023.

(5) Choi, J. U.; Voronina, N.; Sun, Y.-K.; Myung, S.-T. Recent Progress and Perspective of Advanced High-Energy Co-Less Ni-Rich Cathodes for Li-Ion Batteries: Yesterday, Today, and Tomorrow. *Adv. Energy Mater.* **2020**, *10* (42), 2002027. DOI: https://doi.org/10.1002/aenm.202002027.

(6) Institute, C. *Cobalt Mining*. Cobalt Institute, 2021. https://www.cobaltinstitute.org/about-cobalt/cobalt-life-cycle/cobalt-mining/ (accessed 7/18/2023).

(7) Labor, U. S. D. o. 2021 Findings on the Worst Forms of Child Labor. Labor, U. S. D. o., Ed.; United States Department of Labor: 2022; pp 393-406.

(8) Energy, U. S. D. o. Research Plan to Reduce, Recycle, and Recover Critical Materials in Lithium-Ion Batteries. Energy, D. o., Ed.; 2019.

(9) Makuza, B.; Tian, Q.; Guo, X.; Chattopadhyay, K.; Yu, D. Pyrometallurgical options for recycling spent lithium-ion batteries: A comprehensive review. *Journal of Power Sources* **2021**, *491*, 229622. DOI: https://doi.org/10.1016/j.jpowsour.2021.229622.

(10) Bae, H.; Kim, Y. Technologies of lithium recycling from waste lithium ion batteries: a review. *Mater. Adv.* **2021**, *2* (10), 3234-3250. DOI: 10.1039/d1ma00216c.

(11) Su, X. Electrochemical Separations for Metal Recycling. *The Electrochemical Society Interface* **2020**, *29* (3), 55. DOI: 10.1149/2.F08203IF.

(12) Kim, K.; Candeago, R.; Rim, G.; Raymond, D.; Park, A.-H. A.; Su, X. Electrochemical approaches for selective recovery of critical elements in hydrometallurgical processes of complex feedstocks. *iScience* **2021**, *24* (5), 102374. DOI: https://doi.org/10.1016/j.isci.2021.102374.

(13) Le, M. N.; Lee, M. S. Solvent Extraction of Co(II) and Cu(II) from Hydrochloric Acid Solution of Spent Lithium-ion Batteries Containing Li(I), Mn(II), and Ni(II). *Resources Recycling* **2020**, *29* (5), 73-80. DOI: 10.7844/kirr.2020.29.5.73.

(14) Torkaman, R.; Asadollahzadeh, M.; Torab-Mostaedi, M.; Ghanadi Maragheh, M. Recovery of cobalt from spent lithium ion batteries by using acidic and basic extractants in solvent extraction process. *Separation and Purification Technology* **2017**, *186*, 318-325. DOI: https://doi.org/10.1016/j.seppur.2017.06.023.

(15) Bowman, A. C.; England, J.; Sproules, S.; Weyhermüller, T.; Wieghardt, K. Electronic Structures of Homoleptic [Tris(2,2′-bipyridine)M]n Complexes of the Early Transition Metals (M = Sc, Y, Ti, Zr, Hf, V, Nb, Ta; n = 1+, 0, 1–, 2–, 3−): An Experimental and Density

Functional Theoretical Study. *Inorg. Chem.* **2013**, *52* (4), 2242-2256. DOI: 10.1021/ic302799s.

(16) Luo, S.-P.; Tang, L.-Z.; Zhan, S.-Z. A cobalt(II) complex of 2,2-bipyridine, a catalyst for electro- and photo-catalytic hydrogen production in purely aqueous media. *Inorg. Chem. Commun.* **2017**, *86*, 276-280. DOI: https://doi.org/10.1016/j.inoche.2017.10.027.

(17) Jin, R.-F.; Yang, S.-Y.; Li, H.-M.; Long, L.-S.; Huang, R.-B.; Zheng, L.-S. Effect of ionic radius on the assemblies of first row transition metal–5-tert-butylisophthalates–(2,2′-bipyridine or phenanthroline) coordination compounds. *CrystEngComm* **2012**, *14* (4), 1301-1316. DOI: 10.1039/C1CE05959A.

(18) Anderson, K. P.; Mills, H. A.; Mao, C.; Kirlikovali, K. O.; Axtell, J. C.; Rheingold, A. L.; Spokoyny, A. M. Improved synthesis of icosahedral carboranes containing exopolyhedral BC and CC bonds. *Tetrahedron* **2019**, *75* (2), 187-191. DOI: https://doi.org/10.1016/j.tet.2018.11.040.

(19) Ren, W.; Li, J.; Zou, D.; Wu, Y.; Wu, Y. Palladium-catalyzed Suzuki–Miyaura cross-coupling reaction of potassium 2-pyridyl trifluoroborate with aryl (heteroaryl) halides. *Tetrahedron* **2012**, *68* (5), 1351-1358. DOI: https://doi.org/10.1016/j.tet.2011.12.036.

(20) Li, X.; Tong, X.; Yin, Y.; Yan, H.; Lu, C.; Huang, W.; Zhao, Q. Using highly emissive and environmentally sensitive o-carborane-functionalized metallophosphors to monitor mitochondrial polarity. *Chem. Sci.* **2017**, *8* (9), 5930-5940. DOI: 10.1039/C7SC00160F.

(21) Li, B.; Geoghegan, B. L.; Wölper, C.; Cutsail, G. E., III; Schulz, S. Redox Activity of Noninnocent 2,2′-Bipyridine in Zinc Complexes: An Experimental and Theoretical Study. *ACS Omega* **2021**, *6* (28), 18325-18332. DOI: 10.1021/acsomega.1c02201.

(22) Scarborough, C. C.; Wieghardt, K. Electronic Structure of 2,2′-Bipyridine Organotransition-Metal Complexes. Establishing the Ligand Oxidation Level by Density Functional Theoretical Calculations. *Inorg. Chem.* **2011**, *50* (20), 9773-9793. DOI: 10.1021/ic2005419.

(23) Kryatov, S. V.; Mohanraj, B. S.; Tarasov, V. V.; Kryatova, O. P.; Rybak-Akimova, E. V.; Nuthakki, B.; Rusling, J. F.; Staples, R. J.; Nazarenko, A. Y. Nickel(II) Complexes with Tetra- and Pentadentate Aminopyridine Ligands: Synthesis, Structure, Electrochemistry, and Reduction to Nickel(I) Species. *Inorg. Chem.* **2002**, *41* (4), 923-930. DOI: 10.1021/ic010397n.

(24) Krueger, H. J.; Holm, R. H. Chemical and electrochemical reactivity of nickel(II,I) thiolate complexes: examples of ligand-based oxidation and metal-centered oxidative addition. *Inorg. Chem.* **1989**, *28* (6), 1148-1155. DOI: 10.1021/ic00305a026.

(25) Nguyen, H. M.; Morgan, H. W. T.; Chantarojsiri, T.; Kerr, T. A.; Yang, J. Y.; Alexandrova, A. N.; Léonard, N. G. Charge and Solvent Effects on the Redox Behavior of Vanadyl Salen–Crown Complexes. *The Journal of Physical Chemistry A* **2023**, *127* (25), 5324-5334. DOI: 10.1021/acs.jpca.3c00827.

(26) Gangi, D. A.; Durand, R. R. Binding of carbon dioxide to cobalt and nickel tetra-aza macrocycles. *Journal of the Chemical Society, Chemical Communications* **1986**, (9), 697-699. DOI: 10.1039/C39860000697.

(27) Peterson, M.; Hunt, C.; Wang, Z.; Heinrich, S. E.; Wu, G.; Ménard, G. Synthesis, characterization, and electrochemical properties of a first-row metal phthalocyanine series. *Dalton Trans.* **2020**, *49* (45), 16268-16277. DOI: 10.1039/D0DT01372B.

(28) Al-Afyouni, M. H.; Krishnan, V. M.; Arman, H. D.; Tonzetich, Z. J. Synthesis and Reactivity of Manganese(II) Complexes Containing N-Heterocyclic Carbene Ligands. *Organometallics* **2015**, *34* (20), 5088-5094. DOI: 10.1021/acs.organomet.5b00684.

(29) Adams, C. J.; Baber, R. A.; Batsanov, A. S.; Bramham, G.; Charmant, J. P. H.; Haddow, M. F.; Howard, J. A. K.; Lam, W. H.; Lin, Z.; Marder, T. B.; et al. Synthesis and reactivity of cobalt boryl complexes. *Dalton Trans.* **2006**, (11), 1370-1373. DOI: 10.1039/B516594F.

(30) Salmahaminati; Abe, M.; Purnama, I.; Mulyana, J. Y.; Hada, M. Density Functional Study of Metal-to-Ligand Charge Transfer and Hole-Hopping in Ruthenium(II) Complexes with Alkyl-Substituted Bipyridine Ligands. *ACS Omega* **2021**, *6* (1), 55-64. DOI: 10.1021/acsomega.0c01199.

(31) Ferrere, S. New photosensitizers based upon [FeII(L)2(CN)2] and [FeIIL3], where L is substituted 2,2′-bipyridine. *Inorg. Chim. Acta* **2002**, *329* (1), 79-92. DOI: https://doi.org/10.1016/S0020-1693(01)00743-5.

(32) Adamson, A. W.; Demas, J. N. New photosensitizer. Tris(2,2'-bipyridine)ruthenium(II) chloride. *JACS* **1971**, *93* (7), 1800-1801. DOI: 10.1021/ja00736a049.

(33) Wakabayashi, T.; Kamada, K.; Sekizawa, K.; Sato, S.; Morikawa, T.; Jung, J.; Saito, S. Photocatalytic CO2 Reduction Using an Iron–Bipyridyl Complex Supported by Two Phosphines for Improving Catalyst Durability. *Organometallics* **2022**, *41* (14), 1865-1871. DOI: 10.1021/acs.organomet.2c00171.

(34) Karges, J.; Kuang, S.; Maschietto, F.; Blacque, O.; Ciofini, I.; Chao, H.; Gasser, G. Rationally designed ruthenium complexes for 1- and 2-photon photodynamic therapy. *Nat. Commun.* **2020**, *11* (1), 3262. DOI: 10.1038/s41467-020-16993-0.

(35) Guo, L.; Yu, X.; Du, J.; Li, W.; Bregadze, V.; Tu, D.; Lu, C.; Yan, H. Remote Effect from Boron Cluster: Tunable Photophysical Properties of o-Carborane-Based Luminogens. *Chem. Eur. J.* **2022**, *28* (33), e202200303. DOI: https://doi.org/10.1002/chem.202200303.

(36) Müller, I.; Schneider, C.; Pietzonka, C.; Kraus, F.; Werncke, C. G. Reduction of 2,2′-Bipyridine by Quasi-Linear 3d-Metal(I) Silylamides—A Structural and Spectroscopic Study. In *Inorganics*, 2019; Vol. 7.

(37) Yamaguchi, K.; Kume, S.; Namiki, K.; Murata, M.; Tamai, N.; Nishihara, H. UV−Vis, NMR, and Time-Resolved Spectroscopy Analysis of Photoisomerization Behavior of Three- and Six-Azobenzene-Bound Tris(bipyridine)cobalt Complexes. *Inorg. Chem.* **2005**, *44* (24), 9056-9067. DOI: 10.1021/ic0513538.

(38) Sun, F.; Tan, S.; Cao, H.-J.; Lu, C.-s.; Tu, D.; Poater, J.; Solà, M.; Yan, H. Facile Construction of New Hybrid Conjugation via Boron Cage Extension. *JACS* **2023**, *145* (6), 3577-3587. DOI: 10.1021/jacs.2c12526.

(39) Hanan, G. S.; Schubert, U. S.; Volkmer, D.; Rivière, E.; Lehn, J.-M.; Kyritsakas, N.; Fischer, J. Synthesis, structure, and properties of oligo-tridentate ligands; covalently assembled precursors of coordination arrays. *Canadian Journal of Chemistry* **1997**, *75* (2), 169-182. DOI: 10.1139/v97-020.

(40) Stefankiewicz, A. R.; Wałęsa-Chorab, M.; Harrowfield, J.; Kubicki, M.; Hnatejko, Z.; Korabik, M.; Patroniak, V. Self-assembly of transition metal ion complexes of a hybrid pyrazine–terpyridine ligand. *Dalton Trans.* **2013**, *42* (5), 1743-1751. DOI: 10.1039/C2DT31982A.

(41) Grimes, R. N. *Carboranes*; Academic Press, 2016.

(42) Zhu, Z.-H.; Li, Y.; Wang, Y.-B.; Lan, Z.-G.; Zhu, X.; Hao, X.-Q.; Song, M.-P. α-Alkylation of Nitriles with Alcohols Catalyzed by NNN′ Pincer Ru(II) Complexes Bearing Bipyridyl Imidazoline Ligands. *Organometallics* **2019**, *38* (9), 2156-2166. DOI: 10.1021/acs.organomet.9b00146.

(43) Lalancette, J.-M.; Rollin, G.; Dumas, P. Metals Intercalated in Graphite. I. Reduction and Oxidation. *Canadian Journal of Chemistry* **1972**, *50* (18), 3058-3062. DOI: 10.1139/v72-485.

Chapter 5 Other *O*-Carborane Derivatives

5.1. Introduction

In Chapter 5, we explore additional bis-1,2-substituted carborane derivatives and unravel new structural guidelines to consider when developing redox-switchable carborane-based ligands. Particularly, we were interested in switching the phosphine oxide donor moieties to different heteroatoms (sulfur) and functional groups (carboxyl and amide). We synthesized various carborane derivatives and report new structural characterization. We performed cyclic voltammetry and some preliminary metal binding experiments with the derivatized carboranes.

5.2. Results and Discussion

5.2.1. Carboxylic Acid Derivatives

In this section, we explored the use of bis-1,2- carboxylic and carboxylate donor groups adhered to *o*-carborane. We picked the carboxylate functional group, initially, because of the expected electron-withdrawing effects and the ease of synthesis. Accordingly, bis(1,2-carboxcylic acid)*o*-carborane (**^{COOH}Cb**) was synthesized according to literature procedures (Scheme 1.1).[1-3] Cb was deprotonated with 2 equivalents of *n*-BuLi in diethyl ether at −78 °C. The reaction was then stirred at room temperature for 2 hours and subsequently cooled back down to −78 °C. Excess dry ice pellets were added to the reaction under the flow of N_2 and the reaction stirred until reaching room temperature. Subsequently, 1 M HCl was added and following workup and recrystallization from toluene, **^{COOH}Cb** was obtained. Additionally, we obtained unreported carboxylate derivatives using modified literature procedures (Scheme 5.1). The lithium bis(1,2-carboxylate)*o*-carborane (**$Li_2{}^{COO}$Cb**) was obtained using analogous deprotonation and carboxylation procedures with *n*-BuLi and dry ice respectively. The

reaction was not acidified with HCl, instead weak base triethylamine was added to ensure a basic solution. The product was extracted into deionized water which was collected and dried. The product was dissolved in hot THF and recrystallized by layering with hexanes at −40 °C. A white solid was obtained in a 91% yield, corresponding to **$Li_2^{COO}Cb$**. A salt swap was performed by stirring **$Li_2^{COO}Cb$** with 2 equivalents of tetrabutylammonium bromide in THF. A white solid precipitated out after an hour of stirring. The reaction was subsequently filtered over a celite plug and the filtrate was collected to afford tetrabutylammonium bis(1,2-carboxylate)*o*-carborane (**$(Bu_4N)_2^{COO}Cb$**) in an 84% yield. **$(Bu_4N)_2^{COO}Cb$** displayed improved solubility in organic solvents.

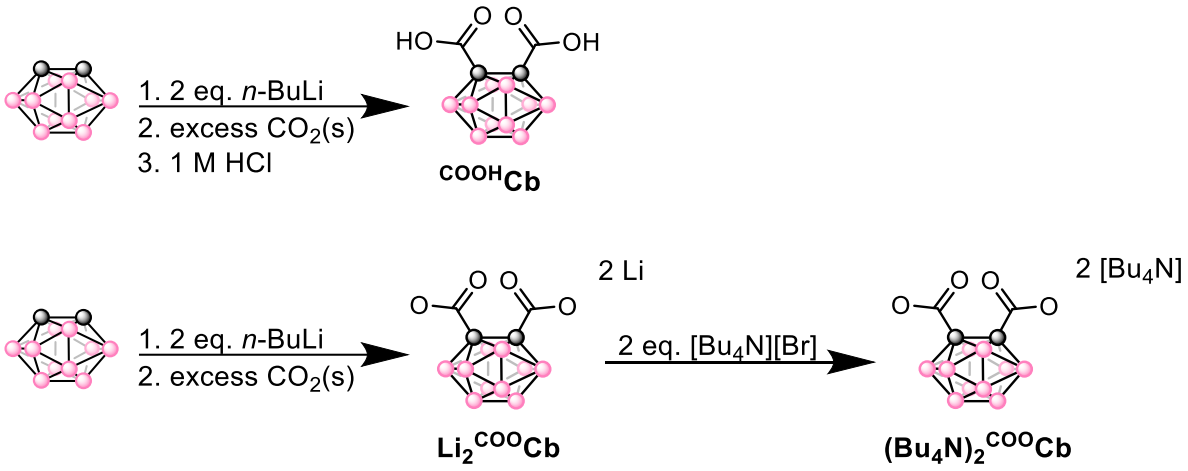

Scheme 5.1. Synthesis of carboxylic acid derivatized *o*-carboranes.

A solid-state molecular structure of **$Li_2^{COO}Cb$** was obtained via X-ray diffraction studies using a crystal grown from THF and hexanes (Figure 5.1). The carborane cage displayed a C−C bond length of 1.67(2) Å. The carboxylate C–O bond lengths (C_1–O_1, 1.237(2) Å; C_1–O_3, 1.32(2) Å; C_2–O_2, 1.31(2) Å; C_2–O_4, 1.20(2) Å) are consistent with those typically observed for carboxylic acids. Interestingly, the discrepancies in C–O bond lengths suggest that the charge is not fully delocalized across the COO^- units. A Li is bound between

two oxygens from opposing carboxylate appendages (Li_1–O_1, 1.93(3) Å; Li_1–O_2, 1.82(3) Å) and a co-crystallized THF molecule. The other Li is only bound to one carboxylate oxygen (Li_2–O_3, 1.85(3) Å) and an additional co-crystallized THF molecule. Thus, the remaining oxygen donor, O_4 is uncoordinated to a metal center.

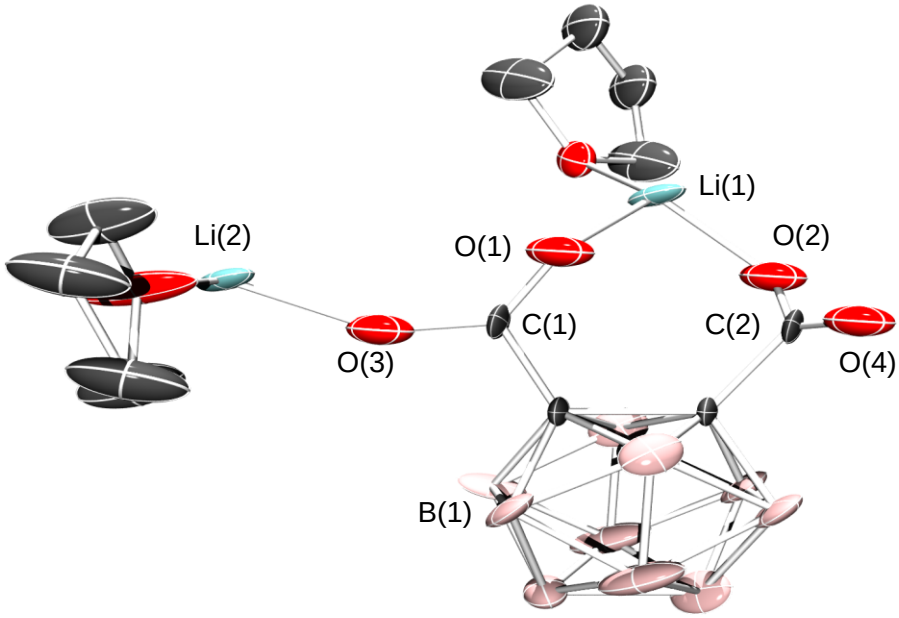

Figure 5.1. Solid-state molecular structure of **Li_2^{COO}Cb** obtained by single crystal X-ray diffraction studies. H atoms omitted for clarity.

We acquired the CVs of **^{COOH}Cb**, **Li_2^{COO}Cb**, and **$(Bu_4N)_2^{COO}$Cb** in 0.1 M [Bu_4N][PF_6] THF using a glassy carbon working electrode, Pt wire counter electrode, and Ag wire pseudo-reference electrode (Figure 5.2) The CV of **^{COOH}Cb** displayed a large cathodic peak at an onset potential of -2.1 V vs. Fc/Fc^+ (Figure 5.2). It appeared catalytic in shape which suggests that hydrogen evolution reaction (HER) may have been occurring with **^{COOH}Cb** as the proton source.[4] An anodic event was observed at 0.12 V which we suspect may correspond to the oxidation of *in situ* generated **$(Bu_4N)_2^{COO}$Cb**. Chemically synthesized **$(Bu_4N)_2^{COO}$Cb** also displayed an oxidation at 0.137 V. Here, the peak oxidative current is 4x

larger than the oxidation observed with **^{COOH}Cb**. This is reasonable considering the bulk concentration of chemically synthesized **$(Bu_4N)_2{}^{COO}$Cb** will be much larger than the concentration of electrogenerated **$(Bu_4N)_2{}^{COO}$Cb** from the HER of **^{COOH}Cb**. The CV of **$(Bu_4N)_2{}^{COO}$Cb** did not display a reduction in the scanned potential window. This confirms that the reduction observed for **^{COOH}Cb** was likely HER whereas **$(Bu_4N)_2{}^{COO}$Cb** lacks a sufficient proton source to participate in HER. The CV of **$Li_2{}^{COO}$Cb** appeared electrochemically inactive in the selected potential window (Figure 5.2). We suspect that the oxidation of **$Li_2{}^{COO}$Cb** is plausible, albeit at higher anodic potentials because strong binding with Li likely shifts the HOMO to lower energies and increases the oxidative stability of the compound.

This work demonstrated that carboxylic and carboxylate derivatized *o*-carboranes are not redox switchable. We did not observe cathodic redox behavior consistent with a carborane cage-based reduction. We advise against using acidic functional groups (COOH, CSSH) that may evolve hydrogen gas. Additionally, this work highlighted the importance of using neutral or electropositive carborane species. Anionic functional groups (-COO^-) are not very electron withdrawing so carborane-based redox events are inhibited or shifted to cathodic values that are inaccessible. Conversely, implementing electropositive cationic functional groups onto the carborane may have the reverse effect which could be an effective strategy for tuning redox behavior.

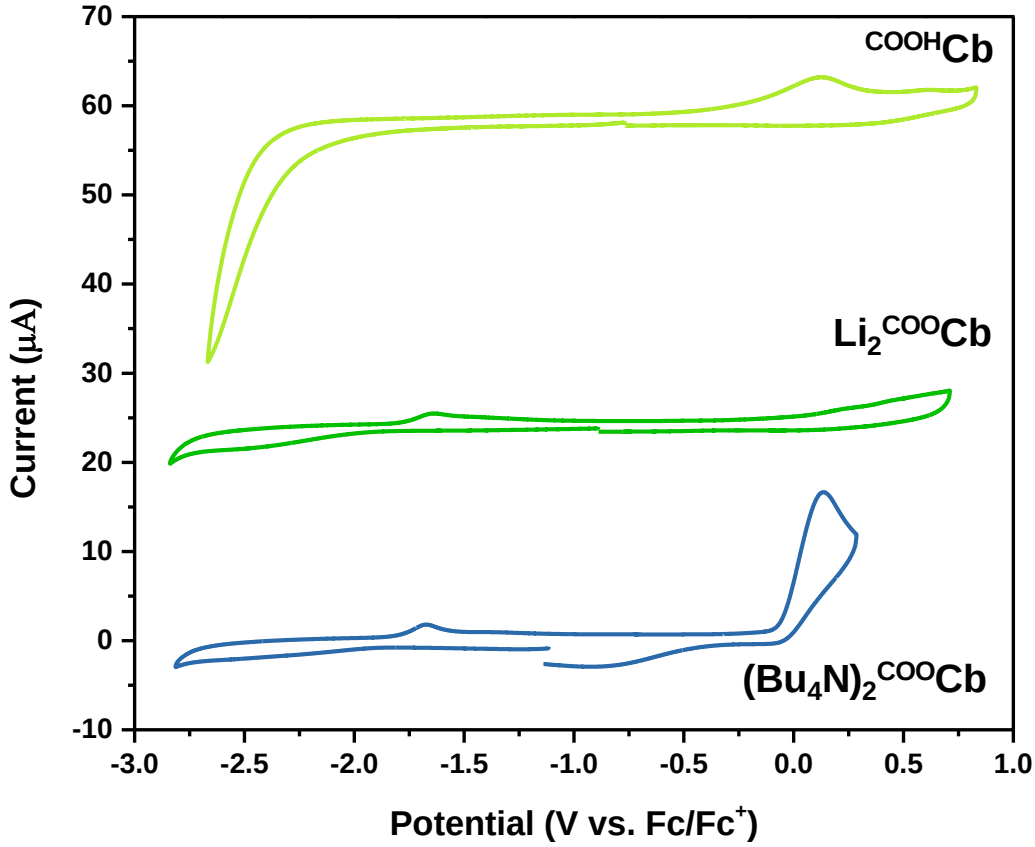

Figure 5.2. CVs of carboxylic acid-derivatized *o*-carboranes in 0.1 M [Bu_4N][PF_6] THF with 2.8 mM analyte at 100 mV/s. A glassy carbon working electrode, Ag wire pseudo-reference electrode, and a Pt wire counter electrode were used.

5.2.2. Amido Derivatives

We investigated the use of bis-1,2-amido functionalized *o*-carboranes. We suspected that they may possess interesting ligating properties to metals because of the additional donicity of the nitrogen atom. The amido carboranes were synthesized utilizing a modified literature procedure.[5, 6] In diethyl ether, Cb was deprotonated with 2 equivalents of *n*-BuLi at −78 °C. The reaction stirred at room temperature for 2 hours. Subsequently, the reaction was refluxed with 2 equivalents of phenyl isocyanate or 2,4-difluorophenyl isocyanate for 5 hours

and then neutralized with dilute HCl to afford reported analog bis(1,2-amido)*o*-carborane (**^{PhNO}Cb**) or new analog bis(1,2-(2,4-difluoroamido))*o*-carborane (**$^{(2F)PhNO}$Cb**) respectively (Scheme 5.2). The products were purified by column chromatography. The yield for **$^{(2F)PhNO}$Cb** (19%) was substantially lower than the yield of **^{PhNO}Cb** (49%) which was surprising since 2,4-difluorophenyl isocyanate is likely more electrophilic than phenyl isocyanate.

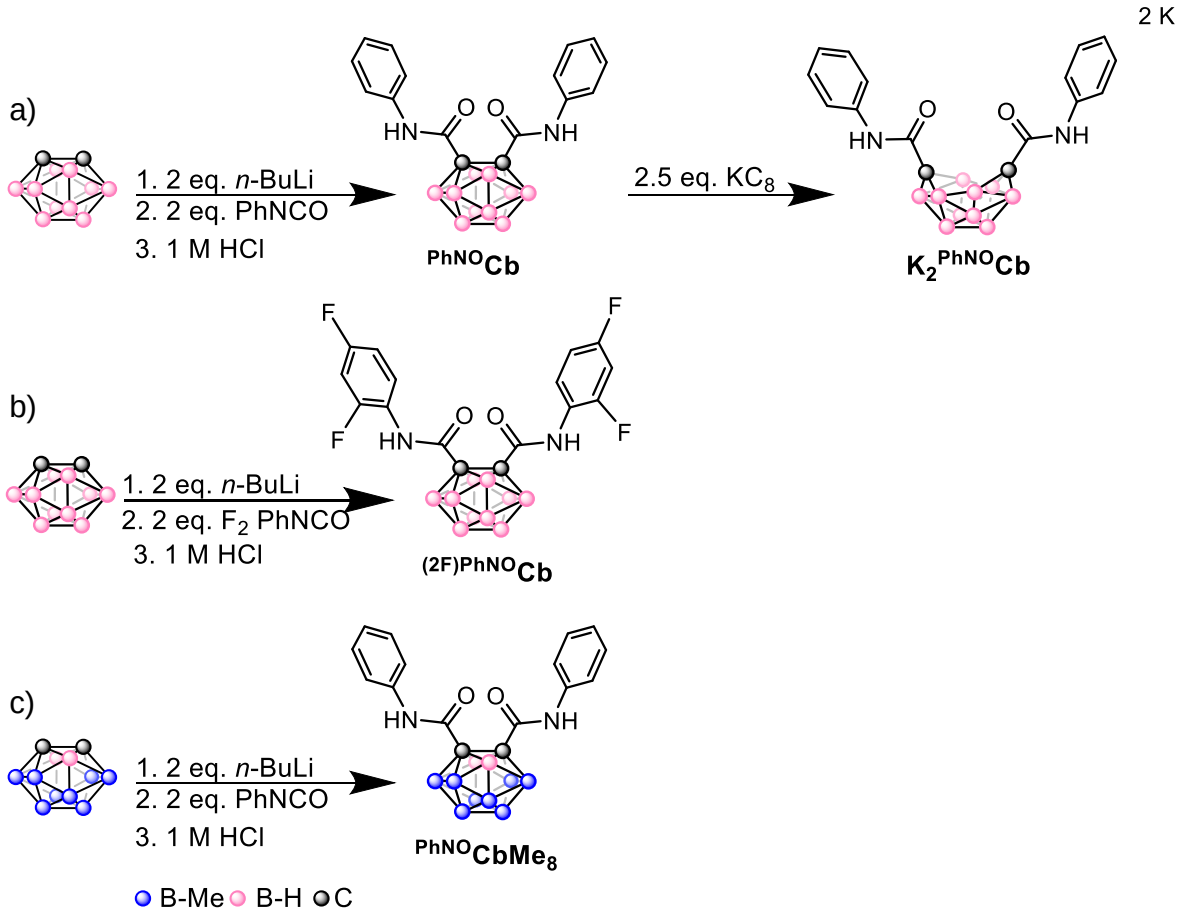

Scheme 5.2. Synthesis of amido-derivatized *o*-carboranes.

The B-octamethylated derivative was obtained analogously to **^{PhNO}Cb**, except we used 4,5,7,8,9,10,11,12-(octamethyl)-1,2-dicarba-*closo*-dodecaborane as the starting carborane species to afford 4,5,7,8,9,10,11,12-octamethyl-bis(1,2-amido)*o*-carborane (**^{PhNO}CbMe$_8$**) in

an 8% yield (Scheme 5.2c) Crystals suitable for X-ray diffraction studies were grown from slow evaporation of a concentrated solution of DCM and hexanes (Figure 5.3).

We chemically reduced ^{PhNO}**Cb** using a slight excess (2.5 equiv.) of KC_8 in THF at −78 °C. After stirring at room temperature for an hour, the reaction was filtered through a celite plug and the filtrate was taken to dryness to afford potassium *nido*-bis(1,2-amido)*o*-carborane (**K_2^{PhNO}Cb**) as a light green solid (Figure 5.3). The solid-state molecular structure of **K_2^{PhNO}Cb** was acquired by X-ray diffraction studies using single crystals grown from layering ether onto a concentrated solution in THF with 18-crown-6 at −40 °C (Figure 5.3).

The solid-state molecular structure of **K_2^{PhNO}Cb** crystallized with two carborane units encapsulating three K atoms between four amido appendages (Figure 5.3a). The remaining K was bound to an 18-crown-6 unit and is omitted from Figure 5.3 for clarity. The carborane C−C bonds are cleaved (2.791 Å and 2.790 Å) which confirmed a 2 e^- carborane-based reduction event. The phenyl rings, though omitted from Figure 5.3, are much further (~5 Å) from the central K_1 metal compared to the *nido*-(1,2-diphenylphosphine oxide)-carboranes bound to various metal centers.[7] This suggests that amido substituted carboranes are less sterically congested which may enhance metal coordination and decrease selectivity.

The solid-state molecular structure of ^{PhNO}**CbMe$_8$** is unremarkable with a C−C bond length of 1.67(2) Å (Figure 5.3b). The oxygens of the amido groups are pointing in opposing directions. The amido C−O bond lengths (1.2098(2) Å and 1.2166(2) Å) are typical for those containing double bond character.

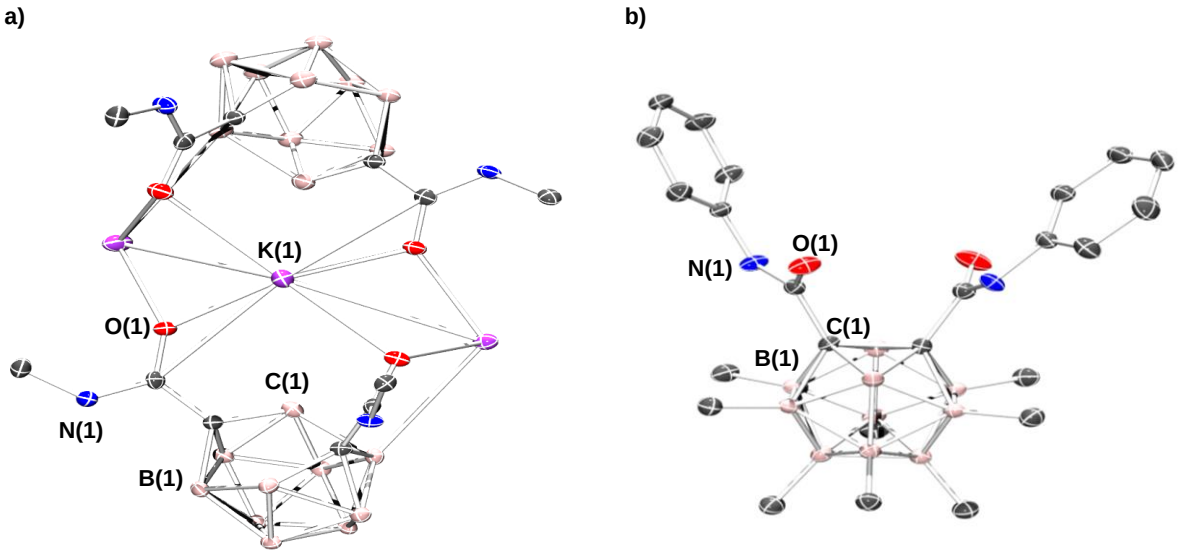

Figure 5.3. Solid-state molecular structures of amido-functionalized *o*-carboranes obtained by single crystal X-ray diffraction studies. H atoms omitted for clarity. a) $\mathbf{K_2{}^{PhNO}Cb}$. Cocrystallized solvent, K-18-crown-6, and phenyl rings omitted for clarity. b) $\mathbf{{}^{PhNO}CbMe_8}$

We performed cyclic voltammetry of the amido-substituted carboranes in 0.1 M $[Bu_4N][PF_6]$ THF. The CVs of $\mathbf{{}^{PhNO}Cb}$ (1.4 mM), $\mathbf{{}^{(2F)PhNO}Cb}$ (1.2 mM), and $\mathbf{{}^{PhNO}CbMe_8}$ (1.0 mM) displayed broad 2 e^- reductions which we attribute to C−C bond cleavage and cage rearrangements to *nido* forms (Figure 5.4). The *nido* oxidations appear to have occurred stepwise with two 1 e^- events. Interestingly, the CV of $\mathbf{{}^{PhNO}CbMe_8}$ became more reversible compared to $\mathbf{{}^{PhNO}Cb}$ or $\mathbf{{}^{(2F)PhNO}Cb}$ which we attribute to the increased steric bulk of the cage hindering reactive sites, as observed in the CVs of bis(1,2-diarylphosphine oxide)*o*-carboranes in Chapter 2 (Figure 2.6) and with *o*-carboranes bearing bulky substituents.[8] The amido-derivatized carboranes redox couples follow similar trends as the bis(1,2-diarylphosphine oxide)*o*-carboranes described in Chapter 2. Herein, both $\mathbf{{}^{PhNO}Cb}$ and $\mathbf{{}^{(2F)PhNO}Cb}$ have the same formal reduction potential ($E_{1/2}$ = -1.58 V vs Fc/Fc^+) (Figure 5.4). This indicates that altering the aryl substituents of bis(1,2-arylamido)*o*-carboranes is also an ineffective strategy for

tuning carborane cage redox properties. However, the redox couple of ^{PhNO}**CbMe$_8$** had a cathodic shift by 120 mV ($E_{1/2}$ = -1.70 V) (Figure 5.4). Again, this follows the same trend as detailed in Chapter 2 that methyl substituents behave as strong π-donor groups and cage substituents affect the carborane redox more dramatically.[9] We suggest using cage substituents to tune redox properties of *o*-carboranes instead of altering the substitution of 1,2-donor groups.

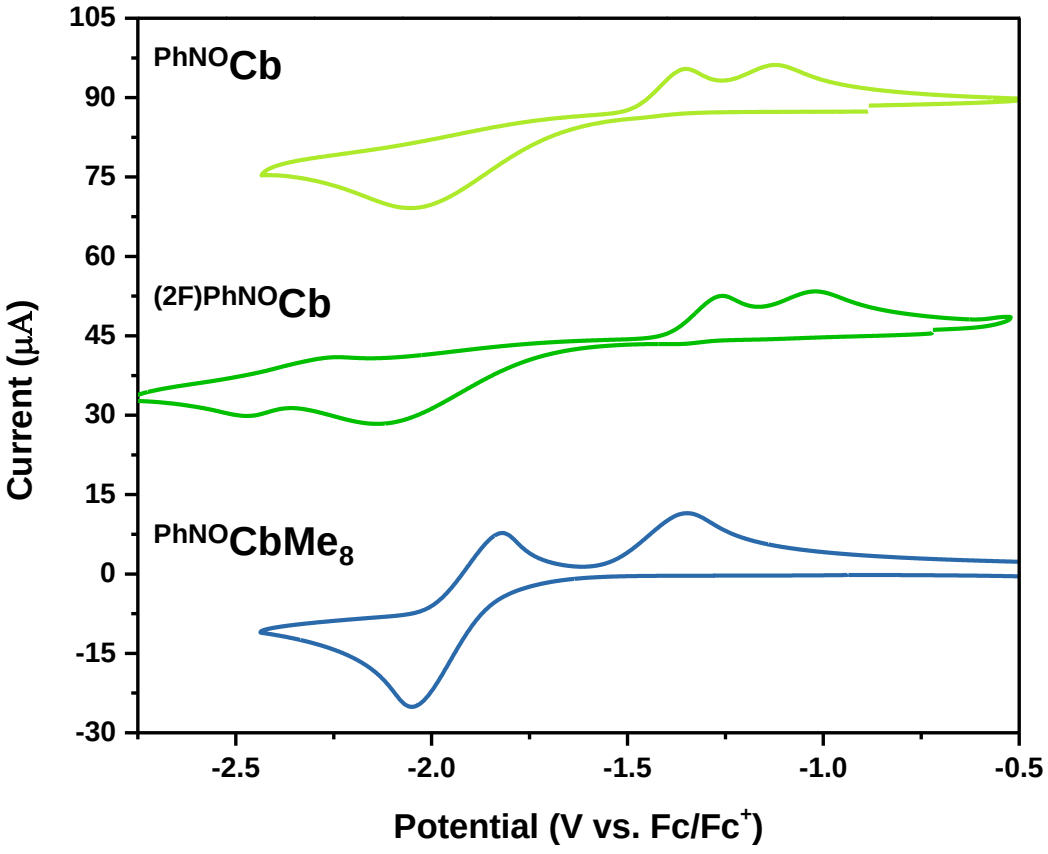

Figure 5.4. CVs of amido-substituted *o*-carboranes performed in 0.1 M [Bu_4N][PF_6] THF with a 100 mV/s scan rate. A glassy carbon working electrode, Ag wire pseudo-reference electrode, and Pt wire counter electrode were used. The analytes ^{PhNO}**Cb** (1.4 mM), $^{(2F)PhNO}$**Cb** (1.2 mM), and ^{PhNO}**CbMe$_8$** (1.0 mM) had varied concentrations.

We performed some preliminary metal binding studies using ^{PhNO}**Cb** and **K$_2$**^{PhNO}**Cb**. C*loso*-carborane, ^{PhNO}**Cb**, was stirred with 0.5 equivalents of $FeCl_3$ in DCM and the color changed from colorless to yellow-orange. After an hour, stirring was discontinued and the volatiles were removed *in vacuo*. ^{1}H and ^{11}B NMR spectra were acquired in CD_2Cl_2. The ^{1}H spectrum displayed paramagnetic ^{1}H resonances that were broadened and shifted upfield. The ^{11}B NMR spectra appeared unaltered. Surprisingly, these findings suggest that the *closo*-carborane ^{PhNO}**Cb** binds to Fe^{3+}. We suspect that the ligating ability in *closo* form arises from increased donicity at the C=O moiety due to the near proximity of donor atom N. Furthermore, the phenyl rings are a further distance from the ligating group, C=O, compared to P=O for bis(1,2-diarylphosphine oxide)*o*-carboranes, which we suspect reduces steric repulsion and improves *closo* metal coordination. We performed an analogous binding experiment in DCM with 1 equivalent of ^{PhNO}**Cb** and 3 equivalents of $LiPF_6$. The $LiPF_6$ appeared insoluble in DCM. After stirring for an hour, ^{1}H, ^{11}B and ^{7}Li NMR spectra were acquired in CD_2Cl_2. The ^{1}H and ^{11}B NMR resonances were unaltered and the ^{7}Li NMR was silent. We suspect that ^{PhNO}**Cb** does not coordinate strongly to Li^+. Similarly, ^{PhNO}**Cb** was stirred with 0.25 equivalents of $[UO_2Cl_2(THF)_2]_2$ in DCM overnight. ^{1}H and ^{11}B NMR spectra were taken in CD_2Cl_2 and displayed no change in resonances. Accordingly, ^{PhNO}**Cb** does not coordinate strongly to UO_2^{2+}.

Next, we stirred *nido*-carborane, **K$_2$**^{PhNO}**Cb**, with 0.25 equivalents of $[UO_2Cl_2(THF)_2]_2$ in DCM. The color changed immediately from light green to brown. After 2 hours, the reaction was filtered over a celite plug. A brown solid remained on top of the celite plug and a yellow filtrate was collected. The ^{1}H and ^{11}B NMR spectra of the yellow filtrate matched the ^{1}H and ^{11}B resonances of ^{PhNO}**Cb**, revealing that UO_2^{2+} is likely being reduced to UO_2(s) and the

carborane becomes oxidized from *nido*- to *closo*-carborane. This is unsurprising considering the $[UO_2I_2(THF)_2]_2$ is reduced to $UO_{2(s)}$ at a potential more anodic than the ^{PhNO}**Cb** *closo/nido* redox couple (Figure 2.7 and Figure 5.4).[10] For redox switchable metal capture and release, prudent consideration should be given to selecting substituted o-carboranes with anodically shifted formal reduction potentials compared to the metals of interest. We suspect that the formal reduction potentials of the carborane redox couple and the metals have a significant role in whether the ligand binds, or outer sphere electron transfer occurs.

5.2.3. Sulfido and Sulfoxyl Derivatives

We explored the use of sulfido and sulfoxyl *o*-carborane derivatives. We suspected that the sulfur analogs could be interesting for soft acid metal capture and release. We synthesized bis(1,2-phenylsulfido)*o*-carborane (**^{S}Cb**) using a literature procedure (Scheme 5.3).[11] Cb was deprotonated with 2 equivalents of *n*-BuLi in diethyl ether at −78 ºC and subsequently stirred for 2 hours at room temperature. The reaction was then cooled in the cold well again and 2 equivalents of diphenyl disulfide were added. The reaction stirred for 30 minutes at room temperature. An aqueous solution of KCl was then added to the stirring reaction. Following a classic organic workup, bis(1,2-phenylsulfido)*o*-carborane, **^{S}Cb** was isolated. The product was recrystallized from hot DCM with hexanes layered on top, at −40 ℃ to yield light pink crystals (Scheme 5.3).

The sulfoxyl derivative was obtained following a modified literature procedure.[12] To a stirring solution of **^{S}Cb** in DCM at 0 ℃, 2 equivalents of *m*CPBA were added dropwise (Scheme 5.3). The reaction was warmed to room temperature and was monitored by thin layer chromatography using a 2:3 ethyl acetate to hexanes eluent. After 2 days, the reaction was quenched with an aqueous solution of sodium bicarbonate. The reaction was extracted with

DCM then dried over magnesium sulfate and the volatiles were removed *in vacuo* to afford a crude mixture. The product was isolated by column chromatography to afford bis(1,2-sulfoxyl)*o*-carborane (**^{SO}Cb**) in a 38% yield (Scheme 5.3). A crystal suitable for X-ray diffraction studies was grown via vapor diffusion of hexanes into a concentrated solution of DCM at room temperature (Figure 5.5).

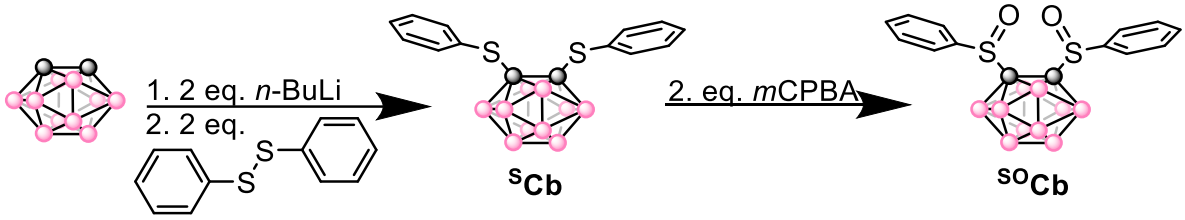

Scheme 5.3. Synthesis of sulfide and sulfoxyl *o*-carborane derivatives.

The unreported solid-state molecular structure of **^{SO}Cb** displays a carborane C_1–C_2 bond of 1.671(5) Å (Figure 5.5). It has S–O bonds (1.469(3) Å and 1.473(3) Å) comparable in length to the P−O bonds in bis(1,2-diarylphosphine oxide)*o*-carboranes (Table 2.1) which suggest that it may have similar Lewis basic properties. Interestingly, the S=O moieties are angled almost horizontally with a C_1–S_1–O_1 angle of 105.19(2)° and C_2–S_2–O_2 angle of 105.64(2)° (Figure 5.5a). The solid-state structure possesses C_{2V} symmetry and the $^{11}B\{^1H\}$ NMR spectrum contains 5 resonances because the phenylsulfoxide substituents are trans to each other (Figure 5.5b).

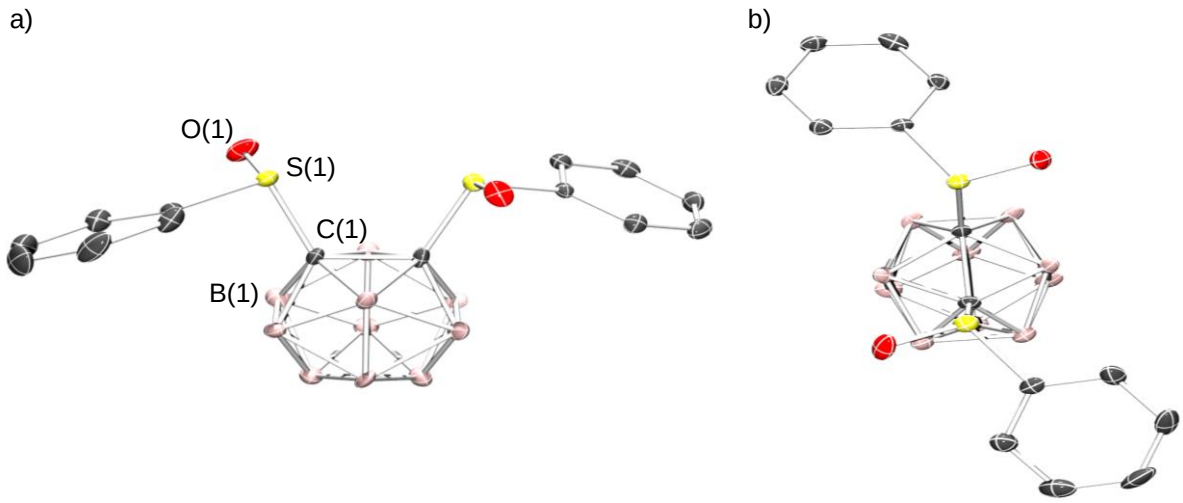

Figure 5.5. Solid-state molecular structure of ^{SO}**Cb** obtained by single crystal X-ray diffraction studies. a) horizontal view b) vertical view

We acquired CVs of ^{S}**Cb** (1.7 mM) and ^{SO}**Cb** (1.0 mM) in 0.1 M [Bu_4N][PF_6] THF (Figure 5.6). Both carboranes displayed a quasi-reversible electron transfer event which we presume to be the 2 e^- *closo/nido* redox couple. The CV of ^{SO}**Cb** displays an additional oxidation at −0.2 V which we suspect may be a contaminant. Adding electron withdrawing oxygens to the sulfide groups to attain sulfoxyl moieties results in a substantial anodic shift in the *closo/nido* redox couple. Specifically, the carborane redox couple of ^{S}**Cb** ($E_{1/2}$ = -1.68 V) shifts by 240 mV upon chemical oxidation to ^{SO}**Cb** ($E_{1/2}$ = -1.44 V) (Figure 5.6). We suspect that oxidizing the sulfoxyls even further to sulfonyl groups would also result in a sizeable anodic shift in the formal reduction potential.

We have attempted to synthesize bis(1,2-phenylsulfonyl)*o*-carborane (^{SO2}**Cb**) from ^{S}**Cb** using 4 equivalents of *m*CPBA. However, attempts have resulted in a mixture of products. We suspect that the oxidation does not go to completion and perhaps a triply oxidized carborane is attained with both a sulfonyl and a sulfoxyl appendage; though, we have not structurally characterized this yet by X-ray diffractions studies. We have also tried to

synthesize ^{SO2}**Cb** directly from Cb by deprotonating with *n*-BuLi or *t*-BuLi and reacting it with electrophile benzene sulfonyl chloride. However, this resulted in a fully deboronated product, likely with bis(1,2-sulfonyl) substituents. This is not surprising because electron withdrawing substituents increase the propensity for deboronation to occur because the 3,6-positions become more electropositive.[13]

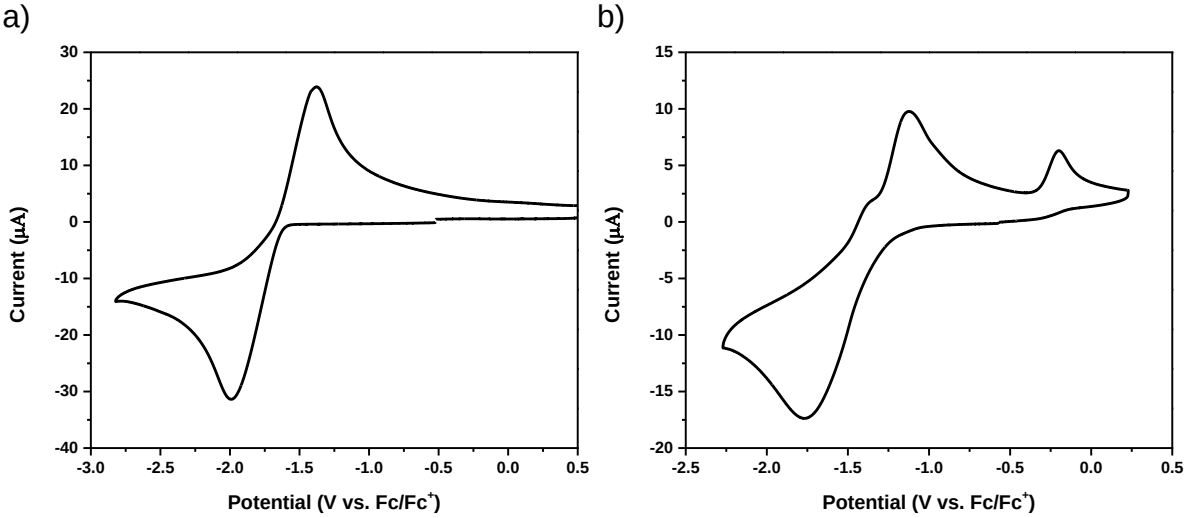

Figure 5.6. CVs of ^{S}**Cb** and ^{SO}**Cb** in 0.1 M $[Bu_4N][PF_6]$ THF at a 100 mV/s scan rate. A glassy carbon working electrode, Ag wire pseudo-reference electrode, and Pt wire counter electrode were used. a) ^{S}**Cb** b) ^{SO}**Cb**.

Preliminary binding experiments were performed with ^{S}**Cb** and soft acid, Hg^{2+}. A slurry of ^{S}**Cb** was stirred with 1 equivalent of mercury(II) acetate in diethyl ether for 3 hours. The reaction was filtered through a celite plug and an NMR taken in $CDCl_3$ was acquired. The ^{1}H and ^{11}B NMR spectra displayed no change relative to ^{S}**Cb** in absence of metal. Similarly, the reaction was attempted in THF wherein the 1 equivalent of fully dissolved mercury(II) acetate along with ^{S}**Cb**. However, the NMR spectra indicated that no change occurred. We suspect that ^{S}**Cb** does not bind to Hg^{2+}.

5.3. Summary

In Chapter 5, we have synthesized reported and new 1,2-substituted *o*-carboranes bearing carboxyl, amido, sulfido and sulfoxyl functional groups. The electrochemical properties of these substituted *o*-carboranes were explored and in conjunction with preliminary binding studies, we have elucidated additional guidelines to consider when designing redox-switchable *o*-carboranes for reversible metal binding.

First and foremost, the 1,2- ligating group has a colossal impact on the carborane redox chemistry. For example, carboxyl substituents did not appear to undergo an electrochemical reduction to *nido*-carborane in the scanned potential window. Conversely, amido derivatives (**$^{(2F)PhNO}$Cb** and **^{PhNO}Cb**) possess a carborane redox couple near -1.58 V whereas sulfido and sulfoxyl analogs undergo a reduction with formal reduction potentials of -1.68 V and -1.44 V respectively. Therefore, proximity of the substitution to the carborane cage is important. For example, adding four fluoro substituents to the phenyl ring on amido carboranes (**$^{(2F)PhNO}$Cb**) has a smaller effect on the carborane redox compared to adding two oxo substituents to sulfido carboranes (**^{SO}Cb**). Cage substituents (e.g., **^{PhNO}CbMe$_8$**) also tune redox properties. Additionally, the formal reduction potential of the carborane species versus the metal is critical for binding to occur. If the *nido*-carborane species is more reducing than the metal, outer sphere electron transfer may occur instead of metal capture.

5.4. Experimental

5.4.1. General Methods and Considerations

General Considerations

All manipulations were performed under an atmosphere of dry, oxygen-free N_2 or Ar by means of standard Schlenk or glovebox techniques (MBraun equipped with a -38 °C freezer, or VAC gloveboxes). Hexanes, pentane, DCM, THF, diethyl ether and benzene were dried on an MBraun solvent purification system. All solvents were stored over molecular sieves (3Å, Fisher). *Ortho*-carborane was purchased from Boron Specialties and sublimed before use. $[Bu_4N][PF_6]$ was purchased from Oakwood Chemicals and purified by twice recrystallizing from hot ethanol. The recrystallized product was then washed with cold water, cold ethanol, and pentane prior to drying at 100 °C under vacuum for 24 h. KC_8 was prepared using literature methods.[14]

5.4.2. Synthesis of Compounds

General Procedure for derivatized bis(1,2-amido)*o*-carboranes: The Cb (0.50 g, 3.5 mmol) was dissolved in diethyl ether and cooled using liquid nitrogen. The 2.5 M *n*-BuLi (2.8 mL, 7.0 mmol) was added dropwise over 10 minutes. The reaction stirred at room temperature for 2 hours. The aryl isocyanate (0.87 g, 7.3 mmol) was added and the reaction refluxed for 5 hours. The reaction was allowed to cool to room temperature and then it was neutralized to a pH of 7 using dilute HCl. The reaction was extracted into diethyl ether and dried over magnesium sulfate. The volatiles were removed *in vacuo* and the product was purified by column chromatography.

bis(1,2-(2,4-difluoroamido))*o*-carborane (**$^{(2F)PhNO}$Cb**): **^{1}H NMR (400 MHz, $CDCl_3$)** δ 8.21 – 7.89 (m, 2H), 6.97 – 6.83 (m, 1H). **^{11}B NMR (128 MHz, $CDCl_3$) δ -1.93, -9.02, -10.83. ^{19}F NMR (376 MHz, $CDCl_3$)** δ -111.90 (ddd, *J* = 13.6, 8.1, 5.5 Hz), -125.26 – -125.40 (m).

4,5,7,8,9,10,11,12-octamethyl-bis(1,2-amido)*o*-carborane (**^{PhNO}CbMe$_8$**): **^{1}H NMR (400 MHz, CDCl$_3$)** δ 7.82 (s, 2H), 7.38 (d, *J* = 7.7 Hz, 4H), 7.31 (dd, 4H), 7.16 (dd, 2H). **^{11}B NMR (128 MHz, CDCl$_3$)** δ 8.87, -1.12, -5.32, -13.03.

Potassium bis(1,2-(amido))*o*-carborane (**K$_2$^{PhNO}Cb**): **^{1}H NMR (400 MHz, CD$_3$CN)** δ 7.54 (d, *J* = 7.5 Hz, 1H), 7.20 (dd, 1H), 6.90 (dd, *J* = 7.4, 7.4 Hz, 1H). **^{11}B NMR (128 MHz, CD$_3$CN)** δ 4.87, -8.63, -18.72, -27.59.

Bis(1,2-sulfoxyl)*o*-carborane (^{SO}Cb**)**: To a stirring solution of **^{S}Cb** (0.100 g, 0.27 mmol) in DCM at 0 °C, 2 equivalents of 70% *m*CPBA (0.137 g, 0.55 mmol) were added dropwise. The reaction warmed to room temperature and was monitored by thin layer chromatography using a 2:3 ethyl acetate to hexanes eluent. After 2 days, the reaction was quenched with an aqueous solution of sodium bicarbonate. The reaction was extracted with DCM then dried over magnesium sulfate and the volatiles were removed *in vacuo* to afford a crude mixture. The product was isolated by column chromatography using 1:5 ethyl acetate to hexanes to afford bis(1,2-sulfoxyl)*o*-carborane (**^{SO}Cb**) as a white solid in a 37% yield. Crystals suitable for XRD studies were grown via vapor diffusion of DCM and hexanes. ^{1}H NMR (**400 MHz, CDCl$_3$**) δ 7.83 (d, *J* = 6.9 Hz, 1H), 7.73 – 7.56 (m, 2H). **^{11}B NMR (128 MHz, CDCl$_3$)** δ -2.15, -8.80, -11.18, -12.32, -14.14.

5.5. References

(1) Kasar, R. A.; Knudsen, G. M.; Kahl, S. B. Synthesis of 3-Amino-1-carboxy-o-carborane and an Improved, General Method for the Synthesis of All Three C-Amino-C-carboxycarboranes. *Inorg. Chem.* **1999**, *38* (12), 2936-2940. DOI: 10.1021/ic990037o.

(2) Heying, T. L.; Ager, J. W., Jr.; Clark, S. L.; Alexander, R. P.; Papetti, S.; Reid, J. A.; Trotz, S. I. A New Series of Organoboranes. III. Some Reactions of 1,2-

Dicarbaclovododecaborane(12) and its Derivatives. *Inorg. Chem.* **1963**, *2* (6), 1097-1105. DOI: 10.1021/ic50010a004.

(3) Kahl, S. B.; Kasar, R. A. Simple, High-Yield Synthesis of Polyhedral Carborane Amino Acids. *JACS* **1996**, *118* (5), 1223-1224. DOI: 10.1021/ja9534260.

(4) Rodríguez-López, N.; Wu, Y.; Ge, Y.; Villagrán, D. Hydrogen Evolution Catalyzed by a Metal-Free Corrole: An Experimental and Theoretical Mechanistic Study. *The Journal of Physical Chemistry C* **2020**, *124* (19), 10265-10271. DOI: 10.1021/acs.jpcc.9b10957.

(5) Nie, Y.; Wang, Y.; Miao, J.; Bian, D.; Zhang, Z.; Cui, Y.; Sun, G. Syntheses and structural characterization of o-carboranylamides with direct cage–amide bond. *Dalton Trans.* **2014**, *43* (13), 5083-5094. DOI: 10.1039/C3DT52785A.

(6) Brown, D. A.; Colquhoun, H. M.; Daniels, J. A.; MacBride, J. A. H.; Stephenson, I. R.; Wade, K. Polymers and ceramics based on icosahedral carboranes. Model studies of the formation and hydrolytic stability of aryl ether, ketone, amide and borane linkages between carborane units. *Journal of Materials Chemistry* **1992**, *2* (8), 793-804. DOI: 10.1039/JM9920200793.

(7) Keener, M.; Mattejat, M.; Zheng, S.-L.; Wu, G.; Hayton, T. W.; Ménard, G. Selective electrochemical capture and release of uranyl from aqueous alkali, lanthanide, and actinide mixtures using redox-switchable carboranes. *Chem. Sci.* **2022**, *13* (12), 3369-3374. DOI: 10.1039/D1SC07070C.

(8) Núñez, R.; Tarrés, M.; Ferrer-Ugalde, A.; de Biani, F. F.; Teixidor, F. Electrochemistry and Photoluminescence of Icosahedral Carboranes, Boranes, Metallacarboranes, and Their Derivatives. *Chem. Rev.* **2016**, *116* (23), 14307-14378. DOI: 10.1021/acs.chemrev.6b00198.

(9) Wahab, A.; Douvris, C.; Klíma, J.; Šembera, F.; Ugolotti, J.; Kaleta, J.; Ludvík, J.; Michl, J. Anodic Oxidation of 18 Halogenated and/or Methylated Derivatives of CB11H12–. *Inorg. Chem.* **2017**, *56* (1), 269-276. DOI: 10.1021/acs.inorgchem.6b02126.

(10) Burn, A. G.; Nash, K. L. Electrochemical behavior of uranyl in anhydrous polar organic media. *Radiochimica Acta* **2017**, *105* (7), 513-522. DOI: doi:10.1515/ract-2016-2684.

(11) Llop, J.; Viñas, C.; Oliva, J. M.; Teixidor, F.; Flores, M. A.; Kivekas, R.; Sillanpää, R. Modulation of the C□C distance in disubstituted l,2-R2-o-carboranes. Crystal structure of closo l,2-(SPh)2-l,2-C2B10H10. *J. Organomet. Chem.* **2002**, *657* (1), 232-238. DOI: https://doi.org/10.1016/S0022-328X(02)01637-6.

(12) Scott, R. N.; Hooks, H., Jr.; Sieckhaus, J. F. Icosahedral carboranes. XVII. Carboranyl sulfoxides and sulfones. *Inorg. Chem.* **1971**, *10* (10), 2358-2360. DOI: 10.1021/ic50104a064.

(13) Taoda, Y.; Sawabe, T.; Endo, Y.; Yamaguchi, K.; Fujii, S.; Kagechika, H. Identification of an intermediate in the deboronation of ortho-carborane: an adduct of ortho-carborane with two nucleophiles on one boron atom. *Chem. Commun.* **2008**, (17), 2049. DOI: 10.1039/b716079h.

(14) Lalancette, J.-M.; Rollin, G.; Dumas, P. Metals Intercalated in Graphite. I. Reduction and Oxidation. *Canadian Journal of Chemistry* **1972**, *50* (18), 3058-3062. DOI: 10.1139/v72-485.